DEFINING THE MOLECULAR MECHANISMS OF UBIQUITIN PROTEASOME SYSTEM DYSFUNCTION AS A DRIVER OF DISEASE: CHIP MUTATION IN SCAR16

Carrie E. Rubel

A dissertation submitted to the faculty of the University of North Carolina in partial fulfillment of the requirements for the degree of Doctor of Philosophy in the Department of Pharmacology.

Chapel Hill
2015

Approved by:

Mike Emanuele

Gary Johnson

Rob Nicholas

Jonathan Schisler

ABSTRACT

Carrie E. Rubel: Defining the Molecular Mechanisms of Ubiquitin Proteasome System Dysfunction as a Driver of Disease: CHIP mutation in SCAR16
(Under the direction of: Gary Johnson)

All cells must respond to changes in their environment including a plethora of physiologic and pathologic stresses in order to maintain homeostasis and survive. Protein homeostasis is particularly critical to cell survival and cells utilize multiple highly specialized and integrated methods of protein quality control (PQC) to ensure that proteins are appropriately folded and terminally misfolded proteins are eliminated to prevent proteotoxicity. PQC depends on an elegant collaboration between molecular chaperones and the ubiquitin-proteasome system (UPS). Disruption of PQC and subsequent proteotoxicity is an underlying molecular phenotype in disease pathologies in the brain and heart. Understanding the molecular mechanisms underlying diseases where disruption of PQC is central to disease pathology is key to our ability to intervene therapeutically. To this end, this thesis focuses on understanding the function of E3 ubiquitin ligases and how mutations in these key players in the UPS can drive disease pathology in the heart and brain. First, I describe and validate a novel method for the identification of E3 ubiquitin ligase substrates addressing a significant technological limitation in the field. Next, I describe the first discovery of human mutation in the E3 ubiquitin ligase CHIP in a form of spinocerebellar ataxia, Gordon Holmes Syndrome that has led to the establishment of a new disease designation, autosomal recessive spinocerebellar ataxia-16 (SCAR16) to describe spinocerebellar ataxia caused by homozygous or compound heterozygous mutation in CHIP.

Finally, I expanded upon this discovery to define the structural and functional consequences of CHIP mutation in SCAR16 and explore the deficits associated with this mutation in a genomic context utilizing a mouse model system providing the first *in vivo*, disease-relevant model of partial CHIP dysfunction. Together these studies provide novel tools to further our understanding of the UPS and reveal fascinating insight into the molecular mechanisms underlying CHIP mutation in SCAR16 disease that not only may facilitate the development of therapies for this devastating disease, but also contribute to our basic understanding of the UPS and its role in disease pathogenesis to drive successful investment, innovation, preclinical investigation and clinical study design in other disease areas.

To my husband and my children, the loves of my life and inspiration in all things

ACKNOWLEDGEMENTS

First and foremost I would like to thank my unofficial mentor Dr. Jonathan Schisler who has supported me through all of the work contained in this document, and a substantial amount that is not. His capacity to remain level headed, guide me in the right direction, and help me when no one else is able are just a few of the many reasons I was able to accomplish what I have during my time at UNC. Jonathan has demonstrated an infinite amount of patience, kindness and has taught me so much about science and life. I have yet to find a topic he knows nothing about and isn't willing to stop whatever he is doing and teach me. I could not be happier that he is now in a role at UNC where he will officially mentor many more students and postdocs as they will be both better scientists and human beings as a result. Jonathan, I sincerely and truly thank you, for everything.

Second, I wish to thank my original thesis advisor Dr. Cam Patterson. Though pulled in so many different directions he remained my steadfast supporter and mentor providing invaluable, well-timed scientific guidance and unyielding encouragement and support both during his time as my advisor and even after his departure to his new role at New York-Presbyterian Weill Cornell Medical Center.

Third, I'd like to thank the Department of Pharmacology and my current advisor Dr. Gary Johnson. Gary has been a great supporter throughout my graduate career and has taken particular care, taking me under his wing to ensure a seamless transition through the challenges of Cam's departure. I have always admired and appreciated his willingness to challenge us as

students to push to do our best science and drive to go out and get what we desire for our futures. I am so proud to be graduating as an alumna of the wonderful department he has been integral in building. All of the students, professors, and staff in the Pharmacology Department have been outstanding to work with each day. There are few places I have enjoyed doing and discussing science more. It has been a unique and wonderful experience to be instructed and educated by so many inspiring and intelligent leaders of their fields. In addition, all these lessons were learned alongside bright peers who have challenged me every day to do better and push further than at times I thought I was capable. Thank you, to all of you.

I'd also like to thank the Schisler and Patterson labs, both past and present. Much like a family, lab mates see all of your worst moments, frustrations, and challenges. They keep you humble and challenge you to be your best. They celebrate your peaks and provide support and guidance through the valleys, in science and in life. And most importantly, they share their highs and lows with you too, which can sometimes be the best distraction and knowing you have company somehow makes those valleys a little less dark. A particular thank you to our amazing former post-doc Dr. Sarah Ronnebaum and our former lab manager Holly McDonough who took me under their wings and taught me so much about CHIP, fielded hundreds of technical questions (many of which I am sure I asked more than once), put up with all my last minute ordering and most importantly kept me smiling. Thank for your help along the way and your continued encouragement and support.

I also must thank the members and administrators of the McAllister Heart Institute. It has been an honor and a pleasure to be a part of such a tremendous group of scientists. And, while I didn't spend nearly as much time studying the heart as I thought I would at the outset, I have

thrived as a result of your tremendous technical expertise, willingness to collaborate and unyielding support.

Finally, thank you to my family. Undoubtedly, from the day I took my first steps my parents have been my biggest cheerleaders. They managed the perfect balance of supporting me and driving me to succeed, somehow without it ever feeling pushy and for that I am so thankful. They instilled in me and my siblings a love for learning that I hope to pass on to my own children. Mom and Dad, you have always been there for me and your frequent visits, support, and love have helped stabilize me through this long journey. To my brother and sister, thank you for your kindness, caring and support through this adventure and most importantly for setting such a high bar to live up to. Thank you to my children, Evan and Leo, for always bringing a smile to my face even after the hardest of days in the lab. You are so sweet and kind and funny. You inspire me to always work harder and use this amazing education I have been so fortunate to receive to leave my mark on the world and make it a better place for you. Finally, thank you to my husband, Ross. You happily joined me on this crazy adventure back to the academic world despite a huge pay cut and the unknowns of a move to a whole new part of the country. I will forever be grateful for your sense of adventure, love and support and for helping me realize that I could have and do more. You have helped me stay focused through my constant stream of thoughts, ideas, complaints and jubilations all of which you've shouldered with an amazing degree of patience, love, endurance and your tremendous sense of humor. For all these reasons, and so many more, I thank and I love you.

TABLE OF CONTENTS

LIST OF TABLES

LIST OF FIGURES

LIST OF ABBREVIATIONS

2D-DIGE	Two-dimensional differential in gel electrophoresis
α	Alpha
β	Beta
β-gal	β-galactosidase
Ad	Adenovirus
AMPK	AMP-activated protein kinase
ANOVA	Analysis of variance
ARCA	Autosomal recessive cerebellar ataxia
ATP	Adenosine triphosphate
Atp5b	ATP Synthase, H+ Transporting, Mitochondrial F1 Complex, Beta Polypeptide
B	Brain
BN PAGE	Blue native polyacrylamide gel electrophoresis
BRDU	5-bromo-2'-deoxyuridine
CA	Cerebellar ataxias
cBSA	Cytoplasmic bovine serum albumin
CC	Charged coiled-coil domain
CD	Circular dichroism spectroscopy
cDNA	Copy deoxyribonucleic acid
CHIP	C-terminus of HSC70 interacting protein
Chr	Chromosome
CHX	Cyclohexamide chase

CryAB	αB-crystallin
CTRL	Control
DIA	Differential in-gel analysis
DLS	Dynamic light scattering
DMEM	Dulbecco's Modified Eagle Medium
DMSO	Dimethyl sulfoxide
DNA	Deoxyribonucleic acid
DRM	Desmin-related cardiomyopathy
DTT	Dithiothreitol
DUB	Deubiquitining enzyme
EPM	Elevated plus maze
FDA	United States Food and Drug Administration
FSH	Follicle-stimulating hormone
g	Grams
GFP	Green fluorescent protein
GHS	Gordon Holmes Syndrome
GL	Granular layer
GnRH	Gonadotropin-releasing hormone
h	Hours
H	Heart
HET	Heterozygous
HOM	Homozygous
HSC70	Heat shock cognate 71 kDa protein

HSF1	Heat shock transcription factor 1
hsp25	Heat shock protein 25
Hsp40	Heat shock protein 40
Hsp60	Heat shock protein 60
Hsp70	Heat shock protein70
Hsp90	Heat shock protein 90
Hspd1	Heat Shock 60kDa Protein 1 (Chaperonin)
Hsps	Heat shock proteins
IB	Immunoblot
IBD	Identical by descendent
indels	Insertions or deletions
IP	Immunoprecipitation
iTRAQ	Isobaric Tags for Relative and Absolute Quantification
K	Lysine
kDa	Kilodalton
KO	Knockout
L	Liver
LH	Leutinizing hormone
LKB1	Liver kinase B1
LOD	Logarithmic ratio
LRRK2	Leucine-rich repeat kinase-2
MAFbx	Muscle atrophy F-box
MALDI-TOF	Matrix Assisted Laser Desorption/Ionization time-of-flight mass spectrometry

MDM2	Murine double minute 2
MEF	Mouse embryonic fibroblast
Met	Methionine
min	Minutes
miRNA	Micro ribonucleic acid
ML	Molecular layer
MRI	Magnetic resonance imaging
mRNA	Messenger ribonucleic
MS	Mass spectrometry
MuRF1	Muscle RING-finger proteins 1
NHLBI	National Heart, Lung, and Blood Institute
nm	Nanometer
NMR	Nuclear magnetic resonanse spectroscopy
NRVM	Neonatal rat ventricular myocytes
OTUD4	OTU Deubiquitinase 4
PBS	Phosphate buffered saline
PCR	Polymerase chain reaction
PKCϵ	Protein kinase C-ϵ
PLSD	Fisher's protected least-significant difference
PLSD	Purkinje cell layer
PPARα	Peroxisome proliferator-activated receptor-α
PQC	Protein quality control
RNF216	Ring Finger Protein 216

SCA1	Spinocerebellar Ataxia Type 1
SCA3	Spinocerebellar Ataxia Type 3
SCAR16	Autosomal Recessive Spinocerebellar Ataxia-16
SDS	Sodium dodecyl sulfate
SDS PAGE	Sodium dodecyl sulfate polyacrylamide gel electrophoresis
sec	Seconds
SEM	Standard error of the mean
shCTRL	Short-hairpin RNA control
SirT6	Sirtuin-6
SNPs	Single nucleotide polymorphisms
SOD1	Superoxide Dismutase 1
STUB1	STIP1 Homology and U-Box Containing Protein 1
T	Testes
Thr	Threonine
Tm	Melting temperature
TMT	Tandem Mass Tags
Tpm1	Tropomyosin 1 (Alpha)
TPR	Tetracopeptide repeat domain
TRIM9	Tripartite Motif-Containing Protein 9
TUBE	Tandem Ubiquitin Binding Entities
Ub	Ubiquitin
UBE3A	Ubiquitin protein ligase E3A
UPS	Ubiquitin-proteasome system

UV	Ultraviolet
Wk	Week
WT	Wildtype

CHAPTER I

INTRODUCTION[1]

Organisms must respond to changes in their environment in order to maintain homeostasis and survive. These environmental changes include a plethora of physiologic and pathologic stresses, such as perturbations in pH, temperature, and osmotic pressure; mechanical strain; oxidative stress; and alterations in the genetic code. In any case, when faced with these challenges, every individual cell that composes each unique organ and tissue must be equipped with and successfully mobilize specific mechanisms corresponding to the needs of that cell type for the overall maintenance of the organism.

While cellular homeostasis encompasses many types of biomolecules, protein homeostasis is particularly critical to cell survival because of the central role proteins play in so many cellular processes. Proteins are the building blocks of the cell and also perform a vast array of functions within living organisms, including catalyzing metabolic reactions, replicating DNA, responding to stimuli, and transporting molecules from one location to another. Cells utilize multiple highly specialized and integrated methods of protein quality control (PQC) to ensure that 1) proteins are appropriately folded, and that 2) terminally misfolded proteins are eliminated

[1]All Figures Contributed by Carrie Rubel and Adapted from Jonathan Schisler

both under basal conditions as well as when exposed to molecular stressors. PQC depends on an elegant collaboration between molecular chaperones and the ubiquitin-proteasome system (UPS). The UPS is largely responsible for targeted proteolysis in the cell. When a misfolded or damaged protein fails to be repaired by chaperone-mediated processes, it will be degraded by the UPS.

The pathophysiological significance of proper PQC is well illustrated during proteotoxicity. If the UPS becomes impaired or overwhelmed, the cell is unable to sufficiently clear misfolded proteins. These proteins may then associate with one another to form sequentially higher order protein aggregates, such as soluble oligomers, soluble aggregates, and eventually, inclusion bodies.[1] Experimental evidence in neurodegenerative diseases suggests that protein aggregates or any one of the preceding intermediaries, even soluble protein oligomers, may induce cell death, a process termed proteotoxicity.[2, 3] With their very limited capacity for self-renewal, this can be quite detrimental to post-mitotic cells in organs such as the heart and brain. In fact, proteotoxicity has long been associated as an underlying molecular phenotype in disease pathologies in the brain, including Alzheimer's, Parkinson's and Huntington's diseases, and is beginning to be appreciated as a driver of disease pathologies in the heart.[1, 4-6] In the heart and brain, proteotoxicity is a common hallmark of proteinopathies – diseases associated with the accumulation of malformed protein. Importantly, the underlying molecular phenotype of proteinopathy has most commonly been attributed to the accumulation of a particular malformed protein, usually as the result of its genetic mutation. However, as our understanding of PQC has expanded, proteinopathies are increasingly appreciated to also encompass diseases that result in the general accumulation of abnormal proteins as a result of disruption of PQC, for example as a result of genetic mutation of a component of the UPS.

Our understanding of the molecular components and mechanisms involved in cellular PQC has grown deeper in recent years and will likely expand exponentially as we fully appreciate and even exploit the opportunities presented by the overlap between pathologies in the heart and brain, both pre-clinically and clinically. In the United States alone, more than 5 million Americans have Alzheimer's disease, and heart disease remains the most common cause of death and disability in our society.[1, 7] Yet, current therapies are severely limited for these and other diseases where disruption of PQC is central to disease pathology, and the need for additional therapies remains substantial. Developing better tools for studying these pathways and uncovering the underlying molecular mechanisms and links between disruption of PQC and disease pathology in humans will undoubtedly generate translational outcomes, allowing for the cultivation of novel and highly specific treatment options for these cardiovascular and neurological conditions.

The work of this thesis focuses on understanding the molecular mechanisms underlying diseases where disruption of PQC is central to disease pathology. Specifically, I focus on understanding the function of E3 ubiquitin ligases and how mutations in these key players in the UPS can drive disease pathology in the heart and brain. One limitation to our understanding of E3 ubiquitin ligases is that current methods to identify E3 ubiquitin ligase substrates rely heavily upon non-physiologic *in vitro* methods, impeding the unbiased discovery of physiological substrates in relevant model systems. In the following, I begin by describing a novel method for identifying ubiquitin ligase substrates utilizing the E3 ubiquitin ligase, MuRF1 (muscle RING-finger proteins 1) because of its importance as a modulator of heart muscle protein homeostasis. However, this method can be applied to any E3 ubiquitin ligase, both in normal and disease model systems, in order to identify relevant physiological substrates under various biological

conditions, opening the door to a clearer mechanistic understanding of E3 ubiquitin ligase function and broadening their potential as therapeutic targets.

I then focus on the protein E3 ubiquitin ligase CHIP (C-terminus of HSC70 interacting protein) encoded by the *STUB1* gene. Loss of CHIP function has long been associated with protein misfolding and aggregation in several genetic mouse models of neurodegenerative disorders, and genetic depletion in mice results in robust hypertrophy and decreased cardiac function.[8, 9] However, a role for CHIP in human disease had yet to be identified. Here I describe the first discovery of CHIP point mutation, *STUB1* c.737C→T, p.Thr246Met, in a form of spinocerebellar ataxia, Gordon Holmes Syndrome, that has led to the establishment of a new disease designation, SCAR16 (Autosomal Recessive Spinocerebellar Ataxia-16) to describe spinocerebellar ataxia caused by homozygous or compound heterozygous mutation in the *STUB1* gene. I then expand upon this discovery to define the structural and functional consequences of CHIP mutation in SCAR16 and explore the deficits associated with this mutation in a mouse model system, providing the first definition of partial CHIP dysfunction and assignment of specific *in vivo* deficits that result as a consequence of partial (but not total) loss of CHIP function. By determining how CHIP mutation contributes to SCAR16 pathology, we will potentially identify means for modulating CHIP and/or its substrates/interactors as therapeutic targets for SCAR16.

Disruption of PQC and Proteotoxicity in Human Disease

Disruption of PQC and subsequent proteotoxicity is being increasingly recognized as a driver of disease pathology in both the heart and brain. This parallel between pathologies in the heart and brain is not largely surprising, given the importance of post-mitotic, terminally

differentiated cell types in these tissues. In these cells, misregulation of protein homeostasis may have more dire consequences, as post-mitotic cells cannot dilute out toxic proteins by cell division, and dead or dying cells cannot be readily replaced.

The heart is a unique organ, constantly barraged with molecular stressors, such as the mechanical stress from perpetual contractions.[10] The cardiomyocyte is well-adapted to withstand this level of stress. Cardiomyocytes are loaded with a huge amount of mitochondria to ensure that the energy demands of the cell are met and allow the heart's perpetual motion to proceed. Cardiomyocytes are equipped with sophisticated and proficient mechanisms of cellular PQC, as discussed above, to eliminate misfolded proteins that could become deleterious if allowed to persist in the sarcoplasm.[1] It has been recently discovered that an underlying molecular phenotype of many types of cardiac dysfunction is the accumulation of misfolded protein, suggesting that a breakdown in the fidelity of misfolded protein removal may play a causative role in cardiac pathologies. Protein misfolding has been suggested as a key contributor to the progression of heart failure, with evidence of proteotoxicity and PQC dysregulation in pathologic cardiac hypertrophy and dilated and ischemic cardiomyopathies.[1, 5, 6] Indeed, it is thought that at least 30% of translated protein, for various reasons, never reaches its appropriate cellular location,[11] so disruption of the PQC mechanisms in the heart can quickly lead to protein buildup and accelerate deleterious effects downstream.

While protein accumulation in the heart has been observed for decades, desmin-related cardiomyopathy (DRM) is probably the best understood cardiac disease stemming from proteinopathy and associated proteotoxicity.[12] DRM is a myofibrillar myopathy characterized by muscle weakness and cardiomyopathy. While the cause of the disease was unknown, histological

analysis showed a striking feature: electron-dense intracellular inclusion bodies that positively immunostained for desmin. Two papers published in 1998 showed that mutations in the intermediate filament protein desmin[13] or its chaperone αB-crystallin (CryAB)[14] can cause DRM. These genes were discovered in two families with DRM, demonstrating that a mutation in either of these genes can lead to heritable disease.

In an attempt to understand these inclusions and how they affect cardiac function, Wang et al developed transgenic mouse models overexpressing DRM-related mutations in desmin (DesD7) or CryAB ($CryAB^{R120G}$) in a cardiac-specific manner.[15, 16] The hearts of these mouse models developed hypertrophy and progressed to heart failure in early adulthood. Pathological analysis revealed that the hearts developed extensive fibrosis and, importantly, displayed the characteristic intracellular inclusions of DRM. These inclusions accumulate in the perinuclear region of cardiomyocytes and contained both CryAB and desmin. In addition, these inclusions were found to also contain proteins involved in the cardiac adaptation to stress, including heat shock protein 25 (Hsp25) and ubiquitin. This evidence suggests that these inclusions may be aggresomes, a common hallmark of neurodegenerative phenotypes. While DRM is a severe and unique case of cardiomyopathy derived from proteotoxicity, it is rare. However, this model clearly demonstrates that deficits in PQC mechanisms can have severe and devastating effects and are sufficient to cause heart failure.

Like cardiomyocytes, the neurons that make up the brain are largely senescent cells, and numerous proteotoxic entities have been shown to affect this cell type, leading to neuronal cell death. In fact, disruption of PQC, accumulation of misfolded proteins, and resulting proteotoxicity has long been appreciated as a key underlying molecular phenotype in disease

pathologies in the brain.[17, 18] More than 100 years ago Dr. Alois Alzheimer observed abnormal accumulations of protein in the brain of his patient who died from what was then described only as “an unusual mental disease.”[19] Since this first observation, the list is ever-expanding as we have come to understand that misfolded proteins are central to the pathophysiology of not only Alzheimer’s disease, but many other neurodegenerative diseases including Huntington's disease, Parkinson's disease, Amyotrophic Lateral Sclerosis, and more recently polyglutamine expansion diseases like Spinocerebellar Ataxia Type 3 (SCA3).[4] In this disease class, the proteotoxic entity can take many forms, including α-synuclein, beta-amyloid and tau, huntingtin, and SOD1, which are the molecular bases for Parkinson’s, Alzheimer’s, Huntington’s, and Amyotrophic Lateral Sclerosis, respectively .

Common to all of these diseases is the presence of misfolded protein accumulated within the cell or within the extracellular space. However, the molecular drivers behind the toxic accumulation of protein in each of these disease pathologies may differ. In some cases, certain polypeptides, such as hyperphosphorylated tau in Alzheimer’s disease, which have a propensity towards misfolding, leads to their spontaneous misfolding and rapid aggregate formation.[20] In others, genetic mutation in specific proteins, such as huntingtin in Huntington’s disease or α-synuclein in Parkinson’s disease, disrupts their folding, leading to aggregate formation.[21, 22] One common thread to these disease pathologies, however, is reduced UPS activity in the brain. Many studies have identified reduced proteasome activity associated with aging, resulting in a diminished capacity to clear misfolded protein, contributing to the formation of pathological protein aggregates.[23-25] To make matters worse, the accumulation of aggregates of both mutated proteins and aggregation-prone proteins has been shown to further inhibit the activities of the UPS, including the proteasome, promoting this vicious cycle of misfolded protein accumulation

and subsequent aggregation.[24, 26-30] For example, ubiquitinated and aggregated tau in Alzheimer's disease as well as aggregated mutant α-synuclein in Parkinson's disease can block the gate of the 19S catalytic subunit of the proteasome by binding to its recognition site, blocking proteasome enzymatic activity and impairing proteasomal degradation. [24, 28, 31]

Inhibition of the proteasome is not the only disruption of PQC that is proposed to drive disease pathogenesis in neurodegeneration. Studies have also implicated impairments in ubiquitination and deubiquitination as well as substrate delivery to the proteasome. Examples include the mutation of the cytosolic E3 ubiquitin ligase parkin in Parkinson's disease and the deubiqutinating enzyme Ataxin-3 in SCA3. Both inherited and/or sporadic mutation of either of these proteins not only leads to increased propensity towards aggregation of these proteins, potentially driving proteasome impairment and proteotoxicity, but also inhibits these proteins' respective UPS functions as an E3 ubiquitin ligase and a deubiquitining enzyme (DUB).[32, 33] Under conditions of stress, parkin is normally recruited to the outer membrane of the mitochondria, where it polyubiqutinates and directs proteasomal degradation of outer mitochondrial membrane proteins, including Mitofusins 1/2.[34, 35] Loss of parkin function has been associated with reduced polyubiquitination of these outer mitochondrial membrane proteins, the accumulation of damaged mitochondria and increased cell death.[33]

Similarly, Ataxin-3 is a highly conserved DUB with a flexible C-terminal tail that features three ubiquitin-interacting motifs flanking a polyQ region of variable length. Abnormal expansion of the polyQ region to more than 53 glutamines is pathological and manifests in SCA3. Like mutant parkin, not only does accumulation of this mutant Ataxin-3 lead to its toxic aggregation, but may also drive proteotoxicity due to loss of DUB function, as expression of pathogenic Ataxin-3 *in vivo* has been associated with higher global levels of ubiquitinated

proteins than the nonexpanded form, likely due to reduced DUB activity of pathogenic Ataxin-3 as a result or impaired substrate binding or proteolysis.[36] Interestingly, Ataxin-3 has also been reported to regulate protein turnover of other UPS proteins, including the E3 ligase CHIP, thus further expanding the potential implications of Ataxin-3 mutation on UPS activity and UPS dysregulation as a driver of disease pathogenesis.[37]

While in many cases the precise molecular mechanisms of protein aggregation, proteotoxicity, and the causative deficiencies in PQC that promote disease pathogenesis in the heart and brain remain to be elucidated, it is clear that disruption of PQC is a key driver of disease in both the heart and brain and modulation of PQC pathways represents a putative therapeutic strategy for the treatment of these devastating diseases.

PQC and the UPS

Coordinated PQC is crucial to the maintenance of the proteome both under basal conditions and particularly under conditions of stress. PQC encompasses both the refolding of misfolded proteins largely by molecular chaperones, as well as their degradation by the degradative machinery of the UPS. We define a molecular chaperone as any protein that interacts with, stabilizes, or helps another protein to acquire its functionally active conformation, without being present in its final structure.[38] As such, molecular chaperones are responsible for not only promoting the proper *de novo* folding of newly synthesized proteins and their translocation across membranes, but also the refolding of stress-denatured substrates. Due to their upregulation during conditions of stress that result in protein denaturation, such as elevated temperature molecular chaperones are often referred to as heat-shock proteins (Hsps). Most Hsps are classified by their molecular weight and include small Hsps, Hsp40, Hsp60, Hsp70 and Hsp90.[39,

[40] With their inherent ability to recognize and bind non-native proteins, chaperones serve as the first line of defense against the accumulation of misfolded proteins and triage them appropriately. This triage occurs either directly by facilitating their refolding to a functional native state, or, when this is not possible or is not energetically favorable, promotes their degradation by the UPS. Interestingly, the activity of some Hsps, including Hsp70 and Hsp90, is regulated by their direct interaction with proteins termed molecular co-chaperones. These molecular co-chaperones, including members of the UPS such as E3 ubiquitin ligase CHIP, modulate chaperone function and expression and consequently regulate the molecular triage decision determining whether substrate proteins enter the productive folding pathway or the degradation pathway.[41] The function of these molecular co-chaperones is particularly intriguing as it represents a direct link between the two mutually exclusive pathways of folding and degradation that are central to PQC.

The UPS

As described extensively in the previous section the UPS is critical to the regulation of protein homeostasis in both the heart and brain, emphasized by myriad cardiovascular and neurodegenerative diseases linked to altered UPS function, including cardiac hypertrophy, heart failure, diabetes, ischemia-reperfusion injury, Alzheimer's, Parkinson's and Huntington's diseases.[42 43] Here I focus on its role as degradative machinery, but it should be noted that the UPS is also increasingly being recognized for its role in non-proteolytic regulatory mechanisms, including membrane transport, chromatin structure and transcription, DNA repair and diverse signaling pathways.[44-46]

Ubiquitination is a multi-step enzymatic process that covalently links the carboxylic acid of the small protein ubiquitin to a substrate protein lysine to form a covalent amide bond. Substrate specificity of the ubiquitination reaction occurs at the level of the E3 ubiquitin ligase.[47, 48] However, prior to substrate recognition and ubiquitin transfer by the E3 ubiquitin ligase, ubiquitin is activated in a two-step process involving the E1 ubiquitin-activating enzyme and the E2 ubiquitin conjugating enzyme. First, in an ATP-dependent process, the E1 enzyme interacts with ubiquitin, forming a thioester linkage between the C-terminal carboxyl group of ubiquitin and the E1 sulfhydryl moiety. Next, the ubiquitin is transferred to the active cysteine of the E2 enzyme. The ubiquitin molecule is now ready to be finally transferred to the substrate protein lysine by the E3 enzyme in a substrate-specific and highly regulated reaction. This process can then be repeated, adding additional ubiquitin molecules to generate a polyubiquitin chain. The human genome encodes >600 E3 ubiquitin ligases that are specific to particular targets, while just two E1 ubiquitin-activating enzymes and 38 E2 ubiquitin conjugating enzymes participate in different ubiquitination reactions.[49]

E3 ubiquitin ligases function as distinct molecular regulators as the modulators of UPS specificity and so are the focus of this thesis work. At least nine E3 ubiquitin ligases have been identified in the heart, including CHIP; MuRF-1, MuRF-2, and MuRF-3 (muscle RING-finger proteins 1, 2, and 3); atrogin-1/MAFbx (muscle atrophy F-box); and MDM2 (murine double minute 2).[50] In the brain, the list is significantly longer, but also includes CHIP and MDM2 as well as UBE3A (ubiquitin protein ligase E3A), Parkin and brain-specific TRIM9 (Tripartite Motif-Containing Protein 9).[51] Ubiquitin post-translational modification can occur by the addition of a single ubiquitin (monoubiquitination) or as a chain of ubiquitins (polyubiquitination), with these chains varying in length and linkage type. Ubiquitin has seven

lysine (K) residues by which polyubiquitination can occur (K6, K11, K27, K29, K33, K48 and K63), as well as the amino-terminus. Both homogenous and heterogeneous ubiquitin chains can be formed, utilizing the same lysine on each ubiquitin in the former and different ubiquitin lysines in the latter.[52] The fate of the ubiquitinated protein depends upon which lysine residue within the protein the ubiquitin is attached to and the length and linkage type of the added ubiquitin. (Fig. 1.1) Addition of canonical K48 polyubiquitin chains of at least four ubiquitin molecules leads to subsequent degradation of the substrate protein by the 26S proteasome. Monoubiquitination and non-canonical polyubiquitination via other linkage types and branched chains containing multiple linkage types can also occur, and generally do not target proteins for UPS-mediated degradation, but rather regulate substrate proteins via non-proteolytic mechanisms, including modulating protein localization, activity, or stability.[53, 54]

The 26S ubiquitin proteasome is a cylindrical molecular machine consisting of a proteolytic 20S core particle capped at both ends by a 19S regulatory particle.[49, 55] The center barrel-shaped proteolytic chamber of the 20S core particle has a narrow diameter of as little as 13 angstroms, thus restricting the size of the entering polyubiquitinated substrate proteins.[56] Thus, upon binding the polyubiquitinated substrate protein, the 19S particle deubiquitinates the substrate, recycling the ubiquitin, and unfolds the protein, feeding the now unfolded polypeptide chain into the center of the 20S core particle for proteolytic degradation. This proteolytic degradation is achieved by the combined activities of the β1, β2 and β5 subunits that have caspase-like, chymotrypsin-like and trypsin-like peptidase activities, respectively.[57-59]
Similar to other post-translational modifications, ubiquitination is reversible. A key component in this process of both proteasomal degradation and non-proteolytic protein regulation by ubiquitin are a family of approximately 100 enzymes called DUBs. DUBs are responsible for

disassembly of polyubiquitin chains and removal of ubiquitin from substrates by cleavage of the bonds between ubiquitin and protein.[60] In this role, DUBs play a critical role in regulating the dynamics of ubiquitination, proofreading ubiquitination and recycling ubiquitin. Functionally this may spare some proteins from degradation, reverse changes in cellular localization or alter protein-protein interactions.[61] An additional layer of specificity is added to the UPS by the work of DUBs, as they contain varying ubiquitin binding domains which confer specificity for different ubiquitin chains.[62, 63]

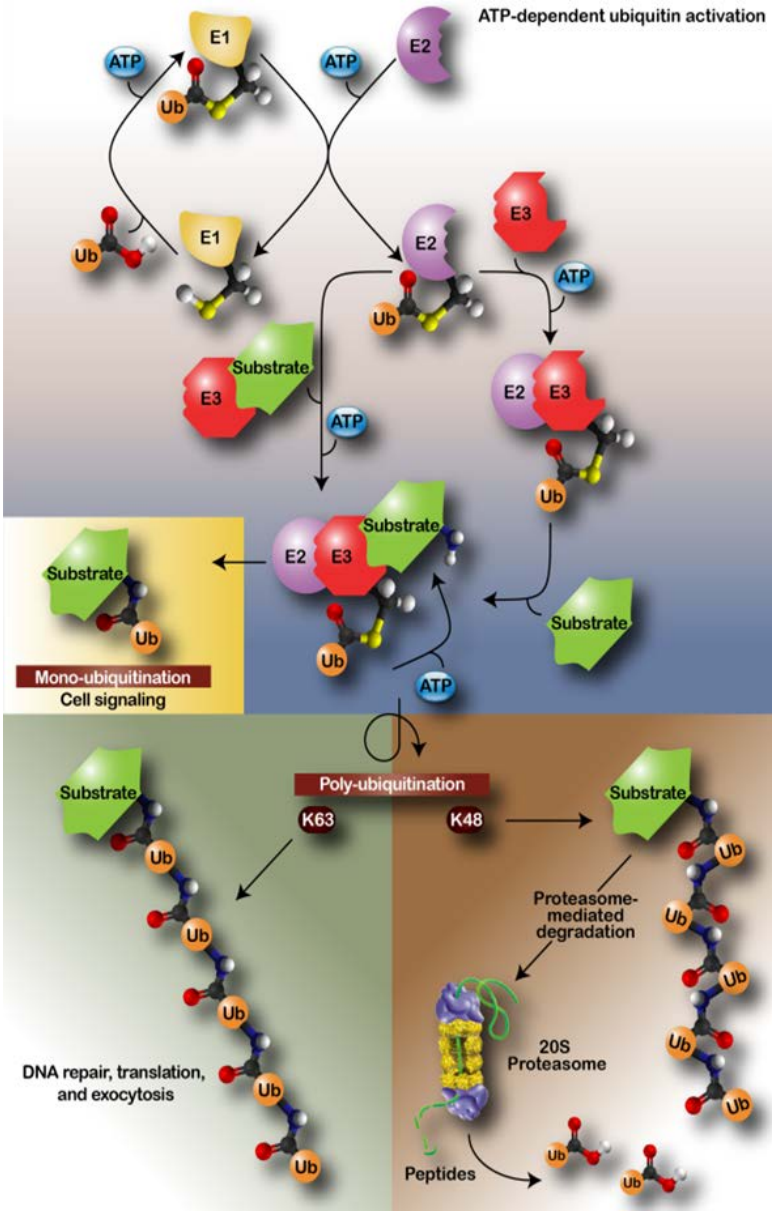

Figure 1.1 The Ubiquitin Pathway. Ubiquitin conjugation of substrates occurs in a series of ATP-dependent reactions facilitated by the coordinated efforts of E1 ubiquitin-activating enzymes, E2 ubiquitin conjugating enzymes and E3 ubiquitin ligases. Substrate specificity of the ubiquitination reaction is determined by the E3 ubiquitin ligase. The fate of ubiquitinated substrates is dependent upon the length and type of the ubiquitin linkage.

MuRF1

This work begins by focusing on the description of a novel method for the identification of E3 ubiquitin ligase substrates, specifically substrates of MuRF1. The development of this methodology addresses a significant gap in our ability to fully understand E3 ubiquitin ligases by creating a novel and improved method to identify relevant substrates under various biological conditions. MuRF1 is a muscle-specific E3 ubiquitin ligase regulating the function and stability of numerous proteins in multiple regions of the cardiomyocyte.[64, 65, 66] It is known to be involved in PQC and reorganization of the cardiac sarcomere by placement of polyubiquitin chains on substrates, including troponin I, β/slow myosin heavy chain and myosin binding protein-C, targeting them for destruction by the proteasome.[66-69] MuRF1 cellular localization is key to the specificity of substrates it regulates and the consequences of this ubiquitination. Outside the sarcomeric M-line, MuRF1-mediated ubiquitination can also regulate its substrates via non-proteolytic mechanisms. For example, in the nucleus of cardiomyocytes, MuRF1 regulates the nuclear export of peroxisome proliferator-activated receptor-α (PPARα), and in the perinuclear region it interacts with the receptor for activated protein kinase C-1, inhibiting the translocation of protein kinase C-ϵ (PKCϵ) to focal adhesions following stimulation with G protein-coupled receptor agonists.[64, 70] At the functional level of the myocardium, MuRF1 has been shown to be important in multiple cardiac disease models. In models of global ischemia-reperfusion (I-R) injury both *in vitro* and *in vivo*, MuRF1 demonstrates dramatic cardioprotection from I-R injury, in part mediating phospho-c-Jun degradation.[66] Additionally, MuRF1 inhibits pathological cardiac hypertrophy induced by pressure overload *in vivo* and is required for induction of cardiac atrophy following transaortic constriction.[71, 72] As a multi-faceted muscle-specific E3 ligase with well-established molecular targets and clear functional links to cardiac pathologies, MuRF1 is clearly a valuable test E3 ubiquitin ligase for validation of our substrate screening methodology.

Furthermore, given our interest in understanding how dysregulation of protein homeostasis can lead to disease pathology in the heart, studying MuRF1 in this capacity not only provides validation of our method but also has led to the identification of physiological substrates of MuRF1 that may provide mechanistic insight these cardiac pathologies and possible therapeutic targets.

CHIP and Spinocerebellar Ataxia

CHIP is an E3 ubiquitin ligase encoded by the *STUB1* gene that is abundantly expressed in most tissues and plays a central role in maintaining PQC. CHIP is uniquely suited as a regulator of PQC due to its dual functions as both a molecular co-chaperone protein and E3 ubiquitin ligase enzyme. As a co-chaperone, CHIP interacts with Hsp-bound proteins to aid in substrate stabilization and refolding.[73] Conversely, as a ubiquitin ligase, CHIP ubiquitinates terminally-defective proteins and prepares them for degradation by the UPS (Fig. 1.2). Additionally, CHIP regulates activation of the stress-chaperone response through induced trimerization, nuclear localization and transcriptional activation of heat shock transcription factor 1 (HSF1),[74] which upregulates levels of Hsps that are then subsequently ubiquitinated and targeted for proteasomal degradation by CHIP after all substrates have been refolded or ubiquitinated.[75] In addition to Hsp chaperone protein substrates,CHIP has also been reported to ubiquitinate numerous other substrates, including neuronal substrates α-synuclein and leucine-rich repeat kinase-2 (LRRK2) and to regulate the proteasomal degradation of tumor suppressor p53.[76-78]

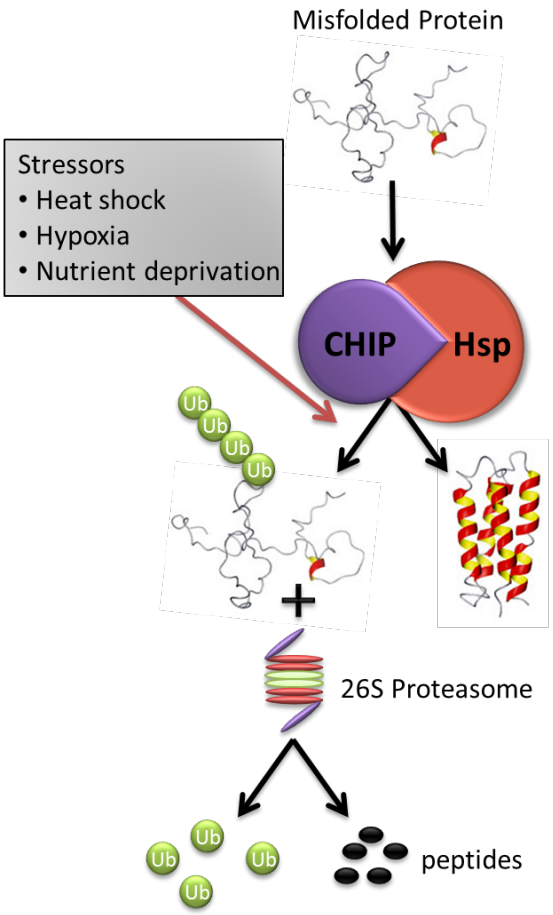

Figure 1.2. Traditional Roles of CHIP in PQC. CHIP bridges two PQC functions with opposite purposes. Under cellular stress, CHIP interacts with Hsp chaperone proteins to determine the fate of misfolded proteins, preventing their accumulation and subsequent proteotoxicity. As an E3 ubiquitin ligase, CHIP can ubiquitinate misfolded proteins, targeting them for proteasomal degradation. Conversely, CHIP can act as a molecular co-chaperone, aiding the Hsp chaperone protein refolding and recycling of the damaged substrate proteins.

CHIP contains three primary functional domains: the tetracopeptide repeat (TPR) domain, the charged coiled-coil (CC) domain, and the U-box domain. The TPR domain is required for chaperone protein binding. CHIP dimerization and structural conformational flexibility are required for activation of the bound E2 conjugating enzyme and subsequent ubiquitin transfer. This dimerization and conformational flexibility are dependent upon both the U-box domain and CC domain.[79, 80]

Since the discovery of CHIP in 1999,[81] numerous reports have been published detailing CHIP's co-chaperone and ubiquitin ligase activities in both the brain and heart. Loss of CHIP function has long been associated with protein misfolding and aggregation in several genetic animal models of neurodegenerative disorders.[9, 77, 82] CHIP modulates the effects of polyglutamine-induced neurodegeneration, protecting cells from neurotoxicity by interacting with and ubiquitinating expanded ataxin-1 in a Drosophila model of Spinocerebellar Ataxia Type 1 (SCA1).[82] Additionally, Dickey et al. showed that genetic depletion of CHIP leads to the accumulation of toxic phospho-tau in mouse brain, demonstrating that polyubiquitination of tau by CHIP may facilitate the formation of less cytotoxic insoluble filamentous tau lesions.[9] Furthermore, genetic depletion of CHIP in mice results significant deficits in multiple models of cardiac disease.[8, 83-86] When CHIP-/- mice undergo ischemia/reperfusion injury, the size of myocardial infarction (as assessed by the ratio of infarct area to area at risk) is increased by 50% relative to wild type controls, and the hearts from these mice lacking CHIP are more susceptible to apoptosis and have a markedly increased frequency of reperfusion arrhythmias.[84] Additionally, induction of cardiac pressure overload in CHIP-/- mice results in robust hypertrophy and decreased cardiac function.[8] Together these data suggest the particular importance of CHIP as a regulator of PQC in the heart under stress. In addition to these

important implications in models of heart disease and neurodegeneration that highlight CHIP's traditional roles as an E3 ubiquitin ligase and co-chaperone, recent reports have also emerged detailing surprising new roles for CHIP, including involvement in cardiac metabolic homeostasis (as a regulator of AMP-activated protein kinase (AMPK)) and DNA damage repair (as a regulator of Sirtuin-6 (SirT6)).[8, 87] However, until recently, a role for CHIP in human disease had yet to be identified.

Here I describe the first direct association between a CHIP polymorphism and a human disease with the discovery of CHIP point mutation, *STUB1* c.737C→T, p.Thr246Met, in a form of spinocerebellar ataxia, Gordon Holmes Syndrome (GHS). GHS is a rare and devastating neurodegenerative disorder characterized by cerebellar ataxia with hypogonadism.[88] GHS belongs to a family of rare recessively inherited ataxia disorders known as autosomal recessive cerebellar ataxia (ARCA) (estimated prevalence is 7 per 100,000).[89] The mutations associated with ARCA affect functionally diverse genes; furthermore, the underlying genetic basis and pathophysiological mechanisms are largely unknown, resulting in severely limited therapeutic options. Interestingly, this and six additional independent reports have identified 10 *STUB1* mutation genotypes in a diverse pool of ARCA patients.[89] In fact, a study cohort of 167 Caucasian ataxia patients identified STUB1 mutation in nearly 2% of ARCA patients.[90] These reports have led to the establishment of a new disease designation, SCAR16 (Autosomal Recessive Spinocerebellar Ataxia-16) to describe spinocerebellar ataxia caused by homozygous or compound heterozygous mutation in the *STUB1* gene.[89] The high frequency of STUB1 mutations in ARCA demands an investigation into the molecular mechanisms that are at play as a result of CHIP mutation and how they result in disease pathology in SCAR16, most importantly to guide therapeutic interventions for this underserved patient population.

This is the precise goal of the remainder of this thesis, where I expand upon our discovery of T246M mutation in GHS to define the structural and functional consequences of CHIP mutation in SCAR16 and explore the deficits associated with this mutation in a mouse model system providing the first definition of partial CHIP dysfunction and assignment of specific *in vivo* deficits that result as a consequence of partial (but not total) loss of CHIP function. Interestingly, cerebellar ataxias can also manifest as a secondary feature of neurodegenerative diseases associated with proteotoxicity, including Huntington's and Parkinson's diseases. Given the multifaceted roles of CHIP in PQC and cellular protein homeostasis as well as other cellular functions, the structural, biochemical and *in vivo* analysis of T246M CHIP provides a unique opportunity to delineate the different functions of CHIP and how they may contribute to specific deficits observed in cells and *in vivo*. Furthermore, these studies allow us the unique opportunity to evaluate how these different CHIP functions specifically contribute to proteotoxicity in the brain, heart and other tissues and whether proteotoxicity and/or other molecular mechanisms are the true drivers behind CHIP-associated disease pathology in ARCAs. Ultimately, by determining how CHIP mutation contributes to SCAR16 pathology, we will potentially identify means for modulating CHIP and/or its substrates/interactors as therapeutic targets for SCAR16 that may even have the potential to be applied clinically to other diseases characterized by proteotoxicity or PQC dysregulation in the heart and brain, areas where disruption of CHIP and/or the UPS has upset the delicate balance required to maintain protein homeostasis in the face of cellular stress resulting in devastating disease pathologies.

Therapeutically Targeting the UPS

Recently there has been increasing interest in focusing on modulation of the UPS as a therapeutic strategy to treat many disease indications, particularly neurodegeneration, cancer and immunological disorders. Because of its central role in PQC, chemically modulating this cellular machinery provides a unique mechanism to alter protein homeostasis in diseases where it has become dysregulated. Specific components of the UPS have been targeted or are currently emerging as targets thus far, including the proteasome, E3 ubiquitin ligases and DUBs. These targets represent a promising therapeutic opportunity, as they provide chemical specificity but with the ability to alter protein homeostasis and cellular processes across a range of disease indications.

The proteasome inhibitor Bortezomib was the first drug targeting the UPS in the clinic and was approved for treatment of multiple myeloma and mantle cell lymphoma by the FDA in 2003.[91] The success of this inhibitor has proven that the proteasome is a feasible and valuable anti-cancer target, and since its approval has led to the development of multiple second-generation proteasome inhibitors with increased potency and oral bioavailability.[92] These proteasome inhibitors are now being evaluated for additional non-cancer indications, including progressive muscular dystrophies and late-stage systemic lupus erythematosus.[93] The success of Bortezeomib and these subsequent next generation proteasome inhibitors has greatly inspired further exploration into other potential UPS targets. However, the complexity of the UPS, including the ubiquitination reaction and its outcomes, has resulted in a significant lag in the development and approval of additional drugs targeting other specific components of the UPS, such as E3 ubiquitin ligases and DUBs.[94] Fortunately, significant improvements in our understanding of the UPS as well as advances in screening technologies now make these much

more tractable therapeutic targets that are being actively and, in some cases successfully, pursued not only for the treatment of cancer but also many other disease indications.

Multiple small-molecule inhibitors are currently in development targeting various steps in the ubiquitination cascade. As described above, the target specificity of the ubiquitination reaction occurs at the level of the E3 ubiquitin ligases. Direct inhibitors of E3 ubiquitin ligase enzymatic activity, E3–E2 or E3–substrate interactions therefore may enable specific targeting of a limited number of substrate proteins, which may translate into a better therapeutic ratio and fewer side effects. Structural constraints specific to each class of E3 ubiquitinating enzyme will likely determine whether targeting protein-protein interaction domains or catalytic sites will prove to be easier, more effective and have greater specificity.[95] Several classes of E3 ubiquitin ligases are being actively targeted in the field. One interesting example of targeting protein-protein interactions to modulate E3 ubiquitin ligase activity that is now being tested clinically for the treatment of cancer are inhibitors of the RING E3 ubiquitin ligase MDM2, specifically, inhibitors of MDM2's interaction with tumor suppressor p53. Stabilization of p53 blocks cancer progression, and MDM2 is a highly selective negative regulator of p53 abundance.[96] Multiple MDM2-targeting compounds have been identified or designed, accounting for a vast majority of the current E3-liagse-targeting molecules, and there are currently at least four small-molecule MDM2 antagonists in clinical development for multiple types of cancer.[96, 97] Most of these compounds antagonize the MDM2-p53 interaction by targeting the p53 binding site of MDM2 as competitive inhibitors directly occupying these interaction domains or inducing conformational changes that alter MDM2-p53 affinity.[95, 96]

Preclinical data demonstrated that these compounds induce apoptosis in human tumor cells with minimal toxicity to normal cells and slow the growth of tumor xenografts in mice.[95, 97]

Unfortunately, one of the first published clinical trial results revealed that the treatment of liposarcoma patients with MDM2 antagonist RG7112 increased p53 levels in biopsy specimens and reduced proliferation in tumors; however, clinical benefit in the study was modest, with only 1 patient (out of 20) showing a partial response and 14 showing stable disease, while the remaining 5 patients had progressive disease. Additionally, trial patients had a high rate of adverse reactions, with hints that some may be the result of on-target toxicities related to stabilization of p53.[98] Clearly, the clinical efficacy and achievable therapeutic window in the appropriate patient population will determine the success of these inhibitors. Success in modulating p53 by antagonizing MDM2 would undoubtedly not only provide real clinical benefit to patients with potentially many different malignancies, but also provide important clinical validation for targeting E3 ubiquitin ligases and specific other components of the UPS beyond the proteasome. This clinical validation would provide important momentum for continued drug development in this burgeoning field, where basic understanding of the UPS and its role in disease pathogenesis as is detailed in this thesis will drive successful investment, innovation, preclinical investigation and clinical study design.

CHAPTER II

DIGGIN' ON U(BIQUITIN): A NOVEL METHOD FOR THE IDENTIFICATION OF PHYSIOLOGICAL E3 UBIQUITIN LIGASE SUBSTRATES[1,2]

The ubiquitin-proteasome system (UPS) plays a central role in maintaining protein homeostasis, emphasized by a myriad of diseases that are associated with altered UPS function such as cancer, muscle-wasting, and neurodegeneration. Protein ubiquitination plays a central role in both the promotion of proteasomal degradation as well as cellular signaling through regulation of the stability of transcription factors and other signaling molecules. Substrate specificity is a critical regulatory step of ubiquitination and is mediated by ubiquitin ligases. Recent studies implicate ubiquitin ligases in multiple models of cardiac diseases such as cardiac hypertrophy, atrophy, and ischemia/reperfusion injury, both in a cardioprotective and maladaptive role. Therefore, identifying physiological substrates of cardiac ubiquitin ligases provides both mechanistic insights into heart disease as well as possible therapeutic targets.

Current methods identifying substrates for ubiquitin ligases rely heavily upon non-physiologic *in vitro* methods, impeding the unbiased discovery of physiological substrates in relevant model systems. Here we describe a novel method for identifying ubiquitin ligase substrates utilizing Tandem Ubiquitin Binding Entities (TUBE) technology, two-dimensional differential in gel electrophoresis (2-D DIGE), and mass spectrometry, validated by the identification of both known and novel physiological substrates of the ubiquitin ligase MuRF1 in

primary cardiomyocytes. This method can be applied to any ubiquitin ligase, both in normal and disease model systems, in order to identify relevant physiological substrates under various biological conditions, opening the door to a clearer mechanistic understanding of ubiquitin ligase function and broadening their potential as therapeutic targets.

---

[1]Elements of the work referenced in this chapter have been published in: Cell Biochemistry and Biophysics

[2]Figures Contributed by:
Carrie E. Rubel: 2.1, 2.2, 2.4, 2.5
Jonathan C. Schisler, M.S., PhD: 2.3

Introduction

Protein ubiquitination and the ubiquitin-proteasome system (UPS) play a critical role in the regulation of protein homeostasis, emphasized by a myriad of diseases associated with aberrant UPS function. Ubiquitin is added to a substrate protein through a covalent linkage to a lysine residue on a substrate protein catalyzed by a class of enzymes called ubiquitin ligases; as an additional layer of regulation, this mechanism is counter-regulated by a class of enzymes called de-ubiquitinating enzymes (DUBs).[99, 100] The effect of protein ubiquitination depends upon which lysine residue within the protein the ubiquitin is attached to as well as the length and linkage type of the added ubiquitin. The UPS is most commonly thought of in terms of regulating the turnover of mis-folded and damaged proteins by the addition of canonical K48 polyubiquitin chains and subsequent proteasomal degradation. However, non-canonical linkages, for example K63 polyubiquitin chains, or single ubiquitin molecules (monoubiquitination) can also occur and mediates non-proteolytic mechanisms such as modulating protein localization, protein-protein interactions, activity or stability.[43, 47, 53] The essential nature of protein ubiquitination is well illustrated in the heart where dysfunction, of both proteolytic and non-proteolytic mechanisms, has been associated with multiple disorders, including cardiac hypertrophy, heart failure, diabetes and ischemia-reperfusion injury.[43 5].

Substrate specificity of the ubiquitination reaction occurs at the level of the ubiquitin ligase; as such, ubiquitin ligases are attractive therapeutic targets for diseases involving aberrant protein ubiquitination.[47, 101] Muscle-specific RING finger protein 1 (MuRF1, Trim63) is a striated muscle-specific ubiquitin ligase involved in PQC of the muscle sarcomere by targeting numerous proteins for polyubiquitin-dependent proteasomal degradation, including troponin I, muscle actin, β/slow myosin heavy chain and myosin binding protein-C.[68, 69, 102, 103] Ubiquitin

ligases, including MuRF family proteins, function as distinct molecular regulators by which the heart controls not only sarcomeric structure, but also cellular signaling pathways implicated in multiple models of cardiac disease, both in maladaptive and cardioprotective roles.[43, 66, 67, 102, 104-107] Targeting ubiquitin ligases in the heart may allow for more precise, single therapy manipulation of a smaller, specific subset of substrate proteins that contribute to disease-causing mechanisms while avoiding the negative cardiovascular effects observed with global proteasome inhibition.[108, 109] Yet the substrates targeted by MuRF1 and their DUB counterparts remain incompletely understood and more robust identification methods for identifying ubiquitin ligase substrates is required for development of successful therapies.[110]

Traditional ubiquitin ligase substrate discovery utilizes protein-protein interaction based methods, such as yeast-two hybrid and co-immunoprecipitation paired with mass spectrometry. Although refined recently by several modifications to increase efficiency in substrate identification[102, 111, 112] interaction-based methods are hindered by the transient, weak nature of the ubiquitin ligase-substrate interaction. To circumvent the limitations of interaction-based methods, high-throughput *in vitro* approaches, such as *in vitro* ubiquitination biochemistry coupled with protein microarrays, have proven to be successful at identifying ubiquitin ligase substrates.[113, 114] The use of *in vitro*-based methods is limited, however, to the content printed on protein arrays, limiting the substrate candidate pool. Importantly, neither yeast-two hybrids nor *in vitro* methods for ubiquitin ligase substrate identification are performed in physiologically relevant conditions, thereby limiting and biasing substrate discovery.[66, 75]

Given the limitations of existing ubiquitin ligase substrate screening methods, our aim was to develop a methodology to better identify candidate ubiquitin ligase substrates under physiological conditions. Tandem Ubiquitin Binding Entities (TUBE) technology allows

unbiased ubiquitome isolation through high affinity binding to polyubiquitinated proteins. TUBE also protects polyubiquitiated proteins from de-ubiquitination and degradation during processing, allowing for detection of even low abundant species.[115] Furthermore, the use of different TUBE types that have higher affinities for specific polyubiquitin lysine linkages can be used to enrich for subsets of the ubiquitome, providing another potential level of specificity to the screen. We used a subtractive approach combining TUBE technology, 2-D DIGE, and mass spectrometry, to develop a method for ubiquitin ligase substrate identification that is translatable to physiologically relevant inputs, either from cells or tissues. We describe and validate this method demonstrated by the identification of both previously identified as well as novel physiological substrates of the ubiquitin ligase MuRF1 in primary cardiomyocytes.

Results

Outline of the methodology used to screen for ubiquitin ligase substrates. Identification of substrates for ubiquitin ligases have traditionally relied on either artificial systems, such as yeast two-hybrid screens, or inefficient candidate substrate screens. Our goal for a more robust and flexible substrate screen included the use of biologically relevant cell systems combined with a proteomic approach for identification. A key component of this method is the selection, as well as the lack of selection, of polyubiquitinated proteins immunoprecipitated by Tandem Ubiquitin Binding Entities (TUBE) conjugated to agarose beads. This allows us to compare the relative ratio of proteins that bind to TUBE (eluate) as well as compare proteins that did not bind (supernatant) across multiple conditions. We have provided a graphical overview of the method (Fig. 2.1) and discuss below the major components of this approach.

1) *Protein source.* Our method relies on a subtractive approach (*i.e.* comparing one state to another); therefore the starting material must include two conditions wherein the expression or activity of the ubiquitin ligase is manipulated. We classify systems where ubiquitin ligase activity is either increased or decreased as gain-of-function or loss-of-function, respectively (see Fig. 2.1 for examples). The starting material can range from protein isolated from animal tissues, primary cells, or stable cell culture models in which either the ubiquitin ligase or a counter-regulatory de-ubiquitination enzyme is manipulated.

2) *Ubiquitome isolation.* Protein extracts are isolated and quantified from each condition and an equal amount of protein is subsequently added to either agarose control beads or beads conjugated with TUBE. We used TUBE that bind equally to K48- and K63-ubiquitin linkages, however, there are other TUBE varieties that preferentially bind certain lysine linkages that can be used depending on the type of substrates desired (*e.g.* canonical versus non-canonical). From each condition we collect both the eluate from the TUBE, containing the selected ubiquitome, as well as the unbound supernatants from both the control agarose and TUBE, which provide an additional measure of the ubiquitome from each condition.

3) *2D-DIGE and pick selection.* In order to reduce the number of false positives, we established a three spot comparison to identify substrate picks. Within each 2D-DIGE gel, relative differences between the two conditions are quantified. We established three independent comparisons that are analyzed in parallel to increase the likelihood of positive substrate identification. The first comparison of the pick selection contrasts the eluted ubiquitome from the experimental and control condition. In the case of gain-of-function studies, a spot pick would be increased in the experimental condition compared to the control condition (converse for loss-of-function models). The second and third gels allow comparisons of the TUBE-selected ubiquitomes within the

experimental condition (Gel 2) or control condition (Gel 3). In these later comparisons, enriched ubiquitinated proteins are identified by comparing the unbound fraction from the control agarose beads (ubiquitin-enriched) versus the unbound fraction from the TUBE agarose (ubiquitin-depleted). Naturally occurring ubiquitinated proteins in the control condition are identified in Gel 3 whereas Gel 2 identifies the enriched (or depleted in the case of loss-of-function) pool of proteins in the experimental conditions.

4) *Spot pick identification.* All of the spots that meet the pick criteria for each Gel are tabulated and subsequently used to identify picks that are common to all multiple comparisons (see Figure 1 for the differences in pick criteria in gain-of-function versus loss-of-function models). These picks are then subjected to MALDI-TOF for protein identification and classified as potential ubiquitin ligase substrates.

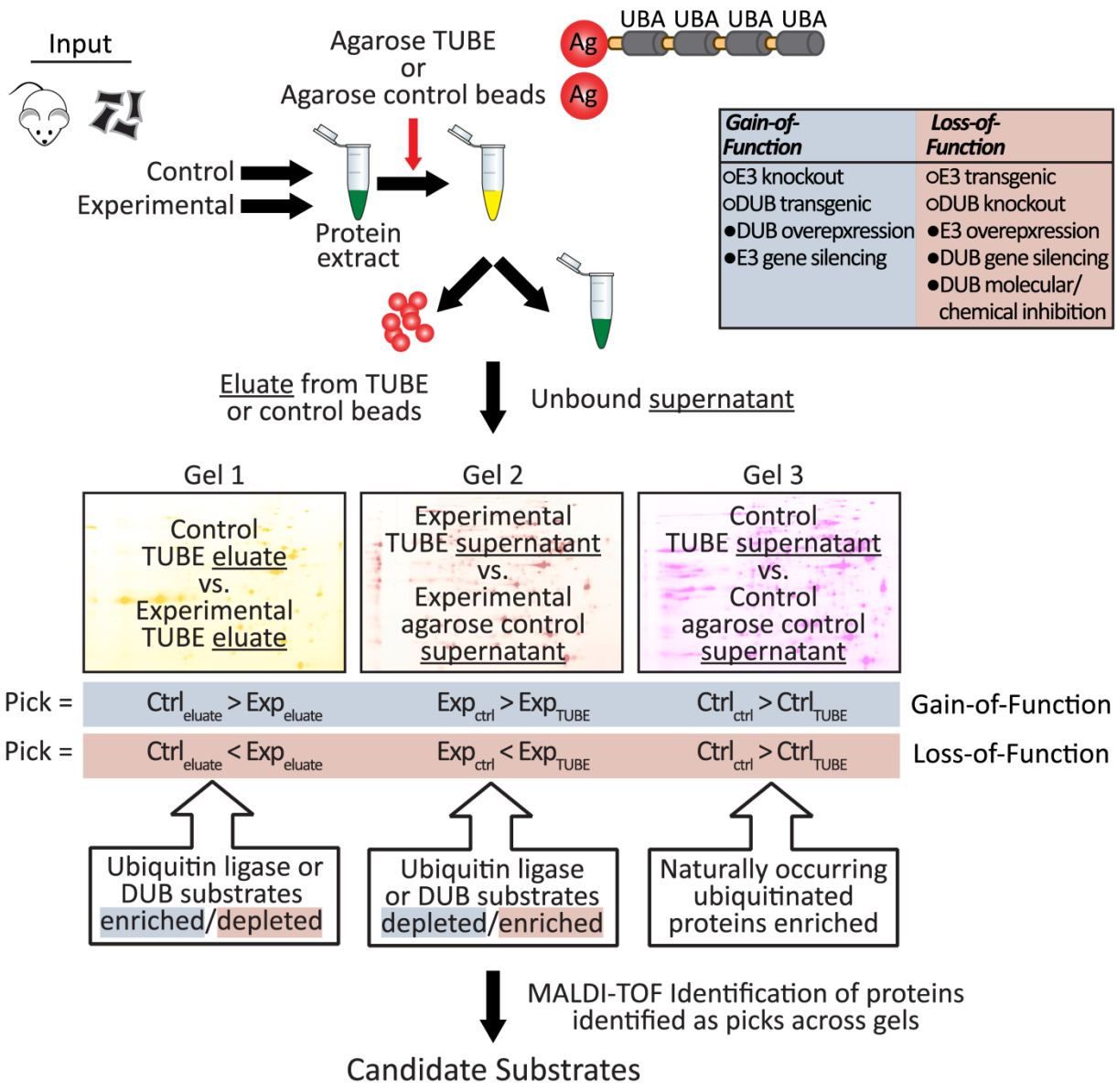

Figure 2.1. Schematic model representing the ubiquitin ligase/deubiquitinating enzyme screening platform.

Protein is isolated from control and experimental animal tissue or cell culture samples where the expression or activity of a ubiquitin ligase or deubiquitinating enzyme of interest is manipulated to increase or decrease, dubbed a gain-of-function or loss-of-function manipulation. Isolated protein is then quantitated and incubated overnight at 4 °C with Tandem Ubiquitin Binding Entities (TUBE) or agarose control beads. Both the bound (eluate) and unbound (supernatant) fractions are collected and subjected to 2D-DIGE. Three different 2D-DIGE gels are run, each also including a pooled internal standard sample. Gel 1 compares the control sample ubiquitin enrichment to the experimental sample ubiquitin enrichment, identifying proteins whose ubiquitination is dependent upon the ubiquitin ligase of interest. The second and third gels allow

comparisons of the TUBE-selected ubiquitomes within the experimental condition (Gel 2) or control condition (Gel 3) by comparing the ubiquitin-depleted supernatants from the sample incubated with TUBE to the ubiquitin-rich sample incubated with agarose control beads. The comparison on Gel 2 identifies proteins whose ubiquitination is potentially dependent upon the ubiquitin ligase of interest. The Gel 3 comparison reveals naturally occurring ubiquitinated proteins, as here, the ubiquitin ligase of interest is unperturbed. Spots are identified as “picks” by DeCyder Analysis Software based upon the determination of relative changes in intensity between the two samples and picks are aligned across all three gel comparisons to select spots for subsequent MS/MS peptide sequencing and protein identification.

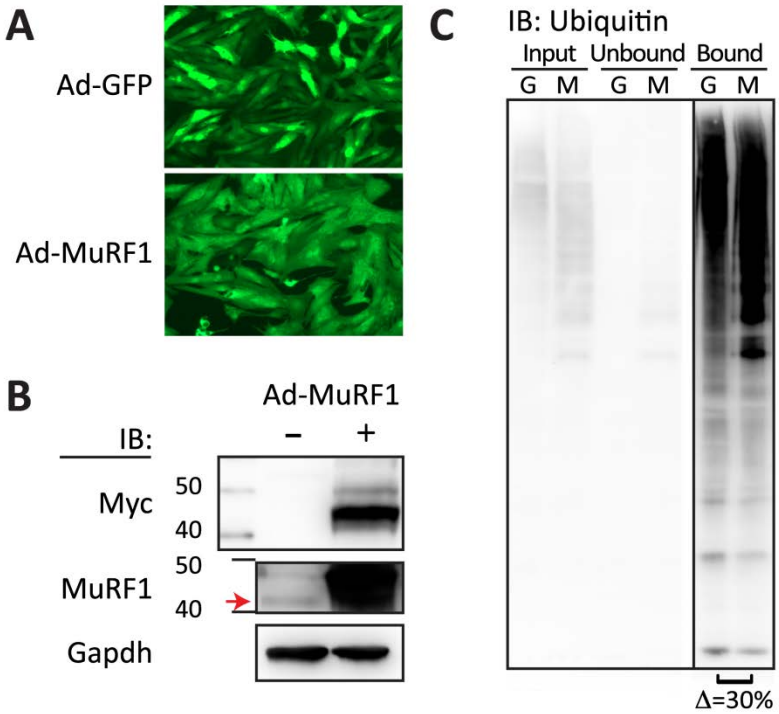

Figure 2.2. MuRF1 ectopic expression and TUBE-mediated ubiquitin enrichment. Fluorescent imaging and immunoblot verified MuRF1 ectopic expression and ubiquitin enrichment prior to 2D-DIGE.

A. Representative fluorescence micrographs of primary cardiomyocytes after 24 h of transduction with adenovirus expressing green fluorescent reporter protein alone (Ad-GFP) or in combination with Myc-tagged MuRF1 (Ad-MuRF1) at MOI of 10.

B. Representative immunoblots (IB) of Myc, MuRF1, and GAPDH protein levels in extracts isolated from primary cardiomyocytes transduced with Ad-GFP (-) or Ad-MuRF1 (+) adenovirus for 24 h. The red arrow indicates endogenous MuRF1, with ectopically-expressed myc-tagged MuRF1 migrating at a slightly higher molecular weight.

C. Representative immunoblot of total ubiquitin from TUBE enrichment in extracts isolated from primary cardiomyocytes transduced with Ad-GFP (G) or Ad-MuRF1 (M) for 24 h as performed in the 2D-DIGE MuRF1 substrate screen. Lanes 1 and 2: input samples; lanes 3 and 4: unbound TUBE supernatant collected; lanes 5 and 6: ubiquitinated protein enrichment eluted from TUBE. From 3 independent experiments we observed an average of 30 ± 14.7% increase in total ubiquitinated protein with MuRF1 ectopic expression as measured by densitometry.

MuRF1 expression in primary cardiomyocytes. Using traditional substrate identification approaches, our laboratory as well as and other groups identified substrates for MuRF1, a striated muscle-specific ubiquitin ligase. As a proof of principle for our method, we screened for MuRF1 substrates in primary rat cardiomyocytes and hypothesized we would identify both previously established substrates as well as potential novel substrates. We utilized a transient gain-of-function model in primary cardiomyocytes as previously described through the use of adenoviral-mediated expression of either the reporter green fluorescent protein (GFP) alone or in combination with MuRF1 (mouse) at a multiplicity of infection of 10 MOI per cell (Fig. 2.2A). Confirmation of the expression of the MuRF1 transgene was performed via immunoblot detection of the myc epitope tag (Fig. 2.2B, top) that corresponded to an approximate 25-fold increase in MuRF1 transgene expression relative to the endogenous MuRF1 expression in control cells, measured by densitometry, after 18 h of adenoviral transduction. These data confirm the successful expression of the MuRF1 transgene in primary cardiomyocytes.

MuRF1 ubiquitome isolation. Prior to 2D-DIGE analyses, we first confirmed that we could successfully isolate the TUBE-selected ubiquitome. Lysates were prepared, quantified, and incubated for 18 h in the presence of either control agarose or TUBE beads. Both the unbound (supernatant) and bound (eluate) fractions were collected and separated via SDS-PAGE. The bound fractions from the TUBE beads in both the Ad-GFP and Ad-MuRF1 conditions contained highly enriched levels of ubiquitinated proteins compared to the unbound fraction determined via immunoblot analysis (Fig. 2.2C). We also consistently noticed a 30% increase in the total densitometry of ubiquitin immunoreactivity in cells transduced with Ad-MuRF1 (Fig. 2.2C, right) suggesting an overall increase in total protein ubiquitination in the presence of increased MuRF1 expression. Given the successful selection of ubiquitinated proteins using the TUBE

isolation procedure, we moved forward to the differential gel analysis to attempt to identify specific proteins that are more readily ubiquitinated in the presence of increased MuRF1 expression.

2D-DIGE and selection of picks corresponding to increased MuRF1 expression. Using the three gel conditions outlined above (Fig. 2.1) we used 2D-DIGE to identify candidate picks from each of the three comparisons. The primary comparison was between the elution profiles of the GFP versus MuRF1 ubiquitome (Gel 1). As shown in Figure 2.3, 2D-DIGE resolved differentially fluorescent-labeled pools of proteins in the same gel separated by both molecular weight (MW, vertical) and isoelectric point (pH, horizontal). A relative ratio of protein species was determined by the ratio of fluorescent intensity at identified spots in the gel. The image of the Cy3-labeled GFP eluate (green) and Cy5-labeled MuRF1 eluate (Fig. 2.3 top left and bottom left, respectively) were overlaid to locate differentially expressed spots (Fig. 2.3 top right). In the eluate comparison, we were interested in spots that were ≥1.5-fold more red than green (yellow spots represent similar protein amounts) indicating potential protein species that were more abundant in the MuRF1 eluate sample. Differential spots in the other two gels that met both quality standards and were changed in the expected direction were also identified as “picks” (for additional gel image data, see Fig. 2.4).

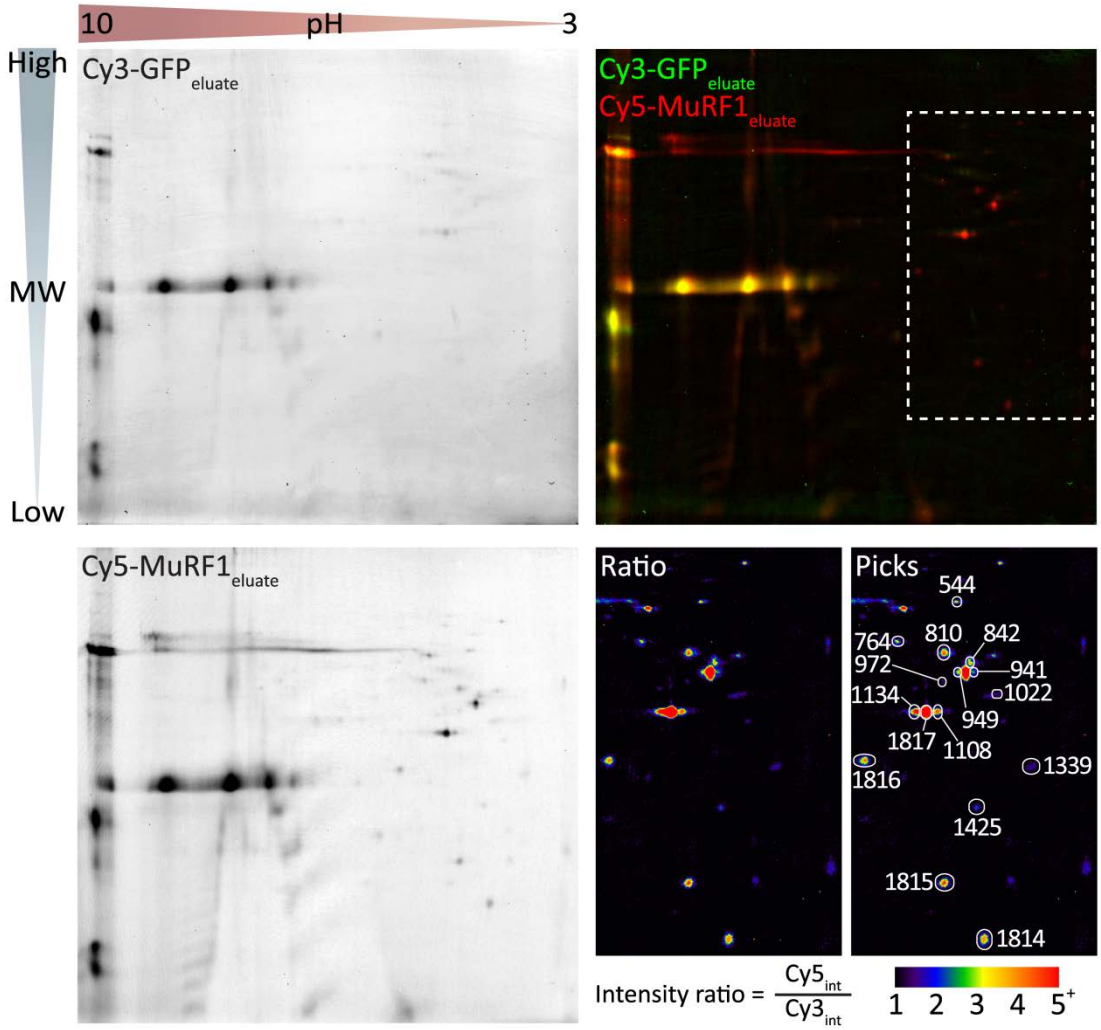

Figure 2.3. 2D-DIGE gel of the TUBE-isolated ubiquitome.

2D-DIGE image analysis of ubiquitin-enriched samples eluted from TUBE identified spots for mass spectrometry protein identification. Proteins eluted from TUBE incubated with protein extract from Ad-GFP or Ad-MuRF1 transduced cardiomyocytes were labeled with Cy3 and Cy5, respectively, and separated by molecular weight and isoelectric point (Cy3-GFP$_{eluate}$ and Cy5-MuRF1$_{eluate}$, top left and bottom left, respectively). Relative changes in protein spots were calculated using the ratio of fluorescence intensity of each fluorescent channel visualized by coloring and overlaying the Cy3-GFP$_{eluate}$ (green) and Cy5-MuRF1$_{eluate}$ images (top right). The region containing the 16 spots selected for mass spectrometry identification (top right, hashed white box) was magnified and used to generate a ratio image (Cy5/Cy3) to highlight the fold-enrichement and identification of each picked spot (bottom right).

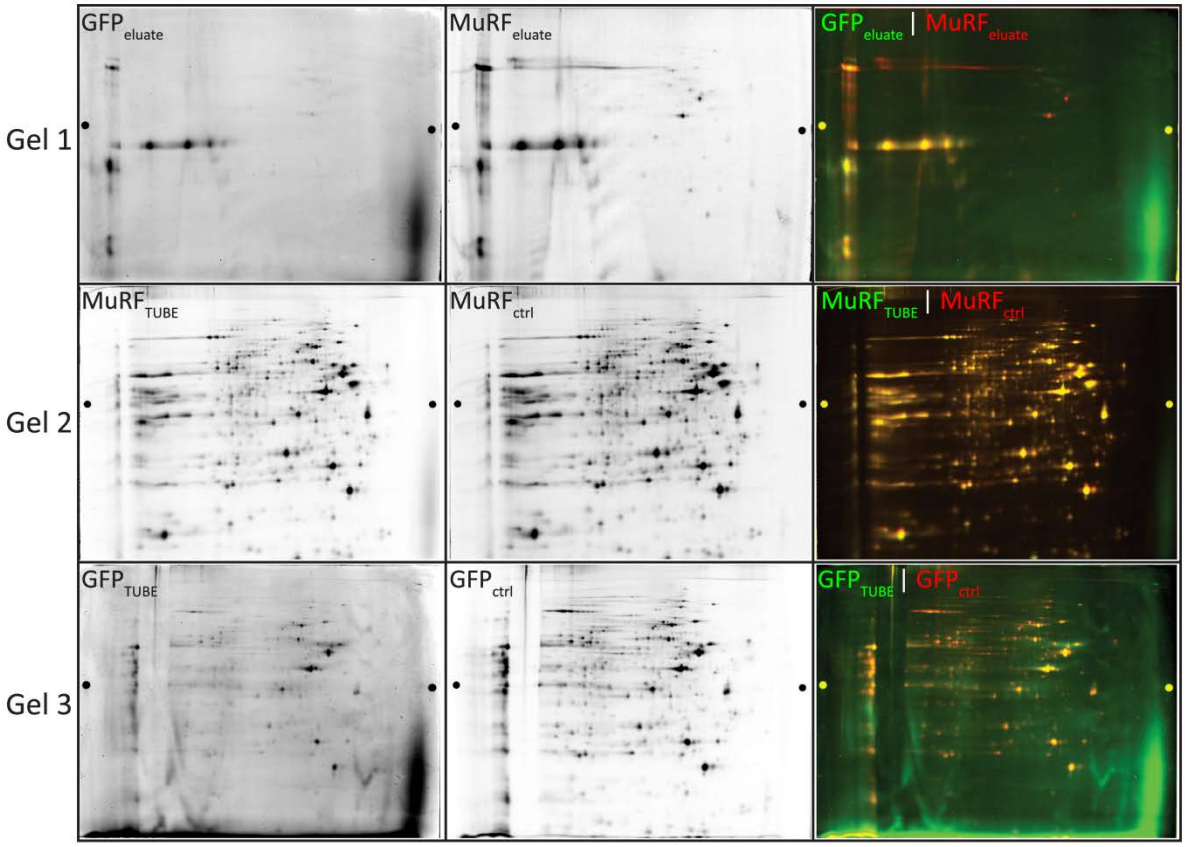

Figure 2.4. Full 2D-DIGE gel images for Gels 1-3.

Full fluorescent micrographs of either the individual Cy3 (left column, green) and Cy5 (middle column, red) channels or the false-colored overlay of both channels (right column) for all three gels used in generation of the "picks".

Picks that pass all three selection criteria and subsequent protein identification by MALDI-TOF identify candidate MuRF1 substrates. We tabulated all of the individual spots that passed the selection criteria from each gel comparison; for a list of all the spots "picked" in each comparison, see Table 2.1. In total, there were nine spots that satisfied all three gel comparison criteria (highest confidence, Table 2.1), and an additional seven spots that satisfied criteria in Gel 1 and Gel 2 (high confidence, Table 2.1) for gain-of-function substrate identification (Fig. 2.1). These 16 spots all fell within the intermediate to low pH range, spanning a molecular weight range of 20-75 x 10^3 Daltons (Fig. 2.3 upper right, boxed region). As a reference, we included a ratio image of this region to highlight the fold enrichment of these samples in the MuRF1 TUBE elution relative to the GFP TUBE elution as well as an annotated ratio image to highlight and label the 16 spots (Fig. 2.3, bottom right). The 16 spots were picked from an independently run "pick" gel and submitted for protein identification using MALDI-TOF. Peptide sequencing identified a total of 20 polypeptides identified from the 16 spots (Table 2.1, Table 2.2, Table 2.3). Consistent with our hypothesis and validation of our proof-of-principal, three of the 20 proteins were previously identified in our yeast two-hybrid screen[102 9] or a published yeast two-hybrid screen[116] and all but one of the proteins (Coq9) have been published as an identified polyubiquitinated protein.[116-119] Additionally, the functional classification of the proteins identified included both structural (sarcomeric) protein components and mitochondrial substrates, two known locations within the cardiomyocyte where MuRF1 is known to function,[116, 120, 121] suggesting this approach may, in fact, identify bona-fide MuRF1 substrates.

Table 2.1. Alignment of 2D-DIGE picks across three gel comparisons for selection of spots for mass spectroscopy identification.

Spots are identified by a common spot number (Spot #) across all three gels based on MW and pI. The table includes if the spot was detectable in the gel (Appearance?) and if so, the average ratio of the comparison (Av. Ratio) indicated in the table header. Spots that also passed additional quality standards as described in the methods are indicated (QualitySpot?). If the criteria were met for an individual spot and the direction of change satisfied the indicated comparison, the spot was considered a "Pick". The last column represents a confidence threshold based on the presence of "Pick" calls across all three gels.

	Gel 1: $MuRF1_{eluate}$ / GFP_{eluate}				Gel 2: $MuRF1_{TUBES}$ / $MuRF1_{ctrl}$				Gel 3: GFP_{TUBES} / GFP_{ctrl}				Confidence
	Pick = $MuRF1_{eluate} > GFP_{eluate}$				Pick = $MuRF1_{TUBES} < MURF1_{ctrl}$				Pick = $GFP_{TUBES} < GFP_{ctrl}$				
Spot #	Appearance?	Av. Ratio	QualitySpot?	M > G ?	Appearance?	Av. Ratio	QualitySpot?	C >T ?	Appearance?	Av. Ratio	QualitySpot?	C >T ?	
1817	Yes	6.17	Yes	Pick	Yes	-6.67	Yes	Pick	Yes	-2.03	Yes	Pick	Highest
1814	Yes	4.68	Yes	Pick	Yes	-2.20	Yes	Pick	Yes	-2.66	Yes	Pick	
1815	Yes	4.58	Yes	Pick	Yes	-1.78	Yes	Pick	Yes	-2.84	Yes	Pick	
941	Yes	3.41	Yes	Pick	Yes	-1.34	Yes	Pick	Yes	-2.00	Yes	Pick	
1134	Yes	3.11	Yes	Pick	Yes	-1.75	Yes	Pick	Yes	-1.79	Yes	Pick	
1425	Yes	2.72	Yes	Pick	Yes	-1.15	Yes	Pick	Yes	-1.66	Yes	Pick	
1339	Yes	2.25	Yes	Pick	Yes	-1.16	Yes	Pick	Yes	-2.06	Yes	Pick	
764	Yes	2.16	Yes	Pick	Yes	-1.56	Yes	Pick	Yes	-2.12	Yes	Pick	
972	Yes	1.82	Yes	Pick	Yes	-1.15	Yes	Pick	Yes	-2.63	Yes	Pick	
949	Yes	7.96	Yes	Pick	Yes	-1.37	Yes	Pick		-1.85			High
1816	Yes	5.13	Yes	Pick	Yes	-1.39	Yes	Pick		-2.42			
810	Yes	4.60	Yes	Pick	Yes	-1.15	Yes	Pick	Yes	-1.52			
1108	Yes	3.21	Yes	Pick	Yes	-1.19	Yes	Pick	Yes	-1.38			
842	Yes	2.82	Yes	Pick	Yes	-1.15	Yes	Pick	Yes	-1.35			
544	Yes	2.49	Yes	Pick	Yes	-1.20	Yes	Pick	Yes	-2.17			
1022	Yes	2.41	Yes	Pick	Yes	-1.16	Yes	Pick		2.23			
931	Yes	11.33	Yes	Pick					Yes	-1.95	Yes	Pick	Medium
1369	Yes	3.19	Yes	Pick	Yes	-1.02			Yes	-1.79	Yes	Pick	
826	Yes	3.14	Yes	Pick	Yes	-1.08			Yes	-1.78	Yes	Pick	
1319	Yes	2.60	Yes	Pick	Yes	-1.11			Yes	-1.96	Yes	Pick	
1006	Yes	2.40	Yes	Pick	Yes	-1.00			Yes	-1.74	Yes	Pick	
1011	Yes	2.36	Yes	Pick	Yes	-1.02			Yes	-2.90	Yes	Pick	
821	Yes	3.54	Yes	Pick	Yes	-1.12			Yes	1.21			Lower
314	Yes	3.12	Yes	Pick	Yes	-1.11			Yes	1.03			
833	Yes	3.11	Yes	Pick	Yes	-1.13			Yes	1.18			
542	Yes	2.89	Yes	Pick	Yes	-1.10			Yes	-2.09			
888	Yes	2.68	Yes	Pick	Yes	-1.06			Yes	1.43			
1145	Yes	2.50	Yes	Pick	Yes	-1.08			Yes	-1.48			
782	Yes	2.26	Yes	Pick	Yes	-1.00			Yes	-2.23			
517	Yes	1.57	Yes	Pick	Yes	1.06			Yes	-1.40			

Table 2.2. Mass spectroscopy summary data for the 16 spots submitted for identification.

The 2D-DIGE master spot number is listed with corresponding protein(s) identified by MALDI-TOF (Protein Name, Species, Database Accession ID, Molecular Weight in Daltons (Da)) including peptide counts MS and MS/MS scores, peptide sequenced ion scores, and scoring for each identified protein.

Master Number	Protein Name	Species	Database Accession ID	MW (Da)	Peptide Count	MS & MS/MS Score	Peptide sequenced Ion Score	Scoring threshold
544	Tax_Id=10116 Gene_Symbol=Hspa5 78 kDa glucose-regulated protein	Rattus	IPI00206624	72302.4	38	2,310	2042	59
764	Tax_Id=10116 Gene_Symbol=Hspd1 60 kDa heat shock protein, mitochondrial	Rattus	IPI00339148	60917.4	36	2,370	2094	59
810	Tax_Id=10116 Gene_Symbol=Vim Vimentin	Rattus	IPI00230941	53700	40	1,880	1526	59
	Tax_Id=10116 Gene_Symbol=Tuba1a Tubulin alpha-1A chain	Rattus	IPI00189795	50103.6	9	169	145	59
842	Tax_Id=10116 Gene_Symbol=Tubb5 Isoform 1 of Tubulin beta-5 chain	Rattus	IPI00197579	49639	25	1,460	1285	59
	Tax_Id=10116 Gene_Symbol=Tubb2c Tubulin beta-2C chain	Rattus	IPI00400573	49769	22	1,170	1036	59
941	Tax_Id=10116 Gene_Symbol=Atp5b ATP synthase subunit beta, mitochondrial	Rattus	IPI00551812	56318.5	27	1,750	1560	59
949	Tax_Id=10116 Gene_Symbol=Atp5b ATP synthase subunit beta, mitochondrial	Rattus	IPI00551812	56318.5	27	1,800	1607	59
972	Tax_Id=10116 Gene_Symbol=Pdia6 protein disulfide-isomerase A6	Rattus	IPI00365929	48729.6	14	1,290	1242	59
	Tax_Id=10116 Gene_Symbol=Atp5b ATP synthase subunit beta, mitochondrial	Rattus	IPI00551812	56318.5	15	400	354	59
	Tax_Id=10116 Gene_Symbol=Hnrnpf Heterogeneous nuclear ribonucleoprotein F	Rattus	IPI00210357	45700.9	7	255	241	59
1022	RecName:MuRF-1 Full=E3 ubiquitin-protein ligase TRIM63; AltName: Full=Muscle-specific RING finger protein 1; Short=MuRF-1; Short=MuRF1; Short=Muscle RING finger protein 1; AltName: Full=Tripartite motif-	Mus musculus	gi|84029592	39465.2	25	1,210	1032	83
	Tax_Id=10116 Gene_Symbol=Ppp1r7 Protein phosphatase 1 regulatory subunit 7	Rattus	IPI00358083	41271.4	9	204	180	59
1108	Tax_Id=10116 Gene_Symbol=Actc1 Actin, alpha cardiac muscle 1	Rattus	IPI00194087	41991.9	22	1,660	1511	59
1134	Tax_Id=10116 Gene_Symbol=Actc1 Actin, alpha cardiac muscle 1	Rattus	IPI00194087	41991.9	22	1,230	1093	59
	Tax_Id=10116 Gene_Symbol=Actb Actin, cytoplasmic 1	Rattus	IPI00189819	41709.7	19	805	704	59
1339	Tax_Id=10116 Gene_Symbol=Tpm1 Isoform 1 of Tropomyosin alpha-1 chain	Rattus	IPI00197888	32660.7	37	1,960	1649	59
1425	Tax_Id=10116 Gene_Symbol=Coq9 Ubiquinone biosynthesis protein COQ9,	Rattus	IPI00365149	35123.5	13	701	627	59
	Tax_Id=10116 Gene_Symbol=Actc1 Actin, alpha cardiac muscle 1	Rattus	IPI00194087	41991.9	8	271	252	59
	Tax_Id=10116 Gene_Symbol=Tollip Toll-interacting protein	Rattus	IPI00366104	30294.9	9	251	218	59
1814	Tax_Id=10116 Gene_Symbol=Myl2 Myosin regulatory light chain 2, ventricular/cardiac	Rattus	IPI00214000	18868.4	24	1,330	1091	59
1815	Tax_Id=10116 Gene_Symbol=Myl3 Myosin light chain 3	Rattus	IPI00231788	22142.1	18	1,330	1209	59
1816	Tax_Id=10116 Gene_Symbol=Ldhb L-lactate dehydrogenase B chain	Rattus	IPI00231783	36589.1	31	1,960	1662	59
	Tax_Id=10116 Gene_Symbol=Mdh1 Malate dehydrogenase, cytoplasmic	Rattus	IPI00198717	36460.1	6	103	89	59
1817	Tax_Id=10116 Gene_Symbol=Actc1 Actin, alpha cardiac muscle 1	Rattus	IPI00194087	41991.9	24	1,630	1464	59

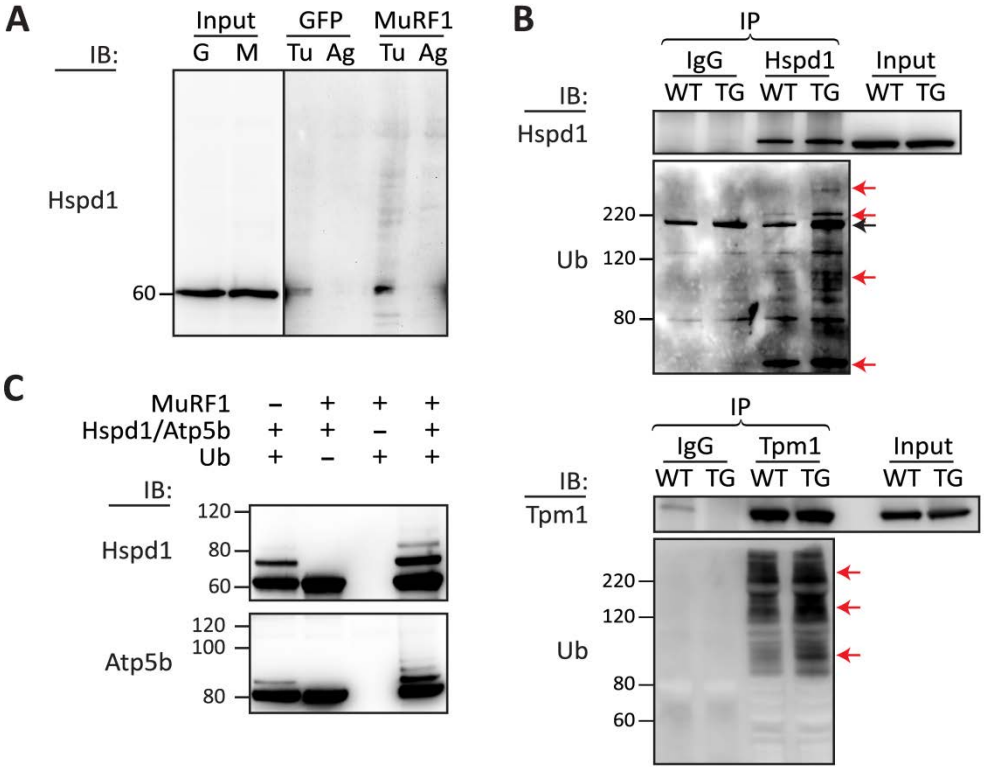

Figure 2.5. Validation of screen-identified proteins Hspd1, Tpm1, and Atp5b as substrates of MuRF.

In vitro and *in vivo* data demonstrate that the screen-identified proteins Hspd1, Tpm1 and Atp5b, are MuRF1 substrates.

A. Representative immunoblot (IB) of Hspd1 protein levels in extracts isolated from primary cardiomyocytes transduced with Ad-GFP (G) or Ad-MuRF1 (M) adenovirus for 24 h. Lane 1 and 2: input samples (light exposure, see Fig. 2.6B); lane 3 and 4: Ad-GFP samples eluted from either TUBE (Tu) or agarose control beads (Ag); Lane 5 and 6: Ad-MuRF1 samples eluted from TUBE (Tu) or agarose control beads (Ag).

B. Immunoprecipitations (IP) of Hspd1 and Tpm1 in extracts isolated from wild-type (WT) or MuRF1 transgenic (TG) mouse hearts, subsequently immunoblotted (IB) for Hspd1 or Tpm1 and ubiquitin (Ub). Lane 1 and 2: IgG control IP; lane 3 and 4: Hspd1 (top) or Tpm1 (bottom) IP; Lane 5 and 6: 10% input of extract. Red arrows indicate ubiquitin-reactive Hspd1 or Tpm1 species in MuRF1 Tg hearts (lane 4) that are not present or are of lower relative abundance in wild-type hearts (lane 3). The black arrow indicates a non-specific band also present in the IgG control IP.

C. *In vitro* ubiquitination assays for MuRF1 ubiquitination of Hspd1 and Atp5b performed in presence or absence of purified ubiquitin or MuRF1 as indicated and detected by immunoblot analysis (IB) for Hspd1 (top) or Atp5b (bottom).

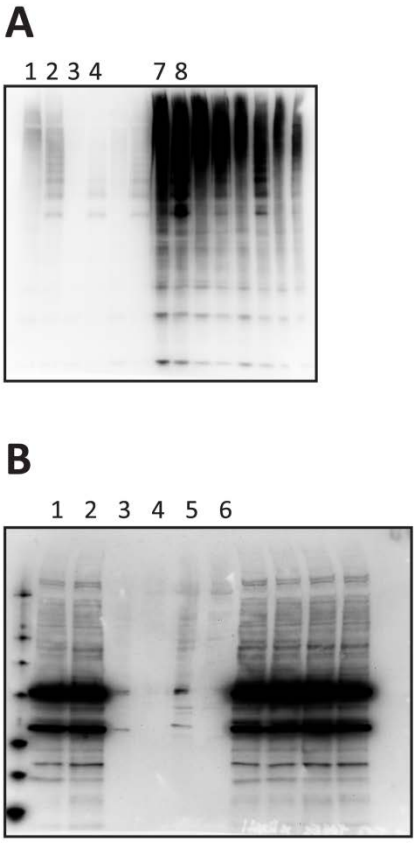

Figure 2.6. Full immunoblot images for figures 2.2C and 2.5A.

A. Full image of total ubiquitin immunoblot from TUBE enrichment in extracts isolated from primary cardiomyocytes transduced with Ad-GFP or Ad-MuRF1 for 24 h as performed in the 2D-DIGE MuRF1 substrate screen as represented in Figure 2.2C. For the figure in the manuscript, only lanes 1-4 and 7-8 contained samples relevant to this manuscript using an equal exposure (Fig. 2.2C).

B. Full image of total Hspd1 immunoblot in extracts isolated from primary cardiomyocytes transduced with Ad-GFP or Ad-MuRF1 as represented in Figure 2.5A. For the figure in the manuscript, only lanes 1-6 contained samples relevant to this manuscript and shown here with an equal exposure.

Validation of Hspd1, Tpm1, and Atp5b as substrates of MuRF1. To determine if the candidate proteins identified in our 2D-DIGE method were substrates of MuRF1, we took advantage of available antibodies and purified recombinant proteins to validate selected candidates. First, we measured the pattern of Hspd1 (Fig. 2.3, spot #764) modification in primary cardiomyocytes transduced with either Ad-GFP or Ad-MuRF1 via SDS-PAGE/immunoblot analysis from independent experiments prepared with TUBE or control agarose identically as described in the 2D-DIGE screen. As expected, in cells overexpressing MuRF1, we detected several higher molecular weight proteins bound to the TUBE beads that were reactive to the Hspd1 antibody (Fig. 2.5A), consistent with a MuRF1-dependent increase in Hspd1 polyubiquitination. To determine if our primary cell system of MuRF1 overexpression accurately reflected the action of increased MuRF1 activity *in vivo*, we immunoprecipitated Hspd1 as well as another MuRF1 substrate candidate Tpm1 (Fig. 2.3, spot #1339) from heart tissue isolated from either wild-type or MuRF1-transgenic mice (Fig. 2.5B). Consistent with the pattern observed in primary cardiomyocytes (Fig. 2.5A), after successful immunoprecipitation of either candidate substrate protein, using immunoblot analysis we observed increases in higher molecular weight proteins reactive to an antibody that recognizes ubiquitin (Fig. 2.5B) in MuRF1-trangenic hearts compared to wild-type hearts. These data suggest that *in vivo*, both Hspd1 and Tpm1 are cardiac substrates of MuRF1; furthermore, the translatability of using this ubiquitin ligase screen in our primary cardiomyocyte culture model to identify *in vivo* cardiac substrates demonstrates the utility of developing methods that are performed in a biologically relevant context. Finally, we used a purified recombinant protein system to test if the candidate substrates Hspd1 and Atp5b (Fig. 2.3, spot #941, #949, #972) could be polyubiquitinated by MuRF1 in a cell-free *in vitro* system. Interestingly, in the absence of MuRF1 we observed E2-mediated monoubiquitination

(an emerging property of E2 enzymes; [122, 123] of both Hspd1 and Atp5b,. As expected, we found both Hspd1 and Atp5b to be polyubiquitinated in the presence of MuRF1, providing further validation that these proteins are direct substrates of MuRF1. Through the use of multiple approaches we demonstrated that all three candidate substrates identified by our 2D-DIGE method were validated as MuRF1 substrates.

Table 2.3. Identities and characterization of MuRF1 substrates identified by MS/MS analysis of selected 2D-DIGE spots.

Symbols, descriptions and PANTHER protein classifications for each of the MuRF1 substrates identified by mass spectroscopy analysis are listed. Also indicated are those proteins previously identified as MuRF1 substrates by yeast two-hybrid screening (Y2H[102, 116] and Cam Patterson – data not shown) and those proteins previously reported as MuRF1 substrates (or interacting proteins) in skeletal muscle.

Symbol	**Protein description**	**Reported substrate**	**Identified by Y2H**	**PANTHER Protein Class**
ACTB	Actin, cytoplasmic 1			actin and actin related protein
ACTC1	Actin, alpha cardiac muscle 1	skeletal [103]	yes [102]	actin and actin related protein
ATP5B	ATP synthase subunit beta, mitochondrial		yes [116]	ATP synthase/ion channel/hydrolase
COQ9	Ubiquinone biosynthesis protein COQ9, mitochondrial			cofactor biosynthesis*
HNRNPF	Heterogeneous nuclear ribonucleoprotein F			ribosomal protein
HSPA5	78 kDa glucose-regulated protein			Hsp70 family chaperone
HSPD1	60 kDa heat shock protein, mitochondrial			chaperonin
LDHB	L-lactate dehydrogenase B chain			dehydrogenase
MDH1	Malate dehydrogenase, cytoplasmic			dehydrogenase
MURF1	E3 ubiquitin-protein ligase TRIM63 (MuRF1)	auto Ub		ubiquitin-protein ligase
MYL2	Myosin regulatory light chain 2, ventricular/cardiac muscle isoform	skeletal [118]	yes [102]	cytoskeletal protein
MYL3	Myosin light chain 3	skeletal [118]	yes[102]	actin family cytoskeletal protein/calmodulin
PDIA6	Protein disulfide-isomerase A6			isomerase
PPP1R7	Protein phosphatase 1 regulatory subunit 7			phosphatase modulator/microtubule family cytoskeletal protein
TOLLIP	Toll-interacting protein			adapter protein*
TPM1	Isoform 1 of Tropomyosin alpha-1 chain			actin binding motor protein
TUBA1A	Tubulin alpha-1A chain			tubulin
TUBB2C	Tubulin beta-2C chain			tubulin
TUBB5	Isoform 1 of Tubulin beta-5 chain			tubulin
VIM	Vimentin			structural protein/intermediate filament

Discussion

Ubiquitin ligases and their counter-regulatory deubiquitinating enzymes (DUBs) play unique roles in protein ubiquitination and the UPS as the regulators of substrate specificity; therefore, substrate identification is critical to the mechanistic understanding of the UPS as well as our ability to modify protein ubiquitination in order to modulate disease. Despite this, the available methods to identify ubiquitin ligase and DUB substrates do not provide robust or unbiased means to identify physiological substrates, often relying upon non-physiological *in vitro* approaches. Given the current limitations in ubiquitin substrate screens, we developed a novel method for the identification of physiological ubiquitin ligase/DUB substrates (Fig. 2.1). As a proof-of-principle for our method, we successfully utilized a transient gain-of-function model to screen for MuRF1 substrates in primary cardiomyocytes (Fig. 2.2) and identified both previously identified MuRF1 substrates as well as novel substrate proteins (Table 2.3). Not surprisingly, nearly all of the candidate substrates were previously identified as polyubiquitinated proteins;[116-119] additionally, the novel candidate substrates were functionally classified in cellular locations where MuRF1 is known to function including the sarcomere and mitochondria, [116, 120, 121] reflective of the physiological approach utilized by our method. Furthermore, we validated several novel MuRF1 substrates both *in vitro* (Hspd1, Atp5b) and *in vivo* (Hspd1, Tpm1). In fact, the increased in polyubiquitination of Hspd1 and Tpm1 in hearts of MuRF1 transgenic animals not only validates the ability of our screen to identify novel substrates but also demonstrates the unique translatability of this screening method performed in a biologically relevant context to an independent *in vivo* model.

Our method circumvents major pitfalls of traditional substrate screens by: 1) using a physiological setting that is relevant to the ubiquitin ligase/DUB or disease model; 2) utilizing

TUBE technology to isolate and protect the ubiquitome,[115] independent of the strength of the physical interaction between the ubiquitin ligase/DUB and substrate; and 3) employing 2D-DIGE with multiple subtractive comparisons to reduce the number of false positives. For our proof-of-principle we used a biologically relevant primary cell culture system; however, TUBE-based ubiquitome isolation can be used with a myriad of other protein sources including stable cell culture models, isolated preparations of subcellular compartments (for example, mitochondria, Rubel and Patterson – data not shown), and animal tissues. The flexibility in starting material allows the study substrates of a ubiquitin ligase, or the action of an opposing DUB (Fig. 2.1), under specific physiological or pathophysiological conditions. We performed our screen using TUBE technology that has an equal affinity to K63 and K48 ubiquitin linkages; however, there are other TUBE variants that bind specific lysine linkages allowing the screen to be biased towards non-canonical ubiquitinated substrates if desired. Moreover, we used semi-quantitative proteomics using 2D-DIGE, allowing high resolution separation and reduction of sample complexity prior to mass spectrometric analysis, and enhancing accuracy of protein identification, while avoiding issues of gel-to-gel variability associated with traditional 1D or 2D gel-based proteomics.[124] To minimize false positives, we coupled our 2D-DIGE strategy with a multi-sample cross-comparison to achieve higher confidence in spot-picking prior to MALDI-TOF peptide identification, the stringency of which could be increased or decreased based on the user's preference for confidence (Table 2.1).

We realize that there are other modifications to this protocol that could be used to refine substrate identification. Although we did not include proteasome inhibition to our protocol, an approach that is often used in interaction-based methods, the inclusion of a proteasome inhibitor such as MG132 for cell-based protein sources prior to protein extraction would likely increase

the pool of K48-linked polyubiquitinated proteins. In addition, there are other protein identification methods that could be used in place of 2D-DIGE/MALDI-TOF as there are limitations to a gel-based approach including difficulty detecting very hydrophobic proteins, proteins with extreme molecular weights and pI values, as well as the potential limited availability of 2D-DIGE facilities and personnel with the required expertise. With minimal modification this method could be used with gel-free quantitative proteomics strategies such Tandem Mass Tags (TMT) or Isobaric Tags for Relative and Absolute Quantification (iTRAQ) to identify and quantitate proteins in each of the collected eluate and supernatant samples.[125] It should be noted that, even with the use of a gel-free based approach, the same subtractive approach could be used to reduce false positives. With the robust, flexible nature of the protocol described here, we are hopeful that this method will be broadly applied to the study of both ubiquitin ligases and DUBs and through the identification of their substrates, aid in the understanding of these unique and important regulatory proteins.

Experimental Procedures

*Neonatal Rat Ventricular Myocyte Isolation and Culture***.** Neonatal rat ventricular myocytes (NRVM) were isolated from day old Sprague–Dawley pups utilizing the Worthington Neonatal Cardiomyocyte Isolation System as previously described and according to manufacturer's instructions. [126] Briefly, isolated neonatal hearts were sequentially digested at 4 °C overnight with trypsin and then at 37 °C for 2 h with collagenase type II. After preplating to minimize nonmyocyte contamination, cells were plated on tissue culture dishes precoated with laminin (Sigma). NRVM were cultured at 37 °C and 5% CO_2 in Dulbecco's Modified Eagle Medium (DMEM, Invitrogen) with 10% horse serum, 5% fetal bovine serum and 100 μM 5-bromo-2'-

deoxyuridine (BRDU) to inhibit non-myocyte growth for the first 24 h post isolation and subsequently in a 4:1 ratio of DMEM:Minimum Essential Medium with 100 μM BRDU. Freshly isolated NRVM were cultured for 72 h prior to adenoviral infection.

Adenoviral Constructs. Full-length mouse MuRF1 was cloned into the Myc-pCMV vector. Adenovirus plasmids Ad-GFP and Ad-MuRF1 (the later expressing GFP and Myc-tagged MuRF1 bicistronically) were constructed in pADTrack-CMV and used as previously described.[102]

Adenoviral Infection and TUBE Enrichment for Ubiquitinated Proteins. Six independent 15 cm plates of cultured NRVM were transduced with Ad-GFP or Ad-MuRF1 at a multiplicity of infection (MOI) of 10 for 18 h. Lysates were prepared by scraping, trituration and brief sonication of cells in cell lysis buffer containing 50 mM Tris-HCl, pH 7.5, 0.15 M NaCl, 1 mM EDTA, 1% NP-40, 10% glycerol, 50 μM deubiquitinating enzyme inhibitor PR619 (LifeSensors) and 1X HALT protease/phosphatase inhibitor (Pierce) followed by clarification by centrifugation at 15,000 x *g*. Lysates from all plates transduced with Ad-GFP or Ad-MuRF1 were pooled and total protein concentration determined by BCA protein assay (Pierce). Lysate containing 1 mg of total protein was incubated for 18 h at 4 °C with 60 μl of prewashed Agarose TUBE 2 beads (LifeSensors) or Control Agarose beads (LifeSensors). Unbound supernatant was removed and frozen at -80 °C. Beads were thoroughly washed in 20 mM Tris-HCl, pH 8.0, 0.15 M NaCl, 0.1% Tween-20 (TBST) and ubiquitinated proteins eluted in 0.2 M glycine, pH 2.5 and neutralized with 1 M Tris pH9.0. Elutions were stored at -80 °C prior to 2D-DIGE and proteomic analysis. Alternatively, ubiquitinated proteins were eluted by resuspending the beads in 20 μl SDS reducing sample buffer and boiling for 5 m followed by centrifugation at 13000 x *g* for 5 m.

Beads were discarded and eluted samples analyzed by SDS-PAGE and immunoblotting for Hspd1 (Abcam, ab59457) or total ubiquitin (Lifesensors, VU-1).

Two-Dimensional Differential In Gel Electrophoresis (2D-DIGE). To detect differential protein expression, samples were first cleaned by methanol/chloroform precipitation and dissolved in lysis buffer (8 M urea, 20 mM tris-HCl, pH 8.5, 4% CHAPS). Aliquots of the MuRF1 TUBE eluate, MuRF1 TUBE supernatant, MuRF1 agarose control supernatant, GFP TUBE eluate, GFP TUBE supernatant, and GFP agarose control supernatant were labeled with either Cy3 or Cy5 fluorescent dyes. An internal control (IC) was prepared by pooling equal amounts of protein (15 µg) from all samples, and then labeled with 200 pmol of Cy2 for every 15 µg of protein. The labeling reaction was carried out on ice for 30 min, protected from light. To quench the reaction, 1 µL of 10 mM lysine was added, and the reaction was then incubated for an additional 10 m on ice in the dark. After labeling, corresponding samples were combined. An equal volume of 2X sample buffer (8 M urea, 4% CHAPS, 20 mg/mL DTT, 2% (v/v) IPG buffer 4–7 (GE Healthcare)) was added and the mixture was placed on ice for 15 m. Rehydration buffer (8 M urea, 4% CHAPS, 2 mg/mL DTT, 1% (v/v) IPG buffer 4-7) was added to a final volume of 250 µL. For each gel IC, Cy3, and Cy5 labeled samples were mixed before applying to immobilized pH gradient (IPG) strips (24 cm, pI range 4–7, GE Healthcare). Isoelectric focusing and the subsequent SDS-PAGE (second dimension) were performed as previously described.[127 37]. Three independent gels were run: the first comparing MuRF1 TUBE eluate to GFP TUBE eluate, the second comparing MuRF1 TUBE supernatant to MuRF1 agarose control supernatant and the third comparing GFP TUBE supernatant to GFP agarose control supernatant. Gels were analyzed using DeCyder 7.0 software (GE Healthcare). A “spot number” of 4500 was used to generate spot maps using the differential in-gel analysis (DIA) component. Spot maps were filtered via

the built-in algorithm using a Max slope of 1.0, and manually edited to remove dust particle signals. Expression changes were assessed using the Volume Ratio between samples within each gel.

Spot selection and MALDI-TOF. Protein spots displaying greater than 1.5 fold expression changes were marked as "picks" and the list of "picks" from all three gel comparisons were aligned to determine spots that were identified as "picks" by all three comparisons. Spots that were identified as "picks" across all multiple gels were selected for further analysis and removed from the 2D gels using an Ettan Spot Picker (GE Healthcare) and submitted to the Michael Hooker Proteomics Center (University of North Carolina) for protein identification by matrix-assisted laser desorption ionization time of flight (MALDI-TOF) mass spectrometry. With the aid of a Progest Protein Digestion System (Digilab), proteins were digested with trypsin, and the resulting peptides were extracted. Peptides were mixed with matrix (α-Cyano-4-Hydroxycinnamic Acid) and analyzed using a MALDI-TOF/TOF mass spectrometer (Applied Biosystems 4800 Plus). MS spectra were obtained in reflector positive ion mode and peaks with signal-to-noise ratio above 10 were selected for MS/MS analysis (maximum of 45 MS/MS spectra per spot). All spectra were searched using GPS Explorer, Version 3.6 (AB Sciex) linked to the Mascot (Matrix Science, Inc.) search engine and compared to the IPI rat database downloaded from European Bioinformatics Institute.

Immunofluorescence. 24 h post infection with Ad-GFP or Ad-MuRF1, cells were washed with PBS, fixed, and permeabilized in phosphate-buffered 2% paraformaldehyde/0.2% Triton X-100 for 30 minutes at 4 °C. Immunofluorescence labeling was carried out with a mouse anti-GFP (Sigma, G6795) followed by a FITC-conjugated goat anti-mouse secondary antibody (Jackson

ImmunoResearch Laboratories Inc.) and DAPI (Sigma-Aldrich). Images were acquired by fluorescence-inverted microscopy.

Western blotting. 24 h post infection with Ad-GFP or Ad-MuRF1, cells were washed with PBS and lysates prepared by scraping, trituration and brief sonication of cells in cell lysis buffer containing 50 mM Tris-HCl, pH 7.5, 0.15 M NaCl, 1 mM EDTA, 1% NP-40, 10% glycerol, 50 μM deubiquitinating enzyme inhibitor PR619 (LifeSensors), and 1X HALT protease/phosphatase inhibitor (Pierce) followed by clarification by centrifugation at 15,000 x *g*. Proteins were separated by SDS-PAGE, transferred to PVDF and detected by Western blot analysis with anti-myc (Sigma, C3956), anti-MuRF1 (R&D Systems, AF5366), or anti-GAPDH (Sigma, G8795).

*In Vitro Ubiquitination Reactions***.** *In vitro* ubiquitination reactions were performed as previously described.[128] In brief, 2 μM human MuRF1 (LifeSensors), 0.25 μM Ube1 (Boston Biochem), 2.5 μM UbcH5c and 10 mg/ml ubiquitin and 500 ng of recombinant Hspd1 (Enzo Life Sciences) or ATP5b (Abnova) were incubated in 20 μM HEPES, pH 7.4, 10 μM KCl, 5mM ATP, 5mM $MgCl_2$, and 1X Energy Regeneration Solution (ERS, Boston Biochem) for 3 h at 30 °C. Samples were analyzed by SDS/PAGE and immunoblotting for ATP5b (Aviva Systems Biology, ARP48186) or Hspd1 (Abcam, ab59457).

Animals. The MuRF1 transgenic (MuRF1-Tg) mice used in this study were previously described.[121] All animal protocols were reviewed and approved by the University of North Carolina Institutional Animal Care Advisory Committee and were in compliance with the rules governing animal use as published by the National Institutes of Health.

Immunoprecipitation from MuRF1 Transgenic Hearts. Whole heart ventricles were excised from anesthetized male wild-type and MuRF1-Tg mice and homogenized on ice in T-Per tissue protein extraction reagent (Pierce) containing 1X HALT protease/phosphatase inhibitor (Pierce), 50uM PR619 (Lifesensors), 50uM MG132 (Millipore) and 10mM N-ethylmaleimide (Sigma) first in a 2 ml glass tissue grinder homogenizer followed by brief homogenization by handheld tissue homogenizer. Homogenates were clarified by centrifugation at 10,000 x *g*. Protein G Dynabeads (Invitrogen) pre-conjugated to 2 μg of Hspd1 (Abcam, ab59457) or Tpm1 (Abcam, ab133292) antibody or appropriate IgG control were incubated for 1 h at 4 °C with clarified homogenates. Beads were washed five times with Tris-Buffered Saline with 0.02% Tween-20 and subsequently, proteins were eluted in SDS-sample buffer and analyzed by SDS-PAGE and western blotting.

CHAPTER III

ATAXIA AND HYPOGONADISM CAUSED BY THE LOSS OF UBIQUTIN LIGASE ACTIVITY OF THE U BOX PROTEIN CHIP[1,2]

Gordon Holmes syndrome (GHS) is a rare Mendelian neurodegenerative disorder characterized by ataxia and hypogonadism. Despite being recognized clinically for nearly 100years, little has been understood about the pathophysiological mechanisms or underlying genetic causes of GHS. However, recently there have been several reports of mutations in *STUB1* (NM_005861), a gene that encodes the protein CHIP, (C-terminus of HSC70 interacting protein) in GHS. Furthermore, it was suggested that disordered ubiquitination underlies GHS though the discovery of exome mutations in another E3 ligase *RNF216* and the deubiquitinase *OTUD4*. Here we describe the first discovery of *STUB1* mutation in GHS. We performed exome sequencing in a family with two of three siblings afflicted with ataxia and hypogonadism and identified a homozygous mutation *STUB1* c.737C→T, p.Thr246Met, the gene encoding CHIP. CHIP plays a central role in regulating PQC, in part through its ability to function as an E3 ligase.

Loss of CHIP function has long been associated with protein misfolding and aggregation in several genetic mouse models of neurodegenerative disorders; however, a role for CHIP in human neurological disease has yet to be identified. Introduction of the Thr246Met mutation into CHIP results in a loss of ubiquitin ligase activity measured directly using recombinant proteins

as well as in cell culture models. Loss of CHIP function in mice resulted in behavioral and reproductive impairments that mimic human ataxia and hypogonadism. We conclude that GHS can be caused by a loss of function mutation in CHIP. Our findings further highlight the role of disordered ubiquitination and PQC in the pathogenesis of neurodegenerative disease and demonstrate the utility of combining whole exome-sequencing with molecular analyses and animal models to define causal disease polymorphisms. Furthermore, our findings and subsequent reports of human STUB1 mutation in various forms of ataxia have led to the establishment of a new disease designation, SCAR16 (Autosomal Recessive Spinocerebellar Ataxia-16) to describe spinocerebellar ataxia caused by homozygous or compound heterozygous mutation in the STUB1 gene.

[1]Elements of the work referenced in this chapter have been published in: Human Molecular Genetics

[2]Figures Contributed by:
Chang-He Shi: 3.1, 3.2
Carrie E. Rubel: 3.3, 3.4, 3.10
Jonathan C. Schisler, M.S., PhD:3.5, 3.6, 3.7, 3.8, 3.9

Introduction

Gordon Holmes syndrome (GHS [MIM 212840]) is a rare neurodegenerative disorder characterized by ataxia with hypogonadism. [129] Generally the term 'Ataxia' is used to describe a loss of coordination and may be caused by a variety of diseases including metabolic disorders, vitamin deficiencies, peripheral neuropathy, cancer, or brain injuries. In the case of GHS, ataxia is the result of progressive deterioration of the cerebellum. As such, GHS belongs to a large family of disorders termed 'cerebellar ataxias,' (CA) all characterized by cerebellar degeneration. The majority of diseases caused by CA mutations, including GHS, are inherited as autosomal recessive CA (ARCA, estimated prevalence is 7 per 100,000). [89] Patients with GHS typically present in early adulthood with variable movement disorders, most notably ataxia but may also include chorea, dysmetria, unsteady gait and dysdiadochokinesis. These deficits are progressive and may be accompanied by a wide range of additional neurological features including dysarthria, brisk reflexes, impulsivity, aggressive behavior, nystagmus, dementia and cognitive impairment.[130-132] As one might expect with this variability in reported neurological symptoms, brain imaging of GHS patients has also revealed significant clinical variability with reports of cortical atrophy, pronounced cerebellar degeneration, diffuse white matter lesions in the cerebrum, brainstem and cerebellum as well as atrophy of the putamen.[131, 132]

This neurologic phenotype is accompanied by hypogonadotropic hypogonadism. In the normally functioning hypothalamic-pituitary axis the hypothalamus releases gonadotropin-releasing hormone (GnRH) which stimulates the pituitary gland to release follicle-stimulating hormone (FSH) and leutinizing hormone (LH). These hormones then act upon the female ovaries or male testes to stimulate the release of estrogen, progesterone and testosterone driving normal sexual development in puberty. Any change in this hormone release chain causes a lack of sex

hormones and prevents normal sexual maturity. Concordant with hypogonadotropic hypogonadism, patients with GHS present with low serum levels of sex steroids and gonadotropins and a lack of sexual development and infertility. Hypogonadotropic refers to a defect in the production or release of gonadotropins by the pituitary gland. In most cases of GHS, the hypogonadism is hypogonadoptropic in nature.[130, 132] However, in some patients extended treatment with physiologic doses of pulsatile GnRH is able to stimulate a gonadotropin response, suggesting that in these patients the pituitary is able to produce and release gonadotropins, but under physiological conditions does not do so normally.[131] It is notable that in addition to that which is observed in association with ataxia in GHS, hypogonadism has a distinctive association with variable neurological disorders including epilepsy, dysmyelination, nerve muscle disease, movement disorders, mental retardation and deafness. This clearly indicates an intrinsic pathophysiological association between neurological function and hypogonadism yet the molecular mechanisms underlying this association remain unknown.[133]

Despite almost 100 years of clinical recognition, there is still little understanding of the pathophysiological mechanisms or underlying genetic causes of GHS. Here we describe the discovery of the first mutation in *STUB1,* the gene encoding the protein CHIP, in humans associated with GHS. We performed exome sequencing in a family with two of three siblings afflicted with ataxia and hypogonadism and identified a homozygous mutation, *STUB1* c.737C→T, p.Thr246Met. CHIP is a 35 kDa protein that functions as both a molecular co-chaperone, autonomous chaperone, and ubiquitin E3 ligase. [8, 128, 134]These activities are facilitated by three functional domains: a tetratricopeptide repeat (TPR) domain required for interaction with heat shock proteins (Hsp), a charged domain that mediates CHIP's dimerization and activity, and a U-box domain that confers ubiquitin ligase activity.[8, 79] As a ubiquitin ligase

CHIP forms a homodimer and associates with ubiquitin conjugating enzymes to ubiquitinate substrates with canonical or noncanonical chains. In cooperation with heat shock chaperone proteins, including HSC70, HSP70, and HSP90, CHIP plays a crucial role in recognizing and modulating the degradation of numerous chaperone-bound proteins.[87] CHIP can also promote the folding and/or activity of substrates, including the metabolic energy sensor AMPK acting directly as an autonomous chaperone.[8, 135]

Recently the E3 ligase RNF216 and deubiquitinase OTUD4 were associated with GHS in multiple non-Asian families.[136] Protein ubiquitination is primarily regulated through E3 ligases that construct covalently-linked polyubiquitin chains on protein substrates, subsequently resulting in the targeting of ubiquitinated proteins for degradation through the 26S proteasome. Together these data suggest that perhaps disordered ubiquitination in general plays an essential role in the pathophysiology of ataxia and hypogonadism.

In genetic mouse models of neurodegenerative disease, the loss of CHIP function is associated with the misfolding and aggregation of several proteins (such as expanded polyglutamine tracts, hyperphosphorylated Tau and oligomeric forms of α-Synuclein), all of which are thought to be associated with multiple neurodegenerative disorders such as Spinocerebellar ataxia, Alzheimer's disease and Parkinson's disease. [82, 137, 138] However, prior to our discovery, mutations in the human *STUB1* gene had not been reported, and information about the physiology of CHIP deficiency in humans was non-existent. We demonstrate that the *STUB1* mutation leads to a loss of function of CHIP resulting in diminished E3 ligase activity; furthermore, mice lacking the expression of CHIP phenocopy some aspects of human GHS, supporting a direct link between CHIP and GHS pathophysiology.

Results

Clinical assessment of two sisters with GHS. We initially observed a pedigree characterized by ataxia with hypogonadism in two sisters (II-1 and II-2) with an autosomal recessive inheritance pattern. The initial behavioral and sexual development of the proband (II-1) appeared normal, but unsteady gait developed when she was 19 years old, followed by dysarthria 2 years later and remarkable ataxia (Table 3.1). Upon neurological examination, patient II-1 exhibited horizontal gaze-evoked nystagmus with no restriction of extraocular movement. Photography and fluoresce angiogram of the ocular fundus revealed no abnormality (data not shown). Additionally, muscle tone, power and deep tendon reflexes of the four limbs were normal without any overt pathology. Neuroelectrophysiological examination was generally normal, except for decreased amplitude of motor-evoked potential in the bilateral lower limbs.

The younger sister (II-2) also had a similar illness recognized at 17 years of age with a progressive deterioration of balance and gait disturbance (Table 3.1). Over the next two years, patient II-2 developed noticeable hand tremors during activity along with coarse head tremors. Further examination revealed findings similar to patient II-1, in addition to increased tendon reflex and positive pathological signs in the four limbs, suggesting pyramidal tract lesions. Patients II-1 and II-2 were administered the mini-mental state examination (MMSE) resulting in normal cognitive scores, whereas the Montreal Cognitive Assessment (MoCA), which is more sensitive to subtle cognitive defects particularly in the early stages of disease, [139] did reveal cognitive deficiencies in both sisters (Table 3.1). Furthermore, patients II-1 and II-2 completed only four and eight years of schooling, respectively. The neurological phenotype consisting of severe ataxia with selective cognitive impairments are consistent with cerebellar ataxia. The diagnosis of cerebellar ataxia was confirmed with MRI brain scans that revealed remarkable

atrophy of the cerebellum in both sisters (Fig. 3.1A).

In addition to the neurological defects, both sisters had poor sexual organ development. At 22 years of age, patient II-1 had still not menstruated, had poor development of secondary sexual characteristics (Table 3.1) and hypoplasia of uterus and ovaries, as revealed via ultrasound analysis (Table 3.1). Similar to her older sister, patient II-2 did not attain menarche or any secondary sexual characteristics, presenting with infantile uterus and ovarian development (Table 3.1). Along with the lack of sexual development in both patients, the serum levels of estradiol and progesterone were much lower than the normal reference range, leading to a diagnosis for both patients of hypogonadotropic hypogonadism (Table 3.1). In addition to the low circulating sex hormones and the lack of menses, levels of the pituitary hormones FSH and LH in both sisters were comparable to pre-pubescent levels (Table 3.1). The nature of the hypogonadism in GHS is still not clear and may derive from either hypothalamic or pituitary hypogonadotropism.[132] Interestingly, a gonadotropin-releasing hormone (GnRH) stimulation test showed the pituitaries in both patients were responsive to a single intravenous dose of GnRH (100 μg) measured by the stimulated release of FSH and LH (Fig. 3.1B), suggesting the primary defect in these sisters may be due to hypothalamic versus pituitary hypogonadotropism. However, the pituitary response to GnRH in other GHS patients is reported to diminish over time, suggesting pituitary dysfunction may still be an issue in these patients,[132, 136] making it difficult to pinpoint the primary lesion of the hypogonadotrophic hypogonadism in GHS. The two patients in this study were referred to a gynecological endocrinologist, and exogenous estrogen and progestin supplement therapy was administered in an attempt to construct an artificial menstrual cycle. After three weeks of therapy, their menarche came, demonstrating that the lack of reproductive organ maturity was due to the lack of circulating hormones.

Table 3.1. Clinical phenotypes of STUB1 genotypes

Subject	II-1	II-2
Ataxia		
SARA	13	15
Cognitive measures		
MMSE	25	27
MoCA	11	24
Sexual development		
Tanner stage	II-III	II-III
Corpus uterus (mm)	35 x 31x 25	28 x 20 x 19
Cervix (mm)	23	16
Ovaries (mm)	14 x 9	13 x 10
Hypogonadism		
Estradiol (pg/ml)	26	28
Progesterone (ng/ml)	0.31	0.33
FSH (mIU/ml)	6.97	6.25
LH (mIU/ml)	5.95	6.44

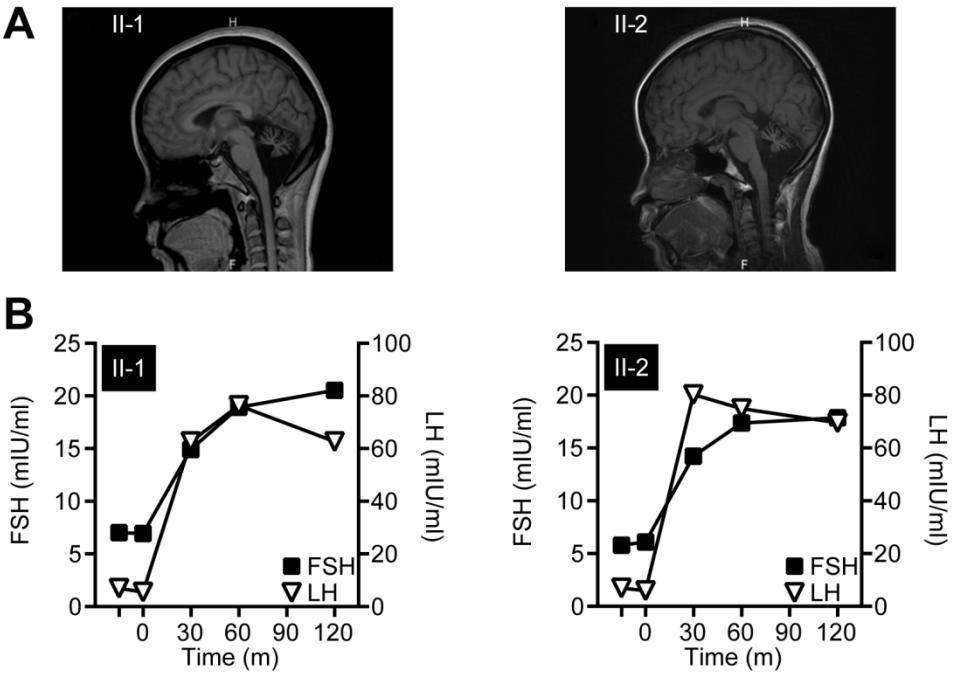

Figure 3.1. Clinical Manifestations in Patients Presenting with Ataxia and Hypogonadism.

A. MRI scans revealed remarkable cerebellum atrophy of patient II-1 (left) and II-2 (right).

B. Gonadotropin-releasing hormone (GnRH) stimulation tests measured the response in circulating FSH and LH serum levels to exogenous GnRH administration (at time = 0) in patient II-1 (left) and II-2 (right).

Exome sequencing reveals a mutation in Stub1 associated with GHS. In an attempt to identify the causative mutation in this family, we performed whole exome sequencing of the two affected patients (II-1, II-2) as well as the unaffected brother (II-3). Using a combination of bioinformatic repositories and functional algorithms, we developed a strategy to identify causal mutations segregating with the GHS phenotype (Fig. 3.2A). After quality control and coverage criteria were met, we started with a total of 98255, 96183, 98507 SNPs, and 7227, 7046, 7159 insertions or deletions (indels) for II-1, II-2, and II-3, respectively. Since ataxia with hypogonadism is a rare disorder but has a clear phenotype, there was a low likelihood that a causal mutation in our patients was present in wider, healthy populations. We therefore filtered for novel variants by comparing our exome data to dbSNP build 132, [140] the 1000 Genomes Project, [141] Hapmap, [142, 143] YH project, [144] and the National Heart, Lung, and Blood Institute (NHLBI) Exome Sequencing Project, [145] further refining our target list to around 2000 SNPs and 130 indels (Fig. 3.2A). Next, we filtered for a recessive inheritance pattern for variants that were present in the affected sisters, but not in the unaffected brother, which reduced the number of candidate variants to six, including three compound heterozygote variants and three homozygous variants (Fig. 3.2A and Table 3.2).

The analysis of chromosomal regions that are identical by descent (IBD) is a form of homozygosity mapping, a fundamental tool in linkage analysis of pedigree data. For Mendelian diseases with a recessive inheritance pattern, affected family members usually share the genomic segment harboring the causal mutation. Therefore, variants inside the IBD regions found among the affected family members are of primary interest and can be exploited to identify genomic regions consistent with inheritance of a recessive monogenic disease. [146, 147] These regions of interest are indicated by an IBD score of two, signifying the intersection between paternal and

maternal haplotypes. [147] Using the criteria of IBD = 2 we excluded three additional variants, reducing the number of candidate variants to three. Finally, we carried out functional-impact prediction on protein mutations by PolyPhen-2, [148] Mutation Taster, [148] and SIFT. [149] Interestingly, only one homozygous variant predicted an impact on protein function in this family, *STUB1* (NM_005861) c.737C→T, resulting in a p.Thr246Met (T246M) amino acid change in the corresponding protein commonly known as CHIP (C-terminus of HSC70 interacting protein, Figure 3.2C). As an additional control, we tested for the *STUB1* c.737C→T mutation in 500 Chinese control individuals; consistent with our data mining of multiple SNP databases used in our filtering strategy (Fig. 3.2A), the c.737C→T mutation was not detected in the Chinese control population.

The genetics of cerebellar ataxia has been intensely pursued over the last decade, identifying over 30 loci that associate with the disease.[150] Therefore, we were not surprised that we did not detect any *STUB1* mutations in an additional cohort of 32 Chinese cerebellar ataxia patients without hypogonadism, suggesting that mutations in *STUB1,* and the recently described mutations in *RNF216/OTUD4,* associate with the distinct pathophysiological phenotype of cerebellar ataxia with hypogonadism. We also sequenced the *STUB1* gene in a cohort of five GHS patients that harbor a single heterozygous RNF216 mutation and eight GHS patients that do not have either RNF216 and OTUD4 mutations; [136] interestingly, we did not identify any mutations in *STUB1* in any of these GHS patients, suggesting additional genetic factors likely remain to be identified in other GHS patient populations. We also performed copy number variations (CNV) analysis and did not find any CNV that co-segregated either separately with the disease phenotype or together with single heterozygous variations in this family,[151] suggesting that gene dosage was not contributing to the GHS phenotype. Taken together, our genetic and

bioinformatics analyses demonstrate the association of the *STUB1* c.737C→T mutation with GHS and predict the T246M in CHIP results in a functional change that directly contributes to the pathophysiology of cerebellar ataxia and hypogonadism.

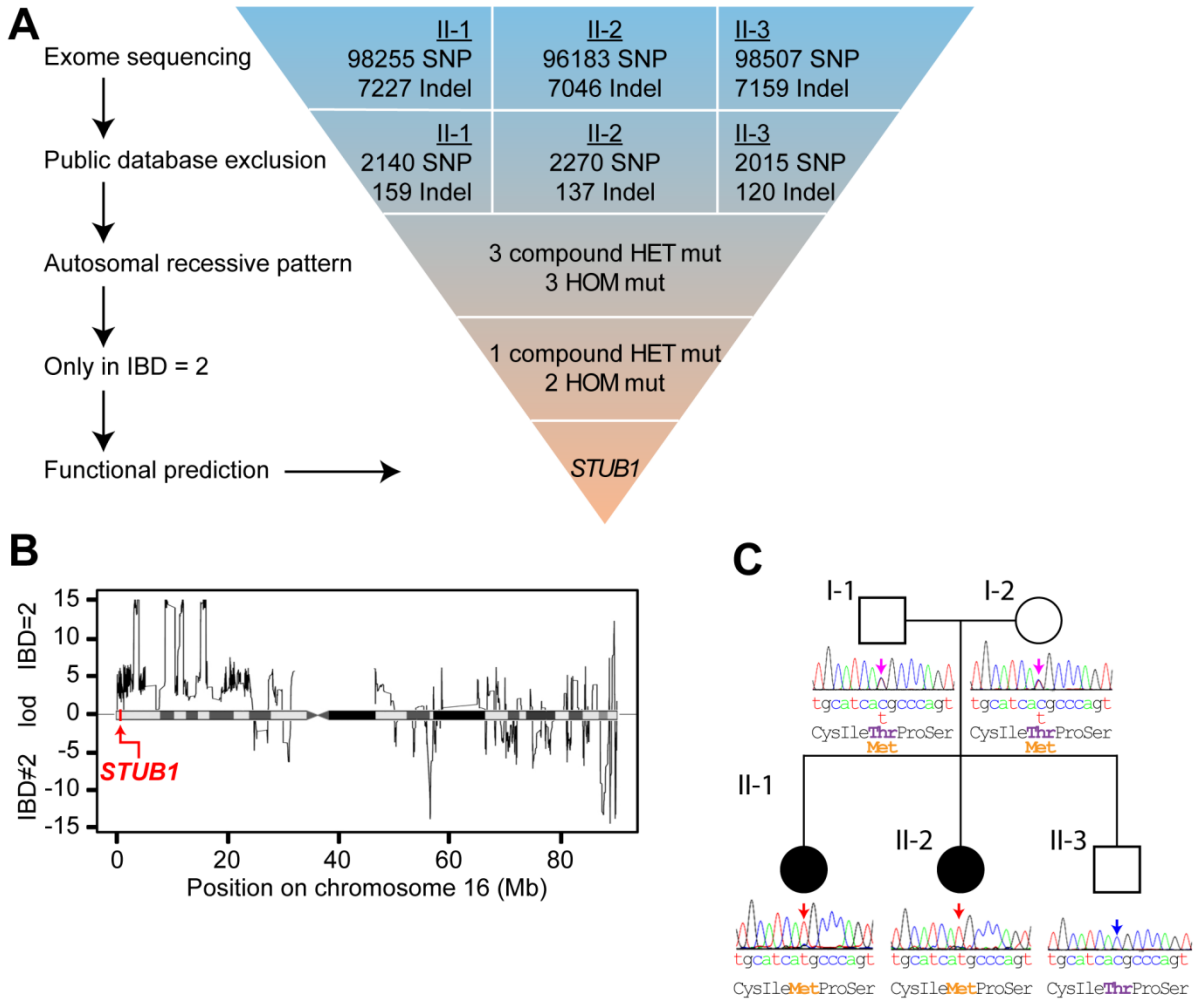

Figure 3.2. Exome Sequencing Identifies a p.Thr246Met Mutation in the GHS Family.

A. Schematic representation of our exome data-filtering approach to identify mutations with recessive inheritance patterns in the family.

B. Posterior probabilities of IBD = 2 classification. The logarithmic ratio (LOD) of the posterior probabilities of being IBD = 2 versus IBD ≠ 2 are plotted for all classified variant positions on chromosome 16. A disease-causing mutation in the *STUB1* gene was identified in an IBD = 2 region of high posterior probability, indicated by the red arrow.

C. A pedigree of the family indicating the unaffected (open symbols) and affected (filled symbols) members. Sanger sequencing confirmed the co-segregation of the c.737C→T resulting in p.Thr246Met mutation in STUB1 within the family.

Table 3.2. Six Candidate Variants from Exome Sequencing Data.

Chromosome	Position	Reference Allele	Variant Allele	HET/HOM	Gene Name	Substitution	IBD=2	Functional Prediction
chr19	9025639	A	G	HOM	MUC16	N12272S	NO	……
chr1	75037091	G	A	HET	C1orf173	G1435R	NO	……
chr1	75039089	C	G	HET	C1orf173	L769V	NO	……
chr2	97914920	T	A	HET	ANKRD36	C1893S	NO	……
chr2	97915322	T	G	HET	ANKRD36	I1914M	NO	……
chr4	151769986	G	T	HET	LRBA	G94V	YES	TOLERATED
chr4	151356766	G	T	HET	LRBA	S2350I	YES	TOLERATED
chr22	24325095	A	G	HOM	GSTT2	K129E	YES	TOLERATED
chr16	732232	C	T	HOM	STUB1	T246M	YES	DAMAGING

The T246M mutation in CHIP abolishes ubiquitin ligase activity. The identification of the homozygous c.737C→T mutation in sibling GHS subjects and the co-segregation of functional mutation algorithms predicting a strong impact on protein function suggested that the resulting T246M substitution mutation in CHIP results in a change in protein function. T246, which is highly conserved across CHIP homologs, is located within the U box domain of CHIP (Figure 3.3A), the domain responsible for ubiquitin ligase activity. [128] In addition, T246 is located in the core of a conversed beta hairpin turn (Fig. 3.3A),[152] likely contributing to the high impact scores of the T246M mutation identified in our functional prediction analysis. In addition to the role that CHIP plays as a ubiquitin ligase, CHIP can also act as a co-chaperone through its direct interactions with cellular chaperones including HSC70, HSP70, and HSP90 via CHIP's tetratricopeptide repeat (TPR) domain (Fig. 3.3A).[81, 128, 134, 153] Both a functional TPR and U box domain are required for CHIP's ability to directly impact PQC and attenuate the cellular stress response in large part through polyubiquitiantion of HSP chaperones.[75, 79] Given that the CHIP mutation identified in our patients resides in the U box domain, we hypothesized that the T246M substitution would result in a loss of CHIP's ubiquitin ligase activity, without affecting CHIP's interaction with cellular chaperones though the intact TPR domain.

To test effect of the T246M substitution on CHIP's ubiquitin ligase activity and its ability to bind to chaperones, we first expressed either wild-type CHIP (CHIP-WT) or CHIP engineered with a methionine substituted for threonine at residue 246 (CHIP-T246M) in COS-7 cells. As expected, both the WT and T246M proteins immunoprecipitated with exogenous HSP70 (Fig. 3.3B and Fig. 3.4A), demonstrating that CHIP-chaperone interactions are not perturbed by the T246M substitution. In fact, more CHIP-T246M protein immunoprecipitated with HSP70 compared to CHIP-WT (Fig. 3.3B and Fig. 3.4A). Surprisingly, the increased interaction

between CHIP-T246M and HSP70 did not result in robust HSP70 ubiquitination compared to CHIP-WT expressing cells (Fig. 3.3B and Fig. 3.4A), indicating that the T246M substitution deleteriously affects CHIP's ubiquitin ligase activity. We subsequently tested both the interaction and ubiquitination function of CHIP-T246M on an endogenously-expressed CHIP substrate, HSC70, and again observed an increased interaction between CHIP-T246M and HSC70 with diminished polyubiquitination (Fig. 3.3C). Together, these data suggest the functional defect in CHIP-T246M is a loss of ubiquitin ligase activity.

To directly test the impact of the T246M substitution on CHIP-dependent substrate ubiquitination we compared the T246M mutation to previously engineered point mutations of CHIP. To do this we used CHIP constructs with mutations located either in the TPR domain (CHIP-K30A) or the U box (CHIP-H260Q), that abolish either the interaction with cellular chaperones, such as HSC70 and HSP70, or the ubiquitin ligase activity of CHIP, respectively (Fig. 3.3A) using cell-free assays comprised of purified recombinant proteins. Similar to the results observed in cell culture models (Fig. 3.3B and 3.3C), CHIP-T246M failed to polyubiquitinate HSC70 in vitro, mimicking the effect of the H260Q (U box) mutant CHIP protein (Fig. 3.3D). To confirm that the lack of chaperone ubiquitination in vitro is due to a defect in the U box domain and not due to the inability to bind to the chaperone substrate, we measured the effect of the CHIP-T246M mutation CHIP's intrinsic ability to autoubiquitinate, a phenomenon that readily occurs in vitro.[79] Similar to the H260Q mutation, the CHIP-T246M mutant did not exhibit any autoubiquitination, in contrast to CHIP-WT and CHIP-K30A proteins that both contain functional U boxes (Fig. 3.3E), confirming that the T246M mutation abolishes CHIP's ubiquitin ligase activity.

Taken together, these data suggest the CHIP-T246M mutation is, at minimum, a partial loss of function mutation, that results in an inability of the mutant protein to polyubiquitinate both chaperone-bound proteins as well as the chaperone proteins themselves, functions that are integral to CHIP's role in PQC. [75, 154]

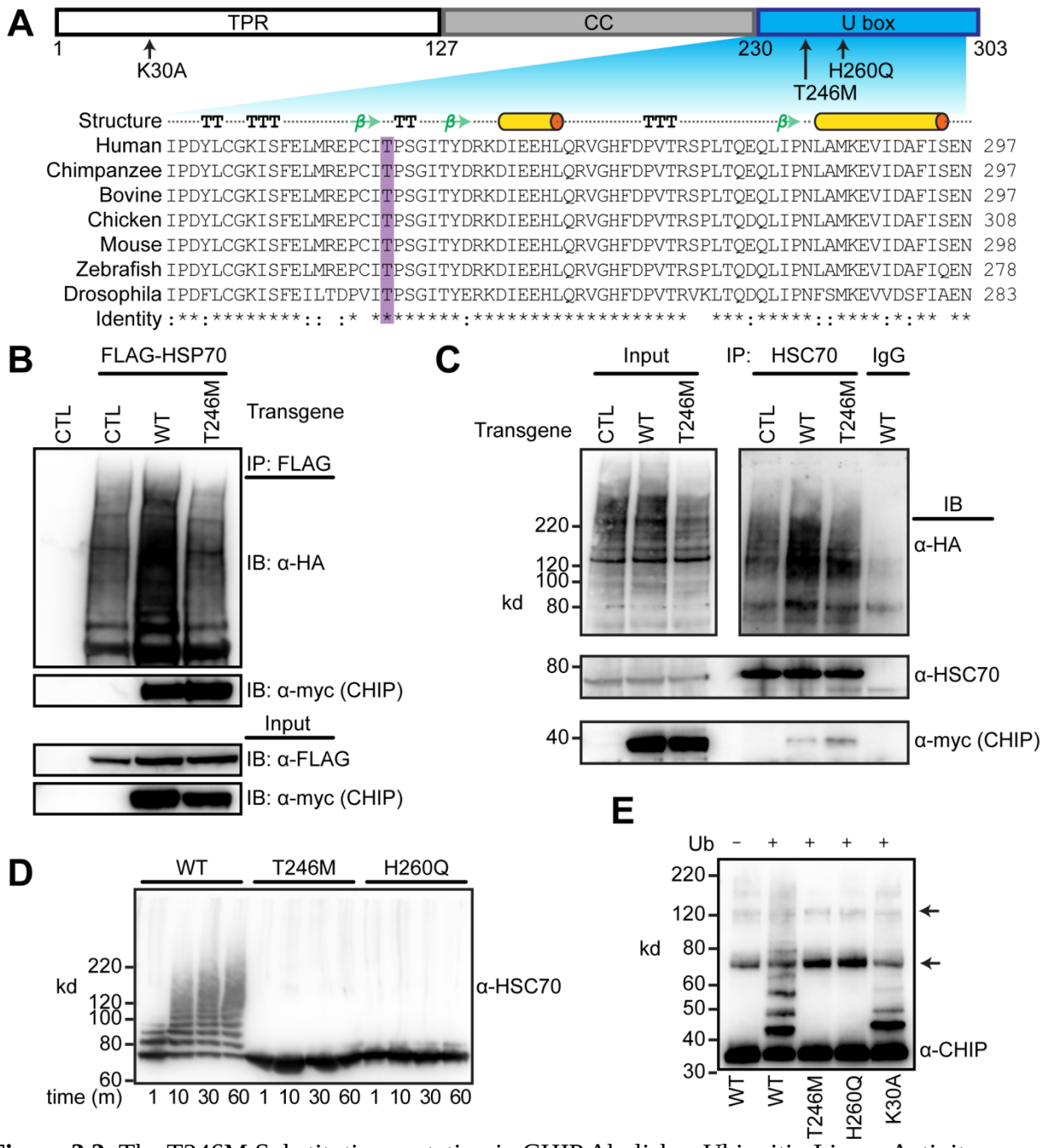

Figure 3.3. The T246M Substitution mutation in CHIP Abolishes Ubiquitin Ligase Activity.

A. CHIP is comprised of three functional domains, tetratricopeptide repeat (TPR), coiled-coil (CC), and U box. The arrows indicate the location and identity of point mutations used to measure the functional parameters of CHIP (top). The structural features of the U box include alpha helices (cylinders), beta strands (arrows), beta turns (TT), and alpha turns (TTT). Sequence alignment demonstrates the evolutionary conservation of the T246 in the U box domain of the CHIP protein across the indicated species. Conservation of residues are labeled as fully conserved (*), strongly similar (:), or non- similar ( ).

B. COS-7 cells were co-transfected with the indicated vectors (transgenes, CTL = pcDNA3, WT = pcDNA3-CHIP, T246M = pcDNA3-CHIP-T246M) in addition to HA-tagged ubiquitin. HSP70 was immunoprecipitated (IP) with FLAG beads and the resulting precipitants as well as inputs were immunoblotted (IB) with the indicated antibodies.

C.COS-7 cells were co-transfected with the indicated transgenes in addition to HA-tagged ubiquitin and immunoprecipitated with either an HSC70 antibody or rat IgG. The inputs and resulting precipitants (IP) were immunoblotted with the indicated antibodies. Approximate molecular weights in kilodaltons (kd) are also provided.

D. and **E**. Cell-free ubiquitination reactions containing recombinant HSC70 and the indicated CHIP proteins resolved via SDS-PAGE and immunoblotted for an antibody recognizing HSC70 (**D**) or CHIP (**E**). Ubiquitin (Ub) was excluded in lane 1 (**E**) to demonstrate the autoubiquitination of CHIP, arrows indicate the incomplete reduction of CHIP oligomers.

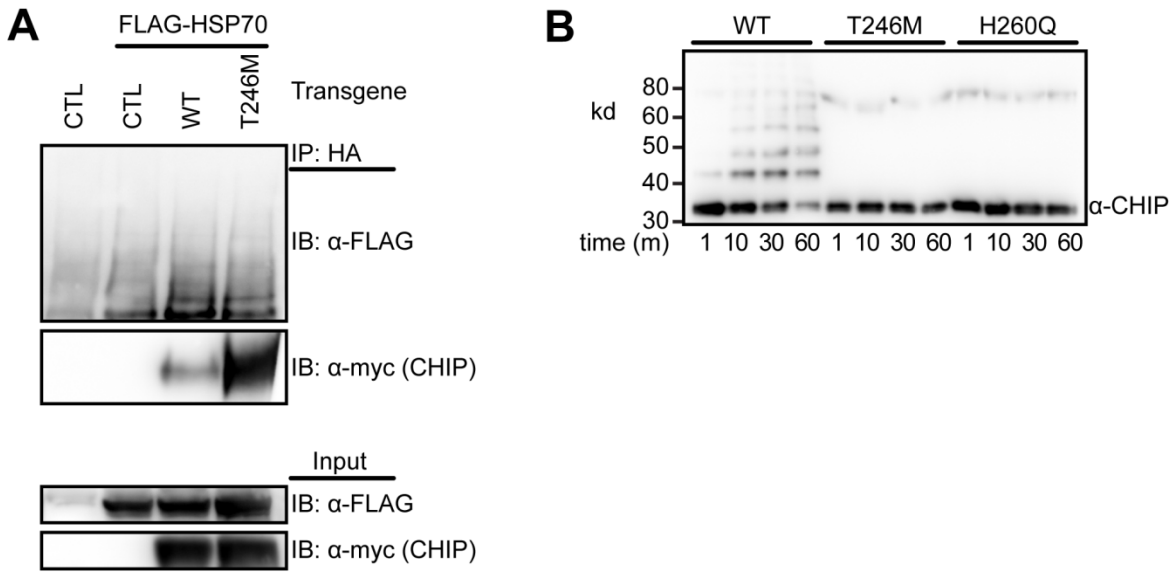

Figure 3.4. CHIP-T246M Interacts with Chaperones but Lacks Ubiquitin Ligase Activity.

A. To confirm the effect of CHIP-T246M on the exogenous HSP70 substrate, we performed the reverse IP shown in Figure 3A. COS-7 cells were co-transfected with the indicated vectors (transgenes, CTL = pcDNA3, WT = pcDNA3-CHIP, T246M = pcDNA3-CHIP-T246M) in addition to HA-tagged ubiquitin. Ubiquitinated proteins was immunoprecipitated (IP) with HA beads and the resulting precipitants as well as inputs were immunoblotted (IB) with the indicated antibodies.

B. Cell-free ubiquitination reactions from the experiment represented in Figure 3D containing recombinant HSC70 and the indicated CHIP proteins resolved via SDS-PAGE and immunoblotted for an antibody recognizing CHIP.

CHIP-deficient mice exhibit defects in motoric, sensory, cognitive and reproductive function. The profound cerebellar ataxia exhibited by both siblings homozygous for the CHIP-T246M substitution suggests that CHIP plays a critical role in maintaining cerebellar function. Given the autosomal recessive nature of CHIP deficiency in our GHS subjects, we first wanted to assess the neurological behavior of *Chip*$^{-/-}$ mice to determine if the loss of CHIP expression leads to impairments associated with cerebellar ataxia. Our group has previously described a line of mice deficient in CHIP expression.[74, 155] Given the data above linking the human CHIP-T246M mutation with cognitive impairments, we evaluated the phenotype of *Chip*$^{-/-}$ mice using a battery of behavioral assessments (Fig. 3.6A). The rotarod test is extensively used in mouse models to detect cerebellar dysfunction by testing motor coordination and motor learning on a rotating dowel. The performance of *Chip*$^{-/-}$ mice on the rotarod demonstrated a severe motoric impairment irrespective of gender, with wild-type mice having between 2.9 ± 0.6 and 4.2 ± 1.8 fold increase in latency to falling times in male and female mice, respectively, compared to *Chip*$^{-/-}$ mice (Fig. 3.5A). The performance of *Chip*$^{-/-}$ mice did not improve with retesting (Fig. 3.5A), demonstrating a lack of motor learning. To further confirm a motoric defect and to test for defects in sensory gating we measured the acoustic startle response in wild-type and *Chip*$^{-/-}$ mice (Fig. 3.5B). Consistent with the motoric impairment observed in *Chip*$^{-/-}$ mice using the rotarod assessment, the magnitude of the startle response was reduced 86% in *Chip*$^{-/-}$ mice compared to wild-type mice (Fig. 3.5C). Additionally, the reaction time to the acoustic startle was delayed across all sound levels by an average of 40% ± 4% (7.8 ms) in *Chip*$^{-/-}$ mice (Fig. 3.5D), consistent with our hypothesis that the loss of CHIP expression results in motoric impairment due to cerebellar dysfunction. Interestingly, pre-pulse inhibition levels were not affected by the loss in CHIP expression (Fig. 3.6B), suggesting that sensory gating (as well as auditory function)

was not impaired. In addition to the deficits attributed to cerebellar dysfunction, *Chip*$^{-/-}$ mice also exhibited an aberrant pattern of exploration in a novel environment demonstrated by increased time in the open arms of the elevated plus maze (EPM, Fig. 3.5E) and a higher error rate in the acquisition of a spatial learning task in the Barnes maze (Fig. 3.5F) compared to wild-type mice, suggesting hippocampal function may also be impaired with the loss of CHIP function. Additional testing found no differences in physical activity, both in the EPM and open field (Fig. 3.6C, 3.6D, and 3.6E), latency measures in a spatial task (Fig. 3.6F), or in social behavior (Fig. 3.6G). In gait testing, *Chip*$^{-/-}$ mice took smaller steps relative to wild-type mice (8% to 16% reduction in stride length, $F(1,16) = 5.515$, $p = 0.032$) however there were no differences in overlap, front paw stride length, or front paw and hind paw base width (data not shown) suggesting that motoric synchrony is not altered. Taken together, the loss of CHIP expression appears to have a selective impact in motoric, sensory, and cognitive function, in particular with tasks attributed to cerebellar function.

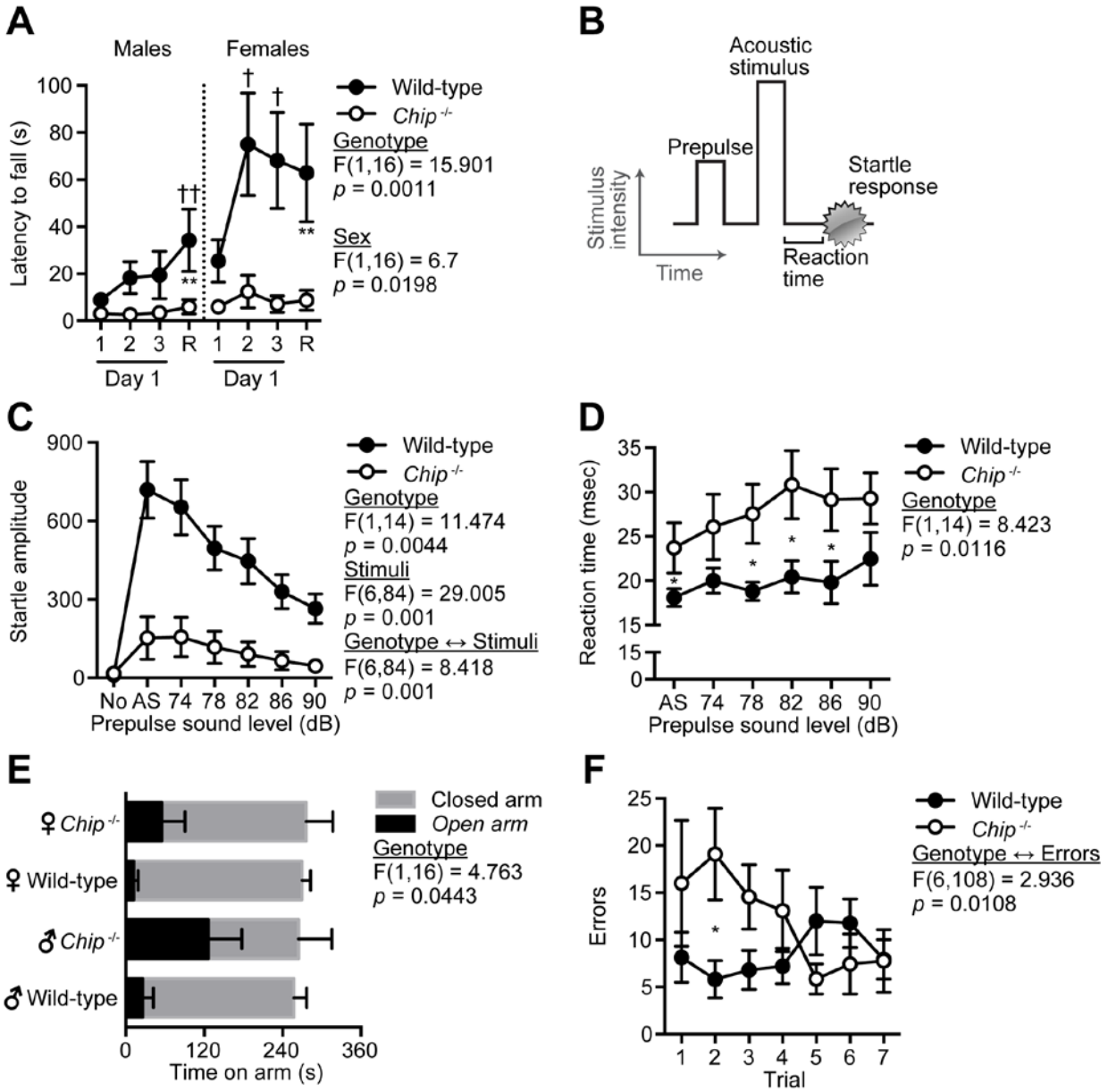

Figure 3.5. Chip$^{-/-}$ Mice Have Extreme Ataxia and Other Selective Motoric and Cognitive Impairments.

A. Latency to fall from an accelerating rotarod represented by the mean ± SEM for either *Chip*$^{-/-}$ or wild-type mice (n = 5 per genotype per gender). The first three trials were given on the first day of rotarod testing. Retest (R) indicates the highest latency across two trials given 48 hours after the day one trials: ** $p < 0.01$ comparing *Chip*$^{-/-}$ versus wild-type mice at the retest; † $p < 0.05$ and †† $p < 0.01$ comparing the indicated time point with first trial within the genotype.

B. The acoustic startle response is comprised of a prepulse followed by an acoustic stimulus (AS, 120 decibels, dB). Both the reaction time to the AS and the magnitude of the response was measured.

C and **D.** Amplitude and reaction time of the startle response following AS is represented by the mean ± SEM for each genotype (n = 6 and 10 for *Chip*$^{-/-}$ and wild-type mice, respectively). Trials included no stimulus trials (No) and AS alone trials: $p < 0.05$ comparing *Chip*$^{-/-}$ versus wild-type mice across all stimulus conditions shown in (**C**) or as indicated by * in (**D**).

E and **F**. Time on the open and closed arms of an elevated plus maze (**E**) and the number of errors (incorrect holes explored) before finding the target hole on the Barnes maze (**F**) represented by the mean ± SEM for each genotype (n = 10): * $p < 0.05$ comparing *Chip*$^{-/-}$ versus wild-type mice.

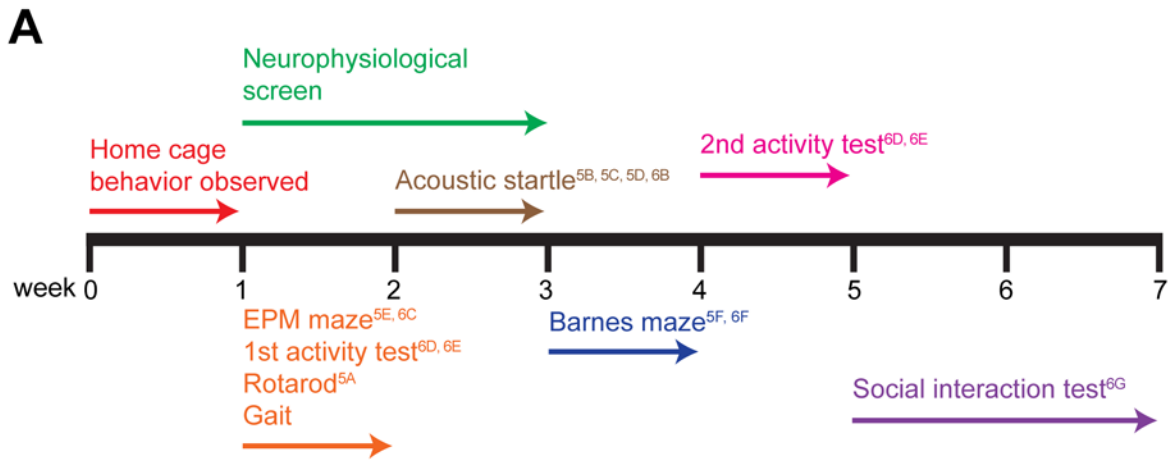

Figure 3.6A. Behavioral Assessment Tests of Chip$^{-/-}$ Mice.

The goal of these assessments was to determine the behavioral phenotype of mice with a deficiency in CHIP expression. Subjects were 10 wild-type mice and 10 *Chip*$^{-/-}$ mice with an equal number of males and females per genotype. In all tests, an observer took measures blind to experimental treatment (genotype). Data were analyzed using two-way ANOVAs, looking for effects of genotype (wild-type or *Chip*$^{-/-}$) or sex, or when indicated, repeated measures ANOVAs. Fisher's protected least-significant difference (PLSD) tests were used for comparing group means only when a significant F value was determined.

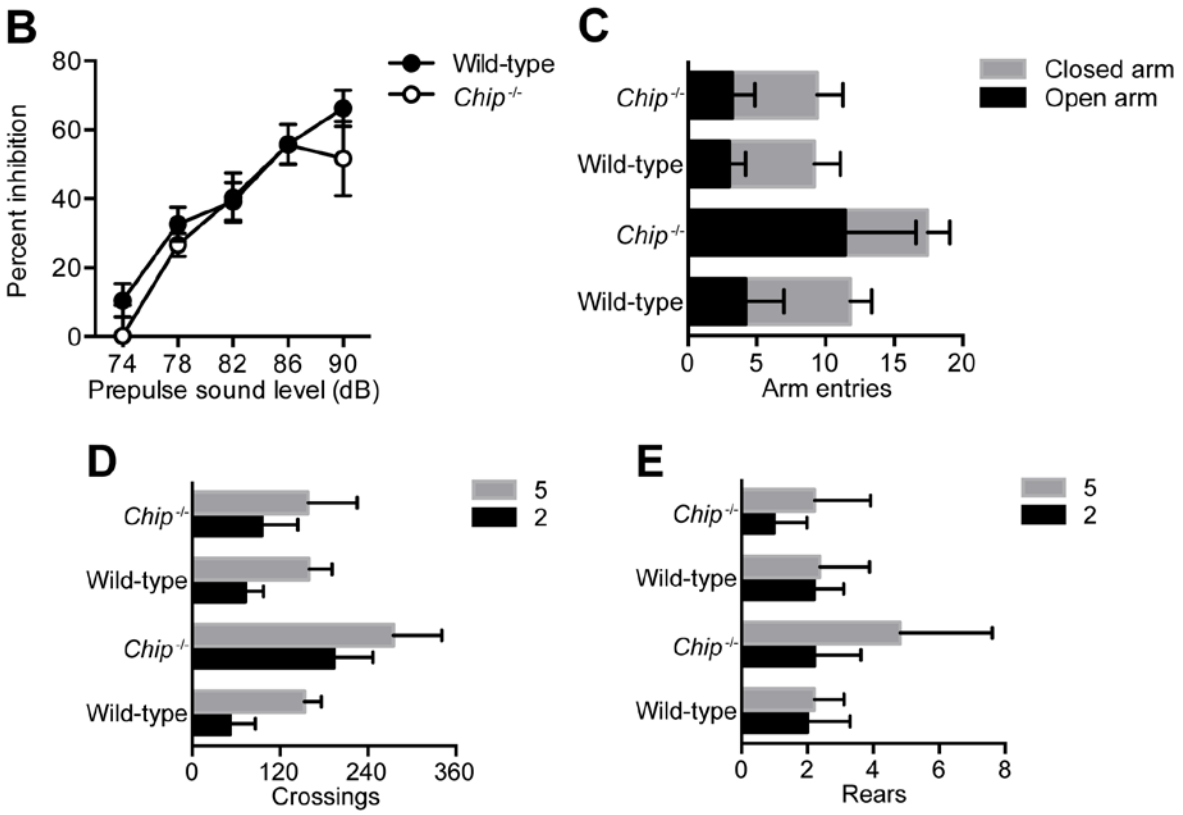

Figure 3.6B-E. Prepulse Inhibition During Acoustic Startle Test and Various Measures of Physical Activity Throughout Behavioral Testing.

B. Prepulse Inhibition During Acoustic Startle Test, depicted in Figure 3.5B. The prepulse inhibition was calculated as 100 - [(response amplitude for prepulse stimulus and startle stimulus together / response amplitude for startle stimulus alone) x 100] and represented by the mean ± SEM for each genotype (n = 6 and 10 for *Chip*$^{-/-}$ and wild-type mice, respectively). Four animals, all *Chip*$^{-/-}$ mice (three males and one female), did not show significant startle responses to the acoustic stimuli, suggesting auditory impairment. Therefore, their data were removed from the analysis. There was no significant effect of genotype on levels of prepulse inhibition, indicating that the Chip deficiency did not lead to impairment in sensory gating. This result also suggested that the remaining knockout mice had normal auditory function, since a prepulse stimulus only 8 dB above background noise (the 78 dB prepulse level) decreased the startle response by more than 25%. These data suggest a possible motoric deficit for the decrease in startle amplitude and reaction time (Fig. 3.5C and 3.5D).

C. The number of entries into the open and closed arms of mice in the elevated plus maze (EPM). There was no difference between the groups for arm entries, suggesting that wild-type and Chip-/- mice have equal levels of activity.

D. and E. The number of crossings and rears in an open-field chamber were counted at two different time points (2 and 5 weeks of testing). For all data shown neither genotype nor sex had a significant impact on the various measures represented by the mean ± SEM for each genotype.

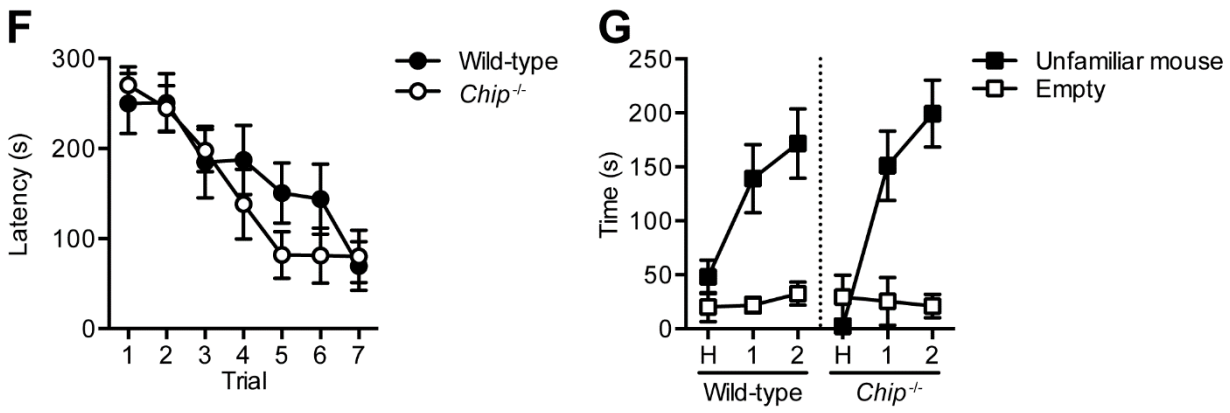

Figure 6F-G: Latency in the Barnes Maze and Social Affiliation Test

F. Latency in the Barnes Maze. Each mouse received one trial per day, across seven days. Measures were taken of latency to find the target hole until reaching the target represented by the mean ± SEM for each genotype (n = 10). Both wildtype and *Chip*$^{-/-}$ mice showed high latency scores, reflecting the performance of some animals which never left the center of the maze (especially on the first and second trials). A repeated measures ANOVA did not result in any significant effects for genotype or gender on latency, although the significant effect for trials (the repeated measure) confirmed that some learning occurred in this task [$F(6,108) = 10.99$, $p = .0001$].

G. Social Affiliation Test. Animals were tested in a three-chambered apparatus, with the chambers connected by short tubes. Each mouse was first set in the middle chamber and allowed to explore for five minutes in the absence of another mouse (habituation period, H). Then measures were taken of the time each mouse spent in either and empty chamber (open squares) or the chamber containing an unfamiliar mouse (closed squares) for the first (1) and second (2) five minutes of the session. Separate repeated measures ANOVAs were performed for time spent in the side with the unfamiliar mouse and time in the empty side. No significant overall effects of either group (wild-type or *Chip*$^{-/-}$) or gender were detected. One-way ANOVAs indicated that *Chip*$^{-/-}$ mice spent less time exploring during the habituation period (when both sides of the chamber were empty, $p < 0.05$), but *Chip*$^{-/-}$ mice subsequently showed normal social preference during the test period. These data indicate that loss of CHIP protein does not cause deficits in the preference for social affiliation.

CHIP expression in the human cerebellum and the neuropathological and reproductive phenotype of Chip$^{-/-}$ mice. In the healthy human brain, CHIP is widely expressed throughout, including the molecular and granular region of the cerebellum where it is abundantly expressed in Purkinje cells (Fig. 3.7A). A similar pattern of CHIP immunoreactivity is found in mouse brains.[156] Histological examination of sagittal cerebellar sections from *Chip*$^{-/-}$ mice revealed cellular loss throughout the various lobes of the cerebellum, specifically in the Purkinje cell layer with noticeable degeneration and a 3-fold increase in the number of pyknotic nuclei compared to an intact Purkinje cell layer in wild-type cerebellum (Fig. 3.7B and Fig. 3.8A), mimicking the observation of Purkinje cell loss identified in the neuropathological analysis in a deceased GHS patient with disordered ubiquitination (*RNF216* and *OTUD4* mutations).[136] The effect on Purkinje cell pathology was confirmed with the Purkinje cell-specific marker, calbindin (Fig. 3.7C, middle). Additionally, calbindin staining revealed a mosaic expression pattern in *Chip*$^{-/-}$ mice where calbindin expression in the molecular layer is reduced or absent in regions with significant Purkinje cell loss (Fig. 3.7C, left) similar to other mouse models of cerebellar ataxia [157]. Likewise, the cerebellar regions of *Chip*$^{-/-}$ mice that do contain intact Purkinje cells exhibited severe dendritic swelling (Fig. 3.7C, right), a common feature in ataxias. [158, 159] Taken together, these data demonstrate that the complete loss of CHIP function in our mouse model results in behavioral and cellular phenotypes consistent with the cerebellar ataxia found in human subjects with the T246M mutation.

The profound lack of sexual development in patients II-1 and II-2 suggests that CHIP plays a role in neuroendocrine signaling and is necessary for proper sexual development. Notably, since originally deriving the *Chip*$^{-/-}$ mice,[74] we have long been aware of the inability of *Chip*$^{-/-}$ breeding pairs to successfully mate, necessitating that the *Chip*$^{-/-}$ colony be maintained

through *Chip*$^{+/-}$ crossings. Not surprisingly, FSH levels in *Chip*$^{-/-}$ mice were reduced more that 50% when compared to wild-type littermate mice, irrespective of gender (Fig. 3.9A), consistent with the low levels of FSH in patients II-1 and II-2 (Table 3.1). As an additional measure of gonadal dysfunction in *Chip*$^{-/-}$ mice, we measured testicular weight and observed a 38% decrease in *Chip*$^{-/-}$ testes compared to wild-type testes (Fig. 3.9B). Not surprisingly, CHIP is expressed in wild-type mouse testes as well as in both male and female human gonads (Fig. 3.8B and 3.8C). Therefore, the *Chip*$^{-/-}$ mice also appear to encompass some of the neuroendocrine deficiencies seen in patients II-1 and II-2 with the CHIP T246M mutation. In summary, given the likeness of the neurological and neuroendocrine phenotypes in the *Chip*$^{-/-}$ mice with those reported in the GHS patients described in this study, it is highly probably that the c.737C→T in the *STUB1* gene results in a loss of CHIP function in these patients and directly contributes to the disease phenotype observed in this pedigree.

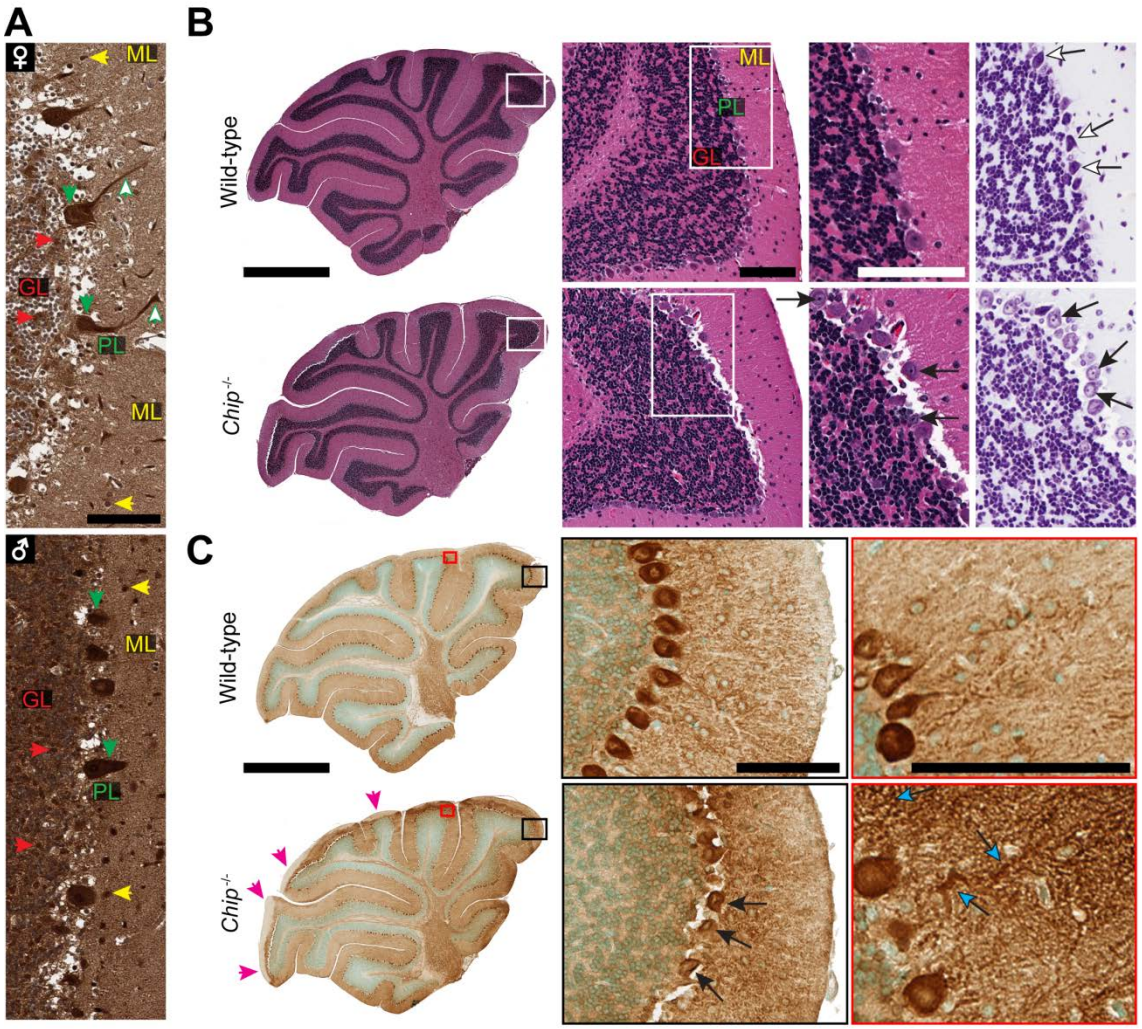

Figure 3.7. CHIP Expression in Human Cerebellum and the Loss of Purkinje Cells in Chip-/- mice.

A. Immunohistochemistry of CHIP expression in adult human cerebellum from a healthy female (♀) and male (♂) with the major regions of the cerebellum identified: molecular layer (ML), Purkinje cell layer (PL), and the granular layer (GL). The colored arrows highlight intense CHIP immunoreactivity throughout the cerebellum including increased reactivity in Purkinje cells, both in the cell body (downward arrows) and dendrites (upward arrows). Scale bar represents 100 microns.

B. Representative whole cerebellar sagittal sections from wild-type and Chip-/- cerebellums (left) with the major regions labeled at higher power (middle) as shown in (A) stained with either hematoxylin and eosin (left, middle) or cresyl violet (right). The open arrows identify normal Purkinje cells in wild-type mice whereas the closed arrows identify the pyknotic uclei in Purkinje cells in Chip-/- cerebellums.

C. Representative whole cerebellar sagittal sections from wild-type and Chip-/- cerebellums immunostained for calbindin (left). Magenta arrowheads (left) indicate regions with no calbindin immunoreactivity and the black and red boxes correspond to the higher power images (middle

and right, respectively). The closed arrows identify the pyknotic nuclei present in Purkinje cells (middle) and the cyan arrows identify swollen dendrites in Chip-/- cerebellums. (B and C) Scale bars for whole cerebellum and higher power images are 1 mm and 100 microns, respectively.

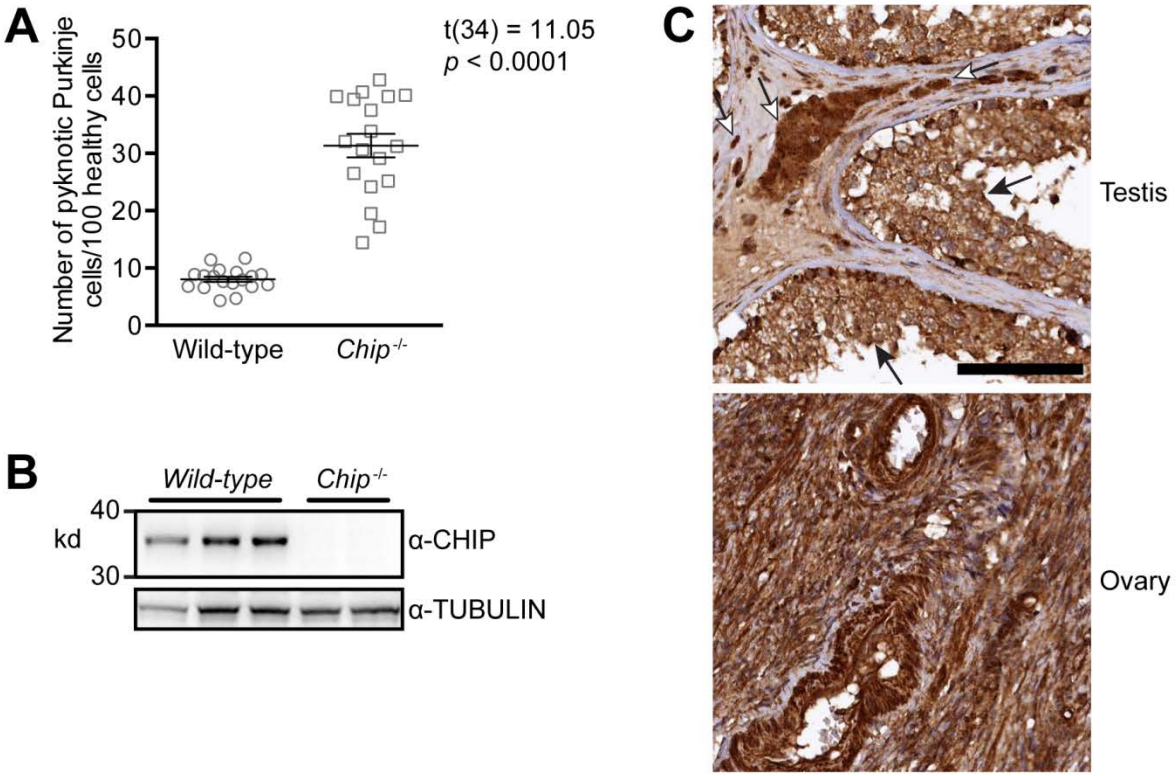

Figure 3.8. Increase in Purkinje Cell Pathology in Chip-/- Mice and CHIP Expression in Mouse and Human Gonads.

A. Sagittal sections of whole cerebellums from either wild-type or Chip-/- mice were stained with crystal violet (Fig. 5B) to measure Purkinje cell pathology. Data are represented by the number of Purkinje cells with pyknotic nuclei per 100 health Purkinje cells with each data point corresponding to one sagittal section (n = 18). A two-tailed t test was used to compare the two genotypes. Chip-/- mice had three-fold more pyknotic Purkinje cells compared to wild-type mice (1079 and 324 across all 18 sections from 3 different mice per genotype, respectively) and a decrease in healthy Purkinje cells (3390 and 4051, respectively).

B. Immunoblot confirmation of CHIP protein expression in extracts isolated from wild-type testes.

C. CHIP is expressed in both human testes (upper) in both Leydig cells (open arrows) and seminiferous ductal cells (closed arrows) and throughout human ovarian stromal cells (lower).

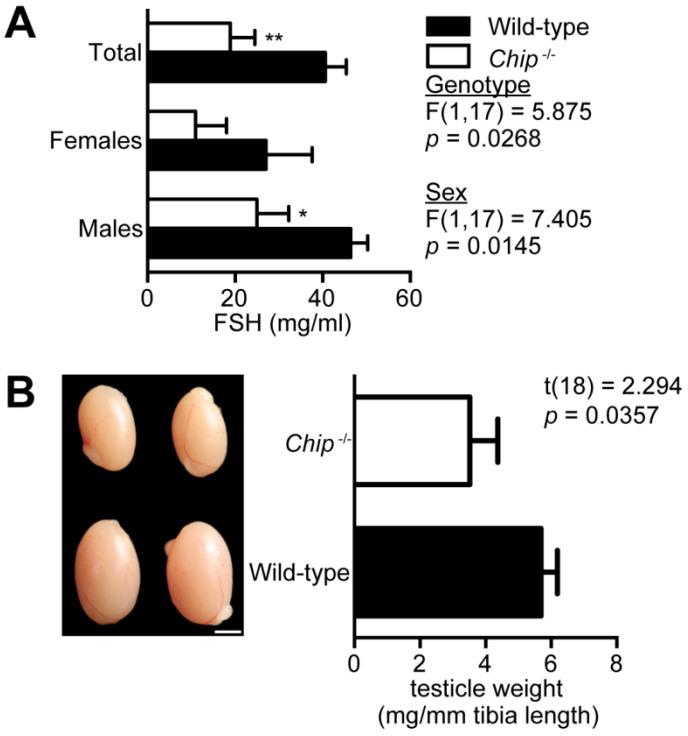

Figure 3.9. Hypogonadism in Chip$^{-/-}$ mice.

A. Serum levels of FSH in wild-type and *Chip*$^{-/-}$ mice represented by the mean ± SEM for each genotype (n = 10): * $p < 0.05$, ** $p < 0.01$ comparing *Chip*$^{-/-}$ versus wild-type mice.

B. Representative pictographs of testes and testicle weights from wild-type and *Chip*$^{-/-}$ mice. Scale bar represents 20 mm. Weights are represented in mg of testicle per mm of tibia length to control for animal size and represented by the mean ± SEM for each genotype (n = 10 and 8, wild-type and *Chip*$^{-/-}$ mice, respectively).

Discussion

There is considerable heterogeneity in terms of age of onset and progression of symptoms within groups of clinical syndromes presenting with both ataxia and hypogonadism.[133] Previous studies have found mutations in *POLR3A* and *GBA2* associated with both ataxia and hypogonadism,[160, 161] but given the additional complex clinical features in these patients, they were not diagnosed with GHS. Immediately prior to our discovery of *STUB1* mutation in GHS, disordered ubiquitination was proposed as a contributing factor to the etiology of GHS, demonstrated by the identification of mutations in the E3 ligase *RNF216* and deubiquitinase *OTUD4* associated with GHS in non-Asian populations.[136] Consistent with an integral role for ubiquitination in GHS pathophysiology, in this study we identified a mutation in the *STUB1* gene encoding the E3 ligase CHIP (Fig. 3.2A and 3.2C) that results in a GHS phenotype (Fig. 3.1A and 3.1B).

Although both hypo- and hypergonadotropic forms of GHS have been reported, most GHS patients, including the *RNF216*-associated GHS patients, usually present with hypogonadotropic-induced hypogonadism.[132, 136] In our patients, the level of gonadotropin is low given their age, but is in the normal range for pre-pubescent individuals; this may indicate a more mild abnormality in the reproductive-endocrine axis, although the lack of sexual development remains remarkable. It is intriguing that deficiency in either *RNF216* or *CHIP* can both lead to a similar clinical syndrome. One possible explanation is RNF216 and CHIP ubiquitin ligase substrates overlap or may converge to a shared pathway that contributes to GHS. Alternatively, RNF216 may have some physiological functions that overlap with the functions of CHIP. It is notable however, that outside of the fundamental phenotype of GHS, ataxia and hypogonadism, there are some other distinct differences in the clinical features of our patients to those harboring *RNF216*

and *OTUD4* mutations; most notably, we did not observe dementia or white matter lesions described previously.[136] However, as mild cognitive impairment was observed in our patients (Table 3.1) and likewise in *Chip*$^{-/-}$ mice (Fig. 3.5), we speculate that cognitive impairment may also act as a core clinical feature in the *STUB1*-associated GHS patients. Long-term follow-up of these patients will be needed to clarify this issue.

Our molecular characterization of the *STUB1* c.737C→T, p.Thr246Met mutation demonstrates a loss in ubiquitin ligase activity (Fig. 3.3D and 3.3E), while still maintaining chaperone interactions (Fig. 3.3B and 3.3C). The ability of CHIP-T246M to maintain its chaperone interaction without a functional U box may result in a dominant-negative phenotype versus a complete loss of CHIP function. Generation of a CHIP-T246M knock-in mouse and comparison of the pathophysiology related to GHS phenotypes will provide valuable insight into the role of CHIP in this disease. Nonetheless, *Chip*$^{-/-}$ mice share several striking physiological similarities to GHS patients with ataxia and hypogonadism (Fig. 3.1), including neuronal degeneration (Fig. 3.7B and 3.7C), pronounced ataxic motor behavior (Fig. 3.5) and reproductive impairments (Fig. 3.9). This strong similarity between the findings in our GHS patients and those in the *Chip*$^{-/-}$ mouse model establishes an important role for CHIP in the maintenance of cerebellar function and the reproductive-endocrine axis. Taken together, our results demonstrate that deficiency of the ubiquitin ligase CHIP causes ataxia with hypogonadism and further highlight the role of aberrant ubiquitin ligase function in the pathogenesis of GHS.

Subsequent to our discovery there have been multiple reports utilizing clinical genomics to identify mutations in *STUB1* in GHS as well as other related forms of ARCA. The majority of these mutations are nicely reviewed by Ronnebaum et al. here.[89] To date, 7 independent reports including our own have identified 10 *STUB1* mutation genotypes in a diverse pool of ARCA

patients.[90, 162-166] These 10 genotypes feature 15 unique mutations that have led to disease pathology in patients harboring either compound heterozygous or homozygous mutations (Fig. 3.10). The amino-acid substitutions reported result in nonsense, missense, frameshift and splicing mutations and are predicted to significantly alter protein function. The CHIP mutations associated with ARCAs are present in all three of CHIP's functional domains, although interestingly the majority are concentrated in the charged domain and the Ubox domain (Fig. 3.10), such that one might predict negative implications for CHIP dimerization and ubiquitin ligase activity. Given the clinical heterogeneity of the ARCA patients harboring these *STUB1* mutations it begs the question whether the affected protein domain may directly correlate to clinical phenotype. For example, cognitive impairment occurs in five out of six genetic signatures harboring mutations in the U-box domain, such that residual CHIP activity involving a defective or truncated U-box domain but intact TPR domain could directly correlate to specific clinical symptoms in some patients.

As a direct result of our report and the subsequent clinical genomics reports of STUB1 mutation in a heterogeneity of ARCAs, including GHS, a novel disease classification, Autosomal Recessive Spinocerebellar Ataxia-16 (SCAR16) has recently been established. SCAR16 is precisely defined as spinocerebellar ataxia caused by homozygous or compound heterozygous mutation in the STUB1 gene on chromosome 16p13. SCAR16 is described as a progressive neurologic disorder characterized by truncal and limb ataxia resulting in gait instability. This novel classification better defines the clinical symptoms specifically correlated with STUB1 mutation in ARCAs to include ataxia, dysarthria, nystagmus, spasticity of the lower limbs, and mild peripheral sensory neuropathy. Additionally, this new definition encompasses those cases of STUB1 ataxia without hypogonadism that would not fall under the GHS terminology. While

STUB1 mutations in GHS may in fact be relatively rare, Synofzik et al. performed whole exome sequencing to evaluate the frequency of STUB1 mutations in ataxia. They screened for STUB1 mutations in a large cohort of Caucasian degenerative ataxia (n=167) and spastic paraplegia patients (n=133) as well as an additional 1707 exomes from 891 index families with other neurological diseases and discovered STUB1 mutations have a high incidence rate of 1.8% (3 of 167) in degenerative ataxia patients, with 0% occurring in the other two groups.[90] This high frequency of STUB1 mutation in ataxia further highlights the importance of this new definition of ataxias specifically linked to STUB1 mutation. Future studies of animal models harboring the identified disease-causing mutations will undoubtedly allow us to better define whether the clinical heterogeneity seen in SCAR16 can be related to the location of the mutations as well as better define the molecular functions of CHIP, particularly in the brain. Furthermore, additional clinical genomics studies across even larger, more diverse cohorts of ataxic patients will more precisely define both the spectrum of STUB1 mutations represented by SCAR16 and the specifically associated clinical symptoms. SCAR16 represents the first definition of human disease caused by dysfunctional CHIP protein, or "CHIPopathy." Pre-clincal data has long implied a role for CHIP not only in neurodegenerative diseases but also cardiac pathologies and cancer such that as whole exome sequencing strategies are more broadly utilized clinically it may not be surprising if other CHIPopathies are discovered. With this increased understanding of clinical CHIPopathies will come an even greater opportunity to utilize the wealth of pre-clinical data surrounding CHIP biology to the guide the potential development of improved therapeutic strategies for these diseases.

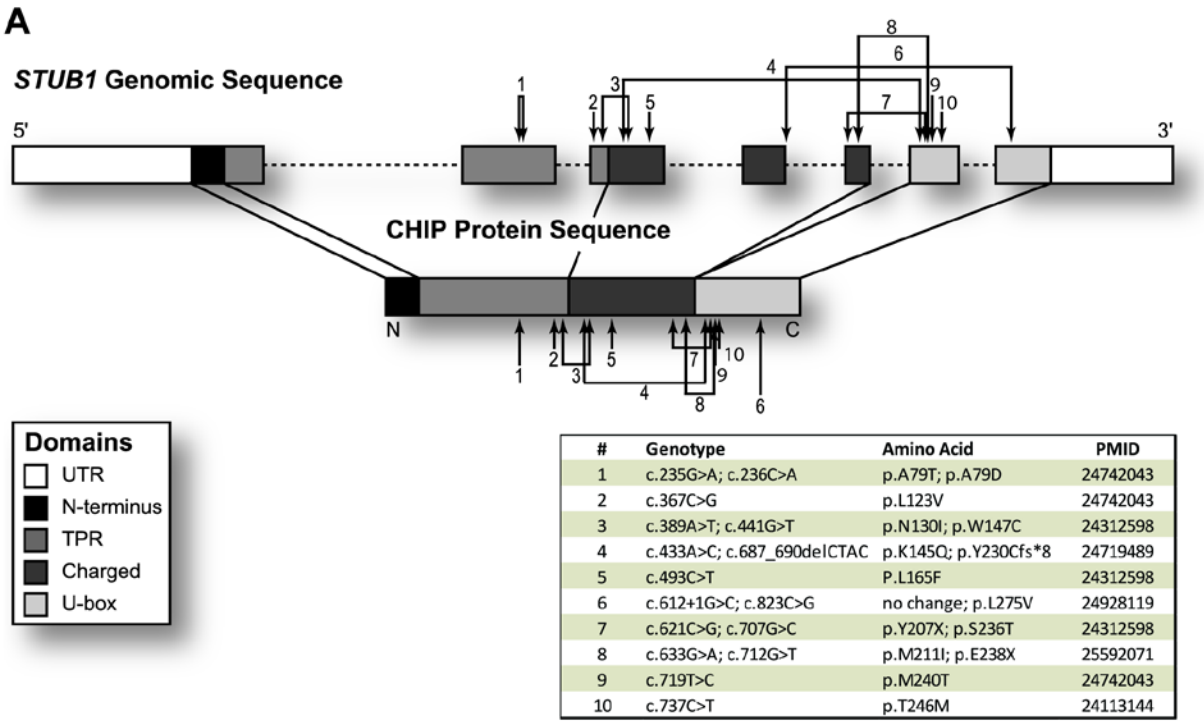

#	Genotype	Amino Acid	PMID
1	c.235G>A; c.236C>A	p.A79T; p.A79D	24742043
2	c.367C>G	p.L123V	24742043
3	c.389A>T; c.441G>T	p.N130I; p.W147C	24312598
4	c.433A>C; c.687_690delCTAC	p.K145Q; p.Y230Cfs*8	24719489
5	c.493C>T	P.L165F	24312598
6	c.612+1G>C; c.823C>G	no change; p.L275V	24928119
7	c.621C>G; c.707G>C	p.Y207X; p.S236T	24312598
8	c.633G>A; c.712G>T	p.M211I; p.E238X	25592071
9	c.719T>C	p.M240T	24742043
10	c.737C>T	p.T246M	24113144

Figure 3.10. SCAR16 human CHIP mutations

A. STUB1 genomic structure and corresponding CHIP protein domains are diagramed. The locations (arrows) of the various mutations associated with SCAR16 and respective nucleic acid and amino acid changes are indicated in the inset table. Joined arrows indicate a compound heterozygous mutation.

Experimental Procedures

Exome sequencing and candidate gene validation. Targeted exon enrichment was performed with the use of the NimbleGen SeqCap EZ Human Exome Library (Roche - NimbleGen Inc). The exon-enriched DNA libraries were subjected to paired-end sequencing with the Illumina Hiseq2000 platform (Illumina). Sequence data were mapped with SOAP2 [167] and BWA [168] onto the hg18 human genome as a reference. We generated an average of 15 Gb of sequence with 90× average coverage for each individual as single-end, 80-bp reads, calls with variant quality less than 20 were filtered out and 99% of the targeted bases were covered sufficiently to pass our thresholds for calling SNPs and small indels (Beijing Genomic Institute, Shenzhen, China). Furthermore, coding regions of the *STUB*1, *RNF216* and *OTUD4* gene were amplified by polymerase chain reaction (PCR) for conventional direct sequencing. Purified PCR products were sequenced on an ABI 3500 Genetic Analyzer (Applied Biosystems, CA). Sanger sequencing results were analyzed by Mutation Surveyor (Softgenetics, PA) and reconfirmed by the same procedure.

Expression plasmids and recombinant proteins. Mammalian expression plasmids pcDNA3-myc-CHIP, pcDNA3-myc-CHIP-K30A, pcDNA3-myc-CHIP-H260Q, HA-Ubiquitin and FLAG-HSP70 were used as described previously [75, 128, 135]. CHIP, CHIP-H260Q, CHIP-K30A, CHIP-T246M and HSC70 recombinant proteins were produced in Escherichia coli BL21(DE3) as His-tagged fusion proteins by induction with 0.1mM isopropyl-1-thio-β-D-galactopyranoside overnight at 18 °C followed by purification with HisTrap™ HP columns (GE Healthcare), concentrated, and stored in in 20 mM HEPES pH 7.4 with 150 mM NaCl.

Mutagenesis. A point mutation of threonine to methionine at position 246 of CHIP was created by site-directed mutagenesis using the Q5 Site-Directed Mutagenesis Kit (New England Biolabs,

E0554S) according to manufacturer's instructions using previously described pcDNA3-myc-CHIP template [128] and mutagenic primers 5'-CCGTGCATCATGCCCAGTGGC-3' and 5'-CTCCCGCATCAGCTCAAAGC-3' (BaseChanger software, New England Biolabs). The myc-CHIP-T246 expression plasmid was produced by transformation in Escherichia coli DH5α, purified, and the single-base pair substitution was verified by DNA sequencing.

In vitro ubiquitination reactions. In vitro ubiquitination reactions were carried out as previously described [128]. Briefly, 0.75 μg (1 μM) of bacterially-expressed HSC70 was incubated in the presence of 2.5 μM CHIP or CHIP mutants, 50 nM purified Ube1 (BostonBiochem, E305), 2.5 μM purified UbcH5c (BostonBiochem, E2-627) and 0.25 μM ubiquitin (BostonBiochem, U100H) in 50 mM Tris pH 7.5, 600 μM DTT, 2.5 mM $MgCl_2$-ATP (BostonBiochem, B20) in a total volume of 10 μl for 1 h at 37 °C. Samples were analyzed by 4-12% Bis-Tris SDS-PAGE and immunoblotting was performed with either anti-HSC70 (Enzo, ADI-SPA-815) or anti-CHIP (Sigma, S1073) antibodies.

Cell culture and transfection. COS-7 cells were maintained in Dulbecco's modified Eagle's medium (Invitrogen) supplemented with 10% fetal bovine serum (Sigma) at 37 °C in an atmosphere of 5% CO_2. Cell transfections were performed using X-tremeGENE 9 (Roche) with the indicated plasmid DNA at a 1:3 DNA to X-tremeGENE 9 ratio.

Immunoprecipitation/Co-immunoprecipitation of FLAG-HSP70/CHIP from COS-7 cells. 1E6 COS-7 cells were plated in normal growth media in 10 cm^2 tissue culture-treated dishes and incubated overnight under normal growth conditions. Cells were then transiently transfected with pcDNA3-mycCHIP (0.5 μg), pcDNA3-mycCHIP T246M (2.5 μg), pcDNA3 (2.5 μg) and/or FLAG-HSP-70 (2 μg) and HA-Ubiquitin (1 μg) and incubated for 24 h under normal growth conditions, followed by treatment with 20 μM MG132 or DMSO for 2.5 h prior to harvest. Cells

were washed in cold PBS and lysed in Cell Lytic M (Sigma) containing 1X HALT protease/phosphatase inhibitor (Pierce) and 50uM PR619 (Lifesensors). Lysates were clarified by centrifugation at 15,000 x *g* for 10 min. Total protein concentration was determined by BCA protein assay (Pierce) and 1 mg total protein clarified lysate incubated overnight at 4 °C with 20 µg of either EZview™ Red ANTI-FLAG® M2 or ANTI-HA Affinity Gel (Sigma). The gel was then washed five times with Tris-Buffered Saline with 0.5% Nonident P-40; subsequently, proteins were eluted in reducing SDS-sample buffer and analyzed by SDS-PAGE and western blotting was performed using anti-Hsp70 (Enzo ADI-SPA-810), anti-FLAG HRP (Sigma, A8592), anti-HA HRP (Sigma, A6533) and anti-myc HRP (Sigma, A5598) antibodies.

Immunoprecipitation/Co-immunoprecipitation of HSC70/CHIP from COS-7 cells. 1E6 COS-7 cells were plated in normal growth media in 100mm tissue culture treated dishes and incubated overnight under normal growth conditions. Cells were then transiently transfected with pcDNA3-mycCHIP (1.5 µg), pcDNA3-mycCHIP T246M (4 µg) or pcDNA3 (1.5 µg) and HA-Ubiquitin and incubated for 24 h under normal growth conditions, followed by treatment with 20 µM MG132 or DMSO control for 2.5 h prior to harvest. Cells were washed 1X in cold PBS and lysed in Cell Lytic M (Sigma) containing 1X HALT protease/phosphatase inhibitor (Pierce) and 50 µM PR619 (LifeSensors). Lysates were clarified by centrifugation at 15,000 x *g* for 10 min. Total protein concentration was determined by BCA protein assay (Pierce) and 1.8 mg total protein clarified lysates were incubated overnight at 4 °C with 10 µg anti-Hsc70 (Enzo ADI-SPA-815) or rat IgG antibodies. 120 µl Protein-G Dynabeads (Invitrogen) were then added to each sample and incubated for 0.5 h at room temperature with rotation. Beads were washed four times with Phosphate-Buffered Saline with 0.05% Tween-20; subsequently, proteins were eluted in SDS-sample buffer and analyzed by SDS-PAGE and western blotting using anti-Hsc70 (Enzo ADI-

SPA-815), anti-CHIP (abcam, Ab4448), anti-HA HRP (Sigma, A6533) and anti-myc HRP (Sigma, A5598) antibodies.

Mouse behavioral assessments.

Home cage behavior. In the first week of testing, a bedding nestlet was added to each home cage of the experimental groups. 24 hours later animals were observed to note if nests had been formed from the bedding material and, in the case of multiply-housed mice, if the animals huddled together in the nest. Nests were observed in each cage, and no aberrant behavior was observed.

Elevated plus maze test for anxiety. The elevated plus maze (EPM) test was performed as the first behavioral test to avoid possible confounding effects of extensive handling. Mice were given one five-minute trial on the plus maze, which had two walled arms (the closed arms) and two open arms. The maze was elevated 52 cm from the floor, and the arms were 51 cm long. Animals were placed on the center section (9.5 cm x 9.5 cm), and allowed to freely explore the maze. Measures were taken of time on, and number of entries into, the open and closed arms.

Activity. One day following the EMP test (week two), exploratory activity in a novel environment was further assessed by a five-minute trial in an open field chamber (40 cm x 30 cm). A grid of squares (10 X 6) was drawn on the floor of the chamber, and counts were taken of number of squares crossed and rears during the trial. A second activity test was performed during week five of testing.

Neurophysiological screen and gait testing. The neurophysiological screen consisted of several measures to assay overall appearance and behavior of the mice. Measures included general observations on the animal's appearance, body posture, and normality of gait. Normal reflexive

reactions to a gentle touch from a Q-tip to the whiskers on each side of the face, and the approach of the Q-tip to the eyes, were assessed. Each mouse was placed in a small, empty plastic cage, and ability to remain upright when the cage was moved from side-to-side or up-and-down was noted. Locomotor coordination was assayed by allowing the mouse to walk across an elevated dowel (wrapped in nylon rope to facilitate grasping) and to climb a similar pole. Each subject was also placed on a wire grid and allowed to hang for two minutes. Reaction to 20 seconds of tail-suspension was observed. For the gait test, a footprint record was generated by painting the paws of the mice and letting the animals run down a narrow alley into a small box. Front paws were painted yellow and hind paws were painted blue with a nontoxic poster paint. Each mouse was given two trials, and measures of front paw and hind paw stride lengths, and front paw and hind paw base widths, were taken. In addition, measures were also taken for paw-print overlap.

Rotarod. Mice were tested on an accelerating rotarod (IITC Inc., Woodland Hills, CA) to assess motor coordination. For the first test session, animals were given three trials, with 45 seconds between each trial. Two additional trials were given 48 hours later. RPM (revolutions per minute) was set at an initial value of three, with a progressive increase to a maximum of 30 RPM across three minutes (the maximum trial length). Measures were taken for latency to fall from the top of the rotating barrel.

Acoustic startle. This test is based on the measurement of the reflexive whole-body flinch, or startle response, that follows exposure to a sudden noise. Assessments included startle magnitude and prepulse inhibition, which occurs when a weak prestimulus leads to a reduced startle in response to a subsequent louder noise. Animals were tested with a San Diego Instruments SR-Lab system, using the procedure as described in [169]. Briefly, mice were placed in

a small Plexiglas cylinder within a larger, sound-attenuating chamber (San Diego Instruments). The cylinder was seated upon a piezoelectric transducer, which allowed vibrations to be quantified and displayed on a computer. The chamber included a houselight, fan, and a loudspeaker for the acoustic stimuli. Background sound levels (70 dB) and calibration of the acoustic stimuli were confirmed with a digital sound level meter (San Diego Instruments). Each mouse was given one session, consisting of 42 trials that began with a five-minute habituation period. There were seven different types of trials: the no-stimulus trials, trials with the acoustic startle stimulus (120 dB) alone, and trials in which a prepulse stimulus (either 74, 78, 82, 86, or 90 dB) occurred 100 ms before the onset of the startle stimulus. Measures were taken of the startle amplitude for each trial, and an overall analysis was performed for each animal's data for levels of prepulse inhibition at each prepulse sound level.

Spatial learning on the Barnes maze. The Barnes maze consisted of a large, brightly lit, circular platform (diameter = 122 cm), elevated 96.5 cm from the floor and positioned like a table, with 40 holes (diameter = 5 cm) drilled along the perimeter. An escape box containing fresh nesting material was placed under one of the holes, and the task required that the animal learn which hole allowed escape from the maze surface. Each mouse was assigned a particular "target" hole, which remained constant across trials, and was different for each subject. At the beginning of each trial, the animal was placed in the center of the maze and allowed 5 minutes to find and enter the escape box. Subjects received one trial per day, across seven days. Measures were taken of latency to find the target hole and number of errors (incorrect holes investigated) until reaching the target.

Social affiliation test. Animals were tested in a three-chambered apparatus, with the chambers connected by short tubes. Each mouse was first set in the middle chamber and allowed to explore

for five minutes. After the habituation period, the animal was removed and an unfamiliar male probe mouse (C57BL/6J strain) was set in one of the side chambers (the particular side alternated between trials). The probe mouse was enclosed in a small metal cage, which allowed nose contact between the bars. The test mouse was then returned to the middle chamber and allowed to freely explore for a ten-minute session. Measures were taken of the amount of time spent in each chamber of the apparatus for the first and second five minutes of the session.

Histology. Mouse brains were carefully excised, gently rinsed, fixed in 4% paraformaldehyde for 24 h, and then placed in 70% ethanol prior to embedding into paraffin. Five micron sections were processed for histology, and stained with either hematoxylin and eosin or cresyl violet for routine histological examination. Unstained sections were used to detect calbindin expression using immunohistochemistry. Slides were stained per the manufacturer instructions using the calbindin D1I4Q rabbit monoclonal antibody (Cell Signaling, 13176) with citrate antigen retrieval, SignalStain® Boost Detection Reagent (Cell Signaling, 8114), and SignalStain® DAB Substate Kit (Cell Signaling, 8059). Degenerating neurons were characterized via light microscopic level by cell body shrinkage, loss of Nissl substance and a small/shrunken darkly stained (pyknotic) nucleus as described [170]. Human cerebellum, testes, and ovary sections were from the Human Protein Atlas tissue array [171] and were stained with anti-CHIP antibody (Sigma, C9243).

CHAPTER IV

THE UNFOLDING TAIL OF CHIP MUTATION IN SCAR16 DISEASE PATHOLOGY: PARTIAL LOSS OF FUNCTION AS A DRIVER OF DISEASE [1]

Our findings and subsequent reports of human STUB1 mutation in various forms of ataxia have led to the establishment of a new disease designation, SCAR16 (Autosomal Recessive Spinocerebellar Ataxia-16), to describe spinocerebellar ataxia caused by homozygous or compound heterozygous mutation in the STUB1 gene that encodes the CHIP protein. Using recombinant proteins as well as in cell culture models, we previously demonstrated that introduction of the T246M mutation into CHIP is associated with SCAR16 and results in loss of CHIP ubiquitin ligase activity, and that CHIP$^{-/-}$ mice have behavioral and reproductive impairments that mimic some of the clinical features of GHS. However, due to the limitations of exogenous overexpression studies and our findings that CHIP$^{-/-}$ mice do not exactly phenocopy the diverse disease heterogeneity in SCAR16, we wanted to extend our initial findings and study the biophysical, cellular and *in vivo* repercussions of T246M CHIP mutation in a more disease-relevant context.

Using multiple biophysical approaches, we demonstrate that T246M mutation results in disorganization and misfolding of the CHIP U-box domain, which disrupts its dimerization and promotes both its aggregation and enhanced clearance by a proteasome-dependent mechanism. In addition to its role as an E3 ubiquitin ligase, CHIP has additional roles within the cell as a co-

chaperone that contribute to PQC as well as emerging roles as a metabolic regulator and nuclear protein involved in DNA repair. Using both *in vitro* assays as well as a primary cell culture model, we demonstrate that while ubiquitin ligase activity is lost as a consequence of T246M mutation, T246M CHIP maintains some function in these other roles that may directly impact the cellular stress response and also contribute to SCAR16 pathophysiology. Furthermore, utilizing CRISPR/Cas genome editing technology, we established a mouse model (T247M) that mimics the human mutation and observed behavioral deficits attributable to cognitive cerebellar dysfunction not observed in our total loss of CHIP animal model, as well as deficits in learning and memory attributable to hippocampal dysfunction that are reflective of cognitive deficits reported in SCAR16 patients. We conclude that T246M mutation is not equivalent to total loss of CHIP and that specific CHIP mutations in SCAR16 likely have varying biophysical and functional consequences to CHIP that may directly correlate to clinical phenotype. Sadly, the therapeutic options for patients with ARCAs, including SCAR16 are severely limited. Our findings both further expand our basic understanding of CHIP biology and provide meaningful mechanistic insight underlying the molecular drivers of SCAR16 disease pathology, which may be used to inform the development of novel therapeutics for this devastating disease.

---

[1]Figures contributed by:
Carrie E. Rubel: 4.1, 4.2, 4.3, 4.4, 4.5, 4.6, 4.7, 4.8, 4.9, 4.10, 4.11, 4.12, 4.13, 4.19
Sheryl Moy, PhD: 4.14, 4.15, 4.16, 4.17, 4.18

Introduction

Our findings and subsequent reports of human STUB1 mutation in various forms of ataxia have led to the establishment of a new disease designation, SCAR16 (Autosomal Recessive Spinocerebellar Ataxia-16) to describe spinocerebellar ataxia caused by homozygous or compound heterozygous mutation in the STUB1 gene that encodes the CHIP protein. Sadly, the therapeutic options for patients with ARCAs, including SCAR16 are severely limited. Understanding the underlying molecular mechanisms associated with CHIP mutation in SCAR16 will provide insight required for the development of effective therapies for this devastating degenerative disease.

Using recombinant proteins, as well as in cell culture models, we demonstrated that introduction of the T246M mutation into CHIP associated with SCAR16 results in loss of CHIP ubiquitin ligase activity. However, the T246M CHIP protein does still bind chaperone proteins, suggesting it may retain some chaperone activity. Interestingly, we also showed that CHIP$^{-/-}$ mice have behavioral and reproductive impairments that mimic some of the clinical features of GHS. However, the complete genetic depletion of CHIP in these mice results in other phenotypic changes, including accelerated aging and metabolic complications. These additional changes may be caused by compensatory mechanisms in the mouse model or may be due to the total loss of all CHIP functions. [8, 155] While these studies provide powerful evidence that SCAR16 can be caused by a loss of function mutation in CHIP and further highlight the role of disordered ubiquitination and PQC in the pathogenesis of neurodegenerative disease, they are limited in their direct application to human pathophysiology by two important constraints. First, these cell-based studies were all performed in the context of exogenous overexpression of T246M CHIP

protein. While these types of studies provided a powerful tool to begin to understand the biology of T246M CHIP in cells, their interpretation is limited because CHIP protein is not expressed at physiologic levels, and in some cases is being studied in cells that normally do not express CHIP protein. Second, while the CHIP$^{-/-}$ mice mimic some of the phenotypes of SCAR16 patients, they are not the appropriate model for understanding the *in vivo* repercussions of CHIP mutation in SCAR16. To date, 7 independent reports, including our own, have identified 10 *STUB1* mutation genotypes in a diverse pool of ARCA patients.[90, 162-166] These 10 genotypes feature 15 unique mutations that have led to disease pathology in patients harboring either compound heterozygous or homozygous mutations. The amino acid substitutions reported result in nonsense, missense, frameshift and splicing mutations and are predicted to significantly alter protein function. There is great clinical heterogeneity of the ARCA patients harboring these *STUB1* mutations. This suggests that specific CHIP mutations may have varying biophysical and functional consequences to CHIP that may directly correlate to clinical phenotype. Clearly, in this context an animal model with a total loss of CHIP does not adequately represent the spectrum of human disease represented by SCAR16. For these reasons, we wanted to extend our initial findings and study the biophysical, cellular and *in vivo* repercussions of T246M CHIP mutation in a more disease-relevant context.

Initially we hypothesized that the functional loss of CHIP ubiquitin ligase activity as a result of T246M mutation was the result of catalytic inactivation of the U-box domain. However, based upon our understanding of the CHIP structure-function relationship, several additional structural consequences of T246M CHIP could also result in functional loss of ubiquitin ligase activity. As described previously, CHIP has three important functional domains: the tetracopeptide repeat (TPR) domain, the charged coiled-coil (CC) domain, and the U-box

domain. The TPR domain is required for chaperone protein binding. Conversely, CHIP dimerization and structural conformational flexibility are required for activation of the bound E2 conjugating enzyme and subsequent ubiquitin transfer. This dimerization and conformational flexibility are dependent upon both the U-box domain and CC domain. [79, 80] Importantly, while the CHIP mutations associated with ARCAs are present in all three of CHIP's functional domains, the majority are concentrated in the charged domain and within the U-box domain, including T246M. This suggests that the structural consequences of T246M mutation may not be as straightforward as simple catalytic activation, but might instead reflect loss of CHIP dimerization ability or general destabilization of the U-box that results in a misfolded protein that may retain some normal functions or may instead be damaging. Here we utilize multiple biophysical methods and cell culture studies to evaluate the consequences of T246M mutation on CHIP dimerization status and U-box domain structure and stability in order to better define the structural implications of CHIP mutation in SCAR16.

In addition to its role as an E3 ubiquitin ligase, CHIP has many additional roles within the cell. As a co-chaperone, CHIP interacts with Hsp-bound proteins to aid in substrate stabilization and refolding and regulates activation of the stress-chaperone response through activation of HSF1.[72-74] Additionally, our laboratory has recently uncovered a range of new and unexpected functional roles for CHIP, including involvement in cardiac metabolic homeostasis (as a regulator of AMP-activated protein kinase (AMPK)) and DNA damage repair (as a regulator of Sirtuin-6 (SirT6)).[8, 87] Because CHIP is such a multi-faceted protein, in order to fully appreciate how CHIP mutation drives disease pathology in SCAR16, we evaluated the consequences of CHIP mutation from multiple angles. Here we determine the effects of T246M mutation on CHIP function in its traditional roles as an E3 ubiquitin ligase and co-chaperone, as

well as on the emerging functions of CHIP as a direct chaperone and regulator of AMPK and as a nuclear protein involved in DNA damage repair.

To evaluate the pathophysiological implications of T246M mutation *in vivo*, we generated a mouse model (T247M) that mimics the human mutation. We used this model to validate our biophysical studies and cellular models in the genomic context of the mutation vs. overexpression studies at super-physiological levels of protein in less disease-relevant cell types. Additionally, we performed an in-depth behavioral assessment of these mice to determine the effects of T246M mutation at a whole-animal level, begin to understand the pathophysiology of T246M *in vivo* and validate this animal model as a representative of SCAR16 human disease. Studying T246M mutation both *in vitro* and *in vivo* has allowed us a unique opportunity to begin to delineate the contribution of co-chaperone, ubiquitin ligase activity and other emerging CHIP activities to specific deficits observed *in vitro* and *in vivo* in a disease-relevant context. This biophysical, cellular and *in vivo* characterization of T246M mutation in SCAR16 will provide valuable insight required for the development of effective therapies for this devastating degenerative disease.

Results

The T246M mutation destabilizes the CHIP U-box and promotes aggregate formation in vitro. Asymmetric homodimerization of CHIP as well as conformational flexibility are required for CHIP ubiquitin ligase activity. Critical to both the dimerization and conformational flexibility is an intact U-box domain [128, 172]. T246, which is highly conserved across CHIP homologs, is located within the U-box domain of CHIP. Furthermore, T246 is located in the core of a conversed beta hairpin turn that lies at the interface between two dimerized CHIP molecules. We hypothesized that this amino acid substitution within the CHIP U-box domain may have overall structural consequences and/or affect its ability to form functional dimers, consequently reducing or abolishing CHIP's ubiquitin ligase function towards both chaperone and non-chaperone substrates and leaving its ability to function as a chaperone intact. To test the effects of T246M substitution on U-box stability, we performed solution structure NMR on the isolated WT and T246M CHIP U-box domain. NMR has evolved as the main technique to obtain structural information at atomic resolution in solution on proteins and allows for the determination of protein's structures as well as their interactions. While the WT CHIP U-box showed distinct peaks across the N and H spectrums, consistent with a stable, structured protein, the T246M spectra revealed broad, fuzzy peaks, overlapping in the middle of the N and H spectrums consistent with misfolded or conformationally diverse molecules (Fig. 4.1A). This was confirmed by collecting spectra at additional temperature (data not shown) with similar results. Having demonstrated that NMR the T246M U-box spectrum was not consistent with a well-folded protein regardless of temperature, we wanted to confirm this lack of stable structure by another method. Circular dichroism spectroscopy was collected for both WT and T246M CHIP U-box protein at 15°C in 10 mM sodium phosphate pH 7.0 with 20 mM NaCl and 1 mM DTT.

The protein was at 0.25 mg/mL in both cases according to UV absorbance at 280 nm. These conditions were chosen to optimize the spectrum of the WT protein, which demonstrates clear secondary structure including significant α-helical character (dips around 208 and 222 nm) (Fig. 4.1B, left). The T246M mutant protein was at the same buffer conditions and protein concentration; however, the signal is much weaker and is consistent with more random coil or less stable protein. Further, we then monitored the protein melting temperature (Tm) at 222 nm, which corresponds to α-helical structures. The WT protein clearly shows a loss of signal as the temperature increases with a Tm around 30°C. Again, the T246M protein was not well-folded to begin with, and I observed no real change with temperature (Fig. 4.1B, left). Together these data suggest the T246M mutation destabilizes the U-box domain, resulting in a loss of secondary α-helical structure and protein misfolding.

To test the effects of T246M substitution on CHIP dimerization status, we purified full-length WT, T246M, K30A and H260Q mutant recombinant protein and performed dynamic light scattering (DLS). DLS measures the intensity of light scattered by molecules as a function of time, such that in solutions of equal concentration one can determine the fraction of each sample that exists in various multimeric states (monomer, dimer, trimer, etc.). Interestingly, by DLS we observed that both WT and K30A CHIP exist primarily as dimer, with a small population of trimer and tetramer (which we were unable to resolve). However, T246M mutation as well as the other U-box domain mutation H260Q result in little to no detectable CHIP dimer and a dramatic shift to primarily large multimeric aggregates (Fig 4.1C). Together these data suggest that T246M mutation results in dramatic structural instability and disorganization of the CHIP U-box that inhibits dimer formation and promotes the formation of large multimeric aggregates, likely resulting in significant functional consequences particularly to CHIP ubiquitin ligase activity.

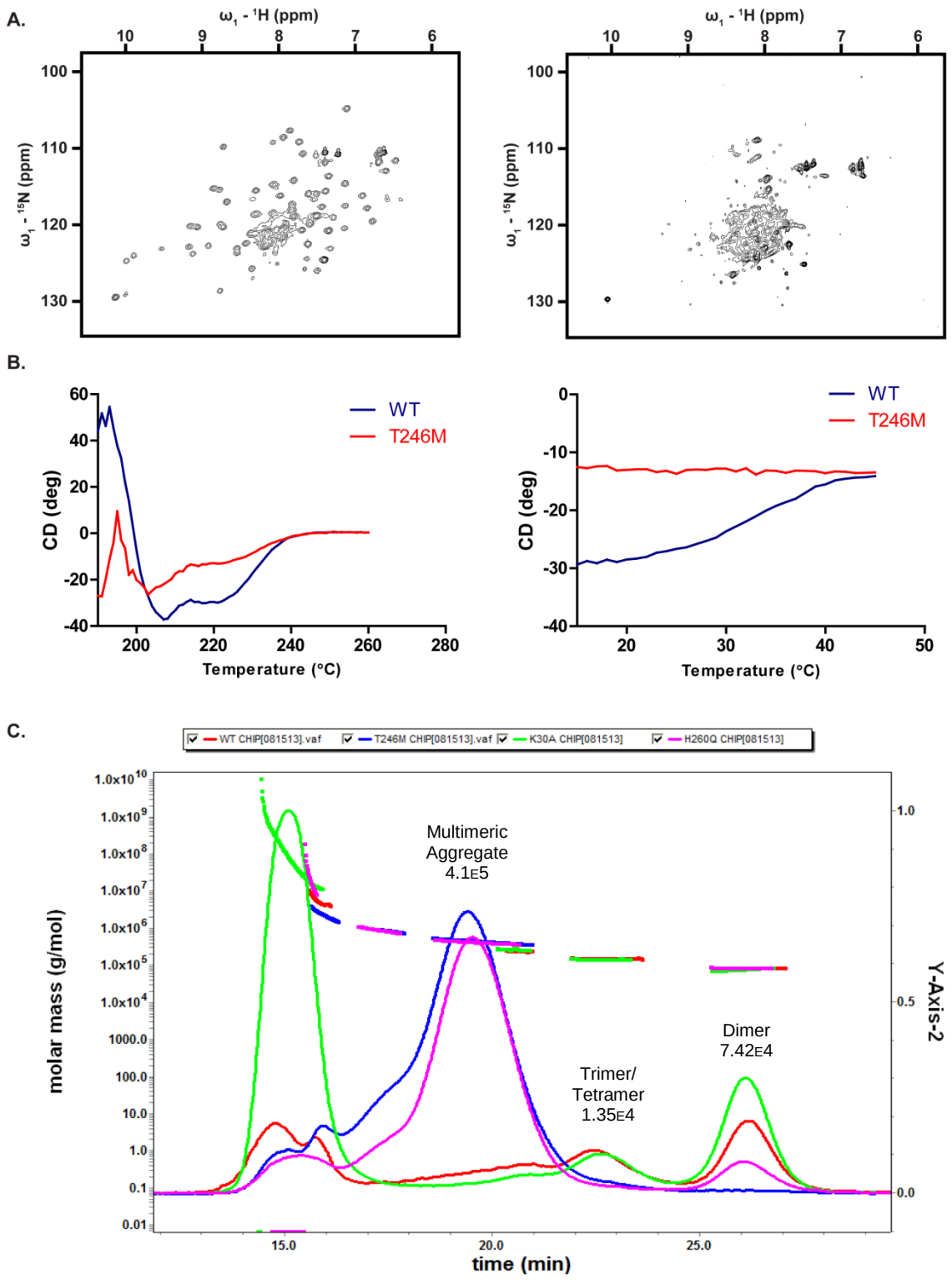
A.
ω1 - 1H (ppm)
ω1 - 15N (ppm)
B.
CD (deg)
Temperature (°C)
WT
T246M
C.
WT CHIP[081513].vaf
T246M CHIP[081513].vaf
K30A CHIP[081513]
H260Q CHIP[081513]
molar mass (g/mol)
time (min)
Y-Axis-2
Multimeric Aggregate 4.1E5
Trimer/ Tetramer 1.35E4
Dimer 7.42E4

Figure 4.1 The T246M mutation in CHIP results in the formation of large multimeric aggregates in cells.

A. 600-MHz ^{15}N-^{1}H transverse relaxation-optimized spectroscopy-HSQC spectra collected at 293K for ^{2}H,^{15}N-labeled WT (left) and T246M (right) CHIP U-box (218-303).

B. Circular dichroism spectroscopy data collected for both WT (blue) and T246M (red) CHIP U-box (218-303) at 0.25 mg/mL at 15°C in 10 mM sodium phosphate pH 7.0 with 20 mM NaCl and 1 mM DTT (left). Melting point (Tm) determination for WT and T246M CHIP U-box (218-303) at 222 nm (right).

C. Size distribution of full-length recombinant WT (red), T246M (blue), K30A (green) and H260Q (pink) CHIP at 0.5mg/mL as determined by DLS measurements. Peaks representing CHIP dimer, trimer/tetramer, and large, multimeric aggregates are indicated with corresponding molar mass values.

The T246M mutation in CHIP results in the formation of large multimeric aggregates in cells. As we observed *in vitro*, T246M mutation in CHIP dramatically destabilizes the CHIP U-box domain and results in a loss of secondary α-helical structure (Fig. 4.1A, B). Given that we observed the formation of large multimeric T246M CHIP aggregates *in vitro* (Fig. 4.1C), we hypothesized that the T246M substitution would also lead to the formation of multimeric CHIP aggregates in cells. To test the effect of the T246M substitution on CHIP's dimerization status, we first expressed either myc-tagged wild-type CHIP (CHIP-WT) or CHIP engineered with a methionine substituted for threonine at residue 246 (CHIP-T246M) as well as a TPR-domain mutant K30A CHIP and an additional U-box domain mutant H260Q in COS-7 cells and performed blue native polyacrylamide gel electrophoresis (BN PAGE) and Western blotting for myc-tagged CHIP. As expected, both the WT and K30A proteins migrate at approximately 70 kDa, as predicted for a CHIP dimer. However, both U-box domain mutants, T246M and H260Q are detected as higher molecular weight species, suggesting they exist in cells predominantly as large, multimeric aggregates (Fig. 4.2A). We subsequently performed immunocytochemistry for myc-tagged CHIP protein to observe CHIP localization and aggregation in the same model of exogenous CHIP expression in COS-7 cells. Not surprisingly, WT protein is detected as diffuse staining throughout the cytoplasm and within the nucleus, while T246M protein appears as punctate staining in the cytoplasm that we hypothesize represents accumulations of multimeric CHIP aggregates (Fig. 4.2B). Taken together, these data suggest that in cells T246M protein is at least partially misfolded as a result of disorganization of the U-box domain that results from the amino acid substitution. This inhibits proper dimerization between T246M CHIP molecules and likely contributes to the loss of ubiquitin ligase activity of T246M CHIP previously observed (Fig. 3.3).

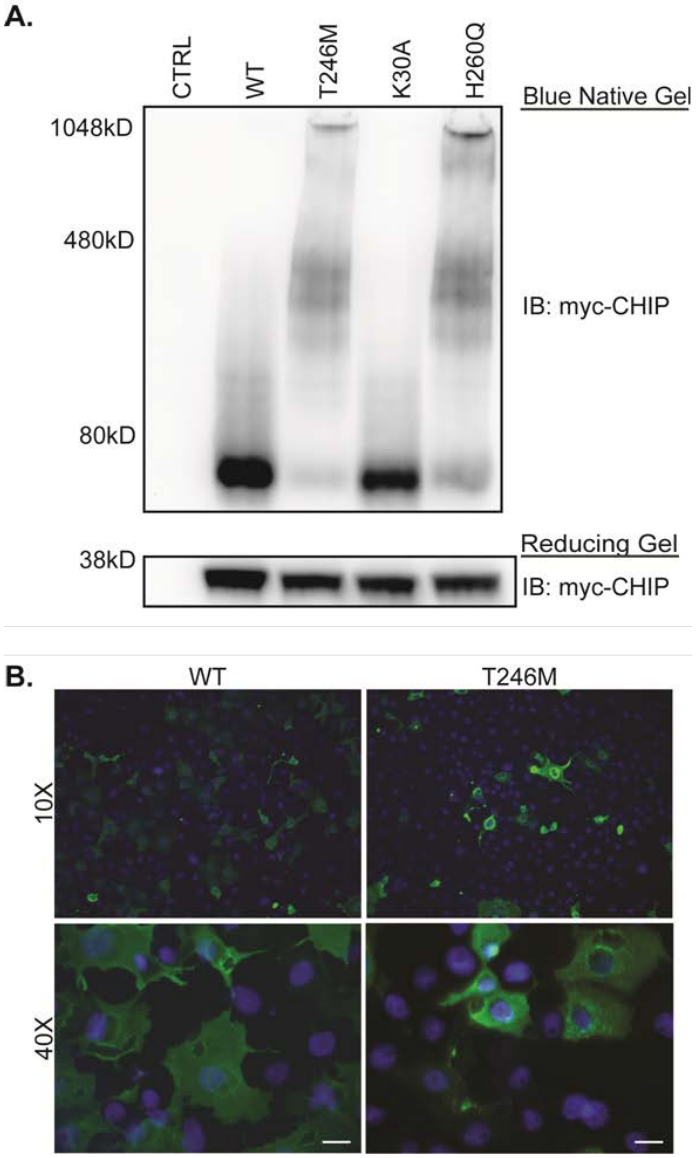

Figure 4.2. The T246M substitution mutation in CHIP results in the formation of large multimeric aggregates in cells.

A. COS-7 cells were co-transfected with the indicated vectors (transgenes, CTL=pcDNA3, WT=pcDNA3-myc tagged CHIP, T246M=pcDNA3-myc tagged CHIP-T246M, K30A=pcDNA3-myc tagged CHIP K30A, H260Q=pcDNA3-myc tagged CHIP-H260Q). Cells were collected on ice and total protein collected and freshly separated by BN PAGE and immunoblotted (IB) with the indicated antibodies. The same samples were also separated on a denatured reducing gel and immunoblotted with the indicated anti-myc CHIP antibody to detect total CHIP protein expression.

B. COS-7 cells were co-transfected with the indicated transgenes. 24 hours post-transfection, cells were fixed and immunostained for myc-CHIP expression. (scale bars=20 μm)

Coexpression of WT CHIP with T246M CHIP does not rescue T246M aggregation or significantly disrupt WT CHIP dimerization and localization. Given the nature of GHS as an autosomal recessive CA, where mutation carriers who are heterozygous for CHIP mutation are clinically unaffected, we hypothesized that the coexpression of T246M CHIP with WT CHIP, as would exist in a heterozygote, would not result in WT-T246M heterodimers that would disrupt normal WT CHIP function. When exogenously expressed alone in COS-7 cells, T246M forms almost no detectable dimer, existing predominantly as large multimeric aggregates (Fig. 4.2). To test whether WT CHIP and T246M CHIP protein interact, we first expressed HA-tagged wild-type CHIP (HA-WT) and myc-tagged T246M CHIP (Myc-T246M) alone or in combination in COS-7 cells and performed coimmunoprecipitation of HA-WT and Myc-T246M from purified cell lysates followed by gel electrophoresis and immunoblotting for HA, Myc or total CHIP. Interestingly, we observed that WT and T246M CHIP protein do interact when coexpressed in COS-7 cells, with each able to be coimmunoprecipitated by direct pull-down of the other. In lysate coexpressing HA-WT and myc-T246M, myc-T246M was detectable following immunoprecipitation of HA-WT and HA-WT was detectable following immunoprecipitation of myc-T246M (Fig. 4.3A). Furthermore, the amount of detectable HA-WT present in the input samples was lower in lysates also expressing myc-T246M than in lysates only expressing HA-WT, which we hypothesize may be due to some portion of HA-WT becoming insoluble or being more rapidly turned over as a result of its association with myc-T246M (Fig. 4.3A). Next, to test whether this interaction between WT and T246M CHIP resulted in heterodimerization, we performed the same coexpression of HA-WT and Myc-T246M CHIP as in Fig. 4.3A but 24 hours post-transfection, we instead directly separated the lysates by BN PAGE to observe the dimerization/aggregation status of CHIP. Interestingly, we observed that coexpression of HA-

WT CHIP did not significantly increase the presence of Myc-T246M-containing dimers (Fig. 4.3B, middle panel), but T246M resulted in a slight increase in higher molecular weight species of HA-WT CHIP (Fig. 4.3B, left panel). Given the lack of phenotype in WT-T246M heterozygotes, we hypothesized that WT CHIP localization would be largely unaffected by T246M coexpression, such that normal CHIP functions would remain intact by the maintenance of fully functional CHIP protein in the appropriate cellular compartments. To test whether WT CHIP localization is affected by coexpression of T246M CHIP, we again coexpressed HA-WT and Myc-T246M in Cos-7 cells and performed immunostaining for HA and Myc. As predicted, we observed that the localization of HA-WT was largely unaffected by coexpression of Myc-T246M (Fig. 4.3C). Taken together, these data suggest that while WT and T246M CHIP interact and their coexpression may result in the aggregation/enhanced turnover of some small portion of total WT CHIP protein, the localization and dimerization status of WT CHIP is largely unaffected by the presence of T246M. Therefore, WT CHIP function likely also remains intact. Furthermore, the presence of WT CHIP does not appear to rescue the misfolding/structural disorganization of T246M CHIP and prevent T246M aggregation to allow formation of functional dimers. Rather, based upon this data, we hypothesize that in heterozygotes, the remaining WT CHIP is sufficient to maintain normal CHIP functions within the cell despite the presence of T246M CHIP.

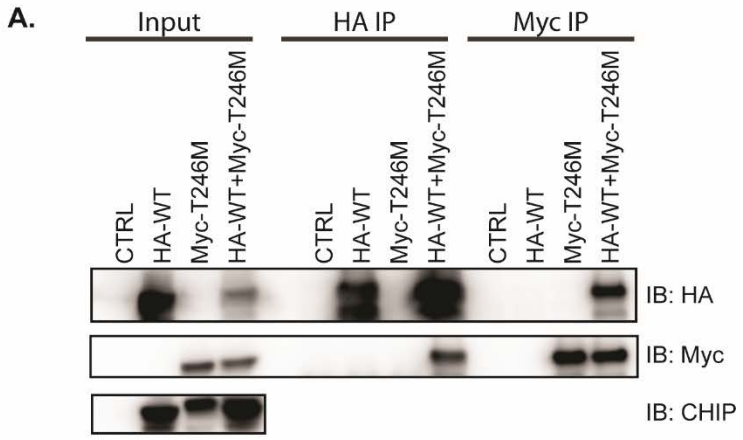
A.
Input
HA IP
Myc IP
CTRL
HA-WT
Myc-T246M
HA-WT+Myc-T246M
IB: HA
IB: Myc
IB: CHIP

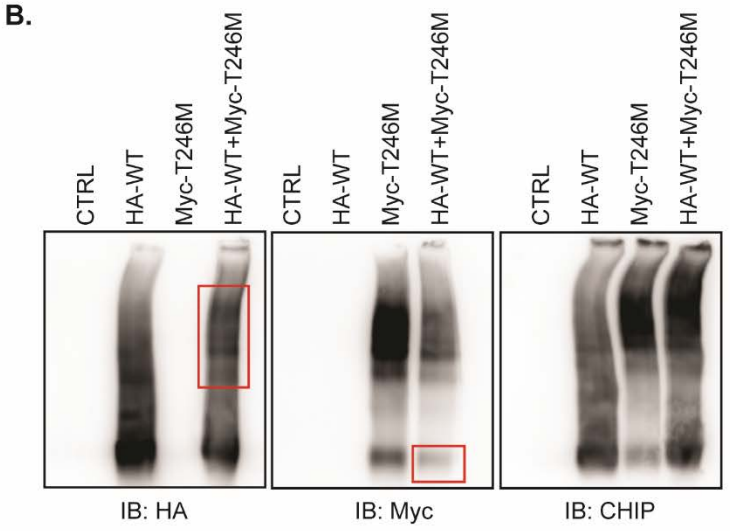
B.
CTRL
HA-WT
Myc-T246M
HA-WT+Myc-T246M
IB: HA
IB: Myc
IB: CHIP

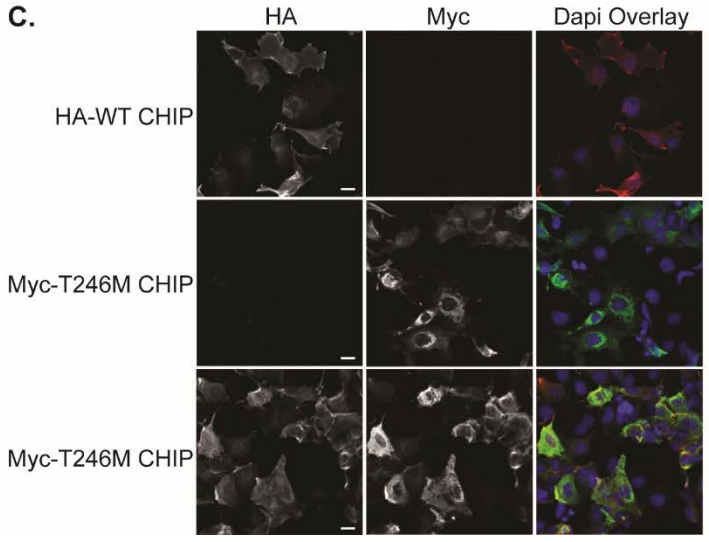
C.
HA
Myc
Dapi Overlay
HA-WT CHIP
Myc-T246M CHIP
Myc-T246M CHIP

Figure 4.3. Coexpression of WT CHIP with T246M CHIP does not rescue T246M aggregation or disrupt WT CHIP dimerization and localization.

A. COS-7 cells were co-transfected with the indicated vectors (transgenes, HA-WT=pcDNA3-HA-tagged CHIP, Myc-T246M=pcDNA3-myc tagged CHIP-T246M) or both. 24 hours post-transfection, cell lysates were collected and immunoprecipitated with EZview Red Anti-HA Affinity Gel or EZview Red Anti-Myc Affinity Gel. The inputs and resulting precipitants (IP) were separated by SDS-PAGE and immunoblotted with the indicated antibodies.

B. COS-7 cells were co-transfected with the indicated transgenes. 24 hours post-transfection, cells were collected on ice and total protein collected and freshly separated by BN PAGE and immunoblotted (IB) with the indicated antibodies. Approximate molecular weights in kilodaltons (kd) are also provided.

C. COS-7 cells were co-transfected with the indicated transgenes. 24 hours post-transfection cells were fixed and immunostained for HA-WT CHIP (left panels) or Myc-T246M CHIP (center panels) expression/localization. DAPI nuclear staining is also shown (right panels). (scale bars=20 μm)

T246M CHIP is more rapidly turned over than WT CHIP, in part by a proteasome-dependent mechanism. We consistently observed lower levels of soluble CHIP protein when expressing equal amounts of transgenes for CHIP U-box domain mutant T246M relative to WT CHIP in COS-7 cells (data not shown). Additionally in this model, we also observed significant amounts of large molecular weight aggregates of T246M CHIP not observed with WT CHIP expression (Fig. 4.2). Taken together with our *in vitro* structural data where we observe disorganization and lack of secondary structure in the U-box of T246M, we believe T246M and other U-box domain mutations dramatically destabilize CHIP structure and likely result in the accumulation of misfolded protein aggregates. One mechanism by which cells attempt to eliminate these types of terminally misfolded proteins and reduce their accumulation in toxic aggregates is by way of the UPS. [173, 174] To test whether T246M CHIP is being degraded via the UPS, we transiently expressed his-tagged wild-type CHIP (WT CHIP) or his-tagged T246M CHIP (T246M CHIP) in COS-7 cells. Twenty-four hours post-transfection, we treated cells with 50 µg/ml cyclohexamide for 0, 1 or 2.5 hours in the presence or absence of 20 µM proteasome inhibitor MG132 and then performed SDS-PAGE and immunoblotting for His-CHIP and β-tubulin (Fig. 4.4A). As expected, the turnover rate of T246M CHIP observed in the presence of cyclohexamide was significantly greater than that observed for WT CHIP, with 50% of soluble T246M CHIP remaining after 2.5 hours of cyclohexamide chase relative to 80% of WT CHIP (Fig. 4.4B,C). Furthermore, when the proteasome was also blocked by MG132 co-treatment, T246M CHIP protein levels were restored to 75% of the untreated control levels whereas WT CHIP was fully restored to control levels (Fig. 4.4B,C).

This suggests that both WT CHIP and T246M CHIP are degraded by the UPS; however, while the turnover of WT CHIP appears to be entirely UPS-dependent, the turnover of T246M CHIP is both more rapid and is also only partially proteasomally regulated. This further suggests that other clearance mechanisms such as autophagy may also contribute to the more rapid turnover of T246M CHIP.

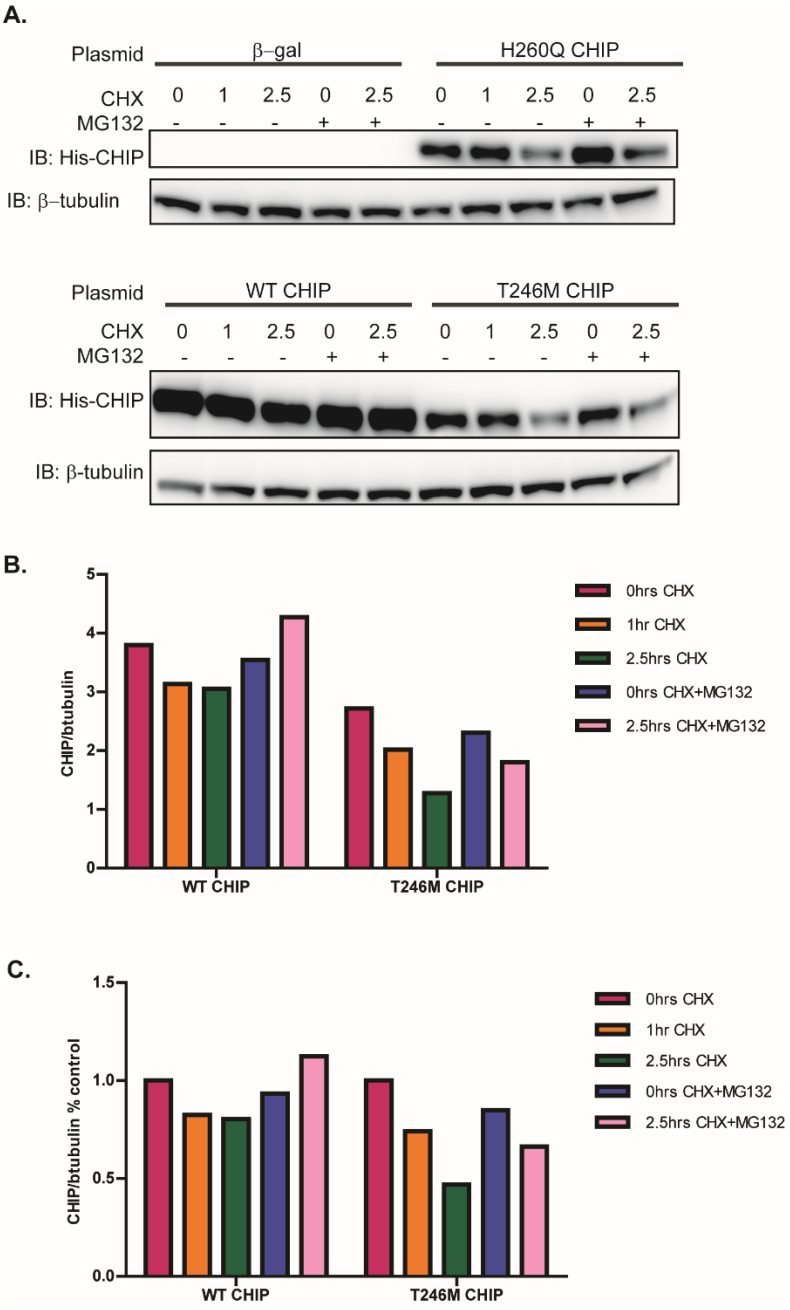

Figure 4.4. T246M CHIP is more rapidly turned over than WT CHIP, in part by a proteasome-dependent mechanism

A. COS-7 cells were co-transfected with the indicated vectors (transgenes, HA-WT=pcDNA3-his-tagged CHIP, Myc-T246M=pcDNA3-his tagged CHIP-T246M). 24 hours post-transfection cells were treated with 50 µg/ml cyclohexamide for 0, 1 or 2.5 hours in the presence or absence of 20 µM proteasome inhibitor MG132 and lysates collected and separated by SDS-PAGE and immunoblotted with antibodies against His-CHIP and β-tubulin.

B. Quantitation of the ratio of total CHIP relative to total β-tubulin protein in immunoblots represented in Fig.4.4A calculated using Licor Image Studio Lite.

C. Quantitation of the ratio of total CHIP relative to total β-tubulin protein as a percentage of this protein ratio in control cells not treated with cyclohexamide or MG132.

Expression of endogenous T247M CHIP protein in primary MEFs is dramatically reduced despite normal mRNA levels. While incredibly useful as an initial tool to understand the cellular effects of T246M CHIP mutation, the COS-7 cell model is significantly limited by potential artifacts of ectopic CHIP expression. Thus, utilizing CRISPR/Cas-mediated genome engineering, we generated mice homozygous for the single amino acid substitution T247M in CHIP (T246M in humans). From these mice, we harvested and cultured primary mouse embryonic fibroblasts (MEFs) and evaluated total CHIP protein and mRNA levels in these cells. Interestingly, total CHIP protein levels as detected by CHIP immunoblot were dramatically reduced in T247M MEFs isolated from 4 different T247M mouse embryos relative to WT MEFs from WT littermates (Fig. 4.5A). However, T247M STUB1 mRNA levels in lysates from the same MEFs as detected by SYBR green quantitative PCR showed no change relative to WT STUB1 mRNA (Fig. 4.5B). Together these data suggest that the reduction in detectable T247M protein is likely a result of post translational regulation, with probable mechanisms including proteasomal degradation and/or clearance by autophagy. miRNA regulation of CHIP/STUB1 translation has also been previously shown and may represent an additional mechanism of T247M CHIP protein downregulation[175].

Endogenous T247M CHIP is detected in a punctate immunostaining pattern in primary MEFs that exhibit slower growth rates. Ectopic expression of T246M CHIP in COS-7 cells resulted in notably punctate immunostaining of CHIP protein relative to a highly diffuse staining pattern observed with WT CHIP expression (Fig. 4.2B), which we hypothesize represents misfolded T246M CHIP protein aggregates. To test whether these aggregates are also present at endogenous protein expression levels, we performed CHIP immunostaining in T247M and WT CHIP MEFs. As expected, we observe a distinct punctate pattern of CHIP staining in T247M

MEFs, with the appearance of more focused regions of high intensity CHIP staining relative to the more diffuse pattern observed in WT MEFs (Fig. 4.5C). This suggests endogenous T247M CHIP may be forming multimeric aggregates or may potentially be accumulating in a particular cellular compartment or clearance vesicle such as an autophagosome. We subsequently measured growth rates of wildtype (WT), T247M and heterozygous (HET) primary MEFs to determine whether CHIP dysfunction as a result of T247M mutation and/or proteotoxicity associated with T247M CHIP expression might affect the growth rate of these cells in culture. We cultured WT, T247M and HET primary MEFs in parallel by tracking the population doubling time with the iCELLigence impedance-based system for real-time monitoring of cell growth under normal growth conditions. Interestingly, T247M MEFs exhibited a significantly slower growth rate relative to WT MEFs (T247M MEF doubling time=45 hours vs WT MEF doubling time=36 hours) (Fig. 4.5D). Taken together these data suggest that when expressed at endogenous levels T247M accumulates within the cell in a distinct pattern relative to WT CHIP that may represent aggregation and/or misfolded protein clearance efforts by the cell. This phenotype may manifest to alleviate proteotoxicity associated with the aggregation and/or dysfunction of this abnormal protein that is, at the very least, negatively impacting cell growth. Given CHIP's multi-faceted role within the cell, this T247M mutation alters multiple cellular processes.

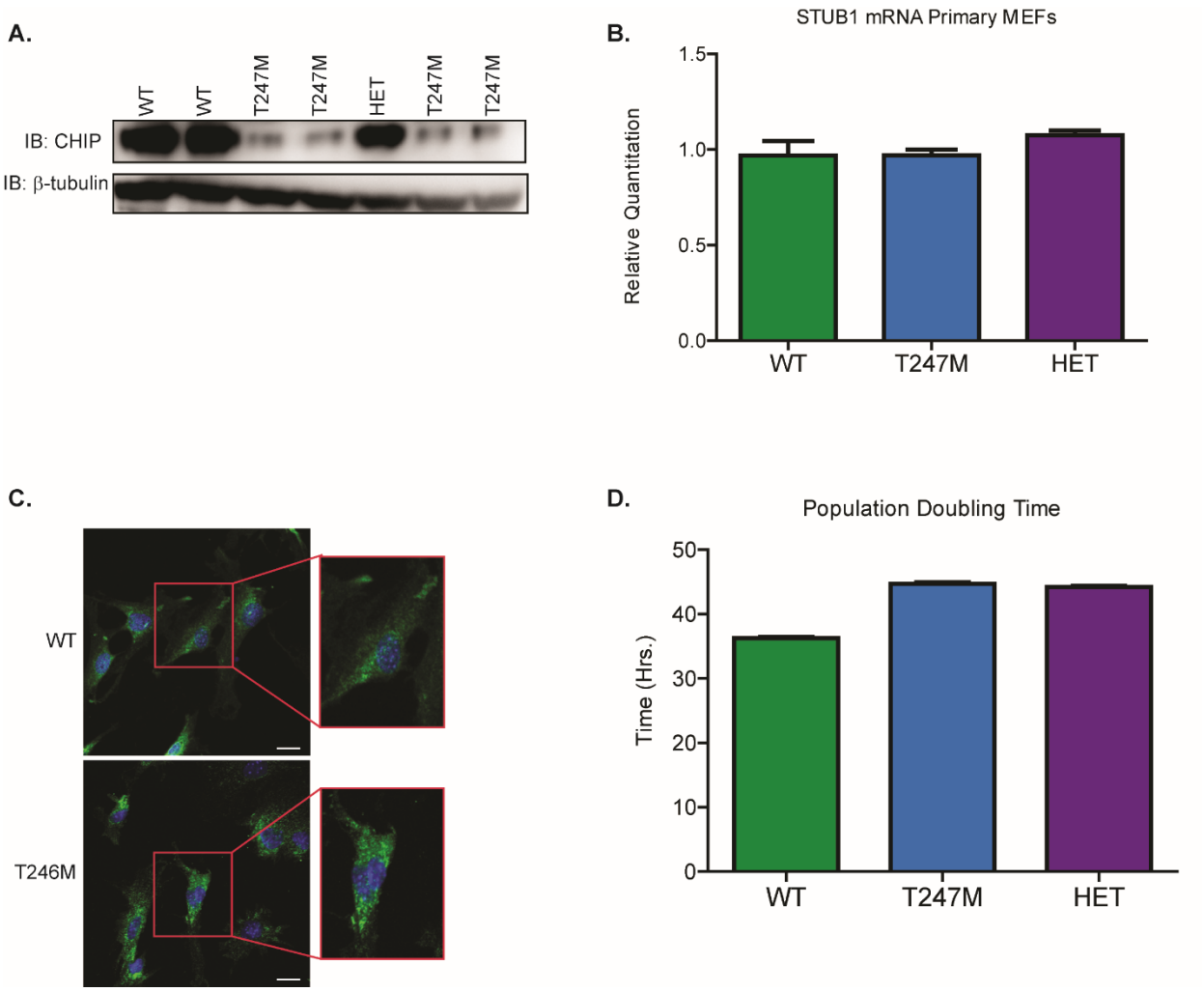

Figure 4.5. Expression of endogenous T247M CHIP protein in primary MEFs is dramatically reduced despite normal mRNA levels and is detected in a punctate immunostaining pattern in primary MEFs that exhibit slower growth rates.

A. Immunoblottting for CHIP and β-tubulin in P1 primary WT, T247M CHIP and Heterozygous (HET) MEFs.

B. Relative quantitation of total STUB1 mRNA in P1 primary WT, T247M CHIP and Heterozygous (HET) MEFs.

C. CHIP immunostaining in P2 primary WT and T247M CHIP MEFs.

D. Cell growth of WT, T247M and HET MEFs was monitored over 72 hours utilizing the iCELLigence impedance-based system for real-time monitoring of cell growth under normal growth conditions. Electrode impedence is directly correlated to cell index and the population doubling time is the time required for the cell index to double and thus represents time when the whole cell population has performed at least 1 division.

Endogenous T247M CHIP is rapidly turned over and UPS inhibition dramatically increases T247M protein levels, particularly in the insoluble fraction. As described above, we observed more rapid rate of T246M CHIP protein turnover observed in the COS-7 cell ectopic expression model (Fig. 4.4) and the dramatic difference in soluble endogenous T247M CHIP protein observed in T247M MEFs relative to WT MEFs (Fig. 4.5A). Therefore, we wanted to evaluate the turnover rate of endogenous T247M CHIP in primary MEFs. To determine the rate of T247M CHIP protein turnover, we blocked protein synthesis in WT, T247M and CHIP knockout primary MEFs by treatment with 50µg/ml cycloheximide for 0, 2, 4 or 6 hours and measured CHIP protein expression. As expected, while the total soluble CHIP protein expression is dramatically reduced in the T247M MEFs as observed previously (Fig. 4.5A) (in fact, requiring separate exposure lengths to most clearly visualize the protein), the turnover rate of T247M CHIP is significantly faster than WT CHIP, with T247M CHIP completely undetectable by 6 hours of cycloheximide chase compared to approximately 75% of WT CHIP remaining after 6 hours (Fig. 4.6A). This suggests increased protein turnover likely contributes significantly to the lower levels of detectable soluble T247M CHIP. Our findings *in vitro* and in COS-7 cells when ectopically expressed demonstrate that T246M CHIP forms less functional dimers and instead may accumulate in large multimeric aggregates, (Fig. 4.1, 4.2). Therefore we hypothesized that another contributing factor to the low levels of detectable soluble T247M CHIP protein may be the accumulation of misfolded/aggregated T247M CHIP in the insoluble fraction. To evaluate the T247M fractional distribution and whether this distribution was effected by proteasome inhibition relative to WT, we treated WT and T247M primary MEFs with 20 µM MG132 or 0.05% DMSO control for 4 hours. We then collected soluble, insoluble and total protein fractions from samples containing equal cell numbers. These samples were separated by SDS-

PAGE and immunoblotted for CHIP and β-tubulin. To allow direct comparison of CHIP protein levels across fractions, we performed 660 nm protein assay to quantitate total protein/sample prior to SDS-PAGE and normalized protein load across fractions. We observed several interesting phenomenon that help us to understand the regulation of T247M CHIP. First, we observed that even when accounting for insoluble protein, total T247M protein (soluble+insoluble) is dramatically lower than total WT protein (Fig. 4.6B, C). Secondly, the change in total protein levels is dramatically higher with proteasome inhibition for T247M (4-fold) protein than WT (<1-fold), suggesting dramatically more UPS-dependent turnover of T247M relative to WT (Fig 4.6C). Surprisingly though, proteasome inhibition did not restore T247M total protein levels to that of WT, suggesting another highly efficient mechanism of T247M turnover that dramatically reduces total T247M protein. We also observed that both the baseline and MG132 treatment-dependent distribution between soluble and insoluble fractions was significantly different for T247M relative to WT (Fig. 4.6D). At baseline WT CHIP appears to exist largely in the soluble fraction, and inhibition of the proteasome only slightly shifts the distribution from soluble to insoluble. This suggests that, as expected, only a small percentage of total WT CHIP is normally turned over by the proteasome under baseline conditions and this CHIP will accumulate in the insoluble fraction upon proteasome inhibition. Interestingly, T247M has > 2-fold greater distribution in the insoluble fraction at baseline relative to WT, and inhibition of the proteasome dramatically increases the total amount of T247M CHIP in both fractions but specifically increases T247M present in the soluble fraction by 2-fold and the insoluble fraction by 6-fold. This suggests that the proteasome appears to be responsible for clearing a large fraction of T247M CHIP that would otherwise accumulate as insoluble protein, but also clears some T247M CHIP that remains soluble but may be functionally defective and

therefore deleterious to the cell (Fig. 4.6D). Together these data suggest that T247M CHIP is rapidly cleared by the proteasome, and much of the protein degraded by the UPS will accumulate in the insoluble fraction, likely due to its misfolded nature. However, other efficient clearance mechanisms must exist within the cell to reduce the total T247M protein burden and prevent large amounts of accumulation of T247M CHIP protein both as soluble, potentially toxic protein as well as in damaging insoluble aggregates.

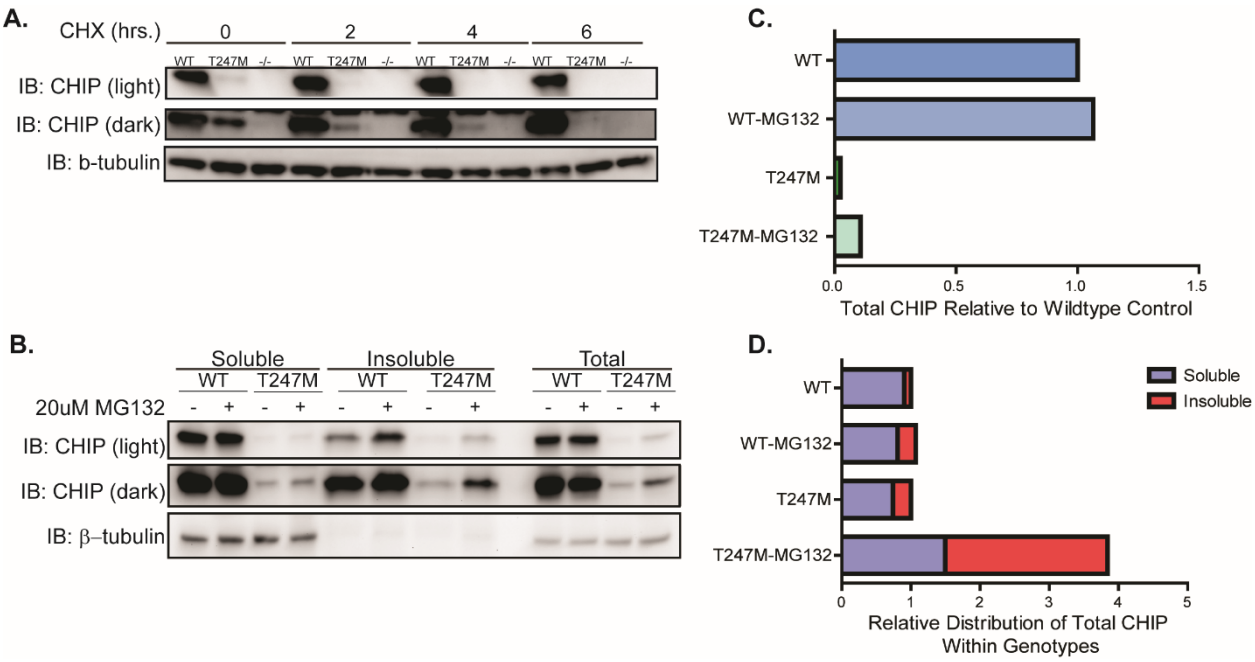

Figure 4.6. Endogenous T247M CHIP is rapidly degraded in part by the UPS, largely reducing accumulation of insoluble protein.

A. Immunoblottting for CHIP and β-tubulin in soluble cell lysates from P2 primary WT, T247M CHIP and CHIP knockout (-/-) MEFs collected after 0, 2, 4 or 6 hours of protein synthesis inhibition by cyclohexamide chase. (light and dark exposure for total CHIP to allow easier visualization of poorly expressed T247M CHIP)

B. P2 primary WT, T247M CHIP and CHIP knockout (-/-) MEFs were treated with 20 µM MG132 or 0.05% DMSO control for 4 hours. Cells were counted and divided into two equal samples that were then processed into soluble, insoluble and total protein lysates. Half of the cells were lysed directly in SDS sample buffer and sonicated (total protein) the other half were lysed in TritonX-100 lysis buffer. The TritonX-100 samples were then separated by centrifugation and the supernatant collected (soluble). The remaining pellet was then rinsed and lysed directly in SDS sample buffer and sonicated (insoluble). Samples were then quantitated by 660 nm protein assay and samples of equal protein concentration separated by SDS-PAGE and immunoblotted for CHIP and β-tubulin.

C. Quantitation of total CHIP protein in each condition relative to total CHIP present in DMSO treated WT CHIP control cells in Fig. 4.6B.

D. Quantitation of the relative distribution of total CHIP between soluble and insoluble fractions within each genotype in Fig. 4.6B. Prior to calculating the relative distribution, CHIP values were normalized for the percentage of each fraction loaded on the gel to allow comparison of CHIP expression across fractions of unequal total volume.

T246M CHIP does not ubiquitinate non-chaperone substrates but has enhanced E2 ligase binding. We have previously shown that both *in vitro* and in cells, T246M CHIP has virtually no detectable ubiquitin ligase activity towards chaperone substrates (Chapter III). We hypothesized that this would also be the case for non-chaperone substrates given the disorganization of the T246M CHIP U-box (Fig. 4.1). To test this, we evaluated the previously reported non-canonical monoubiquitination of non-chaperone neuronal substrate α-synuclein by *in vitro* ubiquitination assay[176]. As expected, we observed a loss of α-synuclein monoubiquitination as a result of T246M mutation (Fig. 4.7A). Since first observing the loss of ubiquitin ligase activity but preserved interaction with chaperone proteins (Chapter III) and the structural disorganization of the T246M U-box domain (Fig. 4.1), we hypothesized that T246M CHIP may still associate with E2 ligases that, when bound to CHIP, normally facilitate the transfer of ubiquitin to ubiquitination substrates, but that the transfer of ubiquitin may be impaired by the structural consequences of T246M mutation. To test whether T246M CHIP still binds to E2 ligases in cells, we transiently expressed myc-tagged wild-type CHIP (WT CHIP), myc-tagged T246M CHIP (T246M CHIP) or myc-tagged H260Q CHIP (H260Q) in COS-7 cells and performed co-immunoprecipitation for CHIP and E2 ligase known to function with CHIP UbcH5c. Interestingly, we observe an enhanced association of U-box domain mutants, T246M CHIP and H260Q CHIP with UbcH5c relative to WT CHIP, suggesting the rate of association/dissociation between CHIP and the E2 enzyme may be impaired by the loss of ubiquitin transfer that results from U-box mutation (Fig. 4.7B). We hypothesize that this may reduce accessibility of the associated E2 ligase to other E3 enzymes, perhaps impairing ubiquitination reactions beyond only CHIP substrates. Together these data suggest that, while it can no longer ubiquitinate substrate proteins, T246M CHIP still binds many of its normal binding partners, but that the

dynamics of these interactions may be altered. This may have larger implications for additional enzymatic reactions outside of direct regulation of CHIP substrates, potentially further impairing the cell's ability to maintain baseline cellular homeostasis and/or allowing the cell to respond to stress.

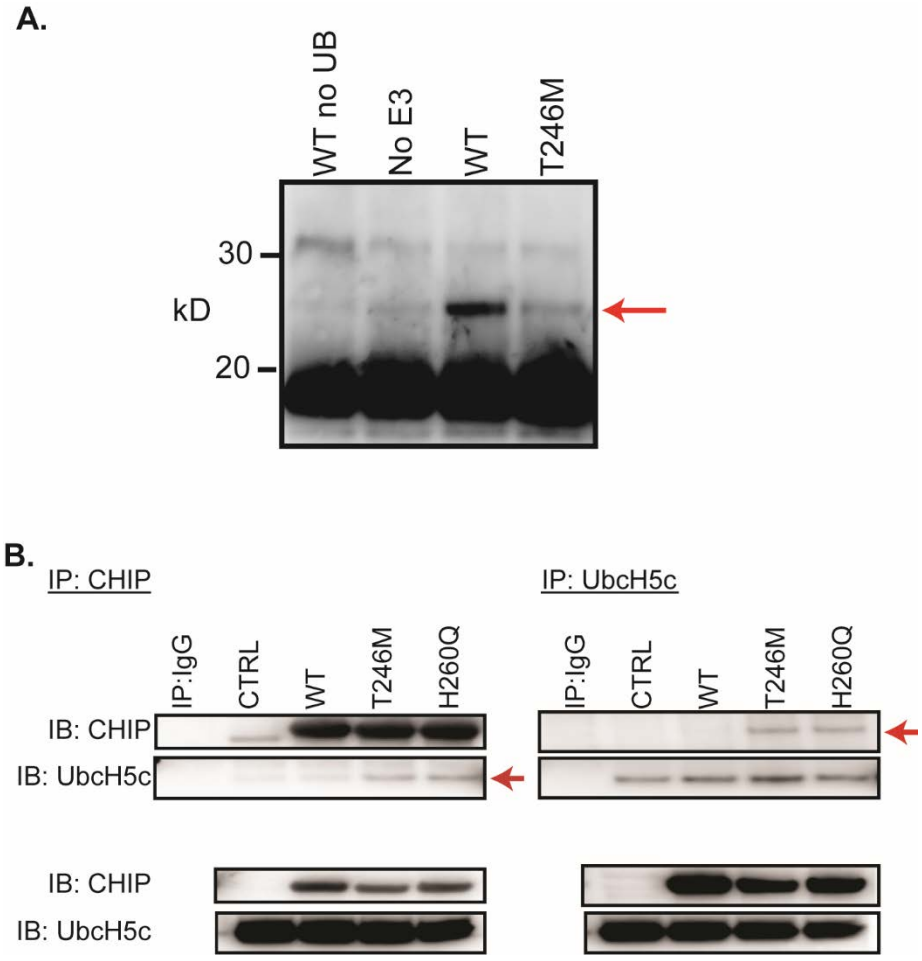

Figure 4.7. T246M CHIP does not ubiquitinate non-chaperone substrates but has enhanced E2 ligase binding.

A. Cell-free ubiquitination reactions containing recombinant α-synuclein and the indicated CHIP proteins resolved via SDS-PAGE and immunoblotted for an antibody recognizing α-synuclein.

B. COS-7 cells were co-transfected with the indicated transgenes and immunoprecipitated with either a UbcH5c antibody, CHIP antibody or IgG. The inputs and resulting precipitants (IP) were immunoblotted (IB) with the indicated antibodies.

T246M CHIP promotes HSF1 translocation to the nucleus and activation of transcription. In addition to its role as a ubiquitin ligase, CHIP can also act as a co-chaperone through its direct interactions with cellular chaperones, including HSC70, HSP70, and HSP90 via CHIP's tetratricopeptide repeat (TPR) domain.[81, 128, 134, 153] Both a functional TPR and U-box domain are required for CHIP's ability to directly impact PQC and attenuate the cellular stress response in large part through polyubiquitination of HSP chaperones.[75, 79] Given that the T246M CHIP mutation resides in the U-box domain, we hypothesized that the T246M substitution would result in a loss of CHIP's ubiquitin ligase activity, without affecting CHIP's interaction and activities with cellular chaperones though the intact TPR domain. Through its interaction with HSP chaperones, CHIP also regulates the transcriptional activation of heat shock factor 1 (HSF1), which is normally under negative regulatory control by molecular chaperones Hsp70 and Hsp90. Furthermore, this activation of HSF1 confers protection from cellular stress and prevents apoptosis[74]. We demonstrated previously by co-immunoprecipitation assay that T246M substitution does not impair its ability to bind to chaperones (Fig. 3.3 and 3.4). To test whether CHIP's regulation of HSF1 remains intact with T246M mutation, we first transiently expressed wildtype (WT) CHIP, T246M CHIP and TPR-domain mutant K30A CHIP in COS7 cells and measured the nuclear translocation of HSF1 induced by CHIP expression. As previously reported[74], we observed that expression of WT CHIP drives HSF1 to the nucleus. As expected, expression of T246M CHIP also resulted in nuclear translocation of HSF1 while expression of TPR domain mutant did not (Fig. 4.8A). These data suggest that despite disruption of the CHIP U-box, T246M mutation leaves the TPR domain sufficiently intact to maintain this activity.

To test whether HSF1 that is driven to the nucleus by T246M CHIP is transcriptionally active, we utilized the Promega HSF1 Dual-Luciferase Reporter (DLR) Assay System in COS7

cells to measure the transcriptional activation of HSF1 with CHIP expression. As previously reported,[74] we observed that expression of WT CHIP results in activation of HSF1 transcriptional activity. Interestingly, expression of T246M CHIP as well as U-box domain mutant H260Q also resulted in activation of HSF1; however, that activation of HSF1 by U-box domain mutants was 1-fold to 2.5-fold higher than that observed with WT CHIP. Importantly, we also observed no significant HSF1 activation by the expression of control protein β-galactosidase (β-gal) or TPR domain mutant K30A CHIP (Fig. 4.8B).

The dramatic increase in HSF1 activation relative to WT CHIP observed with both U-box domain mutants that we have previously shown to form large multimeric aggregates in cells led us to hypothesize that perhaps the increased HSF1 activation was not a CHIP-specific effect but rather driven by a cellular-stress response to the presence of these aggregates. To test this hypothesis, we developed a CHIP double-mutant K30A-T246M CHIP containing the T246M mutation and also the TPR domain mutation K30A that disrupts CHIP-driven HSF1 nuclear translocation and activation. To first characterize the aggregation status of this double mutant, we transiently expressed it in COS-7 cells at both 1X and 2.5X concentrations alongside WT CHIP, T246M CHIP and H260Q CHIP, performed BN PAGE and CHIP immunoblotting. We observed that, like T246M CHIP, K30A-T246M CHIP also forms large multimeric aggregates when transiently expressed in COS7 cells (Fig. 4.8C). To test whether HSF1 activation by U-box domain mutants is driven by chaperone-mediated interaction of HSF1 with CHIP or is merely a consequence of the overexpression of aggregation-prone proteins, we measured HSF1 activation in the presence of K30A-T246M double mutant as well as previously reported misfolded, aggregation-prone derivative of BSA, cBSA[177]. Interestingly, we observed that expression of neither K30A-T246M CHIP nor cBSA promote HSF1 activation relative to WT CHIP,

suggesting that the enhanced potentiation of HSF1 activity by CHIP U-box mutants T246M CHIP and H260Q CHIP is specific and not solely due to their tendency towards forming large multimeric aggregates (Fig. 4.8B).

In our COS-7 transient overexpression model, when transfecting in equal amounts of CHIP DNA across constructs, we consistently observed lower amounts of soluble CHIP protein when expressing T246M CHIP, H260Q CHIP and K30A-T246M CHIP relative to WT CHIP. We hypothesized that due to disorganization of the U-box domain, some portion of these expressed CHIP proteins was becoming insoluble, potentially as multimeric aggregates. To test this hypothesis, we performed SDS-PAGE and immunoblotting for CHIP comparing the soluble fraction (prepared by lysing cells in 1% Triton X-100 lysis buffer) and remaining insoluble pellet (solubilized by sonication in SDS-sample buffer). As expected, we observed significant amounts of T246M CHIP, H260Q CHIP and K30A-T246M CHIP in the insoluble pellet with no detectable WT or K30A CHIP present in the insoluble pellet (Fig. 4.8D).

Based upon this observation that T246M CHIP, H260Q CHIP and K30A-T246M CHIP were all observed significantly in the insoluble fraction, we wanted to confirm that enhanced potentiation of HSF1 activation was specific to soluble CHIP and further confirm it was not aggregate driven. To test this, we repeated the experiment presented in Fig. 4.8B but now expressing higher amounts of T246M, H260Q and K30A-T246M CHIP such that the amount of soluble CHIP detectable by immunoblot was roughly equivalent to WT CHIP (Fig. 4.8E). As expected, we observed that under these conditions where there is likely to be both more soluble and insoluble CHIP, there remains no activation of HSF1 by K30A-T246M CHIP.

Furthermore, the increased expression of either T246M CHIP or H260Q resulted in even greater potentiation of HSF1 activation. Together these data suggest that HSF1 activation is driven by soluble CHIP in a dose-dependent manner and this potentiation is dramatically enhanced by U-box mutants T246M and H260Q.

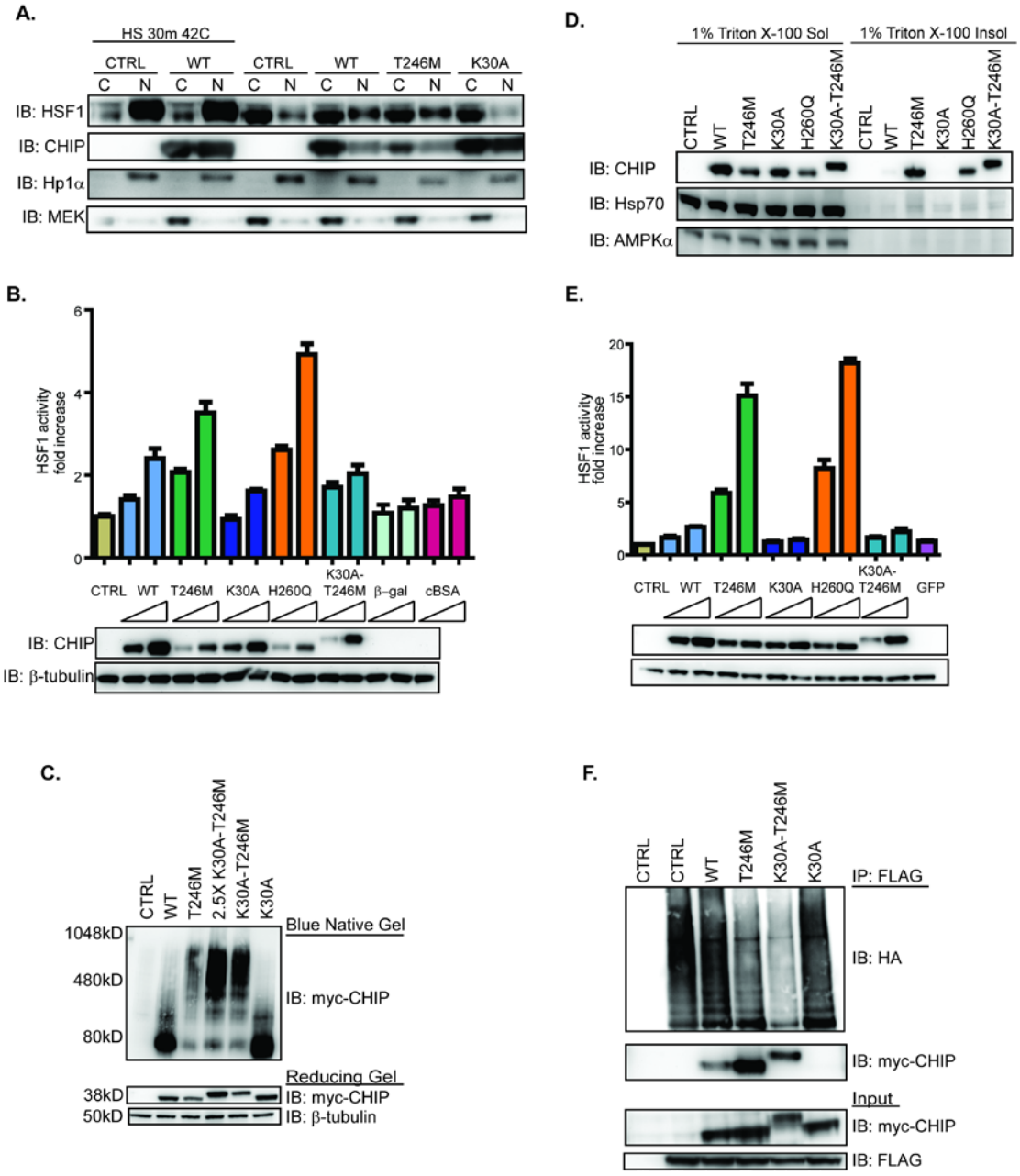

Figure 4.8. T246M CHIP promotes HSF1 translocation to the nucleus and activation of transcription.

A. Immunoblottting for HSF1, CHIP, HP1α and MEK in cytosolic (C) and nuclear (N) fractions from COS7 cells transiently transfected with the indicated vectors (transgenes, CTRL=pcDNA3, WT=pcDNA3-myc tagged CHIP, T246M=pcDNA3-myc tagged CHIP-T246M, K30A=pcDNA3-myc tagged CHIP K30A) and treated with or without heat shock in 42°C water bath for 30 min as marked.

B. Immunoblotting for CHIP, HSP70 and AMPKα in Triton X-100 soluble and insoluble fractions from COS7 cells transiently transfected with the indicated vectors (transgenes,

CTRL=pcDNA3, WT=pcDNA3-myc tagged CHIP, T246M=pcDNA3-myc tagged CHIP-T246M, K30A=pcDNA3-myc tagged CHIP K30A, H260Q=pcDNA3-myc tagged CHIP-H260Q, K30A-T246M=pcDNA3-myc tagged K30A-T246M double mutant).

C. Top, HSF1 transcription activity fold increase relative to control cells as detected by Promega HSF1 Dual-Luciferase Reporter (DLR) Assay System in COS7 cells transiently transfected with the indicated vectors (transgenes, CTRL=pcDNA3, WT=pcDNA3-myc tagged CHIP, T246M=pcDNA3-myc tagged CHIP-T246M, K30A=pcDNA3-myc tagged CHIP K30A, H260Q=pcDNA3-myc tagged CHIP-H260Q, K30A-T246M=pcDNA3-myc tagged K30A-T246M double mutant, β-gal=pcDNA3 beta-galactosidase, cBSA=pcDNA3 cytosolic bovine serum albumin) at low (1X) and high (2X) expression levels. Bottom, immunoblotting for CHIP and β-tubulin of COS7 cells transfected in parallel with top DLR assay.

D. Top, HSF1 transcription activity fold increase relative to control cells as detected by Promega HSF1 Dual-Luciferase Reporter (DLR) Assay System in COS7 cells transiently transfected with the indicated vectors (transgenes, CTRL=pcDNA3, WT=pcDNA3-myc tagged CHIP, T246M=pcDNA3-myc tagged CHIP-T246M, K30A=pcDNA3-myc tagged CHIP K30A, H260Q=pcDNA3-myc tagged CHIP-H260Q, K30A-T246M=pcDNA3-myc tagged K30A-T246M double mutant, GFP=green fluorescent protein) at low (1X) and high (2X) expression levels. Here T246M CHIP, H260Q CHIP and K30A-T246M CHIP were each expressed at adjusted concentrations to produce relative soluble CHIP as that present with WT CHIP expression. Bottom, immunoblotting for CHIP and β-tubulin of COS7 cells transfected in parallel with top DLR assay.

E. Immunoblotting for CHIP aggregation status under native, non-denatured, non-reduced conditions. COS-7 cells were transfected with the indicated vectors (transgenes, CTL=pcDNA3, WT=pcDNA3-myc tagged CHIP, T246M=pcDNA3-myc tagged CHIP-T246M, K30A=pcDNA3-myc tagged CHIP K30A, H260Q=pcDNA3-myc tagged CHIP-H260Q, K30A-T246M=pcDNA3-myc tagged K30A-T246M double mutant at equal and 2.5X WT concentration). Cells were collected on ice and total protein collected and freshly separated by BN PAGE and immunoblotted (IB) with the indicated antibodies. The same samples were also separated on a denatured reducing gel and immunoblotted with the indicated anti-myc CHIP and β-tubulin antibodies to detect total CHIP protein expression.

F. Immunoprecipitation of ubiquitinated Hsp70. COS-7 cells were co-transfected with the indicated vectors (transgenes, CTRL=pcDNA3, WT=pcDNA3-CHIP, T246M=pcDNA3-CHIP-T246M and K30A-T246M=pcDNA3-CHIP K30A-T246M double mutant) in addition to HA-tagged ubiquitin and FLAG-Hsp70. HSP70 was immunoprecipitated (IP) with FLAG beads and the resulting precipitants as well as inputs were immunoblotted (IB) with the indicated antibodies. CTRL lanes shown are (left to right) CTRL=HA-tagged ubiquitin and pcDNA3, CTRL= HA-tagged ubiquitin+pcDNA3+FLAG-Hsp70

T247M CHIP chaperone interactions and co-chaperone activities remain intact and may be enhanced in T247M primary MEFs. We have previously shown that when expressed transiently in COS-7 cells T246M CHIP maintains interactions with chaperone proteins (Fig. 3.3) and promotes chaperone-mediated activities, including the translocation and activation of HSF1 (Fig.4.8A, B, E). To test whether T247M CHIP expressed endogenously in T247M primary MEFs still interacts with chaperone proteins and still maintains previously reported CHIP chaperone functions, particularly under stress conditions, we first performed co-immunoprecipitation (IP) of endogenous CHIP and endogenous Hsc70 from purified P2 primary cell lysates followed by gel electrophoresis and immunoblotting (IB) for CHIP or Hsc70 in the remaining precipitants and input samples (Fig.4.9A). As expected, immunoprecipitation of both WT and T247M CHIP resulted in co-isolation of Hsc70, demonstrating that T247M CHIP maintains its interaction with Hsc70 when expressed endogenously. Interestingly, the amount of Hsc70 isolated with T247M CHIP was proportionally greater than the amount of Hsc70 isolated with WT CHIP. Interestingly, the immunoprecipitation of Hsc70 resulted in detectable levels of co-isolated WT CHIP; however, T247M CHIP was not detectable. Based upon our detection of Hsc70 in the CHIP immunoprecipitation, we hypothesize that this is a reflection of the very low levels of soluble T247M CHIP present in these cells such that it is not detectable by this method and not a true lack of interaction between T247M CHIP and Hsc70. After confirming T247M CHIP chaperone interactions are intact and perhaps even enhanced, we next tested whether this interaction is functional, such that T247M CHIP retains its normal co-chaperone functions. It has been previously shown that CHIP not only enhances Hsp70 induction during acute stress but also mediates its turnover during the stress recovery process, with the former a result of its co-chaperone activities and the later mediated by its ubiquitin ligase activity[75]. To test whether one

or both of these activities remains intact despite T247M mutation we subjected WT, T247M and CHIP knockout (CHIP$^{-/-}$) primary MEFs to heat shock (HS) in a 42°C water bath for 10 min and then collected total cell lysates after 0, 4 and 20 hours of recovery under normal growth conditions. As expected, we observed that in the presence of WT CHIP, Hsp70 expression is significantly increased and then is dramatically reduced again by 20 hours post-HS. Also as expected, we observed that in the absence of CHIP the induction of Hsp70 at 4 hours post-HS is dramatically reduced. Interestingly, in the presence of T247M CHIP the induction of Hsp70 is not only preserved, but is enhanced relative to WT, while the return of Hsp70 to baseline levels is slowed, with more Hsp70 remaining after 20 hours of recovery relative to WT CHIP cells (Fig. 4.9B). In order to further evaluate the regulation of Hsp70 following heat shock in the presence of T247M CHIP, we again subjected WT and T247M primary MEFs to heat shock (HS) in a 42°C water bath for 10 min and then collected total cell lysates in a more extensive timecourse, collecting cells after 0, 2, 4, 8, 12, 16, 20 and 24 hours of recovery under normal growth conditions. As expected, in the presence of WT CHIP, Hsp70 expression was increased following HS, reaching a peak at 12 hours post-HS and returning to near baseline levels by 24 hours post-HS. Interestingly, in the presence of T247M CHIP, Hsp70 expression was induced more rapidly and to a great extent than WT, with a significant increase over baseline levels by just 8 hours post-HS. Furthermore, in the presence of T247M CHIP, the increased expression of Hsp70 was prolonged, as we observed significantly elevated protein levels even at 24 hours post-HS (Fig. 4.9C). Together these data suggest that when expressed at endogenous levels in primary MEFs, like WT CHIP, T247M CHIP interacts with chaperone proteins. Furthermore, via these chaperone interactions, T247M CHIP maintains its ability to enhance Hsp70 induction during acute stress, and in fact may more greatly enhance Hsp70 expression than WT CHIP. However,

its ability to mediate Hsp70 turnover during the stress recovery process is impaired, likely due to its loss of ubiquitin ligase activity. We hypothesize that the observed enhanced induction of Hsp70 expression during stress may be a result of a change in binding kinetics between T247M CHIP and Hsp70 due to changes in T247M protein structure caused by the U-box domain mutation.

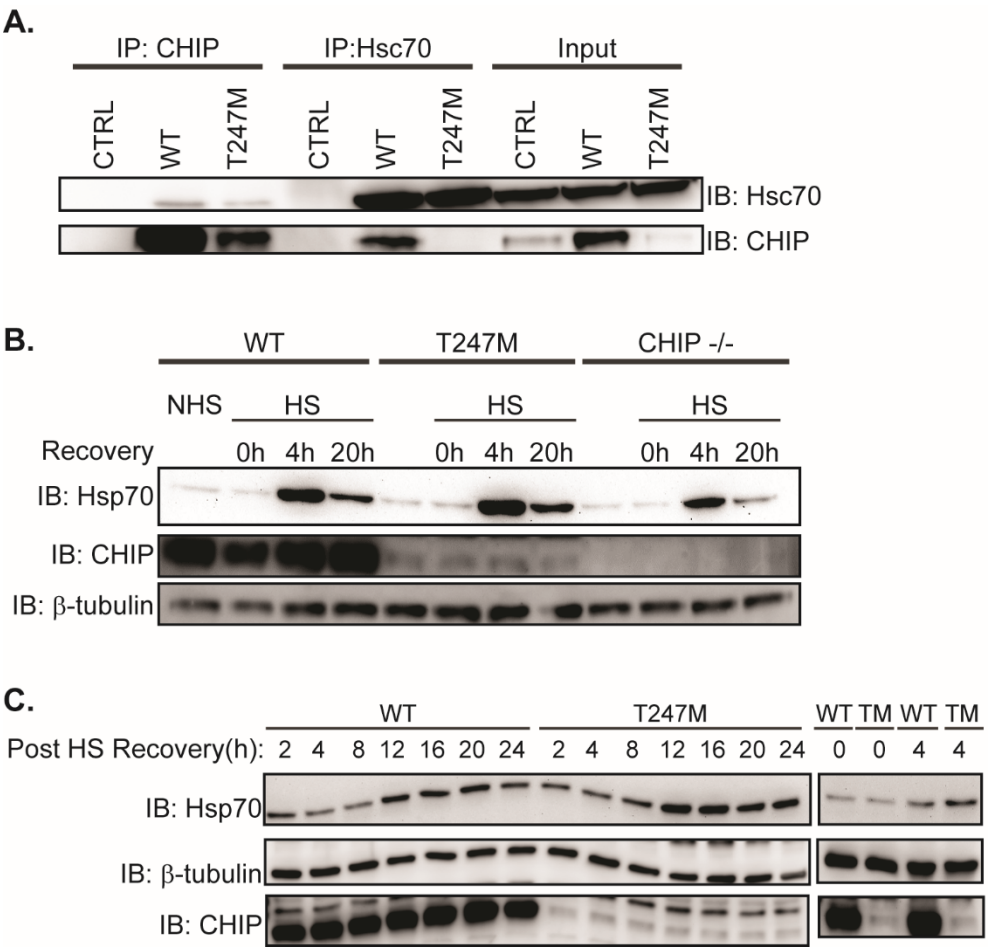

Figure 4.9. T247M CHIP chaperone interactions and co-chaperone activities remain intact and may be enhanced in T247M primary MEFs.

A. CHIP and Hsc70 immunoblot of P2 primary WT and T247M MEF cell lysates collected and immunoprecipitated with a HSC70 antibody or CHIP antibody. The inputs and resulting precipitants (IP) were separated by SDS-PAGE and immunoblotted with the indicated antibodies. Control samples (CTRL) contained a mix of 50% WT lysate and 50% T247M lysate and were immunoprecipitated with either rat IgG or rabbit IgG.

B. CHIP and Hsp70 immunoblot of P2 primary WT, T247M and CHIP knockout ($CHIP^{-/-}$) MEFs treated without heat shock (NHS) or with heat shock (HS) in a 42°C water bath for 10 min. HS cells were then returned to normal growth conditions and total cell lysates collected after 0, 4 or 20 hours of recovery. Cleared lysates were separated by SDS-PAGE and immunoblotted with the indicated antibodies.

C. CHIP and Hsp70 immunoblot of P2 primary WT and T247M (T247M or TM) MEFs heat shocked (HS) in a 42°C water bath for 10 min. HS cells were then returned to normal growth conditions and total cell lysates collected after 0, 2, 4, 8, 12, 16, 20 or 24 hours of recovery. Cleared lysates were separated by SDS-PAGE and immunoblotted with the indicated antibodies.

T246M disrupts CHIP regulation of SIRT6 and does not protect primary MEFs from UVC-induced cell death. We have recently uncovered a connection between CHIP and the nuclear lysine deacetylase/ADP ribosylase SIRT6, which is an essential regulator of inflammatory gene expression and DNA repair CHIP stably interacts with SIRT6 and CHIP-mediated non-canonical ubiquitination promotes SIRT6 protein stability. In the absence of CHIP, SirT6 is subject to canonical ubiquitination and proteasome-mediated degradation, dramatically reducing SIRT6 half-life, reducing DNA repair capacity, and increasing expression of inflammatory genes.[87] Furthermore, our additional preliminary data demonstrate that stress-induced nuclear accumulation of CHIP results in CHIP's association with not only SIRT6, but also other nuclear proteins, including several DNA repair proteins (data unpublished). GHS patients with T246M CHIP mutation have significant loss of cerebellar mass with associated cerebellar ataxia (Fig. 3.1), and CHIP$^{-/-}$ mice have significant degeneration of cerebellar Purkinje cells where CHIP is highly expressed (Fig. 3.7). Apoptosis of these neuronal populations may be a direct consequence of impaired DNA repair as a result of T246M CHIP mutation. We hypothesized that the clinical pathology of T246M CHIP mutation is in part caused by an impairment of CHIP-mediated DNA repair mechanisms by disruption of CHIP protein interactions or CHIP-mediated non-canonical ubiquitination of DNA-repair protein substrates. To test whether CHIP-mediated DNA-repair mechanisms remain intact after T246M mutation we first evaluated T246M CHIP regulation of SIRT6 *in vitro* and in cells. We performed cell free *in vitro* ubiquitination reactions containing SIRT6 and WT or T246M CHIP. As expected, we observed that T246M CHIP is unable to ubiquitinate SIRT6 *in vitro* (Fig. 4.10A). We next performed immunoprecipitation of FLAG-SIRT6 to test whether SIRT6 interaction is preserved after T246M CHIP mutation when expressed in COS-7 cells and evaluated the ubiquitination status of

SIRT6 in the presence of T246M CHIP in these cells. Interestingly, we observed that T246M CHIP maintains its interaction with SIRT6 and, in fact, this interaction appears to be enhanced, with more T246M CHIP precipitating with FLAG-SIRT6 than WT CHIP. Additionally, not only does expression of T246M CHIP result in less ubiquitinated FLAG-SIRT6 relative to that observed in the presence of WT CHIP expression, but in fact, the ubiquitination of FLAG-SIRT6 is reduced relative to control cells with no CHIP expression. Together, these data suggest that T246M CHIP does interact with but does not ubiquitinate SIRT6 *in vitro* or in cells and may inhibit access to SIRT6 by the competing E3. This likely would result in significantly impaired SIRT6 regulation that we hypothesize may negatively impact the DNA repair capacity in cells expressing T246M CHIP.

UVC-radiation has previously been shown to induce apoptosis in DNA-repair deficient cell-models[178]. To test whether T246M mutation inhibits the DNA repair capacity of cells, we subjected WT, T247M and CHIP knockout ($CHIP^{-/-}$) primary MEFs to $10J/m^2$ UVC-radiation and measured viability 24 hours later using MTT cell viability assay. As expected, we observed that WT MEF viability was unaffected but both T247M and $CHIP^{-/-}$ MEF viability was significantly reduced by ~20-25% following exposure to $10J/m^2$ UVC-radiation (Fig. 4.10C). Notably, at higher UVC doses, WT MEFs did also exhibit a reduction in viability as measured by MTT assay, but the loss of viability in T247M and $CHIP^{-/-}$ MEFs was always greater than that observed with WT up to doses of $30J/m^2$ (data not shown). This suggests significant impairment of DNA repair capacity in primary MEFs either by total loss of CHIP or as a result of dysregulation of DNA repair proteins, such as SIRT6, as a result of T247M CHIP mutation.

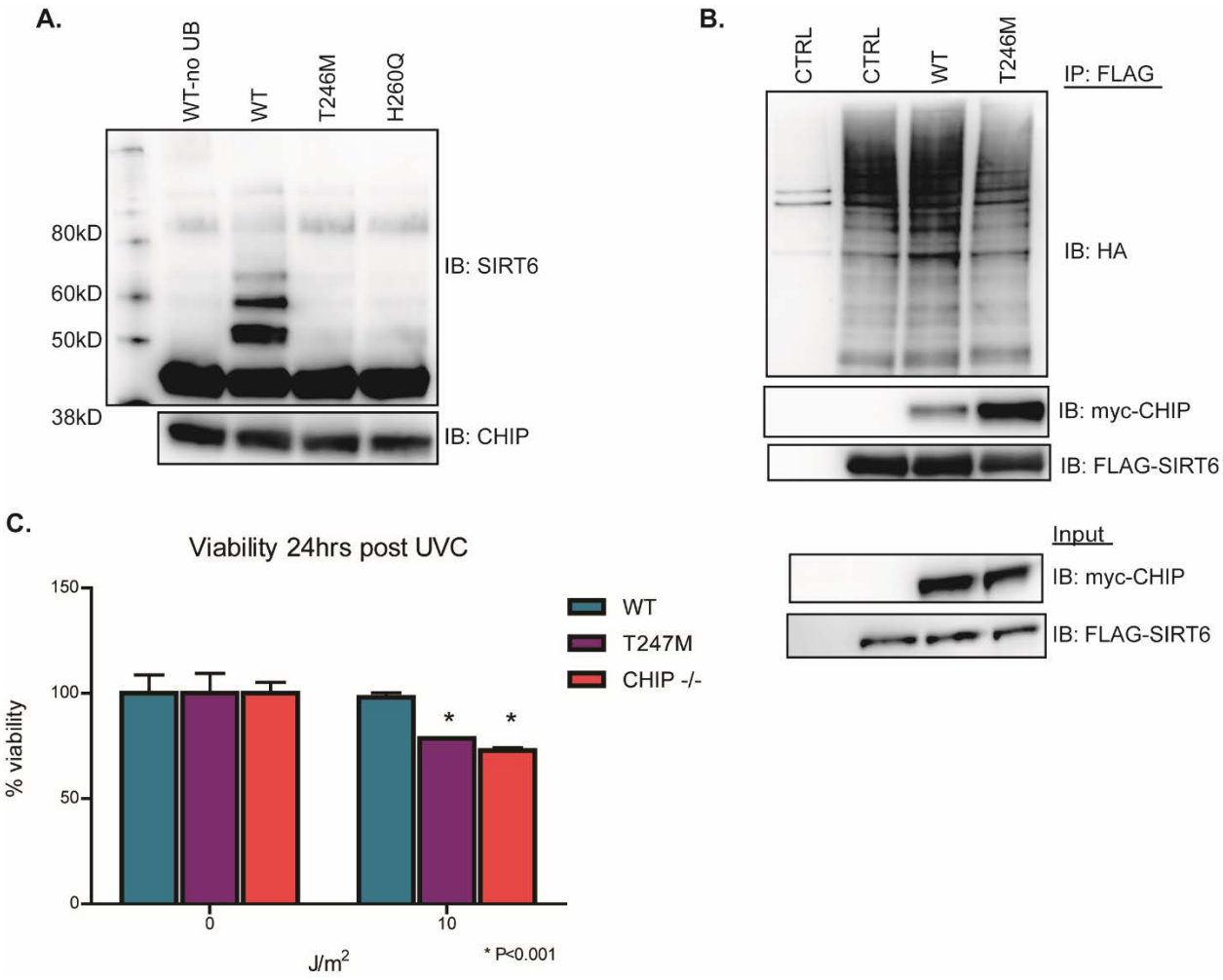

Figure 4.10. T246M disrupts CHIP regulation of SIRT6 and does not protect primary MEFs from UVC-induced cell death.

A. Cell-free ubiquitination reactions containing recombinant SIRT6 and the indicated CHIP proteins resolved via SDS-PAGE and immunoblotted for antibodies recognizing SIRT6 and CHIP.

B. Immunoprecipitation of ubiquitinated FLAG-SIRT6. COS-7 cells were co-transfected with the indicated vectors (transgenes, CTL=pcDNA3, WT=pcDNA3-CHIP and T246M=pcDNA3-CHIP-T246M) in addition to HA-tagged ubiquitin and FLAG-HSP70. HSP70 was immunoprecipitated (IP) with FLAG beads and the resulting precipitants as well as inputs were immunoblotted (IB) with the indicated antibodies. CTRL lane 1 (far left) contains no FLAG-SIRT6.

C. MTT cell viability in WT, T247M and CHIP knockout ($CHIP^{-/-}$) P2 primary MEFs 24 hours after exposure to $10J/m^2$ UVC radiation. % viability calculated relative to untreated cells of the same genotype.

T246M CHIP potentiates AMPK activity in vitro *and interacts with AMPK in cells, protecting them from oxidative stress but does not ubiquitinate upstream AMPK-regulator LKB1*. We recently uncovered a link between proteolytic and metabolic pathways with our discovery that CHIP serves as an autonomous chaperone for AMP-activated kinase (AMPK)[8]. AMPK is a global metabolic sensor, activated by reduced ATP levels to limit energy-consuming processes and promote ATP synthesis[179-181]. The AMPK holoenzyme consists of three subunits: the catalytic α subunit (α1 or α2) and the β and γ regulatory subunits. AMPK is regulated both by phosphorylation of the α subunit, principally mediated by liver kinase B1 (LKB1), and allosterically through the AMP/ATP binding domain found in the γ subunit[182]. CHIP regulation of AMPK is proposed to involve two-fold promotion of AMPK activity during cellular stress, first by enhancing its phosphorylation by upstream kinase LKB1 and by acting as a direct chaperone, binding to AMPK to affect its tertiary structure, agonizing AMPK activity followed by recovery in which CHIP-mediated ubiquitination and subsequent degradation of LKB1 restores AMPK activity to baseline levels[8]. The importance of an intact CHIP U-box domain in these regulatory roles remains incomplete, although FRET studies suggest that the CHIP U-box still binds AMPK but only partially induces changes in its tertiary structure that may mediate CHIP's direct agonism of AMPK activity[8]. Our data suggests that T246M mutation in the CHIP protein disrupts its ubiquitin ligase activity but leaves at least some of its endogenous protein-protein interactions and chaperone functions intact (Figs. 3.3, 3.4, 4.7-4.10). Therefore, we hypothesized that T246M CHIP maintains its ability to bind AMPK and agonize AMPK activity. Furthermore, we hypothesized that this activation is sufficient to protect cells from acute oxidative stress, especially because AMPK activation may be prolonged as a result of loss of CHIP-mediated LKB1 ubiquitination and degradation.

To test whether T246M CHIP regulation of AMPK upstream regulator, LKB1 is preserved we performed cell free *in vitro* ubiquitination reactions containing LKB1 and WT or T246M CHIP. As expected, we observed that T246M mutation results in loss of CHIP-mediated LKB1 monoubiquitination (Fig. 4.11A). We have previously shown that when expressed transiently in COS-7 cells, T246M CHIP maintains interactions with chaperone proteins (Fig. 3.3) and promotes chaperone-mediated activities, including the translocation and activation of HSF1 (Fig.4.8A, B, E). To test whether T246M also maintains its interaction with AMPKα, we transiently expressed myc-tagged WT and T246M CHIP in COS-7 cells and performed co-immunoprecipitation of CHIP and AMPKα1. As expected, we observed that T246M CHIP precipitates with AMPKα1 and, in fact as we observed with other CHIP interacting proteins, the association between AMPKα1 and T246M CHIP appears to be enhanced (Fig. 4.11B).

CHIP binding to AMPKα1 has previously been shown to potentiate AMPK kinase activity[8], therefore to test whether the intact/enhanced binding of T246M CHIP to AMPK also potentiates AMPK, we performed an *in vitro* kinase activity assay utilizing recombinant CHIP, AMPK and Z'LYTE peptide substrate (Invitrogen). Interestingly, we observed that like WT CHIP, T246M CHIP potentiates AMPK substrate phosphorylation in a dose-dependent manner (Fig. 4.11C). Notably, as indicated by the right-shifted dose-response curve, the potentiation appears to be reduced with T246M CHIP relative to WT CHIP. However it is important to point out that the physiological significance of this observation is unclear given the likely large difference in the distribution of WT and T246M CHIP between soluble dimer and multimeric aggregates as indicated by our biophysical characterization of recombinant WT and T246M CHIP. such that the concentration of CHIP protein participating in this potentiation of AMPK

may not truly be equivalent (Fig. 4.1). Based upon this data we can however conclude that T246M CHIP does maintain its ability to potentiate AMPK activity.

AMPK activation has been previously shown to protect cells from acute oxidative stress and we have previously demonstrated that CHIP is required for this AMPK activation[8, 183]. Having observed that the interaction of AMPK and CHIP is preserved and CHIP-mediated potentiation of AMPK is maintained in spite of T246M mutation, we hypothesized that this activation will be sufficient to protect cells from acute oxidative stress, especially because while potentially diminished in amplitude AMPK activation may be prolonged as a result of loss of CHIP-mediated LKB1 ubiquitination and degradation. To test this, utilizing the iCelligence impedance-based system for cell-based assays, we cultured and monitored the growth over time of HEK293 cells that had been stably depleted of WT CHIP by shRNA knockdown (shCHIP) as well as control HEK293 cells expressing wildtype CHIP (shCTRL). WT or T246M CHIP was then reintroduced in these cells by transient transfection, followed by exposure to 0 μM or 200 μM H_2O_2 for 24 hours beginning at 24 hours post-transfection (Fig. 4.11D). As expected, in HEK293 cells stably depleted of WT CHIP, 200 μM H_2O_2 resulted in a dramatic reduction in the recorded delta cell index relative to vehicle treated cells as well as relative to shCTRL cells also treated with 200 μM H_2O_2. The delta cell index is a reflection of the change in total cells over time, thus suggesting that in the absence of CHIP, oxidative stress dramatically inhibits cell proliferation and/or promotes cell death. Interestingly, reintroduction of both WT and T246M partially rescued this loss of cell proliferation/viability, confirming that like WT CHIP, T246M CHIP is protective against oxidative stress, perhaps via its regulation and activation of AMPK activity.

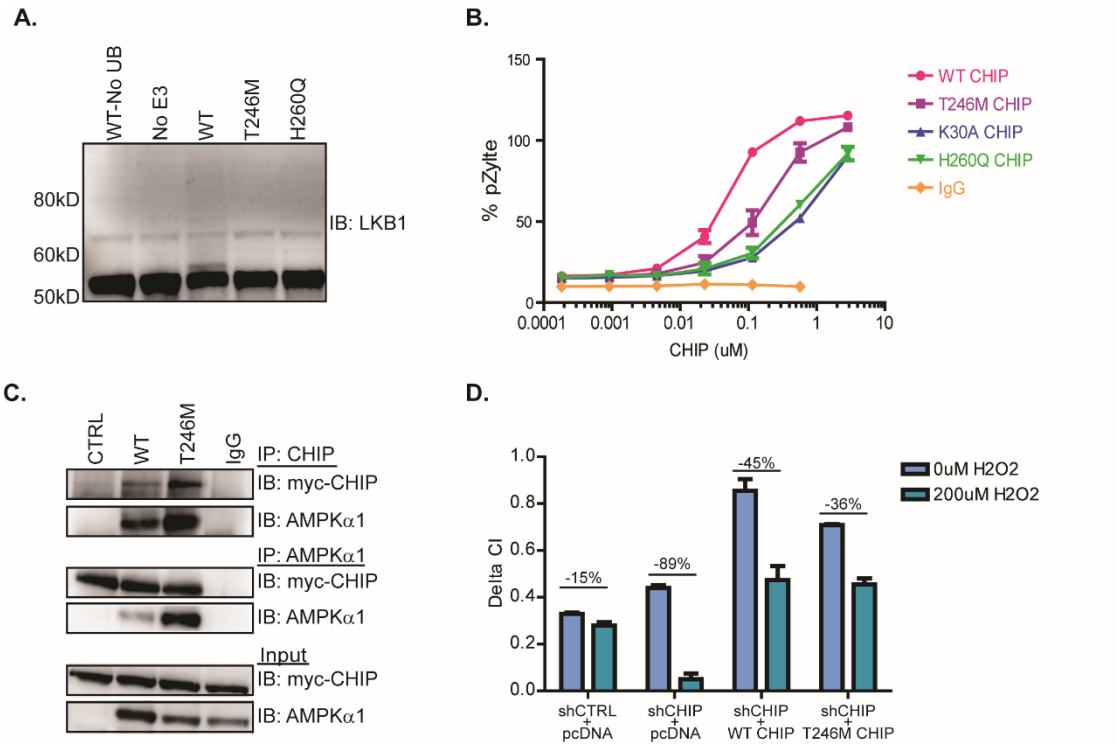

Figure 4.11. T246M CHIP potentiates AMPK activity *in vitro* and interacts with AMPK in cells, protecting them from oxidative stress but does not ubiquitinate AMPK-regulator LKB1.

A. Cell-free ubiquitination reactions containing recombinant LKB1 and the indicated CHIP proteins resolved via SDS-PAGE and immunoblotted for an antibody recognizing LKB1.

B. *In vitro* kinase assay measuring AMPK kinase activity towards Z'LYTE peptide substrate in the presence of increasing amounts of recombinant CHIP protein and IgG protein control.

C. Co-immunoprecipitation of myc-CHIP and AMPKα1. COS-7 cells were co-transfected with the indicated vectors (transgenes, CTL=pcDNA3, WT=pcDNA3-CHIP and T246M=pcDNA3-CHIP-T246M). myc-CHIP or AMPKα1 was then immunoprecipitated (IP) with CHIP or AMPKα antibody. The inputs and resulting precipitants (IP) were separated by SDS-PAGE and immunoblotted (IB) with the indicated antibodies. IgG indicates control immunoprecipitation of cell lysates utilizing rabbit or goat IgG.

D. Delta cell index recorded by iCelligence impedence-based cell monitoring system as a measure of cell proliferation/viability in HEK293 cells stably depleted of CHIP with and without the reintroduction of WT or T246M CHIP in the presence and absence of 200 µM H_2O_2. HEK293 cells were stably depleted of WT CHIP by shRNA knockdown (shCHIP). Control cells were HEK293 cells expressing wildtype CHIP stably transfected with control shRNA (shCTRL). WT or T246M CHIP was then reintroduced in these cells by transient transfection, followed by exposure to 0 µM or 200 µM H_2O_2 for 24 hours beginning at 24 hours post-transfection. Delta cell index (Delta CI) was calculated as the change in cell index before and after exposure to 0 µM or 200 µM peroxide.

T247M CHIP interacts with and regulates AMPK phosphorylation in primary MEFs that are protected from oxidative stress perhaps through an AMPK-mediated mechanism. We observed that i*n vitro* and when expressed transiently in cells, T246M CHIP maintains interactions with AMPK and potentiates AMPK activity, likely promoting the protection of cells from oxidative stress (Fig. 4.11B-D). However, the relationship between T247M CHIP and AMPK when expressed T247M CHIP was expressed endogenously was still unknown. To address this, we utilized WT and T247M primary MEFs to test whether T247M CHIP interacts with AMPK and whether this interaction results in enhanced phosphorylation of AMPK under conditions of oxidative stress and whether expression of T247M protects cells from oxidative stress-induced cell death as is observed in the presence of WT CHIP. We performed co-immunoprecipitation of CHIP and AMPK from WT and T247M MEF whole cell lysates. As expected, we observed that like WT CHIP, endogenous T247M CHIP interacts with AMPKα1. Interestingly, similar to what we observed with exogenous expression of T246M CHIP in COS-7 cells, while the amount of soluble CHIP isolated by immunoprecipitation was significantly higher from WT MEFs vs. T247M MEFs, the amount of co-precipitated AMPK was not significantly different (Fig. 4.12A). This suggests that the amount of soluble T247M CHIP present, while dramatically reduced relative to WT CHIP, is sufficient to accomplish the same AMPK binding. This may reflect a change in T247M CHIP binding kinetics as a consequence of mutation-induced structural changes and/or may result in reduced availability of T247M CHIP to other binding partners.

CHIP has previously been shown to promote AMPK activity during acute oxidative stress by enhancing its phosphorylation by upstream kinase LKB1[8]. Having confirmed AMPK-T247M interaction in this endogenous expression model, we next wanted to evaluate whether the functional consequences of this interaction remain intact. To test this we exposed WT and

T247M primary MEFs to 0, 200 and 400 μM H_2O_2 to induce acute oxidative stress and measured the phosphorylation of AMPKα. Interestingly, the phosphorylation of AMPKα in the presence of T247M CHIP was not significantly different relative to that observed in the presence of WT CHIP (Fig. 4.12B, C). This suggests that despite loss of CHIP-mediated LKB1 ubiquitination and/or changes in T247M CHIP-AMPK binding dynamics, the functional interaction at the level of AMPKα phosphorylation under stress remains intact.

We observed in shCHIP HEK293 cells that re-introduction of T247M CHIP could rescue loss of cell proliferation/viability caused by oxidative stress (Fig. 4.11D). To confirm that like WT CHIP, endogenous T247M CHIP protects cells from oxidative stress we exposed WT, T247M CHIP and CHIP knockout ($CHIP^{-/-}$) primary MEFs to 0 or 500 μM H_2O_2 and utilized the iCelligence impedence-based cell monitoring system to measure the change in cell index recorded as a measure of cell proliferation/viability over time before and after H_2O_2 or vehicle exposure. Primary MEFs lacking CHIP ($CHIP^{-/-}$) had a dramatic reduction in the change in cell index during H_2O_2 exposure, indicating a loss of cell proliferation/viability in response to oxidative stress. However, this loss of proliferation/viability was not observed in MEFs expressing either WT or T247M CHIP, suggesting that CHIP mediates this protection of oxidative stress and, importantly, T247M CHIP is also sufficient to protect primary MEFs from oxidative stress (Fig. 4.12D). Taken together, these data suggest that while some aspects of AMPK regulation by CHIP are affected by T247M mutation either by loss of its ubiquitin ligase activity or changes in its binding dynamics, T247M CHIP is still sufficient to regulate AMPK activity and promote cell survival during oxidative stress.

Furthermore, T247M mutation is a partial-loss of function mutation that results in an inability of the mutant protein to ubiquitinate its substrates, but other functions that are integral to CHIP's role in the cellular stress response that may not be dependent on CHIP ubiquitin ligase activity remain intact.

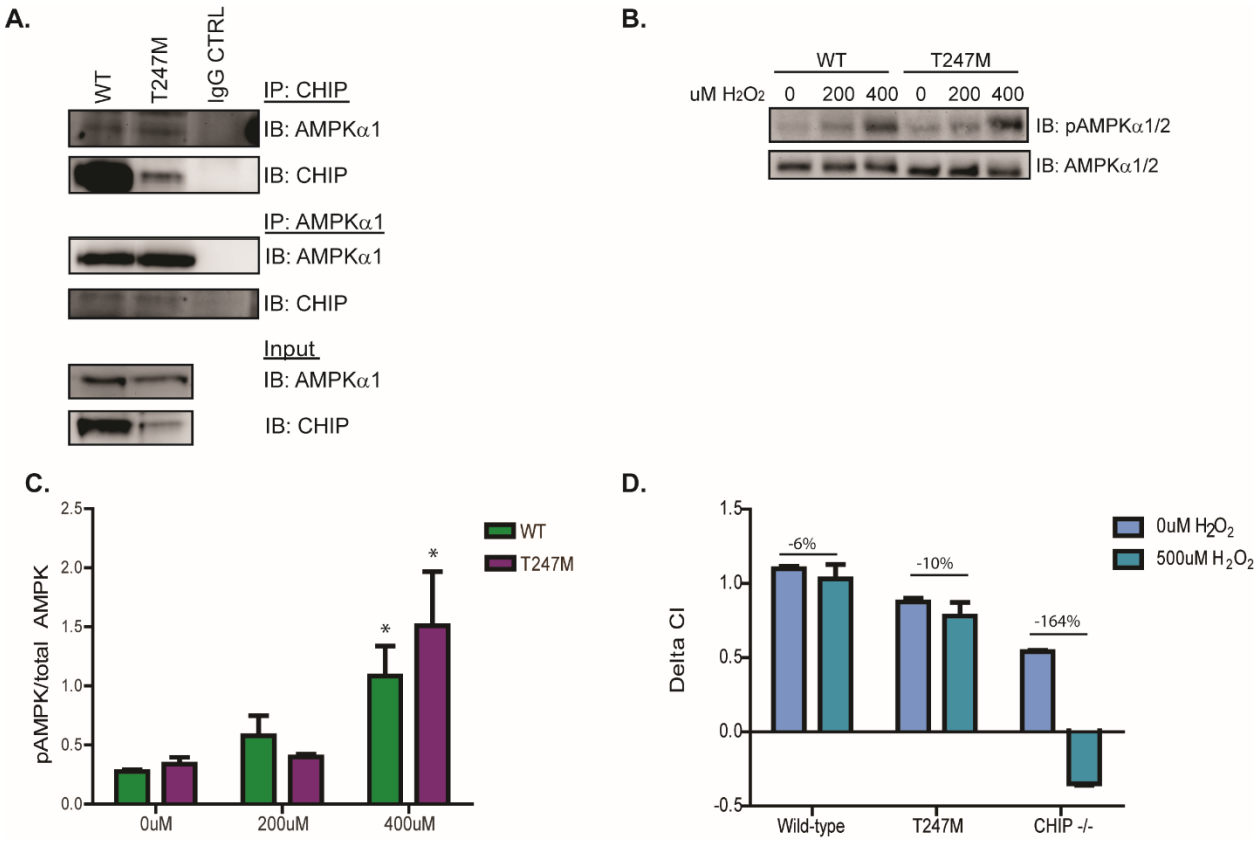

Figure 4.12. T247M interacts with AMPK in cells, protecting them from oxidative stress and promotes phosphorylation of AMPK during acute oxidative stress.

A. Co-immunoprecipitation of CHIP and AMPKα1. Purified whole cell lysates from WT and T247M CHIP P2 primary MEFs were immunoprecipitated (IP) with CHIP or AMPKα antibody. The inputs and resulting precipitants (IP) were separated by SDS-PAGE and immunoblotted (IB) with the indicated antibodies. IgG indicates control immunoprecipitation of cell lysates utilizing rabbit or goat IgG.

B. Immunoblot of purified whole cell lysates from WT and T247M primary MEFs following 10 min exposure to 0, 200 or 400 µM H_2O_2 to induce acute oxidative stress. Lysates were separated by SDS-PAGE and immunoblotted (IB) with the indicated antibodies.

C. Quantitation of phosphorylated AMPKα relative to total AMPKα as shown in representative immunoblot in Fig. 4.12B.

D. Delta cell index recorded by iCelligence impedence-based cell monitoring system as a measure of cell proliferation/viability in WT, T247M CHIP and CHIP knockout ($CHIP^{-/-}$) P2 primary MEFs in the presence of 0 µM or 500 µM H_2O_2. Delta cell index (Delta CI) was calculated as the change in cell index before and after exposure to 0 µM or 500 µM peroxide for 24 hours.

T247M protein is significantly reduced while mRNA remains unchanged in mouse tissues. T247M protein levels are significantly reduced relative to WT CHIP in T247M CHIP primary MEFs (Fig. 4.5A), while T247M CHIP mRNA levels are unchanged (Fig. 4.5B). Additionally, patient fibroblasts from SCAR-16 patients with other CHIP mutations also have significantly reduced CHIP protein expression[184]. However, the expression of SCAR-16 related mutant CHIP in animal tissue was unknown. To test this, we isolated protein and mRNA from brains, testes, livers and hearts of T247M CHIP male mice and their wildtype littermates. Tissue homogenates were separated by SDS-PAGE and immunoblotted for CHIP and β-tubulin. Confirming what we observed in primary MEFs, in all 4 tissue types, T247M CHIP protein expression was dramatically reduced relative to WT CHIP (Fig. 4.13A). Reduced protein expression may be the direct result regulation at the transcriptional level. Therefore, we also isolated mRNA from the same tissues and performed quantitative real-time polymerase chain reaction (qRT-PCR) to evaluate STUB1 (CHIP) mRNA levels. Despite the dramatic difference in protein expression, we measured no significant difference in WT vs. T247M CHIP mRNA levels across all 4 tissues (Fig. 4.13B). Together these data suggest that T247M CHIP protein expression is differentially regulated when compared to WT CHIP, but that this regulation does not occur at the mRNA level. Our primary MEF data showing enhanced T247M turnover, that is at least in part dependent on proteasomal degradation (Fig 4.6) provides one possible mechanism underlying this observed difference in CHIP protein levels. Additionally, cellular mechanisms for clearing large insoluble aggregates such as autophagy may also be involved. However, it is important to note that while levels of soluble T247M CHIP are dramatically reduced relative to WT CHIP, T247M CHIP mutation does not phenocopy total loss of CHIP.

Instead, the remaining T247M CHIP is sufficient to maintain many of CHIP's normal functions such that T247M CHIP likely results in only a partial-loss of function mutation but changes in protein binding dynamics may also, in some contexts cause T247M CHIP to behave as a dominant negative.

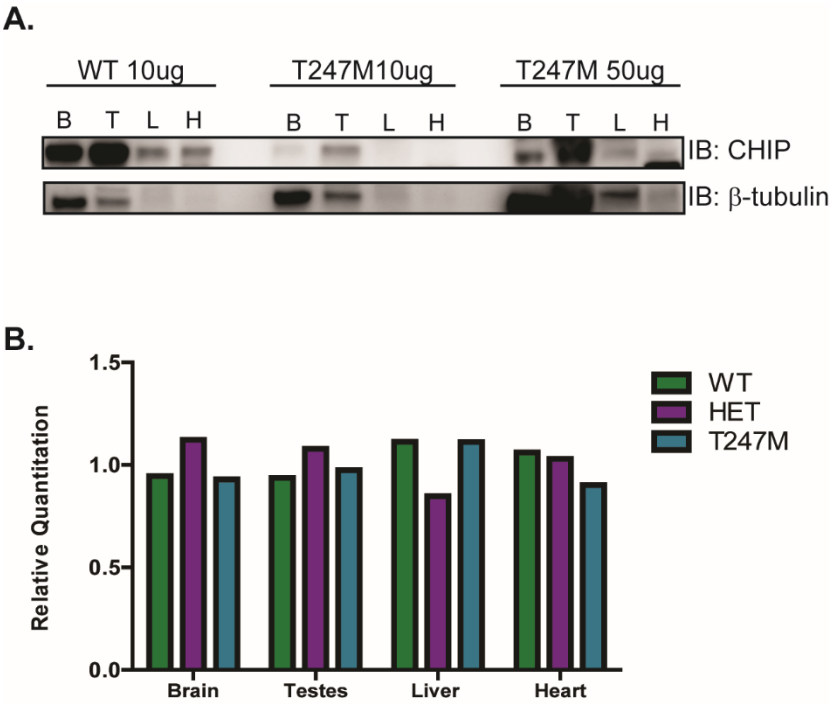

Figure 4.13. T247M protein is significantly reduced while mRNA remains unchanged in mouse tissues.

A. Immunoblottting for CHIP and β-tubulin in WT and T247M male mouse brain (B), testes (T), liver (L) and heart (H) tissue homogenates. T247M tissue homogenates were evaluated loading both 10 µg and 50 µg of total protein to allow for visualization of T247M CHIP.

B. Relative quantitation of total STUB1 mRNA isolated from WT and T247M male mouse brain (B), testes (T), liver (L) and heart (H) tissue.

T247M homozygous mutant mice exhibit dysregulation of inhibitory processes governing activity, exploration, and sensorimotor gating, and to impaired learning and memory. We reported previously that both siblings homozygous for the CHIP T246M substitution have profound cerebellar ataxia as well as selective cognitive impairments. Additional reports of CHIP mutation in other cases of SCAR16 feature cerebellar dysfunction (ataxia) with an additional range of clinical features associated with disease, including a heterogeneity of additional neurological deficits.[90] The profound cerebellar ataxia exhibited in SCAR16 suggests that CHIP plays a critical role in maintaining cerebellar function. And in fact when we examined our CHIP$^{-/-}$ mouse line in a battery of cognitive assessments, we observed that total loss of CHIP expression has a selective impact in motoric, sensory, and cognitive function, in particular with tasks attributed to cerebellar function (Figs. 3.5 and 3.6). However, the results of our biophysical and cell based models suggest that T246M mutation is not functionally equivalent to total loss of CHIP, thus in order to determine the pathophysiological implications of T246M mutation *in vivo* we generated a mouse model (T247M) that mimics the human mutation. We first wanted to assess the neurological behavior of the T247M CHIP mice to determine if this mutation found in human SCAR16 patients leads to neurological impairments associated with SCAR16. Given the autosomal recessive nature of CHIP deficiency in SCAR16, we examined both T247M homozygous and heterozygous mice as well as their wildtype littermates in a battery of neurological assessments.

The rotarod test is extensively used in mouse models to detect cerebellar dysfunction by testing motor coordination and motor learning on a rotating dowel. The performance of CHIP$^{-/-}$ mice on the rotarod demonstrated a severe motoric impairment, and we hypothesized that given the severe ataxia associated with cerebellar dysfunction in SCAR16 patients we would observe

similar deficits in the homozygous T247M mice. However, neither the heterozygous nor homozygous T247M mice exhibited any significant deficits in motor coordination on an accelerating rotarod when tested in 4 different trials at 9-10, 22, 27-28 and 31 weeks of age (Fig. 4.14). While these results are surprising, we predict that this may be a strain dependent effect as strain differences have been reported with the rotarod test in other studies of mouse models of neurdegeneration[185], and when comparing the wildtype animals tested previously against our CHIP$^{-/-}$ mice (C57/Bl6 x 129SVEV) vs. the wildtype tested here (C57/Bl6) the latency to fall from the accelerating rotarod of the C57/Bl6 WT mice is more than 4X longer than the C57/Bl6 x 129SVEV WT animals (Fig 3.5A and 4.14). This suggests that the C57/Bl6 mouse strain may be particularly well-adapted to this task, such that to observe a degenerative deficit may require further advanced aging of the mice. This hypothesis is further supported by the variable age of onset of motor deficits reported previously in additional mouse models of cerebellar degenerative disorders.[186]

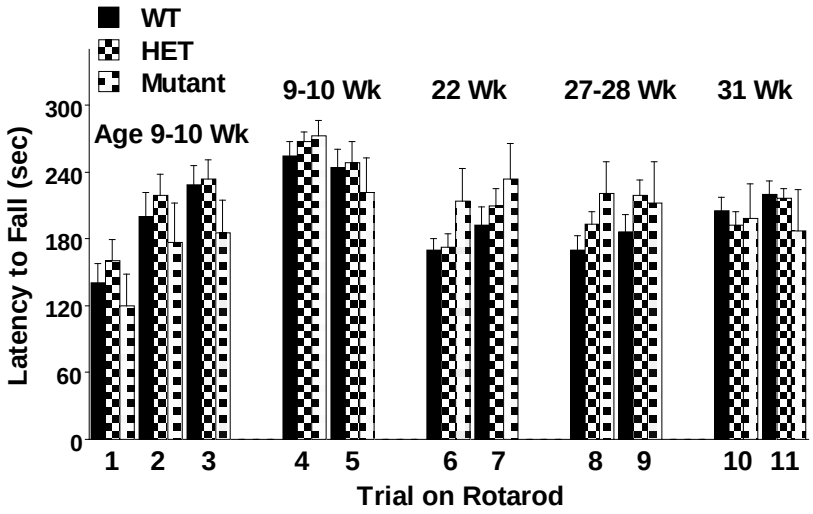

Figure 4.14. Latency to fall from an accelerating rotarod. Maximum trial length was 300 sec. Trials 4 and 5 were given 48 hours after the first 3 trials, when mice were 9-10 weeks (Wk) in age.

Next, to assess auditory function, reactivity to environmental stimuli, and sensorimotor gating the mice were examined in the acoustic startle and prepulse inhibition test. CHIP$^{-/-}$ mice had previously demonstrated significantly reduced magnitude of the startle response as well as a delayed reaction time with no change in prepulse inhibition when evaluated at 25 weeks of age (Fig. 3.5C, D). However, no effects of T247M genotype were observed for acoustic startle amplitudes at either age of testing, 11-13 weeks or 33 weeks (Fig. 4.15A and 4.15B). Similarly, the three genotypes demonstrated comparable levels of prepulse inhibition in the first test (Fig. 4.15C). Interestingly, in the second test, the T247M mutant mice exhibited significant decreases in percent inhibition across every prepulse sound level, indicating the emergence of sensorimotor deficits by age 33 weeks [main effect of genotype, $F(2,41)=9.62$, $p=0.0004$, genotype x decibel interaction, $F(8,164)=2.08$, $p=0.0406$] (Fig. 4.15D). These degenerative deficits in prepulse inhibition are consistent with other mouse models of cerebellar degeneration with profound Purkinje cell loss.[187]

In addition to this deficit in prepulse inhibition attributed to cerebellar dysfunction, the mutant mice demonstrated both hyperactivity and increased impulsivity in an open field test. As shown in Table 4.1, highly significant effects of genotype were found for distance traveled, rearing, and center time at both ages tested (Fig. 4.16). In the first test at age 8-9 weeks, the *CHIP* mutant mice had increased levels of locomotor activity in comparison to WT and HET mice at most intervals in the 1-hr session (Fig. 4.16A). By the second test, the mutant mice were overtly hyperactive across the entire test (Fig. 4.16B). In fact, data from one female mutant mouse was removed from the analysis, because of extreme activity levels (i.e. distance traveled=7,230 cm at the 50 min interval). A different pattern emerged for rearing movements, a measure of vertical activity. At both 8-9 weeks and 32 weeks, the mutant mice had significantly

reduced levels of rearing at the beginning of each session (Fig. 4.16C, D), indicating a deficit in the initial exploration of the open field. In the second open field test, higher levels of rearing emerged in the mutant group in the last half of the session, in line with a hyperactive phenotype (Fig. 4.16D). In both open field tests, the disruption of *CHIP* led to increased time spent in the center region, suggesting a reduction in typical cautionary avoidance of the open area (Figure 4.16E, F). Together these data suggest T247M CHIP expression led to more impulsive and risky exploration, as observed in mouse models for mania and impulsivity[188, 189] and overt hyperactivity. Interestingly, both impulsivity and hyperactivity have been attributed to cognitive cerebellar dysfunction in humans[190-192]. Surprisingly, when we then evaluated the T247M CHIP mutant mice in the elevated plus maze (EPM) test for anxiety-like behavior, no significant effects of genotype were observed. We hypothesize that this may be because the mice were only evaluated in the EPM at 7-8 weeks at which point overt cognitive cerebellar decline may not have yet occurred and significant differences in anxiety-like behavior would be observable (Table 4.2).

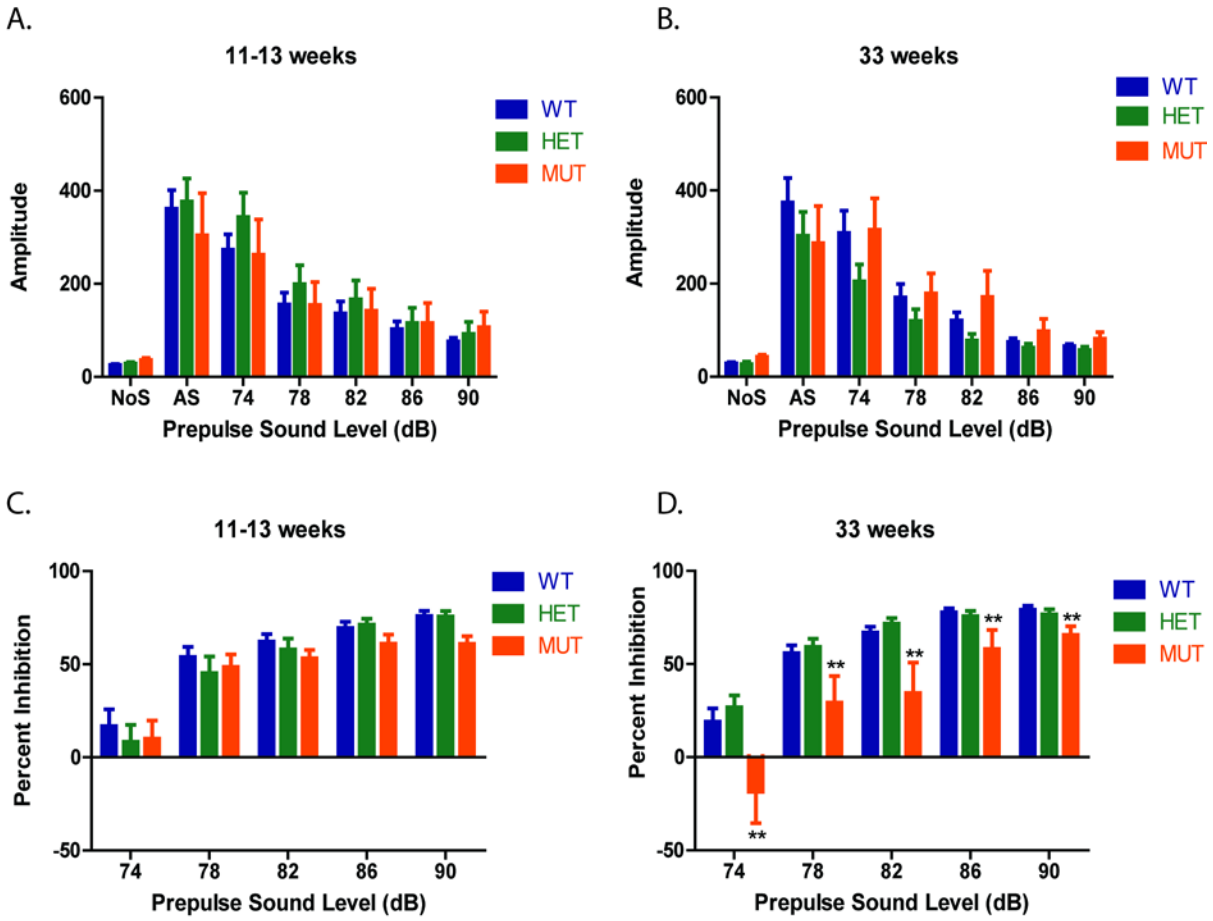

Figure 4.15. Magnitude of startle responses and prepulse inhibition in an acoustic startle test. Trials included no stimulus (NoS) trials and acoustic startle stimulus (AS) alone trials.

A.-B. Magnitude of startle response of WT, T247M HET and T247M homozygous mutant mice at 11-13 weeks (**A**) and 33 weeks (**B**).

C.-D. Prepulse inhibition of WT, T247M HET and T247M homozygous mutant mice at 11-13 weeks (**C**) and 33 weeks (**D**).

Table 4.1. Statistical analysis of open field data. F values, degrees of freedom, and p values from a repeated measures ANOVA, with the factors genotype and time (5-min intervals across a 1 hour test). In the second test, data from one female mutant mouse was removed from analysis, due to extreme levels of hyperactivity.

Measure and Age at Testing	Main Effect of Genotype	Genotype x Age Interaction
Distance traveled		
8-9 weeks	$F(2,45)=7.41$, $p=0.0017$	$F(22,495)=2.00$, $p=0.0047$
32 weeks	$F(2,40)=25.96$, $p<0.0001$	$F(22,440)=1.05$, $p=0.3971$
Rearing movements		
8-9 weeks	$F(2,45)=0.09$, $p=0.9160$	$F(22,495)=3.38$, $p<0.0001$
32 weeks	$F(2,40)=0.82$, $p=0.4495$	$F(22,440)=3.12$, $p<0.0001$
Time spent in center region		
8-9 weeks	$F(2,45)=3.37$, $p=0.0434$	$F(22,495)=4.00$, $p<0.0001$
32 weeks	$F(2,40)=19.21$, $p<0.0001$	$F(22,440)=2.60$, $p=0.0001$

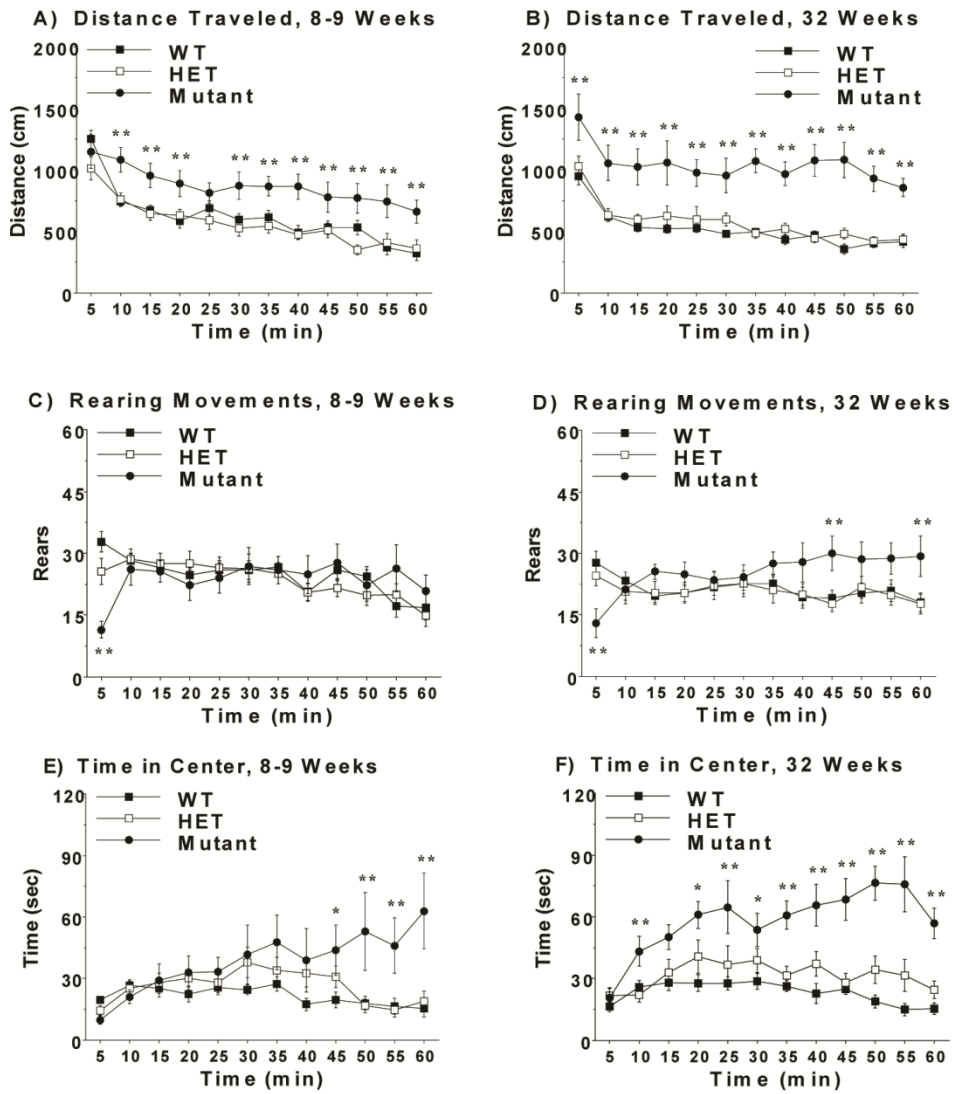

Figure 4.16. Distance traveled, rearing movements and time in spent in the center in two open field tests at ages 8-9 weeks and 32 weeks. *p<0.05, comparison to WT, **p<0.05, comparison to both WT and HET.

A.-B. Distance traveled in open field test of WT, T247M HET and T247M homozygous mutant mice at 8-9 weeks (**A**) and 32 weeks (**B**).

C.-D. Number of rearing movements (vertical activity) in open field test of WT, T247M HET and T247M homozygous mutant mice at 8-9 weeks (**C**) and 32 weeks (**D**).

E.-F. Time spent in the center in open field test of WT, T247M HET and T247M homozygous mutant mice at 8-9 weeks (**E**) and 32 weeks (**F**).

Table 4.2. Performance of WT, HET and T247M CHIP mutant mice in an elevated plus maze test for anxiety-like behavior, a marble-burying assay for exploratory digging, and a buried food test for olfactory function.

	WT	HET	Mutant
Elevated plus maze			
Percent open arm time	32 ± 3	30 ± 4	36 ± 4
Percent open arm entries	39 ± 2	41 ± 2	42 ± 3
Total number of entries	28 ± 2	27 ± 2	28 ± 3
Number of marbles buried in 30 min			
First test (age 12 weeks)	16 ± 0.6	18 ± 0.4	11 ± 1.7**
Second test (age 32 weeks)	17 ± 0.4	16 ± 0.7	13 ± 1.3**
Olfactory test			
Latency to find food (sec)	267 ± 74	189 ± 52	289 ± 95
Percent of group finding food	80%	95%	89%

**$p<0.05$, comparison to both WT and HET.

In addition to the deficits attributed to cerebellar dysfunction, the T247M also demonstrated highly significant impairment in both contextual and cue-dependent learning in the conditioned fear procedure, perhaps suggesting hippocampal dysfunction, resulting in impairment of learning and memory as a result of T247M CHIP mutation. On Day 1, the training day, all of the genotype groups had similar, very low levels of freezing before any exposure to the aversive foot shock (Fig. 4.17A). In contrast, during the test for context learning on Day 2, the mutant mice exhibited significantly less freezing than either the WT or HET mice at every time point [main effect of genotype, $F(2,45)=18.46$, $p<0.0001$; genotype x time interaction, $F(10,225)=3.3$, $p=0.0005$] (Fig. 4.17A). These learning deficits were still evident in the mutant group 2 weeks later, during the second test [main effect of genotype, $F(2,45)=12.17$, $p<0.0001$] (Fig. 4.17B). Strong genotype effects were also observed for cue-dependent learning (Fig. 4.17C, D). For both tests, the mutant mice failed to demonstrate a sharp increase in freezing typically observed with the onset of the auditory cue [Test 1, main effect of genotype, $F(2,45)=4.4$, $p=0.018$; genotype x time interaction, $F(8,180)=3.48$, $p=0.0009$; and Test 2, main effect of genotype, $F(2,45)=11.75$, $p<0.0001$; genotype x time interaction, $F(8,180)=2.78$, $p=0.0063$]. This lack of response could not be attributed to hearing impairment, since the mutant mice had normal performance in the acoustic startle test. Together these data suggest significant impairment in learning and memory as a result of homozygous T247M CHIP expression.

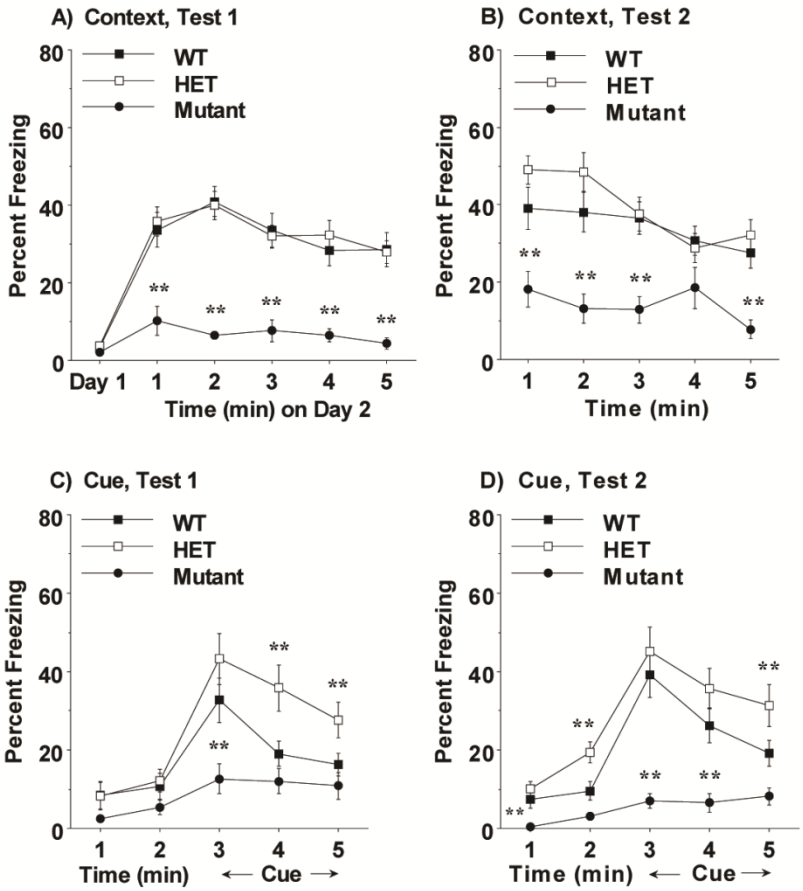

Figure 4.17. Context-dependent and Cue-dependent conditioned fear testing in WT, HET and T247M CHIP mutant mice at age 14-18 weeks. **p<0.05, comparison to both other groups.

A. Context-dependent learning, Test 1. Baseline levels of freezing behavior before shock exposure were determined on Day 1 (the training day). Contextual learning was evaluated across 5 min on Day 2 of testing.

B. Context-dependent learning, Test 2. Test for retention of contextual learning was conducted 2 weeks following the first test.

C. Cue-dependent learning, Test 1. An 80 decibel acoustic stimulus (Cue) was presented 2 min after mice were placed in the conditioned fear chambers.

D. Cue-dependent learning, Test 2. Test 2 was conducted 2 weeks after Test 1.

Additional testing in the 3-chamber choice test found altered social behavior as a result of T247M CHIP expression, such that T247M mutant mice had increased preference for social novelty (Fig. 4.18). During the social novelty phase of testing the T247M mutant mice had a shift in preference towards the newly-introduced stranger 2 [within-genotype repeated measures ANOVAs, following overall significant effect of side, $F(1,44)=8.08$, $p=0.0068$] (Fig. 4.18B**)** and the mutant mice made significantly more entries than either the WT or HET mice into the side containing stranger 2 [genotype x side interaction, $F(2,44)=4.92$, $p=0.0118$, effect of side, $F(1,44)=11.05$, $p=0.0018$] (Fig. 4.18D).

Further behavioral testing revealed the T247M mutant mice also had reduced marble burying, indicating a decrease in exploratory digging (Table 4.2). However, no effects of genotype were observed for olfactory ability in a buried food test (Table 4.2). Overall, the CHIP mutation did not lead to overt signs of poor health; however, both the male and female mutant mice had significantly lower body weights than the WT and HET groups at almost every time point during the behavioral study (Fig. 4.19). Overall, the results of the battery of behavioral assessments performed suggest that homozygous T247M CHIP mutation leads to the dysregulation of inhibitory processes governing activity, exploration, and sensorimotor gating, and to impaired learning and memory in tests for conditioned fear. Interestingly, impaired conditioned fear and decreased marble-burying have also been reported in mice with deletion of maternal E3 ubiquitin ligase Ube3a, a model for Angelman syndrome[193]. Surprisingly, testing at ages up to 31 weeks did not reveal significant motor impairment indicative of cerebellar ataxia as a result of T247M mutation; however, other behavioral deficits attributable to cognitive cerebellar dysfunction were observed as well as deficits in learning and memory attributable to hippocampal dysfunction that are reflective of cognitive deficits sometimes observed in SCAR16

patients. Interestingly, we have observed some behavioral deficits that overlap with those observed in our mouse model of total loss of CHIP; however, the majority were unique to T247M mutation, supporting our cell-based data suggesting T247M mutation and total loss of CHIP are not equivalent. Additional efforts to compare these mouse strains on the same genetic background are on-going to better enable this comparison. Furthermore, it is notable that the deficits observed occur largely in the homozygous mutation setting as would be predicted based upon the recessive inheritance pattern of SCAR16.

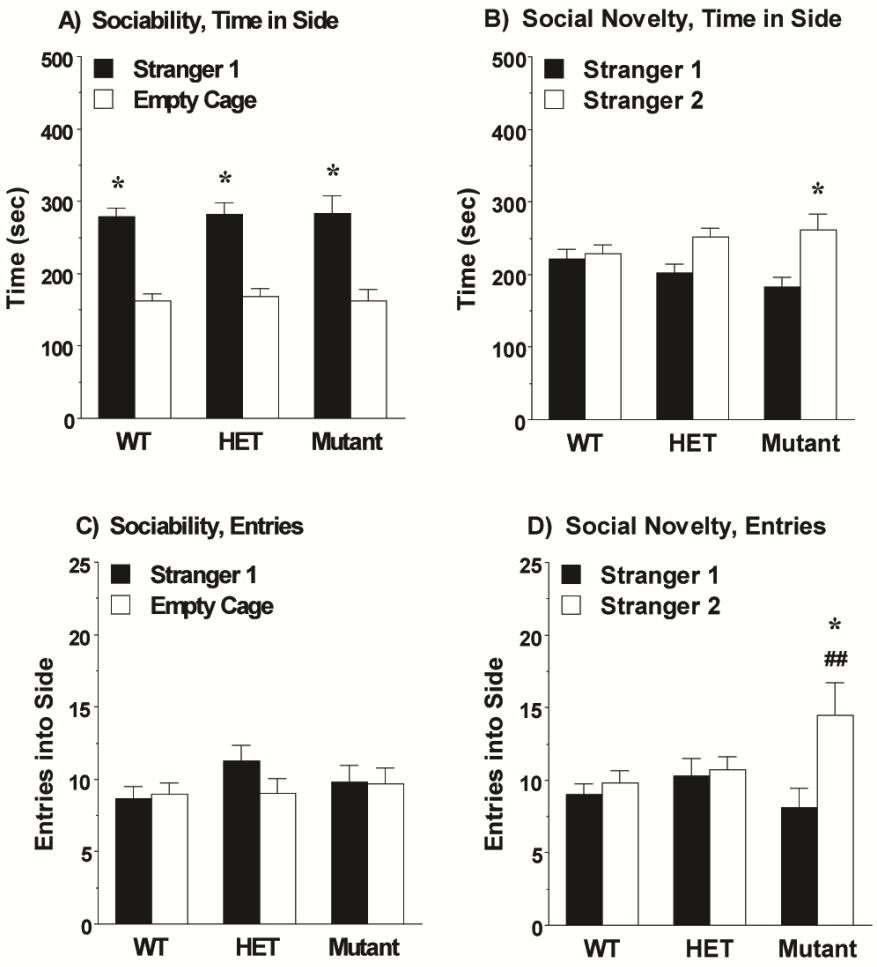

Figure 4.18. Social approach in a 3-chamber choice test of WT, HET and T247M mutant mice at 10-13 weeks of age. * $p < 0.05$, within-genotype comparison between stranger 1 side and opposite side. ## $p < 0.05$, comparison to same measure in both other genotypes.

A.-C. 3-chamber choice test of sociability of WT, HET and T247M mutant mice at 10-13 weeks of age. Time spent with stranger 1 (**A**) and number of entries into side containing stranger 1 (**C**).

B.-D. 3-chamber choice test of social novelty of WT, HET and T247M mutant mice at 10-13 weeks of age. Time spent with already-investigated stranger 1 vs. novel stranger 2 (**B**) and number of entries into side containing already-investigated stranger 1 vs. novel stranger 2 (**D**).

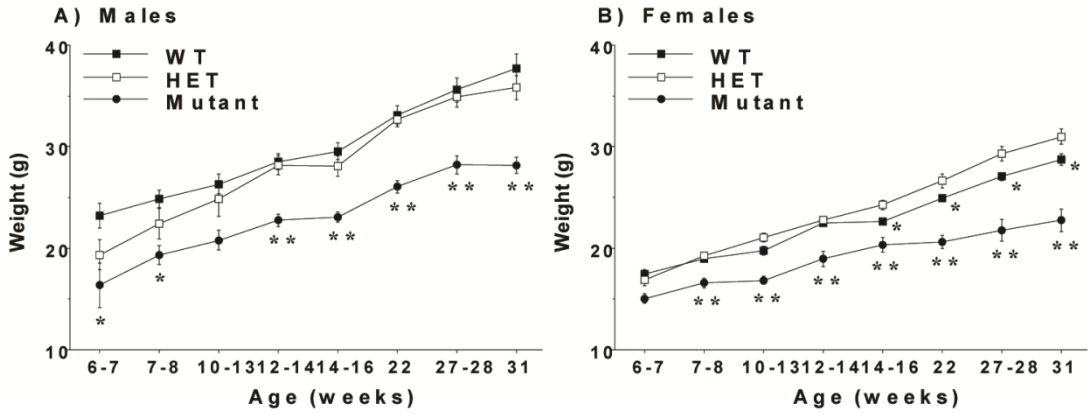

Figure 4.19. Body weights across the behavioral study. Data are missing from one male mutant mouse for the first weight measure. *p<0.05, comparison to WT. **p<0.05, comparison to both WT and HET.

Discussion

Our biophysical, cellular and *in vivo* characterization of T246M mutation in SCAR16 both *in vitro* and *in vivo* has allowed us a unique opportunity to begin to delineate the contribution of co-chaperone, ubiquitin ligase activity and other emerging CHIP activities to specific deficits observed *in vitro* and *in vivo* in a disease-relevant context. Initially we had hypothesized that the functional loss of CHIP ubiquitin ligase activity as a result of T246M mutation was the result of catalytic inactivation of the U-box domain. However, our structural and biophysical data suggest that T246M mutation leads to dramatic destabilization and misfolding of the CHIP U-box that results in a loss of CHIP's ability to form dimers and promotes the formation of large, multimeric CHIP aggregates both *in vitro* and in cells. Furthermore, when T246M is expressed endogenously across multiple tissues and cell types the amount of total soluble protein is dramatically reduced. Additionally, the rate of turnover of T246M is greatly enhanced relative to WT CHIP protein, suggesting that the destabilization of the U-box promotes the clearance of this structurally misfolded mutant CHIP, likely in an effort by the cell to reduce the accumulation of insoluble toxic aggregates, in part through a proteasome-dependent mechanism. Importantly when expressed with WT CHIP, T246M CHIP does not disrupt WT CHIP dimerization status or localization and conversely the presence of WT CHIP does not rescue the misfolding/structural disorganization of T246M CHIP. This data supports the recessive inheritance pattern of SCAR16 and may explain why the heterozygous T246M mutant carriers do not have any disease phenotype.

Interestingly, a small population of soluble, partially-functional endogenous T246M CHIP protein remains. It is particularly fascinating to us that T246M CHIP's E3 ubiquitin ligase activity towards a variety of substrates is completely abolished but T246M CHIP retains the

ability to function in some of CHIP's critical cellular roles in PQC as a co-chaperone and as an autonomous chaperone promoting the phosophorylation and potentiating the activity of AMPK, protecting cells from oxidative stress. This is particularly intriguing given the very low levels of soluble T246M expressed endogenously. Importantly, while T246M CHIP retains co-chaperone activities, binding chaperone proteins and inducing HSF1 nuclear translocation and Hsp70 expression following stress, both chaperone binding and the induction of Hsp70 are enhanced, possibly suggesting abnormal binding kinetics that result from the structural disorganization of the CHIP U-box that may alter normal CHIP-mediated regulation of the chaperone-mediated stress response. CHIP$^{-/-}$ mice are highly stress intolerant[74]; therefore, it will be fascinating to elucidate whether the abnormal aspects of T246M CHIP co-chaperone activity we have observed are functionally deleterious or advantageous in our T247M CHIP mice in *in vivo* stress models. As one might expect due to the multifaceted nature of CHIP activity in cells, our studies suggest that the functional consequences of T246M mutation under stress are stress-specific, as we observed T246M CHIP protects cells from oxidative stress, but similar to total loss of CHIP, T246M mutation does not protect cells from UVC-induced cell death. These data further support our conclusion that T246M mutation is not functionally equivalent to total loss of CHIP.

In order to best understand this distinction when T246M is expressed in a genomic context and to evaluate the pathophysiological implications of T246M mutation *in vivo*, we generated a mouse model (T247M) that mimics the human mutation. Surprisingly, testing at ages up to 31 weeks did not reveal significant motor impairment indicative of cerebellar ataxia as a result of T247M mutation, however other behavioral deficits attributable to cognitive cerebellar dysfunction were observed as well as deficits in learning and memory attributable to hippocampal dysfunction that are reflective of cognitive deficits reported in SCAR16 patients.

These data further support our previous findings from CHIP$^{-/-}$ mice that CHIP plays a critical role in cerebellar maintenance. Interestingly, while we have observed some behavioral deficits that overlap with those observed in our mouse model of total loss of CHIP, the majority were unique to T247M mutation, further validating our cell-based data that suggest T246M mutation and total loss of CHIP are not functionally equivalent. We hypothesize that the phenotypic differences observed between CHIP$^{-/-}$ mice and T247M mice are likely reflective of our cell-based and *in vitro* findings that while T247M CHIP no longer functions as an E3 ubiquitin ligase, other CHIP functions remain intact despite this mutation. And in fact, perhaps even more intriguingly, T247M mutation may in some cases modify CHIP's co-chaperone activities in a functionally advantageous or, more likely, deleterious manner, similar to a dominant-negative mutation. These data further support our previous findings that highlight the role of aberrant ubiquitination in the pathogenesis of SCAR16 however suggest that loss of CHIP ubiquitin ligase activity alone may not fully explain the molecular mechanisms underlying the diverse pathophysiology observed in the heterogeneity of SCAR16 disease. As such, it appears that T246M mutation in SCAR16 is best described as a partial loss of function mutation.

The CHIP mutations that have been associated with SCAR16 are present in all three of CHIP's functional domains, although interestingly the majority are concentrated in the charged domain and the U-box domain, supporting disruption of CHIP ubiquitin ligase activity as a likely driver of disease. Our data clearly support this role of aberrant ubiquitin ligase function in the pathophysiology of SCAR16 but suggest that this is not mechanism whereby CHIP mutation drives disease. Given the diversity of reported mutations and the clinical heterogeneity of the ARCA patients harboring these *STUB1* mutations, we originally hypothesized that the affected protein domain may directly correlate to clinical phenotype. For example, cognitive impairment

occurs in 5 out of 6 genetic signatures harboring mutations in the U-box domain, such that residual CHIP activity involving a defective or truncated U-box domain but intact TPR domain could directly correlate to specific clinical symptoms in some patients. Our extensive behavioral analysis of the T247M CHIP mouse model provides direct evidence to support this hypothesis, demonstrating that particular cognitive deficits are in fact associated *in vivo* with a U-box domain point mutation that has been demonstrated *in vitro* and in cells to have a partially functionally intact TPR domain. The development of additional animal models with isolated domain mutations may help to further validate this hypothesis and identify how the multifunctional roles of CHIP contribute to particular clinical pathologies. It seems clear, however, that while disordered ubiquitination contributes to SCAR16 pathology, CHIP mutation as a driver of disease is not limited to loss of ubiquitin ligase activity but may represent a more multi-faceted disruption of CHIP-mediated PQC.

To date, we have only begun to fully evaluate the *in vivo* consequences of T247M mutation. The results of our behavioral assessment of these mice are fascinating and raise many questions about the underlying pathological, cellular and biochemical changes that are occurring to drive this phenotype. At a cellular level, future studies will aim to elucidate this by evaluating changes in cell signaling pathways that result from T247M mutation *in vivo*. Additionally, having observed significant cerebellar deficits we are interested in evaluating the health of the cerebellum in T247M mice, particularly to evaluate its structure and identify signs of atrophy, quantitate and evaluate localization of CHIP expression, identify the presence of aggregates indicative of proteotoxicity and evaluate Purkinje cell pathology. It will be particularly fascinating to compare these data to our previous data evaluating many of these parameters *in vivo* in the context of total loss of CHIP.

Within the spectrum of disease phenotypes represented by SCAR16, patients with GHS represent a unique group where cerebellar ataxia characteristic of SCAR16 is paired with neuroendocrine deficits and resulting reproductive impairments associated with hypogonadism. We previously observed CHIP$^{-/-}$ mice recapitulate many of the reproductive impairments characteristic of GHS. While developing the T247M mouse model and establishing the mouse colony we have observed impaired breeding of T247M homozygous mice. Additionally, preliminary hormonal studies of male T247M mice suggest abnormal circulating hormone levels and an impairment of the pituitary's ability to respond to stimulation with gonadotropin releasing hormone, similar to that observed in hypogonadism associated with GHS (data not shown). Future studies will seek to characterize the neuroendocrine deficits and reproductive impairments associated with T247M. Both by comparison to the CHIP$^{-/-}$ animals as well as to additional SCAR16 point mutant mice we may be able to delineate the contribution of particular CHIP functions to this unique disease phenotype.

These studies represent the first *in vivo* characterization a CHIP mutation relevant to human disease. Loss of CHIP function has long been associated with protein misfolding and aggregation in several genetic mouse models of neurodegenerative disorders; however, a role for CHIP in human neurological disease had never been identified. In light of the identification of T246M CHIP mutation and subsequent designation of SCAR16, the establishment of the T247M mouse model of SCAR16 represents a novel and important tool to finally evaluate CHIP dysfunction *in vivo* in a disease-relevant context. Our biophysical, cellular and *in vivo* characterization of T246M mutation in SCAR16 has provided significant insight into both the molecular mechanisms driving disease pathology in SCAR16 as well as basic CHIP biology, by shedding new light on the structure-function relationship, particularly how it contributes to the

multifaceted activities of CHIP within the cell. Furthermore, we are hopeful these studies have provided valuable insight required for the future development of effective therapies for this devastating degenerative disease.

Experimental Procedures

Expression plasmids and recombinant proteins. Mammalian expression plasmids pcDNA3-myc-CHIP, pcDNA3-myc-CHIP-K30A, pcDNA3-myc-CHIP-H260Q, HA-Ubiquitin, FLAG-SIRT6, FLAG-HSP70, β-galactosidase, GFP and cBSA were used as described previously [75, 87, 128, 135, 177]. CHIP, CHIP-H260Q, CHIP-K30A, CHIP-T246M and AMPK recombinant proteins were produced in Escherichia coli BL21(DE3) as His-tagged fusion proteins by induction with 0.1mM isopropyl-1-thio-β-D-galactopyranoside overnight at 18°C followed by purification with HisTrap™ HP columns (GE Healthcare), concentrated, and stored in in 20 mM HEPES pH 7.4 with 150 mM NaCl.

Mutagenesis. A point mutation of threonine to methionine at position 246 of CHIP was created for generation of single T246M point mutant and K30A-T246M double point mutant by site-directed mutagenesis using the Q5 Site-Directed Mutagenesis Kit (New England Biolabs, E0554S) according to manufacturer's instructions using previously described pcDNA3-myc-CHIP template or pcDNA3-myc-K30A CHIP template[128] and mutagenic primers 5'-CCGTGCATCATGCCCAGTGGC-3' and 5'-CTCCCGCATCAGCTCAAAGC-3' (BaseChanger software, New England Biolabs). The myc-CHIP-T246M and myc-CHIP-K30A-T246M expression plasmids were produced by transformation in Escherichia coli DH5α, purified, and the single-base pair substitution was verified by DNA sequencing.

In vitro *ubiquitination reactions. In vitro* ubiquitination reactions were carried out as previously described [128]. Briefly, bacterially-expressed 4uM LKB1 (Sigma, SRP0246), 1uM α-synuclein (ab123758) or 1 μM SIRT6 (Sigma, SRP0120) was incubated in the presence of 2.5 μM CHIP or CHIP mutants, 50 nM purified Ube1 (Boston Biochem, E305), 2.5 μM purified UbcH5c

(BostonBiochem, E2-627) and 0.25 μM ubiquitin (BostonBiochem, U100H) in 50 mM Tris pH 7.5, 600 μM DTT, 2.5 mM $MgCl_2$-ATP (BostonBiochem, B20) in a total volume of 10 μl for 1 h at 37°C. Samples were analyzed by 4-12% Bis-Tris SDS-PAGE and immunoblotting was performed with either anti-LKB1 (Santa Cruz, SC32245), anti-SIRT6 (Abcam, Ab62739) or anti-α-synuclein (Abcam, ab138501) antibodies.

Dynamic Light Scattering. The solution molecular weights of WT CHIP, K30A, H260Q and T246M point mutant CHIP were determined using size exclusion chromatography followed by multi-angle light scattering (SEC-MALS). The SEC-MALS system consisted of a GE Superdex 200 column connected to Wyatt DAWN HELEOS-II multi-angle light scattering instrument and a Wyatt T-Rex refractometer (Wyatt Technology, Santa Barbara, CA, USA). 100 μl of 0.5 mg/ml of each sample was loaded onto the column, and the light scattering and refractive index data were collected as the eluted samples passed through light scattering system. The molar masses of the samples eluting in various peaks were calculated from these data using ASTRA 6 software (Wyatt Technology).

Nuclear Magnetic Resonance Spectroscopy. Human WT and T246M U-box (amino acid residues 212-303) recombinant proteins were purified as previously described for WT CHIP U-box.[194] NMR spectra were recorded at 600 MHz (1H) and 20°C in buffer containing 20 mM HEPES (pH 7.5), 50 mM NaCl, and 1 mM DTT as previously described[194]. NMR data were processed with NMRPipe[195] and analyzed with SPARKY.[196]

Circular Dichroism Spectroscopy. CD spectra of WT and T246M U-box CHIP were collected as previously described[197] at 0.25 mg/mL and 15°C in 10 mM sodium phosphate pH 7.0 with 20

mM NaCl and 1 mM DTT. Tm for WT and T246M U-box CHIP was additionally determined by CD at 222 nm.

T247M mouse generation and off-target site mutation anaylsis. Guide RNA Cloning. Guide RNA protospacer (target) sequences were cloned into a T7 promoter vector in context with guide RNA structural elements, allowing T7-mediated *in vitro* transcription to produce the full guide RNA molecule. A guanine was added to the 5' end of protospacer sequences that do not have a native 5' guanine to allow T7 *in vitro* transcriptional initiation, which requires a 5' guanine residue. T7 ligation mixtures were transformed into Stellar competent cells. Miniprep DNA was sequence-verified.

Guide RNA In Vitro Transcription. Guide RNA plasmids were linearized by digestion with DraI, which cleaves at the end of the guide RNA sequence. Linearized material was purified by silica column (Qiaquick) and used as template for T7 *in vitro* transcription using the NEB HiScribe T7 kit. Reactions included 1000 ng linear guide RNA plasmid in a standard reaction recommended by the kit provider. Reactions were incubated at 37°C overnight followed by addition of DNAse I and 30 min additional incubation at 37°C to remove plasmid DNA. Guide RNAs were then purified using Qiagen RNEasy mini kit, eluted in 30 µl RNAse-free microinjection buffer (5 mM Tris-Cl pH7.5, 0.1 mM EDTA) and quantitated on a Nanodrop spectrophotometer.

Guide RNA Activity Test. The Cas9/guide RNA target region was PCR amplified from wild-type C57BL/6 DNA using primers Stub1-ScF1 (5'-GGAGACAGGAGTTGCCCACACA-3') and Stub1-ScR1 (5'- CAGTTCAGAACCCATCAGCAGG-3'). PCR product was purified on a silica minicolumn and eluted in 10 mM Tris-Cl pH8.5.

In Vitro Cleavage Assay. Guide RNAs were tested for activity in an *in vitro* cleavage assay, which included 1x NEB restriction buffer 3, 1 mg/ml BSA, 30 µg/ml Cas9 protein, 300 ng target DNA and 600 ng guide RNA in a 20 µl reaction volume. A control reaction was performed in parallel with all components except guide RNA. Reactions were incubated at 37°C 1 hr, 80°C 10 min, then 4°C until gel analysis. Reaction mixes were separated on 2% Agarose TAE gels with ethidium bromide and imaged using a standard ethidium bromide gel imaging system. Guide RNA Stub1-g82T (GAACCCTGCATTACACCCAGTGG, protospacer associated motif NGG underlined) produced nearly 100% target site cleavage and was selected for embryo microinjection to produce Stub1-T247M knock-in animals.

Mouse production. Genome editing was performed using CRISPR/Cas technology with the modification of mouse sequence NM_019719 at positions #740 and #741: A<u>CA</u>→A<u>TG</u>, resulting in change of Threonine247 to Methionine. Founder animals were produced by microinjection of C57BL/6J embryos with a mixture of 100 ng/ul Cas9 mRNA, 50 ng/ul Stub1 guide RNA g82T and 100 ng/ul donor oligonucleotide Stub1-T247M-T (5'-TGACTACTTGTGTGGCAAGATTAGCTTTGAGCTGATGCGGGAACCCTGCATTATGCCCAGTGGTATCACCTATGACCGCAAGGACATTGAGGAGCACCTGCAGGTAAG-3') in 5 mM Tris pH7.5, 0.1 mM EDTA. Injected embryos were surgically implanted in CD-1 pseudopregnant recipients and resulting pups were genotyped by PCR amplification of the Stub1 T246 region followed by Sanger sequencing. Animals harboring the Stub1 T246M codon change were identified by deconvolution of sequence traces. Founder animals were mated to wild-type C57BL/6J animals and F1 animals harboring the T246M mutation were intercrossed to generate homozygous animals.

Off-target analysis. For off-target analysis, guide RNAs were checked for predicted off-target sites using the web server crispr.mit.edu. The top 10 predicted off-target sites were PCR amplified from the founder biopsy DNA and PCR products were sequenced to detect the presence of mutations at each off-target site. Mutations were detected based on the presence of multiple peaks in the sequence traces.

Cell culture and transfection. $CHIP^{+/+}$, $CHIP^{-/-}$ and T247M CHIP mouse embryonic fibroblasts (MEFs) were cultured as previously described[74]. COS-7 and shCTRL and shCHIP HEK293 cells were maintained in Dulbecco's modified Eagle's medium (Invitrogen) supplemented with 10% fetal bovine serum (Sigma) at 37°C in an atmosphere of 5% CO_2. Cell transfections were performed using X-tremeGENE 9 (Roche) with the indicated plasmid DNA at a 1:3 DNA to X-tremeGENE 9 ratio.

iCelligence Population Doubling/Cell Proliferation/Viability. For determination of primary MEF growth rates, cells were plated on iCelligence E-Plates L8. Cell attachment, spreading, and proliferation were continuously monitored every 30 min for 72 hours using the iCELLigence System (Acea Biosciences). The electronic readout of cell-sensor impedance is displayed continuously in real time as the Cell Index (CI). The CI value at each time point is defined as Rn-Rb/Rb, where Rn is the cell-electrode impedance of the well with the cells, and Rb is the background impedance of the well with media alone. Population doubling was determined from the exponential phase of the growth curve and calculated using the iCELLigence RTCA software (Roche Applied Science) according to manufacturer's protocol. For determination of cell proliferation/viability of HEK293 cells in the presence of 200 µM H_2O_2 HEK293 cells stably depleted of CHIP or shCTRL were used as previously described.[87] Cells were plated in E-plates L8 at 40,000 cells/well and CI continuously monitored for the duration of the experiment. 24

hours later WT or T246M CHIP was reintroduced by transient transfection as described above. Cells were then exposed to 0 µM or 200 µM H_2O_2 for 24 hours beginning at 24 hours post-transfection. Delta cell index (Delta CI) was calculated as the change in cell index before and after exposure to 0 µM or 200 µM peroxide utilizing iCELLigence RTCA software as per manufacturer's instructions. For determination of cell proliferation/viability of WT, T247M and CHIP$^{-/-}$ primary MEFs in the presence of 500 µM H_2O_2 cells were plated in E-plates L8 at 30,000 cells/well and CI continuously monitored for the duration of the experiment. 24 hours post-plating, cells were exposed to 0 µM or 500 µM H_2O_2 for 24 h. Delta cell index (Delta CI) was calculated as the change in cell index before and after exposure to 0 µM or 500 µM peroxide utilizing iCELLigence RTCA software as per manufacturer's instructions.

mRNA analysis. CHIP mRNA levels in primary MEFs were determined using the SingleShot™ SYBR® Green Kit (Biorad, 1725085) and Roche LightCycler 480 with PrimePCR SYBR green primer assays targeting the indicated genes (Biorad) listed below. Relative expression values were calculated using the ΔCT method correcting for PCR efficiency and mean centered across the three genotypes. Expression was normalized to the geometric mean of Actb and Hprt, the two most stable reference genes across genotypes as determined via Normfinder[198] (also tested Gapdh and Tbp).

Table 4.3. qPCR Primers

Gene	*Biorad Assay ID*
Act	qMmuCED0027505
Gapdh	qMmuCED0027497
Hprt	qMmuCED0045738
Stub1	qMmuCED0001075
Tbp	qMmuCID0040542

Protein and mRNA isolation/analysis from mouse tissue. Liver, heart, brain and testes were isolated from anesthetized 4 month old WT, HET and T247M male littermates. Tissue was stored frozen in RNAlater solution (Ambion) until protein and mRNA were isolated using the Ambion PARIS Kit (Ambion, AM1921) as per manufacturer's instructions. Tissue disruption prior to protein/RNA isolation was performed with Ambion PARIS Kit Cell Disruption Buffer and Qiagen TissueLyser LT with 5 mm steel beads. Any contaminating DNA was removed from RNA prepared by PARIS Kit by treatment with TURBO DNA-free™ Kit (Ambion) and mRNA was reverse transcribed using Iscript cDNA synthesis kit (Bio-Rad). Real-time PCR was performed using Roche LightCycler 480 and Sso Advanced Universal SYBR Green Supermix (Biorad) with PrimePCR SYBR green primer assays targeting the indicated genes (Biorad) listed above. Relative expression values were calculated using the ΔCT method correcting for PCR efficiency and mean centered across the three genotypes. Expression was normalized to the geometric mean of Actb and Gapdh, the two most stable reference genes across genotypes as determined via Normfinder[198] (also tested Hprt and Tbp).

Cell lysate collection/nuclear fractionation/isolation of total, soluble and insoluble fractions. For all assays unless otherwise noted, cell lysates were prepared by first washing cells in cold PBS and lysing in Cell Lytic M (Sigma) containing 1X HALT protease/phosphatase inhibitor (Pierce) and 50 µM PR619 (Lifesensors). Lysates were clarified by centrifugation at 15,000 x g for 10 min at 4°C. Total protein concentration was determined by BCA protein assay (Pierce). Alternatively, cells were lysed on ice for 15 m in Triton X-100 cell lysis buffer (50 mM Tris, pH 7.4, 150 mM NaCl, 1% Triton X-100, 1mM EDTA, protease inhibitor [Complete; Roche], 50 µM PR-619 (LifeSensors)). Triton X-100 insoluble material was collected by solubilization of the insoluble pellet following 15,000 x g centrifugation by resuspension in 2X Laemmeli Sample

buffer (Biorad), brief sonication and heating for 5 m at 100°C. Nuclear fractions were prepared using the NE-PER kit (Pierce), as per manufacturer's instructions. Total, soluble and insoluble fractions as shown in Fig. 4.6 were prepared by first trypsinizing and counting P2 primary MEFs grown on 15-cm tissue-culture treated dishes to near 100% confluency. Cells were then divided equally between two tubes, spun at 500 x g, pellet rinsed in PBS and spun again at 500 x g. Cells for total protein fraction (tube 1) were then lysed in 2X Laemmeli SDS sample buffer (65mM Tris-HCl, 10% Glycerol, 2%SDS), sonicated briefly on ice and boiled at 100°C for 5 m. The cell pellet in tube 2 was then lysed for collection of soluble and insoluble fractions. This pellet was lysed in Triton X-100 cell lysis buffer as described above and soluble protein collected following centrifugation at 15,000 x g for 10 m at 4°C. The Insoluble pellet was then rinsed once in lysis buffer and spun again at 15,000 x g for 10 m at 4°C. The pellet was then solubilized in 2X Laemmeli SDS sample buffer (65mM Tris-HCl, 10% Glycerol, 2%SDS), sonicated briefly on ice and boiled at 100°C for 5 min. Total protein concentrations in each fraction were then determined by 660nm Protein Assay (Thermo Scientific) and samples of equal total protein prepared for SDS-PAGE by addition of final concentrations of 0.025% bromophenol blue and 100mM DTT.

Polyacrylamide gel electrophoresis, Blue native polyacrylamide gel electrophoresis, gel immunoblotting, and densitometry. For reduced and denatured conditions, protein samples were resolved on NuPAGE Novex® Bis-Tris Gels (Life Technologies) using the MOPS/LDS buffer system or Mini-PROTEAN® TGX Precast Gels (Bio-Rad) using the Tris/Glycine/SDS buffer. Native protein samples were resolved on 4-16% NativePAGE Novex® Gels (Life Technologies) using 0.001% G-250 cathode buffer. Proteins were transferred to PVDF membranes and incubated with primary antibodies overnight (see following table for antibody information) and

detected with either anti-rabbit or anti-mouse (GE Healthcare), or anti-goat (Sigma) HRP-conjugated antibodies and visualized with ECL Advance substrate (GE Healthcare) using the EC3™ Imaging System (UVP). For quantification of relative protein levels, densitometry analysis was performed using LI-COR Image Studio Lite.

Immunoprecipitation/Co-immunoprecipitation of FLAG-HSP70/CHIP, FLAG-SIRT6/CHIP, HA WT-CHIP/MYC T246M-CHIP from COS-7 cells. COS-7 cells were cultured and transiently transfected as described above with the indicated transgene vectors. 24 h post-transfection cells were treated with 20 μM MG132 or DMSO for 2.5 hours prior to harvest. Cells were washed in cold PBS and lysed in Cell Lytic M (Sigma) containing 1X HALT protease/phosphatase inhibitor (Pierce) and 50 μM PR619 (Lifesensors). Lysates were clarified by centrifugation at 15,000 x *g* for 10 min. Total protein concentration was determined by BCA protein assay (Pierce) and 1 mg total protein clarified lysate incubated overnight at 4°C with 20 μg of EZview™ Red ANTI-FLAG® M2, EZview™ Red ANTI-MYC® M2 or EZview™ Red ANTI-HA® M2 (Sigma). The gel was then washed 5 times with Tris-Buffered Saline with 0.5% Nonidet P-40; subsequently, proteins were eluted in reducing SDS-sample buffer and analyzed by SDS-PAGE and western blotting was performed using anti-FLAG HRP (Sigma, A8592), anti-HA HRP (Sigma, A6533) and anti-myc HRP (Sigma, A5598) antibodies.

Immunoprecipitation/Co-immunoprecipitation of UbcH5c/CHIP, AMPKα1/CHIP, Hsc70/CHIP from COS-7 cells or Primary MEFs. COS-7 cells were cultured and transiently transfected as described above with the indicated transgene vectors. Primary MEFs were cultured as previously described and plated in 2 15cm tissue culture dishes and incubated overnight under normal growth conditions. 24 h post-transfection (COS-7) or plating (Primary MEFs) cells were treated with 20 μM MG132 or DMSO for 2.5 h prior to harvest. Cells were washed 1X in cold PBS and

lysed in Cell Lytic M (Sigma) containing 1X HALT protease/phosphatase inhibitor (Pierce) and 50 μM PR619 (LifeSensors). Lysates were clarified by centrifugation at 15,000 x *g* for 10 min. Total protein concentration was determined by BCA protein assay (Pierce) and 1.5 mg total protein clarified lysates were incubated overnight at 4°C with 10 μg anti-UbcH5c (Cell Signaling Technologies, 4330S), anti-AMPKα1 (R and D Systems, AF3197), anti-CHIP (Abcam, ab4447), anti-Hsc70 (Enzo, ADI-SPA-815), rat IgG, rabbit IgG or goat IgG antibodies. 120 μl Protein-G Dynabeads (Invitrogen) were then added to each sample and incubated for 0.5 h at room temperature with rotation. Beads were washed four times with Phosphate-Buffered Saline with 0.05% Tween-20; subsequently, proteins were eluted in SDS-sample buffer and analyzed by SDS-PAGE and western blotting using anti-UbcH5c (Cell Signaling Technologies, 4330S), anti-CHIP (Sigma, S1073), anti-AMPKα1/2 (Cell Signaling Technologies, 2532) or anti-Hsc70 (Enzo, ADI-SPA 815) antibodies.

Myc-CHIP and endogenous CHIP Immunofluorescence: CHIP Immunofluorescence was performed as previously described[199] with the following modifications. Cells were fixed in 4% paraformaldehyde for 10 min, then incubated in permeabilization buffer (PBS, 0.5% Triton X-100, 1% BSA) for 10 min. Primary and secondary antibodies were prepared at dilutions of 1:500 (CHIP-Sigma HPA043531) or (anti-c-myc, Sigma M4439) and 1:800 (Alexa-Fluor Goat anti-rabbit or Goat anti-mouse), respectively, in blocking buffer (PBS, 0.05% Triton X-100, 1% BSA). Coverslips were mounted using Vectashield Hardset with Dapi (Vector Laboratories). Cells were visualized using a Zeiss LSM 710 spectral confocal.

HSF1 Luciferase Reporter Assay. COS-7 cells were cultured, plated at 5000cells/well in clear-bottom white 96-well plates (Thermo Scientific, 165306) and transiently transfected as described above with the indicated transgene vectors and the Qiagen Cignal Heat Shock Response Reporter

(luc) Kit (CCS4023L) as per manufacturer's instructions. 24 h post-transfection cells were lysed and luciferase assays were performed using a Dual-Luciferase® Reporter Assay System (Promega, Madison, WI) on a BMG Labtech CLARIOstar dual-injection plate reader following the manufacturer's protocol. Transfection of each construct was performed in triplicate in each assay and a total of 3 assays were performed on 3 separate days. Empty vector was transfected in each plate in triplicate to be used for normalization purposes. Ratios of Renilla luciferase readings to Firefly luciferase readings were taken for each experiment and triplicates were averaged. The average values of the tested constructs were normalized to the activity of the empty construct. Bars represent the averages of the normalized values with error bars indicating the range.

Cyclohexamide chase. COS-7 cells were co-transfected with the indicated vectors and 24 h post-transfection treated with 50 µg/ml cyclohexamide for 0, 1 or 2.5 h in the presence or absence of 20 µM proteasome inhibitor MG132 and lysates collected and separated by SDS-PAGE and immunoblotted with antibodies against His-CHIP and β-tubulin as described above. Primary MEFs were plated and incubated for 24 h under normal growth conditions. Cells were then treated with for 0, 2, 4 or 6 h with 50 µg/ml cyclohexamide and lysates collected and separated by SDS-PAGE and immunoblotted with antibodies against CHIP (ab4447) and β-tubulin as described above.

Heat Stress and Recovery. Two models of heat stress and recovery were utilized. For measures of heat stress/CHIP-induced nuclear translocation of HSF1 in COS-7 cells, cells were heat shocked in a water bath for 30 min at 42°C prior to lysate collection and nuclear fractionation as previously described.[74] For Hsp70 induction and recovery assays in primary T247M and WT

MEFs, cells were heat shocked in a water bath for 10 min at 42°C prior to recovery at 37°C under normal growth conditions for the indicated times.

AMPK in vitro *activity assay.* Recombinant proteins CHIP, CHIP point mutants and AMPKα2 in 20 mM HEPES pH 7.4 with 150 mM NaCl prepared as described above and as previously described [8] were diluted to final concentrations of 730nM (pAMPKα2) or 7 point 5X serial dilution curve starting from 2.8 µM in 1X kinase buffer A (50 mM HEPES pH7.5, 1 mM EGTA, 0.01%Brij-35 and 10mM $MgCl_2$) and pre-incubated together at 30°C for 30 min with gentle shaking. Invitrogen Z'-LYTE Kinase Assay Kit-Ser/Thr 23 Peptide was then utilized as per manufacturer's instructions to determine pAMPKα2 enzymatic activity in the presence of CHIP with each condition measured in triplicate in 3 independent assays.

Acute oxidative stress. WT and T247M Primary MEFs were exposed to 0, 200 or 400 µM H_2O_2 for 10 min under normal growth conditions as previously described[8] and lysates collected and separated by SDS-PAGE and immunoblotted with antibodies against pAMPKα1/2 –T172 (Cell Signaling Technologies, 4188) and total AMPK(Cell Signaling Technologies, 2532) as described above. Relative protein levels of phosphorylated AMPKα-T172 normalized to total AMPK are expressed as mean ± SEM from 3 independent experiments. *$P < 0.05$ via Dunnett's comparison to wild-type 0 µM H_2O_2 condition.

UVC Viability Assay. Fresh never frozen primary MEFs (P3) were plated at 5,000 cells/well in 96-well plates 24 h prior to treatment. Cells were then rinsed once with warm PBS and placed in 100 µl of warm PBS and placed uncovered under a UV lamp emitting primarily 254 nm radiation at a fluency rate 0 or 10J/m^2/s as previously described.[200] Cells were then placed back in normal growth media and allowed to recover for 20 hours under normal growth conditions

prior to measuring viability by Promega CellTiter 96® AQueous One Solution Cell Proliferation and Viability MTS assay.

Mouse behavioral assessments.

Table 4.4. Behavioral testing regimen

Age (weeks)	Procedure
7-8	Elevated plus maze test for anxiety-like behavior
	First wire-hang test for grip strength
8-9	First open field test (1 hour)
9-10	First and second rotarod tests for motor coordination
10-13	Social approach in a 3-chamber choice task
11-13	First marble-bury assay and acoustic startle test (index of sensorimotor gating)
12-14	Buried food test for olfactory ability
14-16	Conditioned fear (contextual and cue-dependent learning, first tests)
16-18	Retention test for conditioned fear (2 weeks following first test)
22 (5 months)	Third rotarod test
27-28	Fourth rotarod test
31	Fifth rotarod test, second wire-hang test
32	Second activity test, second marble-bury test
33	Second acoustic startle test

Table 4.5. Number of mice in study. Four mice were taken for histology following the first round of testing (before the third rotarod test).

	WT	HET	Mutant
First behavioral tests			
Male	7	9	5
Female	13	10	4
Follow-up tests			
Male	6	7	4
Female	13	10	4

Data analysis. For each procedure, measures were taken by an observer blind to mouse genotype (*CHIP* WT, HET, or mutant). Behavioral data were analyzed using one-way or repeated measures Analysis of Variance (ANOVA). Fisher's protected least-significant difference (PLSD) tests were used for comparing group means only when a significant F value was determined. For all comparisons, significance was set at $p < 0.05$. Data presented in figures and tables are means (± SEM).

Wire-hang test for grip strength. Mice were suspended from a cage lid for the maximum trial time of 60 sec.

Elevated plus maze for anxiety–like behavior. This procedure is based on a natural tendency of mice to actively explore a new environment, versus a fear of being in an open area. Mice were given one 5 min trial on the plus maze, which had two walled arms (the closed arms, 20 cm in height) and two open arms. The maze was elevated 50 cm from the floor, and the arms were 30 cm long. Animals were placed on the center section (8 cm x 8 cm), and allowed to freely explore the maze. Measures were taken of time on, and number of entries into, the open and closed arms

Marble-burying assay. Mice were tested in a Plexiglas cage located in a sound-attenuating chamber with ceiling light and fan. The cage contained 5 cm of corncob bedding, with 20 black glass marbles (14 mm diameter) arranged in an equidistant 5 x 4 grid on top of the bedding. Subjects were given access to the marbles for 30 min. Measures were taken of the number of buried marbles (two thirds of the marble covered by the bedding).

Buried food test for olfactory function. Several days before the olfactory test, an unfamiliar food (Froot Loops, Kellogg Co., Battle Creek, MI) was placed overnight in the home cages of the mice. Observations of consumption were taken to ensure that the novel food was palatable. Sixteen to twenty hours before the test, all food was removed from the home cage. On the day of the test, each mouse was placed in a large, clean tub cage (46 cm L x 23.5 cm W x 20 cm H), containing paper chip bedding (3 cm deep), and allowed to explore for 5 min. The animal was removed from the cage, and 1 Froot Loop was buried in the cage bedding. The animal was then returned to the cage and given 15 min to locate the buried food. Measures were taken of latency to find the food reward.

Open field test. Exploratory activity in a novel environment was assessed by a one-hour trial in an open field chamber (41 cm x 41 cm x 30 cm) crossed by a grid of photobeams (VersaMax system, AccuScan Instruments). Counts were taken of the number of photobeams broken during the trial in 5-min intervals, with separate measures for ambulation (total distance traveled) and rearing movements. Time spent in the center region of the open field was measured as an index of anxiety-like behavior. Mice were tested at two ages: 8-9 weeks and 32 weeks.

Rotarod. Subjects were tested for motor coordination and learning on an accelerating rotarod (Ugo Basile, Stoelting Co., Wood Dale, IL). For the first test session, animals were given 3 trials, with 45 seconds between each trial. Two additional trials were given 48 hours later. Rpm (revolutions per min) was set at an initial value of 3, with a progressive increase to a maximum of 30 rpm across 5 min (the maximum trial length). Measures were taken for latency to fall from the top of the rotating barrel. Additional tests (2 trials per test) were conducted at 3 other time points during the behavioral study.

Sociability in a 3-chamber choice test. Mice were evaluated for the effects of *Chip* deficiency on social preference. The test session consisted of 3 10-min phases: a habituation period, a test for sociability, and a test for social novelty preference. For the sociability assay, mice were given a choice between being in the proximity of an unfamiliar conspecific ("stranger 1"), versus being alone. In the social novelty phase, mice were given a choice between the already-investigated stranger 1, versus a new unfamiliar mouse ("stranger 2"). The social testing apparatus was a rectangular, 3-chambered box fabricated from clear Plexiglas. Dividing walls had doorways allowing access into each chamber. An automated image tracking system (Noldus Ethovision) provided measures of entries and duration in each side of the social test box, as well as time in spent within 5 cm of the Plexiglas cages (the cage proximity zone).

At the start of the test, the mouse was placed in the middle chamber and allowed to explore for 10 min, with the doorways into the two side chambers open. After the habituation period, the mouse was enclosed in the center compartment of the social test box, and an unfamiliar, sex-matched C57BL/6J mouse (stranger 1) was placed in one of the side chambers.

The stranger mouse was enclosed in a small Plexiglas cage drilled with holes, which allowed nose contact, but prevented fighting. An identical empty Plexiglas cage was placed in the opposite side of the chamber. Following placement of the stranger and the empty cage, the doors were re-opened, and the subject was allowed to explore the entire social test box for 10 min. Measures were taken of the amount of time spent in each chamber and the number of entries into each chamber by the automated tracking system. At the end of the sociability phase, stranger 2 was placed in the empty Plexiglas container, and the test mouse was given an additional 10 min to explore the social test box.

Acoustic startle and prepulse inhibition. This procedure was used to assess auditory function, reactivity to environmental stimuli, and sensorimotor gating. The test was based on the reflexive whole-body flinch, or startle response, that follows exposure to a sudden noise. Measures were taken of startle magnitude and prepulse inhibition, which occurs when a weak prestimulus leads to a reduced startle in response to a subsequent louder noise. Mice were tested at two ages: 11-13 weeks and 33 weeks.

For each test, mice were placed into individual small Plexiglas cylinders within larger, sound-attenuating chambers. Each cylinder was seated upon a piezoelectric transducer, which allowed vibrations to be quantified and displayed on a computer. The chambers included a ceiling light, fan, and a loudspeaker for the acoustic stimuli. Background sound levels (70 dB) and calibration of the acoustic stimuli were confirmed with a digital sound level meter (San Diego Instruments). Each session consisted of 42 trials that began with a 5-min habituation period. There were 7 different types of trials: the no-stimulus trials, trials with the acoustic startle stimulus (40 msec; 120 dB) alone, and trials in which a prepulse stimulus (20 msec; either 74,

78, 82, 86, or 90 dB) occurred 100 ms before the onset of the startle stimulus. Measures were taken of the startle amplitude for each trial across a 65-msec sampling window, and an overall analysis was performed for each subject's data for levels of prepulse inhibition at each prepulse sound level (calculated as 100 - [(response amplitude for prepulse stimulus and startle stimulus together / response amplitude for startle stimulus alone) x 100].

Fear conditioning. Mice were evaluated for learning and memory in a conditioned fear test, using the Near-Infrared image tracking system (MED Associates, Burlington, VT). The procedure had the following phases: training on Day 1, a test for context-dependent learning on Day 2, and a test for cue-dependent learning on Day 3. Follow-up tests for retention of learning were conducted 2 weeks later.

Training. On Day 1, each mouse was placed in the test chamber, contained in a sound-attenuating box, and allowed to explore for 2 min. The mice were then exposed to a 30-sec tone (80 dB), followed by a 2-sec scrambled foot shock (0.4 mA). Mice received 2 additional shock-tone pairings, with 80 sec between each pairing.

Context- and cue- dependent learning. On Day 2, mice were placed back into the original conditioning chamber for a test of contextual learning. Levels of freezing (immobility) were determined across a 5-min session. On Day 3, mice were evaluated for associative learning to the auditory cue in another 5-min session. The conditioning chambers were modified using a Plexiglas insert to change the wall and floor surface, and a novel odor (dilute vanilla flavoring) was added to the sound-attenuating box. Mice were placed in the modified chamber and allowed to explore. After 2 min, the acoustic stimulus (an 80 dB tone) was presented for a 3-min period. Levels of freezing before and during the stimulus were obtained by the image tracking system.

Two weeks following each test, mice were given second tests to evaluate retention of context- and cue- dependent learning.

Study approval. All animal procedures were approved by the Institutional Animal Care and Use Committee of The University of North Carolina at Chapel Hill.

CHAPTER V

CONCLUSIONS AND FUTURE DIRECTIONS

Throughout the lifetime of an organism all cells must respond to changes in their environment, including a plethora of physiologic and pathologic stresses, in order to maintain homeostasis and survive. Protein homeostasis is particularly critical to cell survival because of the central role proteins play in so many cellular processes. Both under basal conditions and in response to stress, cells utilize multiple highly specialized and integrated methods of PQC to ensure that proteins are appropriately folded and terminally misfolded proteins are eliminated to prevent proteotoxicity. This is particularly crucial to post-mitotic organs such as the heart and brain, with their very limited capacity for self-renewal. PQC depends on an elegant collaboration between molecular chaperones and the ubiquitin-proteasome system (UPS). Disruption of PQC and subsequent proteotoxicity has long been considered an underlying molecular phenotype in disease pathologies in the brain and is being increasingly recognized as such in disease pathologies in the heart as well. Using a multifaceted approach, we focused on understanding the molecular mechanisms underlying diseases where disruption of PQC is central to disease pathology. Specifically, we focused on understanding the function of E3 ubiquitin ligases and how mutations in these key players in the UPS can drive disease pathology in the heart and brain. Chapter II described and validated a novel method for the identification of E3 ubiquitin ligase substrates addressing a significant technological limitation in the field. In Chapter III, I described

the first discovery of human mutation in the E3 ubiquitin ligase, CHIP in a form of spinocerebellar ataxia, Gordon Holmes Syndrome, that has led to the establishment of a new disease designation, SCAR16 to describe spinocerebellar ataxia caused by homozygous or compound heterozygous mutation in CHIP. In Chapter IV, I expanded upon this discovery to define the structural and functional consequences of CHIP mutation in SCAR16 and explored the deficits associated with this mutation in a genomic context utilizing a mouse model system providing the first definition of partial CHIP dysfunction and assignment of specific *in vivo* deficits that result as a consequence of partial but not total loss of CHIP function. In this chapter, I will consider how these observations can guide future investigations.

E3 Ubiquitin Ligase Substrate Identification

In Chapter II, we described a novel method for the identification of E3 ubiquitin ligase substrates. The development of this methodology addresses a significant gap in our ability to study these key PQC components as existing methods to identify their substrates have relied heavily upon non-physiologic *in vitro* methods, impeding the unbiased discovery of physiological substrates in relevant model systems. In order to validate this methodology, we utilized it to identify physiological substrates of MuRF1 in cardiomyocytes. MuRF1 has recently been shown to be an important regulator of mitochondrial function *in vivo*[201]. Not only did this work validate our methodology, but also identified several very intriguing MuRF1 substrates, including mitochondrial proteins Hspd1 and Atp5b. MuRF1has been shown both *in vitro* and *in vivo* to be cardioprotective in models of global ischemia-reperfusion injury, and given the pivotal role of mitochondria in ischemia-reperfusion injury, further characterization of MuRF1

regulation of these novel substrates in mitochondria may provide important mechanistic clues towards this dramatic cardioprotection.

With the robust, flexible nature of the protocol we have described in Chapter II, we are hopeful that this method can be easily adapted to fit the needs, technical expertise and resource availability of many users. For example, due to the limitations of 2D-DIGE/MALDI-TOF as discussed in Chapter II, with minimal modification this method could be used with gel-free quantitative proteomics strategies such Tandem Mass Tags (TMT) or Isobaric Tags for Relative and Absolute Quantification (iTRAQ) to identify and quantitate proteins in each of the collected eluate and supernatant samples.[125] Furthermore, it is our hope that this protocol will be broadly applied to the study of both ubiquitin ligases and DUBs. In fact, applying this methodology to the identification of novel CHIP substrates, particularly in the cerebellum, could provide important mechanistic understanding of the underlying drivers of SCAR16 disease pathology.

CHIP in SCAR16

In Chapters III and IV we reported the first discovery of CHIP mutation in GHS (T246M), which led to the SCAR16 disease designation and began to elucidate the biophysical and functional consequences of CHIP mutation in SCAR16 *in vitro*, in cells and *in vivo*. In Chapter III and IV, it was determined that T246M point mutation results in loss of CHIP ubiquitin ligase activity that is likely a result of dramatic destabilization and misfolding of the CHIP U-box that results in a loss of CHIP's ability to form dimers and promotes the formation of large, multimeric CHIP aggregates both *in vitro* and in cells. The CHIP mutations that have been associated with SCAR16 are present in all three of CHIP's functional domains and there is great clinical heterogeneity within SCAR16 disease. Therefore, the extension of the biophysical, structural and *in vitro* studies to include additional SCAR16 CHIP mutations both within the U-

box domain and elsewhere will provide valuable insight into the structure-function relationship. This will allows us to better understand how mutations across multiple structural domains may uniquely affect CHIP function but result in the same disease. Importantly, this provides insights in how these structural and resulting functional changes may directly correlate to specific aspects of the disease phenotype to result in the observed clinical heterogeneity.

In Chapter IV, we observed that T246M CHIP is prone to aggregation and likely in an attempt to prevent the accumulation of insoluble toxic aggregates the turnover of this protein is dramatically increased relative to WT CHIP. Furthermore, we observed that the expression of soluble T246M CHIP in primary MEFs and across multiple tissues is dramatically reduced, in part through a proteasome-dependent mechanism. However, inhibition of the proteasome only partially blocks this turnover of T246M CHIP, suggesting other cellular mechanisms are at work to remove this damaged protein before its accumulation becomes damaging to the cell. We do not believe this is unique to T246M CHIP mutation. Of the many mutations associated with SCAR16, only one is a truncating mutation, and we can assume that in the majority of these cases the mutated CHIP protein is also being translated and then must be cleared by the cell. In fact, similar to what we observed with T246M mutation in our mouse model, in another reported case of SCAR16, soluble mutant CHIP protein expression was also dramatically reduced in primary patient fibroblasts.[184] Autophagy is one possible mechanism known to clear protein aggregates and has even been shown to be activated to clear ubiquitinated proteins in a compensatory manner when the UPS cannot meet the proteolytic demands of the cell.[202] Evaluating the turnover of T246M CHIP in primary MEFs in the presence of autophagy inhibitor bafilomycin as well as evaluating markers of autophagy such as LC-3 and p62 would allow us to

further understand the molecular mechanisms the cell is utilizing to eliminate this damaging protein.

In Chapters III and IV, we determined that T246M mutation results in the loss of CHIP ubiquitin ligase activity while retaining the ability to function in some of CHIP's critical cellular roles in PQC as a co-chaperone and as an autonomous chaperone promoting the phosophorylation and potentiating the activity of AMPK, protecting cells from oxidative stress. Importantly, while T246M CHIP retains co-chaperone activities, binding chaperone proteins and inducing HSF1 nuclear translocation and Hsp70 expression following stress, both chaperone binding and the induction of Hsp70 are enhanced. This suggests that while it remains partially intact ,T246M mutation may alter normal CHIP-mediated regulation of the chaperone-mediated stress response in a deleterious manner. These data and our findings in our analysis of behavioral deficits in the T246M mice demonstrate that T246M mutation is not equivalent to total loss of CHIP. In order to better understand this distinction at a molecular mechanistic level, we performed preliminary protein microarray studies comparing protein expression and phosphorylation of over 800 proteins in lysates from primary WT, CHIP$^{-/-}$ and T246M MEFs.

While there was a subset of overlapping changes in protein expression and phosphorylation, the majority of detectable changes relative to WT cells were unique to total loss of CHIP or T246M CHIP point mutation. This supports our functional data that total loss of CHIP and T246M mutation are not equivalent and suggests that, in fact, this can be dissected down to the level of protein expression and cell signaling. Validation of the protein changes identified in this preliminary study as well as additional protein microarray studies comparing genotypes in the context of different cellular stresses would provide valuable insight into important cellular signaling pathways that contribute to T246M disease pathology. Particularly

evaluating the changes in cell signaling following oxidative stress and UVC-induced damage, where we have observed functional differences between total loss of CHIP and T246M CHIP would provide insight into the distinct molecular mechanisms that underlie this difference in phenotype. Furthermore, exploring the key signaling pathways uniquely affected by T246M CHIP mutation both under basal conditions and during stress has the potential to provide additional downstream therapeutic targets for modulation of SCAR16 disease.

In Chapters III and IV, we demonstrated that CHIP$^{-/-}$ mice have behavioral and reproductive impairments that mimic some of the clinical features of SCAR16. However, these mice do not directly phenocopy the diverse disease heterogeneity in SCAR16, leading us to establish a point mutant mouse model (T247M) that mimics the human mutation in order to study the *in vivo* repercussions of T246M CHIP. We observed behavioral deficits attributable to cognitive cerebellar dysfunction not observed in our total loss of CHIP animal model, as well as deficits in learning and memory attributable to hippocampal dysfunction that are reflective of cognitive deficits reported in SCAR16 patients. We concluded that T246M mutation is not equivalent to total loss of CHIP, and that specific CHIP mutations in SCAR16 likely have varying biophysical and functional consequences to CHIP that may directly correlate to clinical phenotype. Surprisingly, testing of these mice at ages up to 31 weeks did not reveal significant motor impairment in the accelerating rotarod test indicative of cerebellar ataxia as a result of T246M mutation. We hypothesize that this may be a strain-dependent effect, as even the WT mice are particularly skilled at this task and other studies have suggested strong strain-dependence in the ability of the mice to perform this task and consequently to detect deficits by this measure.[185, 203] Additionally, variable age of onset of motor deficits has been reported previously in additional mouse models of cerebellar degenerative disorders.[186] For these reasons,

retesting of our animals at a more advanced age as well as performing additional measures of motor dysfunction including the parallel rod floor test reported to have significantly less strain-dependence[204] will allow us to determine with confidence the presence or absence of cerebellar ataxia in the T246M mouse model.

In Chapter III, we observed motor dysfunction in CHIP$^{-/-}$ mice as well as cellular loss throughout the various lobes of the cerebellum, specifically in the Purkinje cell layer with noticeable degeneration, mimicking the observation of Purkinje cell loss identified in the neuropathological analysis in a deceased GHS patient with disordered ubiquitination (*RNF216* and *OTUD4* mutations). [136] Together, these data suggest CHIP is required for cerebellar maintenance. In Chapter IV, we described behavioral deficits attributable to cognitive cerebellar dysfunction in our T246M mouse model, many of which unique to this model and not present in our total loss of CHIP animal model. In order to fully appreciate the distinction between T246M CHIP mutation and total loss of CHIP, as well better understand the molecular mechanisms underlying SCAR16 disease pathophysiology, a careful analysis of brain pathology should accompany the behavioral analysis we have already performed. These studies would include longitudinal MRI studies to assess progressive cerebellar atrophy in T246M mice as well as histological staining of the cerebellum using hematoxylin and eosin stain to detect morhphological changes. Additionally, they would include immunohistochemical staining of the cerebellum for CHIP to evaluate CHIP expression and localization, calbindin staining to evaluate Purkinje cell health, morphology and abundance and Congo red staining to evaluate for signs of proteotoxic protein aggregation. Given our observation of additional functional deficits in the T246M mice attributable to other brain regions, such as deficits in learning and memory related to hippocampal dysfunction and reports of similar deficits in SCAR16 patients, these studies may

be extended to other brain regions including the hippocampus as well in order to determine whether observed changes in brain pathology as a result of T246M mutation occur similarly throughout affected brain regions and/or whether these changes directly correlate to functional deficits. Careful and thorough analysis of the brain pathology associated with T246M mutation in mice and the accompanying behavioral deficits would not only provide important mechanistic clues into disease pathology but also provide validation of this model for use in the development of SCAR16 therapies and may suggest important study endpoints for the preclinical validation of these future clinical candidates.

In Chapter III, we observed that CHIP$^{-/-}$ mice recapitulate many of the reproductive impairments characteristic of GHS. Within the spectrum of disease phenotypes represented by SCAR16, patients with GHS represent a unique group where cerebellar ataxia characteristic of SCAR16 is paired with neuroendocrine deficits and resulting reproductive impairments associated with hypogonadism. While developing the T247M mouse model and establishing the mouse colony, we have observed impaired breeding of T247M homozygous mice. Additionally, preliminary hormonal studies of male T247M mice suggest abnormal circulating hormone levels and an impairment of the pituitary's ability to respond to stimulation with gonadotropin releasing hormone (GnRH), similar to that observed in hypogonadism associated with GHS (data not shown). Future studies to characterize the neuroendocrine deficits and reproductive impairments associated with T246M, both by comparison to the CHIP$^{-/-}$ animals as well as to additional SCAR16 point mutant mice, would have the potential to allow us to delineate the contribution of particular CHIP functions to this unique disease phenotype within the SCAR16 disease spectrum. In order to fully assess neuroendocrine deficits and reproductive impairments associated with T246M in mice, these studies would include measurements of circulating

hormone levels of the hypothalamic-pituitary axis, including lutenizing hormone, follicle stimulating hormone, testosterone, estrogen and progesterone, assessment of pituitary function by GnRH stimulation test, pathological and morphological evaluation of the pituitary and sex organs, including immunohistochemical staining for CHIP expression and localization, and observation and quantitation of reproductive patterns of these mice. Together these studies would bring to light the neuroendocrine deficits and reproductive impairments associated with T246M mutation in mice and begin to describe an as-yet unexplored aspect of CHIP biology in hormonal signaling, pituitary function and reproductive health.

In Chapters III and IV, we report neurobehavioral deficits associated with total loss of CHIP and T246M mutation in mice. However, importantly previous studies of CHIP$^{-/-}$ mice have revealed significant cardiac deficits in multiple models of cardiac disease as well as dramatically reduced longevity and stress-intolerance as a result of genetic depletion of CHIP.[8, 83-87, 155] While the studies presented in Chapters III and IV highlight the importance of fully functional CHIP protein in the brain, these previous reports also strongly suggest the particular importance of CHIP as a regulator of PQC in the heart and elsewhere. Studying the T246M mice in the context of cardiac disease and stress models as well as evaluating their longevity would allow us to more fully characterize this model in terms of our existing knowledge of CHIP biology, as well as gain further insight into SCAR16 disease pathology. Furthermore, in Chapter IV, we determined that T246M CHIP's E3 ubiquitin ligase activity towards a variety of substrates is completely abolished, but T246M CHIP retains the ability to function in some of CHIP's critical cellular roles in PQC as a co-chaperone and as an autonomous chaperone towards AMPK. Thus, by direct comparison of results observed with T246M mice in cardiac disease models and other models of stress to those observed with total genetic depletion of CHIP would provide a unique

opportunity to a unique opportunity to delineate the contribution of co-chaperone, ubiquitin ligase activity and other emerging CHIP activities to these specific deficits observed *in vivo* in a disease-relevant context.

Implications for SCAR16 therapeutics

Recently there has been increasing interest in modulation of the UPS as a therapeutic strategy to treat many disease indications, particularly neurodegeneration, cancer and immunological disorders, and some clinical success in doing so. In Chapters III and IV, we defined T246M as a causative mutation in SCAR16 and began to uncover the underlying structural and functional changes in CHIP that result from its mutation and serve as the molecular drivers of SCAR16 disease pathogenesis. Furthermore, we established and evaluated neurobehavioral deficits of a mouse model of human CHIP mutation in SCAR16. This biophysical, cellular and *in vivo* characterization of T246M mutation in SCAR16 provides valuable insight required for the development of effective therapies for this devastating degenerative disease.

Central to any successful therapeutic development process is the identification of druggable therapeutic targets. The data we have presented in Chapters III and IV clearly validate CHIP as a driver of SCAR16 disease pathogenesis and suggest that loss of CHIP ubiquitin ligase activity as a consequence of structural misfolding of the U-box domain is central to disease. In light of this, one potential therapeutic strategy would be the direct modulation of mutant CHIP to prevent the disorganization of the U-box domain and restore CHIP ubiquitin ligase activity. Crispr-mediated gene editing is being increasingly utilized pre-clinically and is actively being developed for use therapeutically in humans. Application of this technology is particularly

attractive for SCAR16, as it would provide a mechanism to restore normal CHIP sequence at the genomic level, restoring normal CHIP protein expression and function and could be done early in disease before significant degeneration occurs potentially curing and at the very least halting disease progression.

While repairing the disease-causing CHIP mutation is ideal, many hurdles still exist before this technology is likely to be successfully applied in humans. In the meantime, our data suggests other strategies for modulating CHIP activity as well. In Chapter IV, we demonstrated that T246M mutation results in only partial loss of CHIP function, such that while ubiquitin ligase function is completely lost, many of CHIP's other integral cellular functions remain intact. If SCAR16 disease is largely driven by loss of CHIP ubiquitin ligase function as this suggests, then activating CHIP ubiquitin ligase activity may be sufficient to prevent disease. Thus, activating CHIP ubiquitin ligase activity, independent of CHIP itself, may be a viable strategy to treat SCAR16. In terms of specific therapeutic targets, this could include the activation of other E3 ubiquitin ligases that could ubiquitinate CHIP substrates in a compensatory manner. Identification of disease relevant CHIP substrates utilizing methodology as described in Chapter II would likely aid in this pursuit.

Activation of other E3 ubiquitin ligases may not represent the only path to modulating CHIP without directly targeting CHIP. Utilizing a whole-genome cDNA overexpression and/or siRNA screening strategy to identify other genes that when overexpressed or depleted rescue the phenotype associated with T246M mutation (for example, UVC-induced cell death) would be a useful approach to begin to identify additional therapeutic targets. Furthermore, additional protein microarray studies comparing the protein expression and phosphorylation profile of T246M expressing cells to WT cells both under basal conditions and during stress has the

potential to provide additional downstream therapeutic targets for modulation of SCAR16 disease. Extending these studies to identify changes in protein expression in the cerebellums of T247M mice relative to wildtype mice by SILAC studies may also provide valuable *in vivo* cerebellum-specific therapeutic targets. By these efforts targets may even be identified for which clinically approved or pre-clinical well-validated specific chemical entities already exist that can be applied to this novel disease indication.

Our understanding of CHIP and its role in SCAR16 disease pathogenesis as detailed in this thesis is ongoing, yet the data presented here represents validation of CHIP's importance in human disease and makes great strides towards explaining the molecular mechanisms underlying SCAR16 disease pathology. Interestingly, it highlights similarities but also some distinct and likely clinically relevant differences between total and partial loss of CHIP function (Fig. 5.1), deepening both our basic understanding of CHIP biology and SCAR16 and potentially guiding future therapeutic strategies. More broadly, this work extends our understanding of the UPS and its role in disease pathogenesis that will undoubtedly drive successful investment, innovation, preclinical investigation and clinical study design to treat patients suffering from not only SCAR16 but many other devastating diseases.

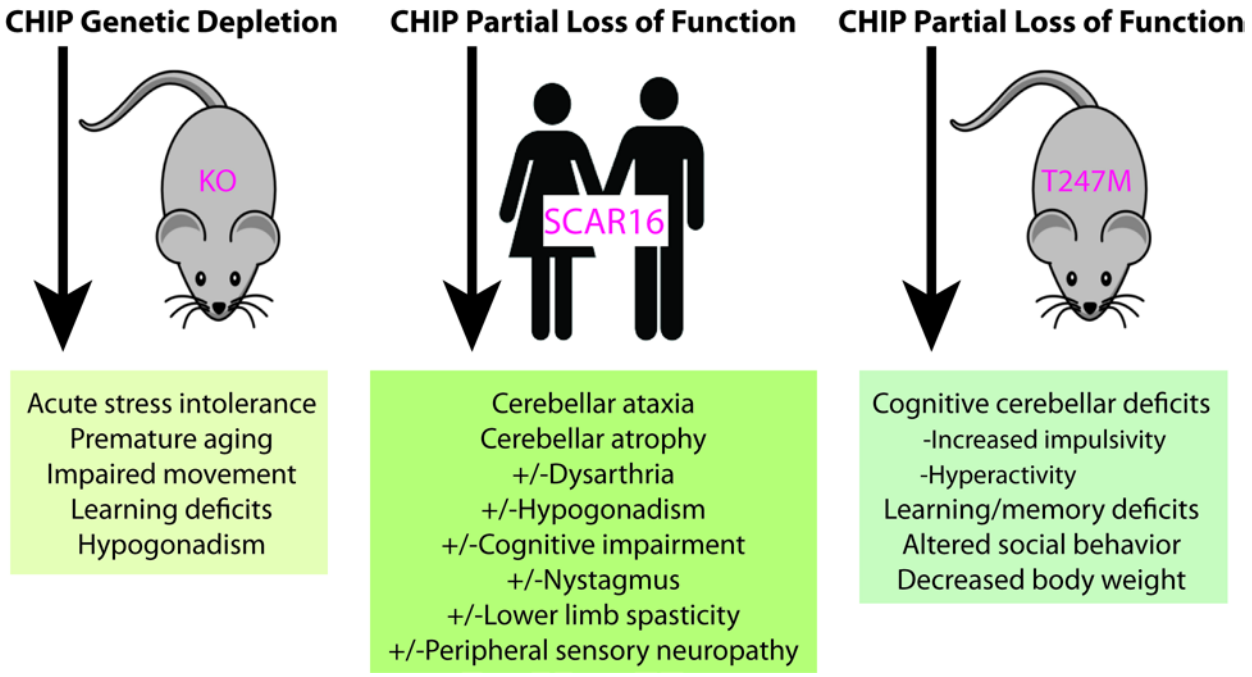

Figure 5.1. Phenotypic effects of total vs. partial loss of CHIP function in humans and mice.

A. The effects of CHIP genetic depletion in the CHIP KO mouse model (left), clinical phenotype of humans with SCAR16 CHIP partial loss of function mutations (center) and the effects of CHIP partial loss of function in the T247M mouse model (right).

REFERENCES

1. Willis MS, Patterson C. Proteotoxicity and cardiac dysfunction--alzheimer's disease of the heart? *N Engl J Med*. 2013;368:455-464

2. El-Agnaf OM, Mahil DS, Patel BP, Austen BM. Oligomerization and toxicity of beta-amyloid-42 implicated in alzheimer's disease. *Biochem Biophys Res Commun*. 2000;273:1003-1007

3. Eisele YS, Monteiro C, Fearns C, Encalada SE, Wiseman RL, Powers ET, Kelly JW. Targeting protein aggregation for the treatment of degenerative diseases. *Nat Rev Drug Discov*. 2015

4. Seidel K, Meister M, Dugbartey GJ, Zijlstra MP, Vinet J, Brunt ER, van Leeuwen FW, Rub U, Kampinga HH, den Dunnen WF. Cellular protein quality control and the evolution of aggregates in spinocerebellar ataxia type 3 (sca3). *Neuropathol Appl Neurobiol*. 2012;38:548-558

5. Sandri M, Robbins J. Proteotoxicity: An underappreciated pathology in cardiac disease. *J Mol Cell Cardiol*. 2014;71:3-10

6. Zheng H, Tang M, Zheng Q, Kumarapeli AR, Horak KM, Tian Z, Wang X. Doxycycline attenuates protein aggregation in cardiomyocytes and improves survival of a mouse model of cardiac proteinopathy. *J Am Coll Cardiol*. 2010;56:1418-1426

7. Mitchell SL. Clinical practice. Advanced dementia. *N Engl J Med*. 2015;372:2533-2540

8. Schisler JC, Rubel CE, Zhang C, Lockyer P, Cyr DM, Patterson C. Chip protects against cardiac pressure overload through regulation of ampk. *The Journal of clinical investigation*. 2013;123:3588-3599

9. Dickey CA, Patterson C, Dickson D, Petrucelli L. Brain chip: Removing the culprits in neurodegenerative disease. *Trends Mol Med*. 2007;13:32-38

10. Hill JA, Olson EN. Cardiac plasticity. *New England Journal of Medicine*. 2008;358:1370-1380

11. Vabulas RM, Hartl FU. Protein synthesis upon acute nutrient restriction relies on proteasome function. *Science (New York, N.Y.)*. 2005;310:1960-1963

12. McLendon PM, Robbins J. Desmin-related cardiomyopathy: An unfolding story. *Amer J Physiol Heart Circ Physiol*. 2011;301:H1220-H1228

13. Goldfarb LG, Park KY, Cervenakova L, Gorokhova S, Lee HS, Vasconcelos O, Nagle JW, Semino-Mora C, Sivakumar K, Dalakas MC. Missense mutations in desmin associated with familial cardiac and skeletal myopathy. *Nature genetics*. 1998;19:402-403

14. Vicart P, Caron A, Guicheney P, Li Z, Prevost MC, Faure A, Chateau D, Chapon F, Tome F, Dupret JM, Paulin D, Fardeau M. A missense mutation in the alphab-crystallin chaperone gene causes a desmin-related myopathy. *Nature genetics*. 1998;20:92-95

15. Wang X, Osinska H, Dorn GW, 2nd, Nieman M, Lorenz JN, Gerdes AM, Witt S, Kimball T, Gulick J, Robbins J. Mouse model of desmin-related cardiomyopathy. *Circulation*. 2001;103:2402-2407

16. Wang X, Osinska H, Klevitsky R, Gerdes AM, Nieman M, Lorenz J, Hewett T, Robbins J. Expression of r120g-alphab-crystallin causes aberrant desmin and alphab-crystallin aggregation and cardiomyopathy in mice. *Circulation research*. 2001;89:84-91

17. Moore DJ, Dawson VL, Dawson TM. Role for the ubiquitin-proteasome system in parkinson's disease and other neurodegenerative brain amyloidoses. *Neuromolecular Med*. 2003;4:95-108

18. Mann DM. The pathogenesis and progression of the pathological changes of alzheimer's disease. *Ann Med*. 1989;21:133-136

19. Gottfries CG. Alzheimer's disease. A critical review. *Compr Gerontol C*. 1988;2:47-62

20. Ward SM, Himmelstein DS, Lancia JK, Binder LI. Tau oligomers and tau toxicity in neurodegenerative disease. *Biochem Soc Trans*. 2012;40:667-671

21. Uversky VN. Neuropathology, biochemistry, and biophysics of alpha-synuclein aggregation. *J Neurochem*. 2007;103:17-37

22. Williams A, Sarkar S, Cuddon P, Ttofi EK, Saiki S, Siddiqi FH, Jahreiss L, Fleming A, Pask D, Goldsmith P, O'Kane CJ, Floto RA, Rubinsztein DC. Novel targets for huntington's disease in an mtor-independent autophagy pathway. *Nat Chem Biol*. 2008;4:295-305

23. Keller JN, Huang FF, Markesbery WR. Decreased levels of proteasome activity and proteasome expression in aging spinal cord. *Neuroscience*. 2000;98:149-156

24. Dantuma NP, Lindsten K. Stressing the ubiquitin-proteasome system. *Cardiovasc Res*. 2010;85:263-271

25. Yang S, Liu T, Li S, Zhang X, Ding Q, Que H, Yan X, Wei K, Liu S. Comparative proteomic analysis of brains of naturally aging mice. *Neuroscience*. 2008;154:1107-1120

26. Tydlacka S, Wang CE, Wang X, Li S, Li XJ. Differential activities of the ubiquitin-proteasome system in neurons versus glia may account for the preferential accumulation of misfolded proteins in neurons. *J Neurosci*. 2008;28:13285-13295

27. Gregori L, Fuchs C, Figueiredo-Pereira ME, Van Nostrand WE, Goldgaber D. Amyloid beta-protein inhibits ubiquitin-dependent protein degradation in vitro. *J Biol Chem*. 1995;270:19702-19708

28. Snyder H, Mensah K, Theisler C, Lee J, Matouschek A, Wolozin B. Aggregated and monomeric alpha-synuclein bind to the s6' proteasomal protein and inhibit proteasomal function. *J Biol Chem*. 2003;278:11753-11759

29. Lindersson E, Beedholm R, Hojrup P, Moos T, Gai W, Hendil KB, Jensen PH. Proteasomal inhibition by alpha-synuclein filaments and oligomers. *J Biol Chem*. 2004;279:12924-12934

30. Kristiansen M, Deriziotis P, Dimcheff DE, Jackson GS, Ovaa H, Naumann H, Clarke AR, van Leeuwen FW, Menendez-Benito V, Dantuma NP, Portis JL, Collinge J, Tabrizi SJ. Disease-associated prion protein oligomers inhibit the 26s proteasome. *Mol Cell*. 2007;26:175-188

31. Tai HC, Serrano-Pozo A, Hashimoto T, Frosch MP, Spires-Jones TL, Hyman BT. The synaptic accumulation of hyperphosphorylated tau oligomers in alzheimer disease is associated with dysfunction of the ubiquitin-proteasome system. *Am J Pathol*. 2012;181:1426-1435

32. Matos CA, de Macedo-Ribeiro S, Carvalho AL. Polyglutamine diseases: The special case of ataxin-3 and machado-joseph disease. *Prog Neurobiol*. 2011;95:26-48

33. Vives-Bauza C, Przedborski S. Mitophagy: The latest problem for parkinson's disease. *Trends Mol Med*. 2011;17:158-165

34. Yoshii SR, Kishi C, Ishihara N, Mizushima N. Parkin mediates proteasome-dependent protein degradation and rupture of the outer mitochondrial membrane. *J Biol Chem*. 2011;286:19630-19640

35. Tanaka A, Cleland MM, Xu S, Narendra DP, Suen DF, Karbowski M, Youle RJ. Proteasome and p97 mediate mitophagy and degradation of mitofusins induced by parkin. *J Cell Biol*. 2010;191:1367-1380

36. Winborn BJ, Travis SM, Todi SV, Scaglione KM, Xu P, Williams AJ, Cohen RE, Peng J, Paulson HL. The deubiquitinating enzyme ataxin-3, a polyglutamine disease protein, edits lys63 linkages in mixed linkage ubiquitin chains. *J Biol Chem*. 2008;283:26436-26443

37. Scaglione KM, Zavodszky E, Todi SV, Patury S, Xu P, Rodriguez-Lebron E, Fischer S, Konen J, Djarmati A, Peng J, Gestwicki JE, Paulson HL. Ube2w and ataxin-3 coordinately regulate the ubiquitin ligase chip. *Mol Cell*. 2011;43:599-612

38. Hartl FU. Molecular chaperones in cellular protein folding. *Nature*. 1996;381:571-579

39. Chen B, Retzlaff M, Roos T, Frydman J. Cellular strategies of protein quality control. *Cold Spring Harb Perspect Biol*. 2011;3:a004374

40. McClellan AJ, Tam S, Kaganovich D, Frydman J. Protein quality control: Chaperones culling corrupt conformations. *Nat Cell Biol*. 2005;7:736-741

41. McDonough H, Patterson C. Chip: A link between the chaperone and proteasome systems. *Cell Stress Chaperones*. 2003;8:303-308

42. McKinnon C, Tabrizi SJ. The ubiquitin-proteasome system in neurodegeneration. *Antioxid Redox Signal*. 2014;21:2302-2321

43. Zolk O, Schenke C, Sarikas A. The ubiquitin-proteasome system: Focus on the heart. *Cardiovasc Res*. 2006;70:410-421

44. Bhat KP, Greer SF. Proteolytic and non-proteolytic roles of ubiquitin and the ubiquitin proteasome system in transcriptional regulation. *Biochim Biophys Acta*. 2011;1809:150-155

45. Yao T, Ndoja A. Regulation of gene expression by the ubiquitin-proteasome system. *Semin Cell Dev Biol*. 2012;23:523-529

46. Bekker-Jensen S, Mailand N. The ubiquitin- and sumo-dependent signaling response to DNA double-strand breaks. *FEBS Lett*. 2011;585:2914-2919

47. Edelmann MJ, Nicholson B, Kessler BM. Pharmacological targets in the ubiquitin system offer new ways of treating cancer, neurodegenerative disorders and infectious diseases. *Expert Rev Mol Med*. 2011;13:e35

48. Mattiroli F, Sixma TK. Lysine-targeting specificity in ubiquitin and ubiquitin-like modification pathways. *Nat Struct Mol Biol*. 2014;21:308-316

49. Pickart CM, Eddins MJ. Ubiquitin: Structures, functions, mechanisms. *Biochim Biophys Acta*. 2004;1695:55-72

50. Pagan J, Seto T, Pagano M, Cittadini A. Role of the ubiquitin proteasome system in the heart. *Circ Res*. 2013;112:1046-1058

51. Tanji K, Kamitani T, Mori F, Kakita A, Takahashi H, Wakabayashi K. Trim9, a novel brain-specific e3 ubiquitin ligase, is repressed in the brain of parkinson's disease and dementia with lewy bodies. *Neurobiol Dis*. 2010;38:210-218

52. Reyes-Turcu FE, Wilkinson KD. Polyubiquitin binding and disassembly by deubiquitinating enzymes. *Chem Rev*. 2009;109:1495-1508

53. Ikeda F, Dikic I. Atypical ubiquitin chains: New molecular signals. 'Protein modifications: Beyond the usual suspects' review series. *EMBO Rep*. 2008;9:536-542

54. Hicke L. Protein regulation by monoubiquitin. *Nat Rev Mol Cell Biol*. 2001;2:195-201

55. Gu ZC, Enenkel C. Proteasome assembly. *Cell Mol Life Sci*. 2014;71:4729-4745

56. Ruschak AM, Religa TL, Breuer S, Witt S, Kay LE. The proteasome antechamber maintains substrates in an unfolded state. *Nature*. 2010;467:868-871

57. Rivett AJ. The multicatalytic proteinase complex. *Revis Biol Celular*. 1989;20:113-123

58. Orlowski M. The multicatalytic proteinase complex, a major extralysosomal proteolytic system. *Biochemistry*. 1990;29:10289-10297

59. Peters JM, Harris JR, Kleinschmidt JA. Ultrastructure of the approximately 26s complex containing the approximately 20s cylinder particle (multicatalytic proteinase/proteasome). *Eur J Cell Biol*. 1991;56:422-432

60. Reyes-Turcu FE, Ventii KH, Wilkinson KD. Regulation and cellular roles of ubiquitin-specific deubiquitinating enzymes. *Annu Rev Biochem*. 2009;78:363-397

61. Komander D, Clague MJ, Urbe S. Breaking the chains: Structure and function of the deubiquitinases. *Nat Rev Mol Cell Biol*. 2009;10:550-563

62. Searle MS, Garner TP, Strachan J, Long J, Adlington J, Cavey JR, Shaw B, Layfield R. Structural insights into specificity and diversity in mechanisms of ubiquitin recognition by ubiquitin-binding domains. *Biochem Soc Trans*. 2012;40:404-408

63. Dikic I, Wakatsuki S, Walters KJ. Ubiquitin-binding domains - from structures to functions. *Nat Rev Mol Cell Biol*. 2009;10:659-671

64. Arya R, Kedar V, Hwang JR, McDonough H, Li HH, Taylor J, Patterson C. Muscle ring finger protein-1 inhibits pkc{epsilon} activation and prevents cardiomyocyte hypertrophy. *J Cell Biol*. 2004;167:1147-1159

65. McElhinny AS, Kakinuma K, Sorimachi H, Labeit S, Gregorio CC. Muscle-specific ring finger-1 interacts with titin to regulate sarcomeric m-line and thick filament structure and may have nuclear functions via its interaction with glucocorticoid modulatory element binding protein-1. *J Cell Biol*. 2002;157:125-136

66. Li HH, Du J, Fan YN, Zhang ML, Liu DP, Li L, Lockyer P, Kang EY, Patterson C, Willis MS. The ubiquitin ligase murf1 protects against cardiac ischemia/reperfusion injury by its proteasome-dependent degradation of phospho-c-jun. *Am J Pathol*. 2011;178:1043-1058

67. Willis MS, Zungu M, Patterson C. Cardiac muscle ring finger-1--friend or foe? *Trends Cardiovasc Med*. 2010;20:12-16

68. Spencer JA, Eliazer S, Ilaria RL, Jr., Richardson JA, Olson EN. Regulation of microtubule dynamics and myogenic differentiation by murf, a striated muscle ring-finger protein. *J Cell Biol*. 2000;150:771-784

69. Centner T, Yano J, Kimura E, McElhinny AS, Pelin K, Witt CC, Bang ML, Trombitas K, Granzier H, Gregorio CC, Sorimachi H, Labeit S. Identification of muscle specific ring finger proteins as potential regulators of the titin kinase domain. *J Mol Biol*. 2001;306:717-726

70. Rodriguez JE, Liao JY, He J, Schisler JC, Newgard CB, Drujan D, Glass DJ, Frederick CB, Yoder BC, Lalush DS, Patterson C, Willis MS. The ubiquitin ligase murf1 regulates pparalpha activity in the heart by enhancing nuclear export via monoubiquitination. *Mol Cell Endocrinol*. 2015;413:36-48

71. Willis MS, Ike C, Li L, Wang DZ, Glass DJ, Patterson C. Muscle ring finger 1, but not muscle ring finger 2, regulates cardiac hypertrophy in vivo. *Circ Res*. 2007;100:456-459

72. Willis MS, Rojas M, Li L, Selzman CH, Tang RH, Stansfield WE, Rodriguez JE, Glass DJ, Patterson C. Muscle ring finger 1 mediates cardiac atrophy in vivo. *Am J Physiol Heart Circ Physiol*. 2009;296:H997-H1006

73. Kampinga HH, Kanon B, Salomons FA, Kabakov AE, Patterson C. Overexpression of the cochaperone chip enhances hsp70-dependent folding activity in mammalian cells. *Mol Cell Biol*. 2003;23:4948-4958

74. Dai Q, Zhang C, Wu Y, McDonough H, Whaley RA, Godfrey V, Li HH, Madamanchi N, Xu W, Neckers L, Cyr D, Patterson C. Chip activates hsf1 and confers protection against apoptosis and cellular stress. *The EMBO journal*. 2003;22:5446-5458

75. Qian SB, McDonough H, Boellmann F, Cyr DM, Patterson C. Chip-mediated stress recovery by sequential ubiquitination of substrates and hsp70. *Nature*. 2006;440:551-555

76. Esser C, Scheffner M, Hohfeld J. The chaperone-associated ubiquitin ligase chip is able to target p53 for proteasomal degradation. *J Biol Chem*. 2005;280:27443-27448

77. Shin Y, Klucken J, Patterson C, Hyman BT, McLean PJ. The co-chaperone carboxyl terminus of hsp70-interacting protein (chip) mediates alpha-synuclein degradation decisions between proteasomal and lysosomal pathways. *J Biol Chem*. 2005;280:23727-23734

78. Ko HS, Bailey R, Smith WW, Liu Z, Shin JH, Lee YI, Zhang YJ, Jiang H, Ross CA, Moore DJ, Patterson C, Petrucelli L, Dawson TM, Dawson VL. Chip regulates leucine-rich repeat kinase-2 ubiquitination, degradation, and toxicity. *Proc Natl Acad Sci U S A*. 2009;106:2897-2902

79. Qian SB, Waldron L, Choudhary N, Klevit RE, Chazin WJ, Patterson C. Engineering a ubiquitin ligase reveals conformational flexibility required for ubiquitin transfer. *The Journal of biological chemistry*. 2009;284:26797-26802

80. Nikolay R, Wiederkehr T, Rist W, Kramer G, Mayer MP, Bukau B. Dimerization of the human e3 ligase chip via a coiled-coil domain is essential for its activity. *J Biol Chem*. 2004;279:2673-2678

81. Ballinger CA, Connell P, Wu Y, Hu Z, Thompson LJ, Yin LY, Patterson C. Identification of chip, a novel tetratricopeptide repeat-containing protein that interacts with heat shock proteins and negatively regulates chaperone functions. *Mol Cell Biol*. 1999;19:4535-4545

82. Al-Ramahi I, Lam YC, Chen HK, de Gouyon B, Zhang M, Perez AM, Branco J, de Haro M, Patterson C, Zoghbi HY, Botas J. Chip protects from the neurotoxicity of expanded and wild-type ataxin-1 and promotes their ubiquitination and degradation. *J Biol Chem*. 2006;281:26714-26724

83. Willis MS, Min JN, Wang S, McDonough H, Lockyer P, Wadosky KM, Patterson C. Carboxyl terminus of hsp70-interacting protein (chip) is required to modulate cardiac hypertrophy and attenuate autophagy during exercise. *Cell Biochem Funct*. 2013

84. Zhang C, Xu Z, He XR, Michael LH, Patterson C. Chip, a cochaperone/ubiquitin ligase that regulates protein quality control, is required for maximal cardioprotection after myocardial infarction in mice. *Am J Physiol Heart Circ Physiol*. 2005;288:H2836-2842

85. Woo CH, Le NT, Shishido T, Chang E, Lee H, Heo KS, Mickelsen DM, Lu Y, McClain C, Spangenberg T, Yan C, Molina CA, Yang J, Patterson C, Abe J. Novel role of c terminus of hsc70-interacting protein (chip) ubiquitin ligase on inhibiting cardiac apoptosis and dysfunction via regulating erk5-mediated degradation of inducible camp early repressor. *FASEB J*. 2010;24:4917-4928

86. Le NT, Takei Y, Shishido T, Woo CH, Chang E, Heo KS, Lee H, Lu Y, Morrell C, Oikawa M, McClain C, Wang X, Tournier C, Molina CA, Taunton J, Yan C, Fujiwara K, Patterson C, Yang J, Abe J. P90rsk targets the erk5-chip ubiquitin e3 ligase activity in diabetic hearts and promotes cardiac apoptosis and dysfunction. *Circ Res*. 2012;110:536-550

87. Ronnebaum SM, Wu Y, McDonough H, Patterson C. The ubiquitin ligase chip prevents sirt6 degradation through noncanonical ubiquitination. *Molecular and cellular biology*. 2013

88. Quinton R, Barnett P, Coskeran P, Bouloux PM. Gordon holmes spinocerebellar ataxia: A gonadotrophin deficiency syndrome resistant to treatment with pulsatile gonadotrophin-releasing hormone. *Clin Endocrinol (Oxf)*. 1999;51:525-529

89. Ronnebaum SM PC, Schisler JC. Emerging evidence of coding mutations in the ubiquitin–proteasome system associated with cerebellar ataxias. *Human Genome Variation*. 2014;1

90. Synofzik M, Schule R, Schulze M, Gburek-Augustat J, Schweizer R, Schirmacher A, Krageloh-Mann I, Gonzalez M, Young P, Zuchner S, Schols L, Bauer P. Phenotype and frequency of stub1 mutations: Next-generation screenings in caucasian ataxia and spastic paraplegia cohorts. *Orphanet J Rare Dis*. 2014;9:57

91. Guedat P, Colland F. Patented small molecule inhibitors in the ubiquitin proteasome system. *BMC Biochem*. 2007;8 Suppl 1:S14

92. Richardson PG. Update on proteasome inhibitors in multiple myeloma. *Clin Adv Hematol Oncol*. 2014;12:179-181

93. Teicher BA, Tomaszewski JE. Proteasome inhibitors. *Biochem Pharmacol*. 2015;96:1-9

94. Landre V, Rotblat B, Melino S, Bernassola F, Melino G. Screening for e3-ubiquitin ligase inhibitors: Challenges and opportunities. *Oncotarget*. 2014;5:7988-8013

95. Zhang W, Sidhu SS. Development of inhibitors in the ubiquitination cascade. *FEBS Lett*. 2014;588:356-367

96. Liu J, Shaik S, Dai X, Wu Q, Zhou X, Wang Z, Wei W. Targeting the ubiquitin pathway for cancer treatment. *Biochim Biophys Acta*. 2015;1855:50-60

97. Khoo KH, Verma CS, Lane DP. Drugging the p53 pathway: Understanding the route to clinical efficacy. *Nat Rev Drug Discov*. 2014;13:217-236

98. Ray-Coquard I, Blay JY, Italiano A, Le Cesne A, Penel N, Zhi J, Heil F, Rueger R, Graves B, Ding M, Geho D, Middleton SA, Vassilev LT, Nichols GL, Bui BN. Effect of the mdm2 antagonist rg7112 on the p53 pathway in patients with mdm2-amplified, well-differentiated or dedifferentiated liposarcoma: An exploratory proof-of-mechanism study. *Lancet Oncol*. 2012;13:1133-1140

99. Colland F. The therapeutic potential of deubiquitinating enzyme inhibitors. *Biochem Soc Trans*. 2010;38:137-143

100. Lim KH, Baek KH. Deubiquitinating enzymes as therapeutic targets in cancer. *Curr Pharm Des*. 2013;19:4039-4052

101. Wilkie N, Davies S. Drug discovery world, drug discovery and development news.

102. Kedar V, McDonough H, Arya R, Li HH, Rockman HA, Patterson C. Muscle-specific ring finger 1 is a bona fide ubiquitin ligase that degrades cardiac troponin i. *Proc Natl Acad Sci U S A*. 2004;101:18135-18140

103. Polge C, Heng AE, Jarzaguet M, Ventadour S, Claustre A, Combaret L, Bechet D, Matondo M, Uttenweiler-Joseph S, Monsarrat B, Attaix D, Taillandier D. Muscle actin is polyubiquitinylated in vitro and in vivo and targeted for breakdown by the e3 ligase murf1. *FASEB J*. 2011;25:3790-3802

104. Mearini G, Schlossarek S, Willis MS, Carrier L. The ubiquitin-proteasome system in cardiac dysfunction. *Biochim Biophys Acta*. 2008;1782:749-763

105. Powell SR, Herrmann J, Lerman A, Patterson C, Wang X. The ubiquitin-proteasome system and cardiovascular disease. *Prog Mol Biol Transl Sci*. 2012;109:295-346

106. Powell SR. The ubiquitin-proteasome system in cardiac physiology and pathology. *Am J Physiol Heart Circ Physiol*. 2006;291:H1-H19

107. Zhang Y, Zeng Y, Wang M, Tian C, Ma X, Chen H, Fang Q, Jia L, Du J, Li H. Cardiac-specific overexpression of e3 ligase nrdp1 increases ischemia and reperfusion-induced cardiac injury. *Basic Res Cardiol*. 2011;106:371-383

108. Yu X, Kem DC. Proteasome inhibition during myocardial infarction. *Cardiovasc Res*. 2010;85:312-320

109. Nowis D, Maczewski M, Mackiewicz U, Kujawa M, Ratajska A, Wieckowski MR, Wilczynski GM, Malinowska M, Bil J, Salwa P, Bugajski M, Wojcik C, Sinski M, Abramczyk P, Winiarska M, Dabrowska-Iwanicka A, Duszynski J, Jakobisiak M, Golab J. Cardiotoxicity of the anticancer therapeutic agent bortezomib. *Am J Pathol*. 2010;176:2658-2668

110. Deshaies RJ, Joazeiro CA. Ring domain e3 ubiquitin ligases. *Annu Rev Biochem*. 2009;78:399-434

111. Wu Z, Chen Y, Yang T, Gao Q, Yuan M, Ma L. Targeted ubiquitination and degradation of g-protein-coupled receptor kinase 5 by the ddb1-cul4 ubiquitin ligase complex. *PLoS One*. 2012;7:e43997

112. Peschiaroli A, Dorrello NV, Guardavaccaro D, Venere M, Halazonetis T, Sherman NE, Pagano M. Scfbetatrcp-mediated degradation of claspin regulates recovery from the DNA replication checkpoint response. *Mol Cell*. 2006;23:319-329

113. Kus B, Gajadhar A, Stanger K, Cho R, Sun W, Rouleau N, Lee T, Chan D, Wolting C, Edwards A, Bosse R, Rotin D. A high throughput screen to identify substrates for the ubiquitin ligase rsp5. *J Biol Chem*. 2005;280:29470-29478

114. Loch CM, Eddins MJ, Strickler JE. Protein microarrays for the identification of praja1 e3 ubiquitin ligase substrates. *Cell Biochem Biophys*. 2011;60:127-135

115. Hjerpe R, Aillet F, Lopitz-Otsoa F, Lang V, England P, Rodriguez MS. Efficient protection and isolation of ubiquitylated proteins using tandem ubiquitin-binding entities. *EMBO Rep*. 2009;10:1250-1258

116. Witt SH, Granzier H, Witt CC, Labeit S. Murf-1 and murf-2 target a specific subset of myofibrillar proteins redundantly: Towards understanding murf-dependent muscle ubiquitination. *J Mol Biol*. 2005;350:713-722

117. Kim W, Bennett EJ, Huttlin EL, Guo A, Li J, Possemato A, Sowa ME, Rad R, Rush J, Comb MJ, Harper JW, Gygi SP. Systematic and quantitative assessment of the ubiquitin-modified proteome. *Mol Cell*. 2011;44:325-340

118. Cohen S, Brault JJ, Gygi SP, Glass DJ, Valenzuela DM, Gartner C, Latres E, Goldberg AL. During muscle atrophy, thick, but not thin, filament components are degraded by murf1-dependent ubiquitylation. *J Cell Biol*. 2009;185:1083-1095

119. Wagner SA, Beli P, Weinert BT, Nielsen ML, Cox J, Mann M, Choudhary C. A proteome-wide, quantitative survey of in vivo ubiquitylation sites reveals widespread regulatory roles. *Mol Cell Proteomics*. 2011;10:M111 013284

120. Portbury AL, Willis MS, Patterson C. Tearin' up my heart: Proteolysis in the cardiac sarcomere. *J Biol Chem*. 2011;286:9929-9934

121. Willis MS, Schisler JC, Li L, Rodriguez JE, Hilliard EG, Charles PC, Patterson C. Cardiac muscle ring finger-1 increases susceptibility to heart failure in vivo. *Circ Res*. 2009;105:80-88

122. David Y, Ternette N, Edelmann MJ, Ziv T, Gayer B, Sertchook R, Dadon Y, Kessler BM, Navon A. E3 ligases determine ubiquitination site and conjugate type by enforcing specificity on e2 enzymes. *J Biol Chem*. 2011;286:44104-44115

123. Hoeller D, Hecker CM, Wagner S, Rogov V, Dotsch V, Dikic I. E3-independent monoubiquitination of ubiquitin-binding proteins. *Mol Cell*. 2007;26:891-898

124. Friedman DB, Hoving S, Westermeier R. Isoelectric focusing and two-dimensional gel electrophoresis. *Methods Enzymol*. 2009;463:515-540

125. Zhu W, Smith JW, Huang CM. Mass spectrometry-based label-free quantitative proteomics. *J Biomed Biotechnol*. 2010;2010:840518

126. Toraason M, Luken ME, Breitenstein M, Krueger JA, Biagini RE. Comparative toxicity of allylamine and acrolein in cultured myocytes and fibroblasts from neonatal rat heart. *Toxicology*. 1989;56:107-117

127. Osorio C, Sullivan PM, He DN, Mace BE, Ervin JF, Strittmatter WJ, Alzate O. Mortalin is regulated by apoe in hippocampus of ad patients and by human apoe in tr mice. *Neurobiol Aging*. 2007;28:1853-1862

128. Jiang J, Ballinger CA, Wu Y, Dai Q, Cyr DM, Hohfeld J, Patterson C. Chip is a u-box-dependent e3 ubiquitin ligase: Identification of hsc70 as a target for ubiquitylation. *J Biol Chem*. 2001;276:42938-42944

129. Holmes G. A form of familial degeneration of the cerebellum. *Brain*. 1908;30:466-489

130. Santens P, Van Damme T, Steyaert W, Willaert A, Sablonniere B, De Paepe A, Coucke PJ, Dermaut B. Rnf216 mutations as a novel cause of autosomal recessive huntington-like disorder. *Neurology*. 2015;84:1760-1766

131. Berciano J, Amado JA, Freijanes J, Rebollo M, Vaquero A. Familial cerebellar ataxia and hypogonadotropic hypogonadism: Evidence for hypothalamic lhrh deficiency. *J Neurol Neurosurg Psychiatry*. 1982;45:747-751

132. Seminara SB, Acierno JS, Jr., Abdulwahid NA, Crowley WF, Jr., Margolin DH. Hypogonadotropic hypogonadism and cerebellar ataxia: Detailed phenotypic

characterization of a large, extended kindred. *J Clin Endocrinol Metab*. 2002;87:1607-1612

133. Alsemari A. Hypogonadism and neurological diseases. *Neurol Sci*. 2013;34:629-638

134. Connell P, Ballinger CA, Jiang J, Wu Y, Thompson LJ, Hohfeld J, Patterson C. The co-chaperone chip regulates protein triage decisions mediated by heat-shock proteins. *Nat Cell Biol*. 2001;3:93-96

135. Rosser MF, Washburn E, Muchowski PJ, Patterson C, Cyr DM. Chaperone functions of the e3 ubiquitin ligase chip. *J Biol Chem*. 2007;282:22267-22277

136. Margolin DH, Kousi M, Chan YM, Lim ET, Schmahmann JD, Hadjivassiliou M, Hall JE, Adam I, Dwyer A, Plummer L, Aldrin SV, O'Rourke J, Kirby A, Lage K, Milunsky A, Milunsky JM, Chan J, Hedley-Whyte ET, Daly MJ, Katsanis N, Seminara SB. Ataxia, dementia, and hypogonadotropism caused by disordered ubiquitination. *N Engl J Med*. 2013;368:1992-2003

137. Petrucelli L, Dickson D, Kehoe K, Taylor J, Snyder H, Grover A, De Lucia M, McGowan E, Lewis J, Prihar G, Kim J, Dillmann WH, Browne SE, Hall A, Voellmy R, Tsuboi Y, Dawson TM, Wolozin B, Hardy J, Hutton M. Chip and hsp70 regulate tau ubiquitination, degradation and aggregation. *Hum Mol Genet*. 2004;13:703-714

138. Tetzlaff JE, Putcha P, Outeiro TF, Ivanov A, Berezovska O, Hyman BT, McLean PJ. Chip targets toxic alpha-synuclein oligomers for degradation. *J Biol Chem*. 2008;283:17962-17968

139. Lessig S, Nie D, Xu R, Corey-Bloom J. Changes on brief cognitive instruments over time in parkinson's disease. *Movement disorders : official journal of the Movement Disorder Society*. 2012;27:1125-1128

140. Sherry ST, Ward MH, Kholodov M, Baker J, Phan L, Smigielski EM, Sirotkin K. Dbsnp: The ncbi database of genetic variation. *Nucleic acids research*. 2001;29:308-311

141. Genomes Project C, Abecasis GR, Altshuler D, Auton A, Brooks LD, Durbin RM, Gibbs RA, Hurles ME, McVean GA. A map of human genome variation from population-scale sequencing. *Nature*. 2010;467:1061-1073

142. International HapMap C, Frazer KA, Ballinger DG, Cox DR, Hinds DA, Stuve LL, Gibbs RA, Belmont JW, Boudreau A, Hardenbol P, Leal SM, Pasternak S, Wheeler DA, Willis TD, Yu F, Yang H, Zeng C, Gao Y, Hu H, Hu W, Li C, Lin W, Liu S, Pan H, Tang X, Wang J, Wang W, Yu J, Zhang B, Zhang Q, Zhao H, Zhao H, Zhou J, Gabriel SB, Barry R, Blumenstiel B, Camargo A, Defelice M, Faggart M, Goyette M, Gupta S, Moore J, Nguyen H, Onofrio RC, Parkin M, Roy J, Stahl E, Winchester E, Ziaugra L, Altshuler D, Shen Y, Yao Z, Huang W, Chu X, He Y, Jin L, Liu Y, Shen Y, Sun W, Wang H, Wang Y, Wang Y, Xiong X, Xu L, Waye MM, Tsui SK, Xue H, Wong JT, Galver LM, Fan JB, Gunderson K, Murray SS, Oliphant AR, Chee MS, Montpetit A, Chagnon F, Ferretti V, Leboeuf M, Olivier JF, Phillips MS, Roumy S, Sallee C, Verner A, Hudson TJ, Kwok

PY, Cai D, Koboldt DC, Miller RD, Pawlikowska L, Taillon-Miller P, Xiao M, Tsui LC, Mak W, Song YQ, Tam PK, Nakamura Y, Kawaguchi T, Kitamoto T, Morizono T, Nagashima A, Ohnishi Y, Sekine A, Tanaka T, Tsunoda T, Deloukas P, Bird CP, Delgado M, Dermitzakis ET, Gwilliam R, Hunt S, Morrison J, Powell D, Stranger BE, Whittaker P, Bentley DR, Daly MJ, de Bakker PI, Barrett J, Chretien YR, Maller J, McCarroll S, Patterson N, Pe'er I, Price A, Purcell S, Richter DJ, Sabeti P, Saxena R, Schaffner SF, Sham PC, Varilly P, Altshuler D, Stein LD, Krishnan L, Smith AV, Tello-Ruiz MK, Thorisson GA, Chakravarti A, Chen PE, Cutler DJ, Kashuk CS, Lin S, Abecasis GR, Guan W, Li Y, Munro HM, Qin ZS, Thomas DJ, McVean G, Auton A, Bottolo L, Cardin N, Eyheramendy S, Freeman C, Marchini J, Myers S, Spencer C, Stephens M, Donnelly P, Cardon LR, Clarke G, Evans DM, Morris AP, Weir BS, Tsunoda T, Mullikin JC, Sherry ST, Feolo M, Skol A, Zhang H, Zeng C, Zhao H, Matsuda I, Fukushima Y, Macer DR, Suda E, Rotimi CN, Adebamowo CA, Ajayi I, Aniagwu T, Marshall PA, Nkwodimmah C, Royal CD, Leppert MF, Dixon M, Peiffer A, Qiu R, Kent A, Kato K, Niikawa N, Adewole IF, Knoppers BM, Foster MW, Clayton EW, Watkin J, Gibbs RA, Belmont JW, Muzny D, Nazareth L, Sodergren E, Weinstock GM, Wheeler DA, Yakub I, Gabriel SB, Onofrio RC, Richter DJ, Ziaugra L, Birren BW, Daly MJ, Altshuler D, Wilson RK, Fulton LL, Rogers J, Burton J, Carter NP, Clee CM, Griffiths M, Jones MC, McLay K, Plumb RW, Ross MT, Sims SK, Willey DL, Chen Z, Han H, Kang L, Godbout M, Wallenburg JC, L'Archeveque P, Bellemare G, Saeki K, Wang H, An D, Fu H, Li Q, Wang Z, Wang R, Holden AL, Brooks LD, McEwen JE, Guyer MS, Wang VO, Peterson JL, Shi M, Spiegel J, Sung LM, Zacharia LF, Collins FS, Kennedy K, Jamieson R, Stewart J. A second generation human haplotype map of over 3.1 million snps. *Nature*. 2007;449:851-861

143. International HapMap C. A haplotype map of the human genome. *Nature*. 2005;437:1299-1320

144. Li G, Ma L, Song C, Yang Z, Wang X, Huang H, Li Y, Li R, Zhang X, Yang H, Wang J, Wang J. The yh database: The first asian diploid genome database. *Nucleic acids research*. 2009;37:D1025-1028

145. Tennessen JA, Bigham AW, O'Connor TD, Fu W, Kenny EE, Gravel S, McGee S, Do R, Liu X, Jun G, Kang HM, Jordan D, Leal SM, Gabriel S, Rieder MJ, Abecasis G, Altshuler D, Nickerson DA, Boerwinkle E, Sunyaev S, Bustamante CD, Bamshad MJ, Akey JM, Broad GO, Seattle GO, Project NES. Evolution and functional impact of rare coding variation from deep sequencing of human exomes. *Science*. 2012;337:64-69

146. Krawitz PM, Schweiger MR, Rodelsperger C, Marcelis C, Kolsch U, Meisel C, Stephani F, Kinoshita T, Murakami Y, Bauer S, Isau M, Fischer A, Dahl A, Kerick M, Hecht J, Kohler S, Jager M, Grunhagen J, de Condor BJ, Doelken S, Brunner HG, Meinecke P, Passarge E, Thompson MD, Cole DE, Horn D, Roscioli T, Mundlos S, Robinson PN. Identity-by-descent filtering of exome sequence data identifies pigv mutations in hyperphosphatasia mental retardation syndrome. *Nat Genet*. 2010;42:827-829

147. Rodelsperger C, Krawitz P, Bauer S, Hecht J, Bigham AW, Bamshad M, de Condor BJ, Schweiger MR, Robinson PN. Identity-by-descent filtering of exome sequence data for

disease-gene identification in autosomal recessive disorders. *Bioinformatics*. 2011;27:829-836

148. Adzhubei IA, Schmidt S, Peshkin L, Ramensky VE, Gerasimova A, Bork P, Kondrashov AS, Sunyaev SR. A method and server for predicting damaging missense mutations. *Nature methods*. 2010;7:248-249

149. Kumar P, Henikoff S, Ng PC. Predicting the effects of coding non-synonymous variants on protein function using the sift algorithm. *Nature protocols*. 2009;4:1073-1081

150. Sailer A, Houlden H. Recent advances in the genetics of cerebellar ataxias. *Current neurology and neuroscience reports*. 2012;12:227-236

151. Sathirapongsasuti JF, Lee H, Horst BA, Brunner G, Cochran AJ, Binder S, Quackenbush J, Nelson SF. Exome sequencing-based copy-number variation and loss of heterozygosity detection: Exomecnv. *Bioinformatics*. 2011;27:2648-2654

152. Zhang M, Windheim M, Roe SM, Peggie M, Cohen P, Prodromou C, Pearl LH. Chaperoned ubiquitylation--crystal structures of the chip u box e3 ubiquitin ligase and a chip-ubc13-uev1a complex. *Mol Cell*. 2005;20:525-538

153. Meacham GC, Patterson C, Zhang W, Younger JM, Cyr DM. The hsc70 co-chaperone chip targets immature cftr for proteasomal degradation. *Nat Cell Biol*. 2001;3:100-105

154. Kumar P, Pradhan K, Karunya R, Ambasta RK, Querfurth HW. Cross-functional e3 ligases parkin and c-terminus hsp70-interacting protein in neurodegenerative disorders. *J Neurochem*. 2012;120:350-370

155. Min JN, Whaley RA, Sharpless NE, Lockyer P, Portbury AL, Patterson C. Chip deficiency decreases longevity, with accelerated aging phenotypes accompanied by altered protein quality control. *Mol Cell Biol*. 2008;28:4018-4025

156. Anderson LG, Meeker RB, Poulton WE, Huang DY. Brain distribution of carboxy terminus of hsc70-interacting protein (chip) and its nuclear translocation in cultured cortical neurons following heat stress or oxygen-glucose deprivation. *Cell stress & chaperones*. 2010;15:487-495

157. Becker EB, Oliver PL, Glitsch MD, Banks GT, Achilli F, Hardy A, Nolan PM, Fisher EM, Davies KE. A point mutation in trpc3 causes abnormal purkinje cell development and cerebellar ataxia in moonwalker mice. *Proceedings of the National Academy of Sciences of the United States of America*. 2009;106:6706-6711

158. Sleat DE, Wiseman JA, El-Banna M, Price SM, Verot L, Shen MM, Tint GS, Vanier MT, Walkley SU, Lobel P. Genetic evidence for nonredundant functional cooperativity between npc1 and npc2 in lipid transport. *Proceedings of the National Academy of Sciences of the United States of America*. 2004;101:5886-5891

159. Yang Q, Hashizume Y, Yoshida M, Wang Y, Goto Y, Mitsuma N, Ishikawa K, Mizusawa H. Morphological purkinje cell changes in spinocerebellar ataxia type 6. *Acta neuropathologica*. 2000;100:371-376

160. Bernard G, Chouery E, Putorti ML, Tetreault M, Takanohashi A, Carosso G, Clement I, Boespflug-Tanguy O, Rodriguez D, Delague V, Abou Ghoch J, Jalkh N, Dorboz I, Fribourg S, Teichmann M, Megarbane A, Schiffmann R, Vanderver A, Brais B. Mutations of polr3a encoding a catalytic subunit of rna polymerase pol iii cause a recessive hypomyelinating leukodystrophy. *Am J Hum Genet*. 2011;89:415-423

161. Martin E, Schule R, Smets K, Rastetter A, Boukhris A, Loureiro JL, Gonzalez MA, Mundwiller E, Deconinck T, Wessner M, Jornea L, Oteyza AC, Durr A, Martin JJ, Schols L, Mhiri C, Lamari F, Zuchner S, De Jonghe P, Kabashi E, Brice A, Stevanin G. Loss of function of glucocerebrosidase gba2 is responsible for motor neuron defects in hereditary spastic paraplegia. *Am J Hum Genet*. 2013;92:238-244

162. Shi Y, Wang J, Li JD, Ren H, Guan W, He M, Yan W, Zhou Y, Hu Z, Zhang J, Xiao J, Su Z, Dai M, Jiang H, Guo J, Zhang F, Li N, Du J, Xu Q, Hu Y, Pan Q, Shen L, Wang G, Xia K, Zhang Z, Tang B. Identification of chip as a novel causative gene for autosomal recessive cerebellar ataxia. *PLoS One*. 2013;8:e81884

163. Depondt C, Donatello S, Simonis N, Rai M, van Heurck R, Abramowicz M, D'Hooghe M, Pandolfo M. Autosomal recessive cerebellar ataxia of adult onset due to stub1 mutations. *Neurology*. 2014;82:1749-1750

164. Cordoba M, Rodriguez-Quiroga S, Gatto EM, Alurralde A, Kauffman MA. Ataxia plus myoclonus in a 23-year-old patient due to stub1 mutations. *Neurology*. 2014;83:287-288

165. Heimdal K, Sanchez-Guixe M, Aukrust I, Bollerslev J, Bruland O, Jablonski GE, Erichsen AK, Gude E, Koht JA, Erdal S, Fiskerstrand T, Haukanes BI, Boman H, Bjorkhaug L, Tallaksen CM, Knappskog PM, Johansson S. Stub1 mutations in autosomal recessive ataxias - evidence for mutation-specific clinical heterogeneity. *Orphanet J Rare Dis*. 2014;9:146

166. Bettencourt C, de Yebenes JG, Lopez-Sendon JL, Shomroni O, Zhang X, Qian SB, Bakker IM, Heetveld S, Ros R, Quintans B, Sobrido MJ, Bevova MR, Jain S, Bugiani M, Heutink P, Rizzu P. Clinical and neuropathological features of spastic ataxia in a spanish family with novel compound heterozygous mutations in stub1. *Cerebellum*. 2015;14:378-381

167. Li R, Yu C, Li Y, Lam TW, Yiu SM, Kristiansen K, Wang J. Soap2: An improved ultrafast tool for short read alignment. *Bioinformatics*. 2009;25:1966-1967

168. Li H, Durbin R. Fast and accurate short read alignment with burrows-wheeler transform. *Bioinformatics*. 2009;25:1754-1760

169. Paylor R, Crawley JN. Inbred strain differences in prepulse inhibition of the mouse startle response. *Psychopharmacology (Berl)*. 1997;132:169-180

170. Garman RH. Histology of the central nervous system. *Toxicologic pathology*. 2011;39:22-35

171. Uhlen M, Oksvold P, Fagerberg L, Lundberg E, Jonasson K, Forsberg M, Zwahlen M, Kampf C, Wester K, Hober S, Wernerus H, Bjorling L, Ponten F. Towards a knowledge-based human protein atlas. *Nature biotechnology*. 2010;28:1248-1250

172. Graf C, Stankiewicz M, Nikolay R, Mayer MP. Insights into the conformational dynamics of the e3 ubiquitin ligase chip in complex with chaperones and e2 enzymes. *Biochemistry*. 2010;49:2121-2129

173. Zwickl P, Seemuller E, Kapelari B, Baumeister W. The proteasome: A supramolecular assembly designed for controlled proteolysis. *Adv Protein Chem*. 2001;59:187-222

174. Shiber A, Ravid T. Chaperoning proteins for destruction: Diverse roles of hsp70 chaperones and their co-chaperones in targeting misfolded proteins to the proteasome. *Biomolecules*. 2014;4:704-724

175. Guo J, Ren F, Wang Y, Li S, Gao Z, Wang X, Ning H, Wu J, Li Y, Wang Z, Chim SM, Xu J, Chang Z. Mir-764-5p promotes osteoblast differentiation through inhibition of chip/stub1 expression. *J Bone Miner Res*. 2012;27:1607-1618

176. Kalia LV, Kalia SK, Chau H, Lozano AM, Hyman BT, McLean PJ. Ubiquitinylation of alpha-synuclein by carboxyl terminus hsp70-interacting protein (chip) is regulated by bcl-2-associated athanogene 5 (bag5). *PLoS One*. 2011;6:e14695

177. Zhang X, Qian SB. Chaperone-mediated hierarchical control in targeting misfolded proteins to aggresomes. *Mol Biol Cell*. 2011;22:3277-3288

178. Dunkern TR, Kaina B. Cell proliferation and DNA breaks are involved in ultraviolet light-induced apoptosis in nucleotide excision repair-deficient chinese hamster cells. *Mol Biol Cell*. 2002;13:348-361

179. Ingwall JS, Weiss RG. Is the failing heart energy starved? On using chemical energy to support cardiac function. *Circ Res*. 2004;95:135-145

180. Tian R, Musi N, D'Agostino J, Hirshman MF, Goodyear LJ. Increased adenosine monophosphate-activated protein kinase activity in rat hearts with pressure-overload hypertrophy. *Circulation*. 2001;104:1664-1669

181. Zhang P, Hu X, Xu X, Fassett J, Zhu G, Viollet B, Xu W, Wiczer B, Bernlohr DA, Bache RJ, Chen Y. Amp activated protein kinase-alpha2 deficiency exacerbates pressure-overload-induced left ventricular hypertrophy and dysfunction in mice. *Hypertension*. 2008;52:918-924

182. Kim AS, Miller EJ, Young LH. Amp-activated protein kinase: A core signalling pathway in the heart. *Acta Physiol (Oxf)*. 2009;196:37-53

183. Choi SL, Kim SJ, Lee KT, Kim J, Mu J, Birnbaum MJ, Soo Kim S, Ha J. The regulation of amp-activated protein kinase by h(2)o(2). *Biochem Biophys Res Commun*. 2001;287:92-97

184. Casarejos MJ, Perucho J, Lopez-Sendon JL, Garcia de Yebenes J, Bettencourt C, Gomez A, Ruiz C, Heutink P, Rizzu P, Mena MA. Trehalose improves human fibroblast deficits in a new chip-mutation related ataxia. *PLoS One*. 2014;9:e106931

185. Bearzatto B, Servais L, Cheron G, Schiffmann SN. Age dependence of strain determinant on mice motor coordination. *Brain Res*. 2005;1039:37-42

186. Cendelin J. From mice to men: Lessons from mutant ataxic mice. *Cerebellum Ataxias*. 2014;1:4

187. Porras-Garcia E, Cendelin J, Dominguez-del-Toro E, Vozeh F, Delgado-Garcia JM. Purkinje cell loss affects differentially the execution, acquisition and prepulse inhibition of skeletal and facial motor responses in lurcher mice. *Eur J Neurosci*. 2005;21:979-988

188. van Enkhuizen J, Geyer MA, Halberstadt AL, Zhuang X, Young JW. Dopamine depletion attenuates some behavioral abnormalities in a hyperdopaminergic mouse model of bipolar disorder. *J Affect Disord*. 2014;155:247-254

189. Matzel LD, Babiarz J, Townsend DA, Grossman HC, Grumet M. Neuronal cell adhesion molecule deletion induces a cognitive and behavioral phenotype reflective of impulsivity. *Genes Brain Behav*. 2008;7:470-480

190. Schmahmann JD. Disorders of the cerebellum: Ataxia, dysmetria of thought, and the cerebellar cognitive affective syndrome. *J Neuropsychiatry Clin Neurosci*. 2004;16:367-378

191. Hoche F, Frankenberg E, Rambow J, Theis M, Harding JA, Qirshi M, Seidel K, Barbosa-Sicard E, Porto L, Schmahmann JD, Kieslich M. Cognitive phenotype in ataxia-telangiectasia. *Pediatr Neurol*. 2014;51:297-310

192. Schmahmann JD, Sherman JC. The cerebellar cognitive affective syndrome. *Brain*. 1998;121 (Pt 4):561-579

193. Huang HS, Burns AJ, Nonneman RJ, Baker LK, Riddick NV, Nikolova VD, Riday TT, Yashiro K, Philpot BD, Moy SS. Behavioral deficits in an angelman syndrome model: Effects of genetic background and age. *Behav Brain Res*. 2013;243:79-90

194. Soss SE, Yue Y, Dhe-Paganon S, Chazin WJ. E2 conjugating enzyme selectivity and requirements for function of the e3 ubiquitin ligase chip. *J Biol Chem*. 2011;286:21277-21286

195. Delaglio F, Grzesiek S, Vuister GW, Zhu G, Pfeifer J, Bax A. Nmrpipe: A multidimensional spectral processing system based on unix pipes. *J Biomol NMR*. 1995;6:277-293

196. Goddard T. D., G. KD. Sparky 3. 2006

197. Feldkamp MD, Mason AC, Eichman BF, Chazin WJ. Structural analysis of replication protein a recruitment of the DNA damage response protein smarcal1. *Biochemistry*. 2014;53:3052-3061

198. Andersen CL, Jensen JL, Orntoft TF. Normalization of real-time quantitative reverse transcription-pcr data: A model-based variance estimation approach to identify genes suited for normalization, applied to bladder and colon cancer data sets. *Cancer Res*. 2004;64:5245-5250

199. Dai Q, Qian SB, Li HH, McDonough H, Borchers C, Huang D, Takayama S, Younger JM, Ren HY, Cyr DM, Patterson C. Regulation of the cytoplasmic quality control protein degradation pathway by bag2. *J Biol Chem*. 2005;280:38673-38681

200. Heffernan TP, Simpson DA, Frank AR, Heinloth AN, Paules RS, Cordeiro-Stone M, Kaufmann WK. An atr- and chk1-dependent s checkpoint inhibits replicon initiation following uvc-induced DNA damage. *Mol Cell Biol*. 2002;22:8552-8561

201. Mattox TA, Young ME, Rubel CE, Spaniel C, Rodriguez JE, Grevengoed TJ, Gautel M, Xu Z, Anderson EJ, Willis MS. Murf1 activity is present in cardiac mitochondria and regulates reactive oxygen species production in vivo. *J Bioenerg Biomembr*. 2014;46:173-187

202. Zheng Q, Su H, Tian Z, Wang X. Proteasome malfunction activates macroautophagy in the heart. *Am J Cardiovasc Dis*. 2011;1:214-226

203. Rustay NR, Wahlsten D, Crabbe JC. Assessment of genetic susceptibility to ethanol intoxication in mice. *Proc Natl Acad Sci U S A*. 2003;100:2917-2922

204. Kamens HM, Crabbe JC. The parallel rod floor test: A measure of ataxia in mice. *Nat Protoc*. 2007;2:277-281